COMPUTATIONAL STUDIES OF MONO- AND BIMETALLIC NANOCLUSTERS FOR POTENTIAL POLYMER ELECTROLYTE FUEL CELL APPLICATIONS

by

PAUL CHRISTOPHER JENNINGS

A thesis submitted to the

University of Birmingham

for the degree of

DOCTOR OF PHILOSOPHY

Centre for Hydrogen and Fuel Cell Research

School of Chemical Engineering

College of Engineering and Physical Sciences

University of Birmingham

April 2014

Abstract

One of the main problems with the Polymer Electrolyte Fuel Cell (PEFC) is the expensive platinum (Pt) electrocatalyst. This thesis aims to investigate alloying of Pt with cheaper metals that not only reduce the overall cost but also alter the electronic properties to improve reaction kinetics. At the cathode, where the Oxygen Reduction Reaction (ORR) takes place, strong binding of oxygen (O) inhibits PEFC performance.

A Genetic Algorithm (GA) coupled with Density Functional Theory (DFT) approach has been used to perform structural searches on small Pt clusters doped with early transition metals (M). Spin effects have been studied and the global minimum structures predicted for the various spin multiplicities. It is found that varying spin can have significant effects on the pure Pt clusters, while doping with early transition metals leads to spin quenching.

DFT studies have been performed to predict potential Pt-based alloy nanoparticles that will result in weaker Pt–O interactions. This is achieved by investigating nanoalloys that lead to filling of the Pt *d*-band. When the *d*-band is filled there is a reduction in the low energy states available for oxygen to interact, with resulting weakening of the Pt–O bond. Early transition metals are found to be most promising, where donation of electron density from M to Pt results in additional filling of the Pt *d*-band. This filling can be "tuned" based on cluster size, shape and composition.

The surfaces of pure Pt clusters are found to distort, facilitating fast oxygen dissociation. Further DFT studies have been performed to investigate the effect of alloying Pt on the early stages of the ORR. It is found that the strong Pt-M interactions, which lead to filling of the d-band, can lead to Pt clusters becoming more structurally rigid, which inhibits oxygen dis-

sociation. A search has been performed to find the best compromise for a system that retains flexibility of the Pt surface, to allow fast dissociation while also allowing M to Pt electron donation, leading to filling of the Pt *d*-band.

Acknowledgements

Firstly, I am grateful to my supervisor Prof. Roy Johnston for his help, guidance and support, as well as guidance from Prof. Lynne Macaskie and Dr Bruno Pollet. I am thankful to the other members of the Johnston and Hydrogen & Fuel Cell research groups for their assistance with various aspects of this work. Special thanks to Prof. Konstantin Neyman and Dr Hristiyan Aleksandrov for welcoming me to Barcelona and giving guidance on several aspects of the work.

This research was funded through RCUK doctoral training centre in hydrogen, Fuel cells and their applications (EP/G037116/1). I would like to thank COST Action MP0903: "Nanoalloys as Advanced Materials: From Structure to Properties and Applications" for financial support. The oxygen dissociation work was performed under the HPC-EUROPA2 project (project number: 228398) with the support of the European Commission - Capacities Area - Research Infrastructures. The computations described in this thesis were performed using The University of Birmingham's BlueBEAR HPC service, as well as time on MidPlus. Via membership of the UK's HPC Materials Chemistry Consortium, which is funded by EPSRC (EP/F067496), this work made use of the facilities of HECToR, the UK's national high-performance computing service, which is provided by UoE HPCx Ltd at the University of Edinburgh, Cray Inc and NAG Ltd, and funded by the Office of Science and Technology through EPSRC's High End Computing Programme. Furthermore, computational time granted by the Barcelona Supercomputing Centre on the Marenostrum supercomputers is gratefully acknowledged.

On the personal note, I would like to thank my fiancée Sarah for her constant support and love and my parents Jacqueline and Peter as well as my grandmother Margaret.

Papers Published

1. "*Theoretical studies of Pt-Ti nanoparticles for potential use as PEMFC electrocatalysts*". Paul C. Jennings; Bruno G. Pollet; and Roy L. Johnston. *Phys. Chem. Chem. Phys.*, **2012**, *14* (9), pp 3134–3139.

2. "*Electronic Properties of Pt-Ti Nanoalloys and the Effect on Reactivity for Use in PEM-FCs*". Paul C. Jennings; Bruno G. Pollet; and Roy L. Johnston. *J. Phys. Chem. C*, **2012**, *116* (29), pp 15241–15250.

3. "*Structures of small Ti- and V-doped Pt clusters: a GA-DFT study*". Paul C. Jennings; and Roy L. Johnston. *Comp. Theor. Chem.*, **2013**, *1021*, pp 91–100.

4. "*A DFT study of oxygen dissociation on platinum based nanoparticles*". Paul C. Jennings; Hristiyan A Aleksandrov; Konstantin M Neyman; and Roy L Johnston. *Nanoscale*, **2014**, *6*, pp 1153–1165.

Glossary of Abbreviations

DFT – Density Functional Theory

DOS – Density of States

FS – Final State

HOR – Hydrogen Oxidation Reaction

IS – Initial State

NEB –Nudged Elastic Band

ORR – Oxygen Reduction Reaction

pDOS –Partial Density of States

PEFC – Proton Electrolyte Fuel Cell

TO – Truncated Octahedron

TS – Transition State

Contents

List of Figures

List of Tables

Chapter 1

Introduction

1.1 Motivation

The increase in greenhouse gas emissions are an increasing problem, where world power generation is dominated by hydrocarbons. Security of supply is a cause for concern for various economic and political reasons. Furthermore, it is currently estimated that around 89% of the United Kingdom's energy is supplied by fossil fuels. This can be split into approximately 18% from coal, 38% from gas and 33% from oil. It is predicted that at current combustion rates (which are expected to increase) there are over 200 years of coal, 60 years of gas and 40 years of oil remaining [1]. The need for a clean, more environmentally friendly and sustainable energy source has been emphasised by many public and governmental bodies.

Along with security of supply, extraction, processing and utilisation of fossil fuels has led to a dramatic increase in greenhouse gas emissions (e.g. CO_2, CH_4, N_2O) with atmospheric CO_2 concentrations far beyond the natural historical maximum. Historically the maximum concentration of CO_2 in the atmosphere was around 300 ppm, whilst the current concentration is $\sim$390 ppm which is considered to present a significant risk of irreversible climate change [2].

To reduce dependency on hydrocarbons, there are several alternative forms of power generation: nuclear, biomass, solar, wind, hydroelectric, tidal and geothermal. There are both advantages and drawbacks to all of these energy sources [3–5]. A further option for energy

production is that of fuel cells, using fuels such as hydrogen or methanol. Fuel cells have the advantage of being more efficient than internal combustion engines [6], converting chemical energy directly to electricity [7]. Furthermore, if pure hydrogen is used as the fuel, then the only outputs are electricity, heat and water. This makes hydrogen significantly more environmentally friendly than hydrocarbon fuels. As fuel cells are powered by a transportable fuel, this means they are not reliant on environmental factors such as sun, light or wind. Therefore, the cells can be turned on or off when needed without loss of potential energy generation, negating problems associated with electrical storage.

1.2 The Hydrogen Economy

The term "hydrogen economy" refers to using hydrogen as a low-carbon energy source. However, hydrogen is not found in elemental form (H_2) on Earth, so it must be produced from other compounds such as natural gas, biomass, alcohols or water. Energy is therefore required to convert these into pure hydrogen, as well as other products. Hydrogen is therefore an energy carrier or storage medium rather than an energy source itself. The impact of using hydrogen as an energy source is dependent on the carbon footprint of the method used to produce it. Hydrogen can be produced from a diverse range of primary energy sources, with a low carbon footprint, e.g. by electrolysis [8–10]. It is therefore possible to produce hydrogen and aid balancing the national grid by using intermittent renewable energy at times when demand is low. For example, in 2013, energy companies were paid £30 million for wind farms to stand idle either when the National Grid was unable to cope with the extra power produced during high winds, or during periods of low demand [11].

Hydrogen does represent a promising clean energy vector as it can be stored, distributed and converted into energy at point of use and the only by-product when combusted, or reacted electrochemically with oxygen, is water. While there is an absence of emissions at point of use, distribution and storage of hydrogen in large volumes represents a significant challenge because of hydrogen's low volumetric energy density [12]. Although challenges must be overcome to

realise the potential of a "hydrogen economy", the most significant benefit is the utilisation of more efficient energy conversion technologies. The chemical simplicity of hydrogen, when compared to hydrocarbon compounds, makes it an ideal fuel for electrochemical conversion technologies, such as fuel cells. Complex hydrocarbon fuels are generally unsuitable for use in fuel cells, although some simple hydrocarbons can be used in high temperature fuel cells [13].

1.3 Fuel Cells

Welsh Physicist William Grove developed the first crude fuel cells in 1839, producing electricity from hydrogen and oxygen through a process that he dubbed "reverse electrolysis" [14]. Fuel cells provide a technology for clean, efficient power generation and show promise for many applications. Such applications include motor vehicles [15, 16], generators [17] and portable electronic devices [18]. Fuel cells are a subclass of electrochemical devices known as Galvanic cells, which also includes batteries. These devices convert chemical energy into electrical energy, although where a battery has a finite supply of reactants, the fuel cell is supplied by an external source and will continue to produce energy until the reactants are depleted [14].

Fuel cells generally consist of an anode and cathode (electrodes) separated by an electrolyte. The fuel cell field has developed with five main types of fuel cell currently being actively researched [19]; these are:

1. Phosphoric Acid
2. Alkaline
3. Molten Carbonate
4. Solid Oxide
5. Polymer Electrolyte

In all cases, a fuel supply, usually hydrogen, is oxidised at the anode, while oxygen is reduced at the cathode. The electrolytic charge carrier varies for the different fuel cell types. These can

be H^+ (Phosphoric Acid and Polymer Electrolyte), OH^- (Alkaline), CO_3^{2-} (Molten Carbonate) and O^{2-} (Solid Oxide) [20].

Phosphoric acid fuel cells use phosphoric acid as the electrolyte with platinum catalysts and operate in the temperature range of 150°C to 200°C. This means that they are used for continuous onsite stationary applications; furthermore, this type of fuel cell is not susceptible to carbon monoxide poisoning. Alkaline fuel cells utilise a porous matrix saturated with an aqueous alkaline solution as the electrolyte, such as potassium hydroxide (KOH), and also use platinum catalysts. The fuel cell can easily become poisoned through conversion of potassium hydroxide to potassium carbonate (K_2CO_3). This means that the cell must run on either pure oxygen or purified air with a "scrubber" fitted. Cells have been developed that can operate at low or high temperatures. The low temperature cells can operate at temperatures as low as 25°C to 75°C whilst the high temperature cells operate in the range of 100°C to 250°C.

Molten carbonate fuel cells have an electrolyte composed of a molten carbonate salt mixture which is suspended in a porous, chemically inert ceramic matrix (beta-alumina solid electrolyte). At the high operating temperatures of 650°C and over, non-precious metals can be used as catalysts, leading to cost reductions. These fuel cells are not prone to poisoning from carbon oxides and can even use them as a fuel. However, as a result of the high operating temperatures, components have reduced life expectancies. Solid oxide fuel cells have solid oxide electrolytes, for example yttria-stabilised zirconia, which are capable of conducting oxygen ions. Operating temperatures range between 500°C and 1000°C, meaning once again expensive precious metal catalysts are not required and CO poisoning is not an issue.

Proton exchange membrane (PEM) fuel cells utilise a polymer electrolyte membrane capable of conducting protons whilst preventing the transport of oxygen ions. PEM fuel cells run at low temperatures of between 50°C and 100°C. However the precious metal catalyst is susceptible to poisoning so it requires a pure supply of hydrogen and oxygen. They do have advantages of high power density, relatively quick start up and rapid response to varying loads. Direct methanol fuel cells are a subcategory of PEM fuel cells, operating at temperatures between 50°C and 120°C. Whereas hydrogen is commercially produced through steam methane

reforming, in this fuel cell, methanol is supplied directly. Water is required at the anode as an additional reactant to form CO_2.

1.4 Fuel Cell Systems

When considering implementing fuel cells it is important to consider that a system will most likely be required to provide the energy when needed. A set of fuel cells is often required, known as a fuel cell stack, as well as devices to provide fuel supply, cooling, power regulation and system monitoring [21]. The exact systems implemented will depend on their desired function. Systems required to be portable will have as few components as possible, whereas stationary systems will maximise the number of beneficial components for increased efficiency [22]. An advantage of the utilisation of stacks of fuel cells is that it is possible to scale the size of the stack to the required energy output. This means that it is not necessary to redesign the cell for applications requiring a larger output of energy. Instead it will be possible to increase stack size, or number of stacks, leading to increased output whilst only having to modify certain devices in the system. There is also interest in researching more efficient stack technologies [23].

1.5 Polymer Electrolyte Fuel Cells

The results in this thesis will be discussed with emphasis on energy production using a PEFC. A schematic of the basic PEFC is shown in Figure 1.1. Whilst the various types of fuel cell have slightly different mechanisms, the end products of water and energy are usually the same. PEFC contain two electrocatalysts and a proton conducting membrane. The fuel cell reaction is a chemical process, separated into two half-cell reactions.

Electrons produced at the anode continuously flow through an electrical circuit to the cathode. The protons are free to migrate through the cation-conducting polymer (or ionomer) membrane. The polymer separating the anode and cathode may contain mobile protons (the proton exchange membrane), but will prevent cross-over of oxygen. The membrane is thin ($\sim$20 μm) and light, so PEM fuel cells have high power densities. The membrane material dictates the

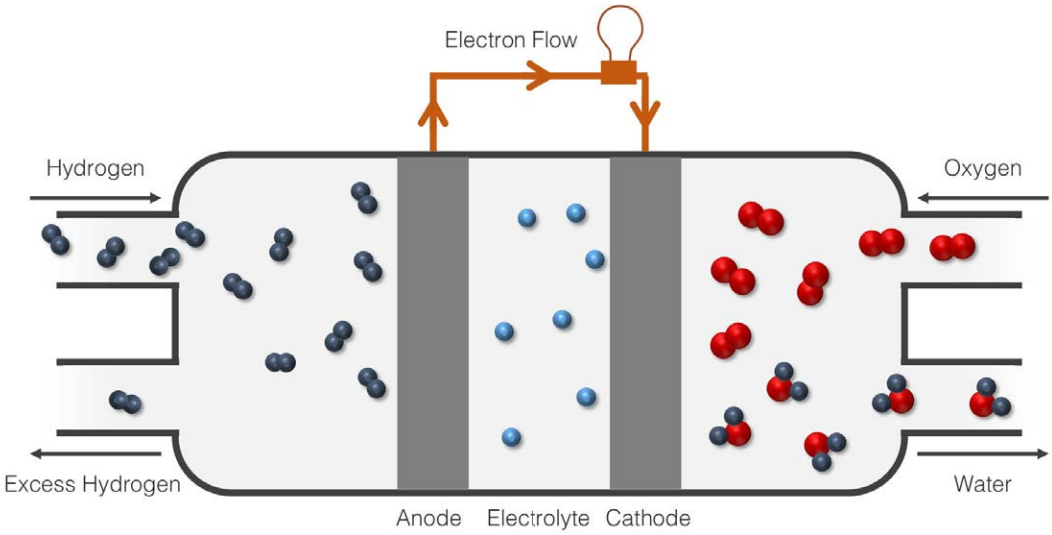

Figure 1.1: Schematic of a basic PEFC.

operating temperature of the cell, with common membranes such as Nafion or Aquivion [24] limiting temperatures to less than 100°C [21]. Cell operation at low temperatures has disadvantages, as it demands the use of precious-metal catalysts in order to facilitate electrode reactions (particularly at the cathode). There is therefore much work into the development of membrane materials that can operate at higher temperatures (up to 200°C) [25, 26]. Although precious metal catalysts would still be required at these operating temperatures, the electrodes would be less prone to poisoning by contaminants [27].

1.5.1 Anodic Processes

The hydrogen oxidation reaction (HOR) takes place at the anode, where hydrogen gas is oxidised, releasing electrons and creating protons, as shown in Reaction 1.1 [28].

$$2\,\mathrm{H_2(g)} \rightarrow 4\,\mathrm{H^+(aq)} + 4\,\mathrm{e^-} \tag{1.1}$$

This proceeds by hydrogen (H_2) adsorbing onto the surface (*) of the catalyst, breaking the H–H bond to give adsorbed atomic hydrogen (H^*), as shown in Reaction 1.2.

$$\tfrac{1}{2}\,\mathrm{H_2(g)} + {}^* \rightarrow \mathrm{H^*(ads)} \tag{1.2}$$

The adsorbed hydrogen is then oxidised, producing a proton, which desorbs from the surface, as well as an electron, as shown in 1.3.

$$\mathrm{H^*(ads) \rightarrow H^+(aq) + {}^* + e^-} \tag{1.3}$$

The HOR kinetics are very fast on the Pt electrode; this has meant that focus for catalyst improvement has been on the reduction of poisoning from CO.

1.5.2 Cathodic Processes

At the cathode, the oxygen reduction reaction (ORR) takes place by the electrons from the anode reacting with protons from the electrolyte to form water, as in Reaction 1.4.

$$\mathrm{O_2(g) + 4\,e^- + 4\,H^+(aq) \rightarrow 2\,H_2O(l)} \tag{1.4}$$

The more complicated mechanism of the ORR results in sluggish kinetics, limiting PEFC performance. The corrosive conditions at the cathode present a challenging environment where the catalyst must be stable but chemically active enough to activate O_2. Furthermore, once the oxygen has been activated, the catalyst must be noble enough to facilitate the release of the product. Due to the complexity and sluggish nature of the ORR, the cathode typically requires Pt loading several times higher than that of the anode.

Despite much research, the exact mechanism by which the ORR occurs is unknown, although it can take place by either the dissociative four-electron or associative two-electron pathway [29, 30]. There are three commonly proposed mechanisms by which the ORR is likely to take place [31–33], these being through O_2 dissociation, HO_2 dissociation and H_2O_2 dissociation [34–37]. The preferred four-electron pathway results in the direct formation of water. This proceeds via two of the proposed mechanisms, where in the first, O_2 is adsorbed on the catalyst surface followed by breaking of the O–O bond, as shown in Reaction 1.5.

$$\mathrm{\tfrac{1}{2}\,O_2(g) + {}^* \rightarrow O^*(ads)} \tag{1.5}$$

Dissociated O atoms are then protonated by H^+ and reduced by electrons from the anodic reaction, as shown in Reaction 1.6.

$$O^*(ads) + H^+(aq) + e^- \rightarrow OH^*(ads) \tag{1.6}$$

OH is then further protonated and reduced producing water that desorbs from the catalyst surface, as in Reaction 1.7.

$$OH^*(ads) + H^+(aq) + e^- \rightarrow H_2O(l) + * \tag{1.7}$$

In the second mechanism, the O–O bond is not broken when it is adsorbed on the catalyst surface, as in Reaction 1.8.

$$O_2(g) + * \rightarrow O_2{}^*(ads) \tag{1.8}$$

The ORR will then occur as in Reactions 1.9–1.12.

$$O_2{}^*(ads) + H^+(aq) + e^- \rightarrow HO_2{}^*(ads) \tag{1.9}$$

$$HO_2{}^*(ads) \rightarrow OH^*(ads) + O^*(ads) \tag{1.10}$$

$$O^*(ads) + H^+(aq) + e^- \rightarrow OH^*(ads) \tag{1.11}$$

$$OH^*(ads) + H^+(aq) + e^- \rightarrow H_2O(l) + * \tag{1.12}$$

When the O–O bond is not broken it is also possible for the unfavourable two-electron pathway to take place. O_2 protonation and reduction leads to the formation of H_2O_2. This is possible through Reactions 1.13–1.15.

$$O_2(g) + * \rightarrow O_2{}^*(ads) \tag{1.13}$$

$$O_2{}^*(ads) + H^+(aq) + e^- \rightarrow HO_2{}^*(ads) \tag{1.14}$$

$$HO_2{}^*(ads) + H^+(aq) + e^- \rightarrow H_2O_2{}^*(ads) \tag{1.15}$$

H_2O_2 can be further reduced, as in Reaction 1.16.

$$H_2O_2{}^*(ads) + 2\,H^+(aq) + 2\,e^- \rightarrow 2\,H_2O(l) \tag{1.16}$$

However, H_2O_2 can also desorb from the catalyst surface, which is unfavourable as it can then lead to oxidative degeneration of the membrane.

1.5.3 The Electrocatalyst

Four main characteristics are essential for any PEFC electrocatalyst [38], these are:

- Activity to bind the reactants strongly enough to facilitate a reaction but not too strongly so that active sites are blocked.
- Selectivity toward maximising the production of the desired product e.g. the dissociative four-electron reduction.
- Stability to withstand the operating conditions of the PEFC such as corrosive conditions at the anode.
- Resistance to poisoning from impurities in the fuel supply such as at the anode where CO can contaminate the hydrogen feed stock.

The activity of an electrocatalyst is related to its ability to adsorb molecules strongly enough that they become activated, but at the same time, weakly enough that they later desorb. If the reactants bind too weakly, then the reaction will be slow or possibly not take place at all. If the reactants bind too strongly, then active sites will be blocked, thereby reducing the rate of reaction and possibly preventing the reaction even taking place. According to the Sabatier principle, the rate of a catalytic reaction is maximised when a balance is achieved between the rate of activation and the rate of product desorption [39]. This principle has been illustrated by volcano diagrams which plot the catalyst activity against adsorption energy for a given reaction.

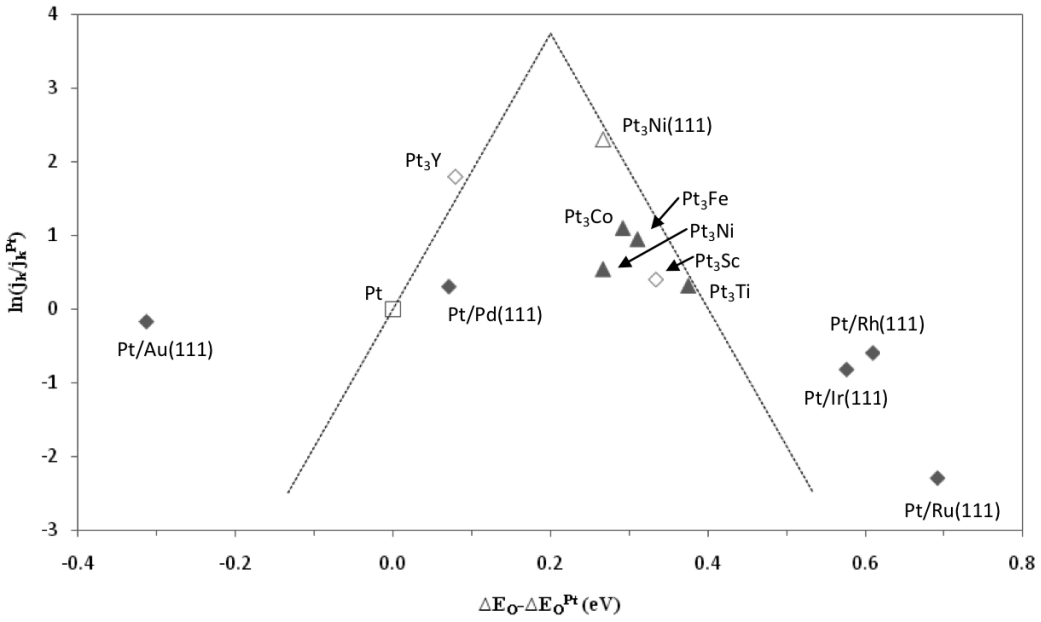

Figure 1.2: Kinetic current density measured for a range of Pt-based electrocatalysts, plotted against oxygen adsorption energy (ΔE_O) [41].

For the HOR, it is found that Pt sits close to the pinnacle of the volcano [40]. However, for the ORR Pt binds to oxygen too strongly. An example volcano plot for the PEFC ORR is shown in Figure 1.2, where Pt is found to the left of the peak. The Pt–O binding energy is found to be $\sim$2.0 eV too high.

As mentioned in Section 1.5.2, selectivity is particularly important at the cathode. The selectivity of the the electrocatalyst is determined in the first step, where O_2 is either dissociated as it is adsorbed on the catalyst surface, or is bound in the molecular form as in Reactions 1.5 and 1.13, respectively. Pt binds O strongly enough that the O–O bond is usually broken, leading to little production of H_2O_2, with the four-electron reduction being heavily favoured [42]. However, it is an important consideration that when weakening Pt–O interactions to improve activity, the selectivity of the electrocatalyst is not compromised.

The presence of strong oxidants, reactive radicals, low pH, high temperatures and rapid potential fluctuations, especially at the cathode, means that stability of the electrocatalyst is an important consideration. It is found that very few transition metals are sufficiently noble to avoid dissolution at the low pH and large electrode potential experienced by the PEFC electrocatalyst.

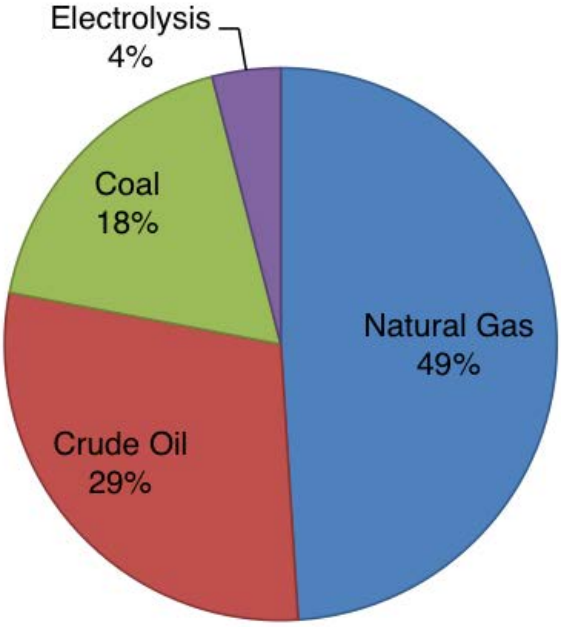

Figure 1.3: Breakdown of worldwide hydrogen production [46].

Once again, it is found that Pt is relatively stable at the high cell potential and low pH found at the cathode, while other stable metals do not tend to exhibit sufficient activity or selectivity [43].

The most problematic poison encountered in the PEFC is CO at the anode and sulphur species at the cathode [44]. As mentioned in Section 1.2, H_2 is not found in elemental form on earth. The majority of H_2 is produced through steam methane reforming, derived from natural gas. As seen in Figure 1.3 over 95% of the worlds hydrogen supply is derived from fossil fuels, with only a small percentage from electrolysis. CO is a side product of the steam methane reformation process and although much work is done to remove this contaminant [45], inevitably a small amount remains in the final product.

Whilst it has proved difficult to remove poisons entirely from the feedstock, there are other methods by which the susceptibility of the electrocatalyst to poisons can be reduced. These mainly involve alloying Pt with other metals, with certain binary and tertiary systems being proven to be particularly successful [47]. Oxygen is supplied from ambient air, directly to the cathode, meaning sulphides will ultimately be present. It is possible to utilise an air intake filter to remove as many pollutants as possible.

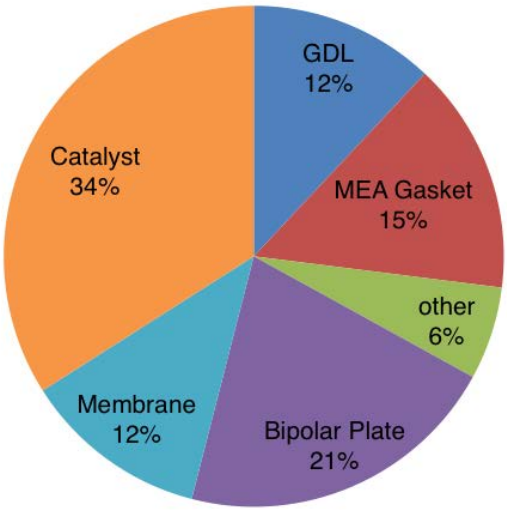

Figure 1.4: Projected cost distribution for an 80 kW PEM fuel cell stack at a production volume of 500,000 units per year [49].

1.5.4 Commercialisation

At present, the most significant barriers to mass-market penetration of PEFC systems are considered to be issues of cost and durability. Commercialisation of the PEFC will depend on achieving a high specific power and power density for a cost of $\$\sim$30 kW^{-1} [48]. Fuel cells must compete cost-effectively with traditional methods of energy production before they will be considered as an alternative energy source. A breakdown of the projected cost of a PEFC stack is shown in Figure 1.4. It can be seen that the components contributing most to the overall cost of the stack are the electrocatalysts. Therefore, the catalyst will ultimately limit the use of PEFC due to the cost and availability of the precious metals required.

The PEFC catalyst layer usually consists of dispersed platinum group metal (PGM) nanoparticles on a porous carbon support. 34% of the overall cost of the fuel cell is the electrocatalyst; Pt is responsible for the vast majority of this with the remaining components of the catalyst ink accounting for a very small proportion. It is therefore the high intrinsic cost of Pt (£900.00 per ounce as of March 2014 [50]) that forms a barrier to the widespread commercialisation of PEFCs. The price of Pt is very susceptible to fluctuations in the global markets, as seen in Figure 1.5, with a significant drop in 2008, which coincided with a significant global financial crisis.

Figure 1.5: Monthly averaged price of Pt between March 1994 and March 2014 [50].

However, aside from during the financial crisis, the price of Pt has typically increased over time. A 10-fold decrease in the Pt loading of PEFC stacks is required to make PEFCs a commercially viable option [51]. There are several ways to do this:

- replace Pt with a non-precious electrocatalyst
- lower the Pt loading by using a Pt alloy
- maximise the effective surface area of the Pt catalyst

The use of a non-precious metal electrocatalyst has the potential to reduce the cost of the PEFC catalyst significantly [52–54]. However, as mentioned in Section 1.5.3, whilst certain non-precious metal catalysts have shown activity comparable to that of Pt, as a result of low selectivity (formation of H_2O_2) and poor stability, these materials remain inferior to traditional Pt-based catalysts [55]. Much work has been done on alloying Pt with other transition metals, a significant proportion of which are cheaper. The advantages of alloying can be two-fold. It is possible to reduce the amount of Pt in the electrocatalyst nanoparticles through e.g. the formation of core shell particles. Through alloying, it is also possible to increase the reactivity of the electrocatalyst; this can lead to a reduction in the amount of catalyst required at the

cathode. Finally, loading can be reduced through increasing the surface contact between the electrode catalyst layers, the carbonaceous electronic conductor-gas diffusion layer, the polymer electrolyte membrane and the reactants.

As one of the most promising methods of reducing Pt loading, whilst simultaneously increasing reactivity, much research, both theoretical and experimental, is being carried out on alloyed PEFC electrocatalysts [21, 56–85]. A vast array of binary, ternary and even quaternary systems has been investigated, including Pt-, as well as other platinum group metal (PGM)-based alloys. These systems exhibit a range of properties, some of which are advantageous over the pure Pt electrocatalysts. Although an improvement of certain properties is observed, in many cases a concurrent effect is the inhibition of other characteristics when compared to the pure Pt system.

1.6 Clusters

Clusters are aggregates of between 2–10^7 particles, where these particles can be either atoms or molecules. For the purposes of this thesis, only atomic clusters will be investigated. Clusters in which the constituent species are identical are termed homo-atomic, while those containing two or more atoms are hetero-atomic. Atomic clusters are formed by most elements in the periodic table such as many of the metals [86–93] and even nonmetals [94–98]. In this work, emphasis is placed on studies of transition metal clusters. Pt-based clusters are amongst the most interesting and have been widely investigated because of their wide ranging use in heterogeneous catalysis. The utilisation of Pt for numerous reactions e.g. oxygen reduction reaction (ORR) and hydrogen oxidation reaction (HOR) in the PEFC, has driven the investigation of small to large Pt clusters as well as extensive work on bulk Pt [32, 99, 100].

Although clusters have been used for thousands of years (e.g. Egyptian makeup, medieval pottery and stained glass windows from the middle ages), it is only recently that their exact nature has been discovered. Nano- and sub-nanoscale clusters are of scientific interest because they have distinct optical, magnetic, and catalytic properties which differ from bulk materials

[101]. The application of nanoclusters in catalysis is a growing field of research [102]. An area of particular recent interest is catalysis on bi- and multi-metallic nanoparticles ("nanoalloys") [101, 103, 104] - where catalytic properties can be tuned by varying the size, shape, elemental composition and chemical ordering of the nanoparticles.

A major area of scientific research involves the study of size-dependent evolution of geometric and electronic properties and the effect this has on the chemical and physical character of the cluster. Certain cluster sizes produce closed geometric or electronic shells, resulting in so-called magic numbers [105–107]. These magic number clusters are of interest as they can have distinct properties e.g. greater stability. Many traits of the cluster are directly related to the fraction of atoms lying on the surface. There is typically a high ratio of surface atoms which have lower coordination numbers. It is these under-coordinated surface atoms that make clusters of interest in catalytic applications where the reactivity of clusters differs when compared to the bulk surface. In fact, it has been shown that clusters in the size range of 8–10 atoms (consisting solely of "surface" atoms) are highly catalytically active [102].

The shape of the cluster has been found to play a significant role in the activity of any potential catalyst [108]. Transition metal clusters present both crystalline (e.g. bulk-like Face Centred Cubic for Pt) and non-crystalline structures. The stability of different geometric structures is dependent on the relationship between the exposed surface area, surface energy of the exposed facets and the internal strain caused by atomic rearrangement compared to the bulk crystal lattice [109]. It is typically found that whilst large clusters tend towards crystalline structures, smaller clusters tend to occupy the non-crystalline phase space. Cluster reactivity can be dependent on which surface sites are available to reactants and products. This is largely dependent on the type and size of the facets that are present.

1.7 Nanoalloys

Whilst the size and shape of the cluster can be used to change the characteristics of a catalyst, the combination of two or more elements to form nanoalloys can result in a range of unique

properties not observed for the pure cluster [103]. Furthermore, the introduction of another species allows for existing characteristics to be further tuned by controlling composition and chemical ordering. For nanoalloys, an expansive range of combinations and compositions are possible, where A_nB_m clusters can be generated with well controlled size (m + n) and composition (m:n ratio). Furthermore, segregation can be controlled through the cluster generation methodology, although this is somewhat dependent on atom types (A & B).

When considering nanoalloys, the presence of additional atom types leads to a sometimes vast number of homotops. Homotops are isomers with fixed number of atoms and composition, which have the same geometrical arrangement of atoms but differ in the arrangement of A and B atom types. The number of possible homotops increases as the total number of atoms (N) increases and the m:n ratio approaches the 50:50 composition. For a bimetallic cluster, with N_A atoms of type A and N_B atoms of type B, the number of possible homotops can be calculated using Equation 1.17 [110].

$$N_H = \frac{N!}{N_A!N_B!} \tag{1.17}$$

For a 38-atom cluster, with 50:50 composition, there are over 3.5×10^{10} possible homotops, although as the symmetry of the isomer increases, the number of symmetry-equivalent homotops also increases.

The atomic arrangements of A_mB_n clusters conform to a number of mixing patterns (chemical ordering), these exhibit mixed or segregated behaviour. A schematic of several common mixing patterns is shown in Figure 1.6. Core-shell structures are segregated, where one element occupies the core positions and the other occupies the shell position. In the schematic representation, the shell comprise a single layer (perfect monolayer) of atoms, although in reality, the shell thickness can vary and defects will most likely be present. Onion-like structures are similar to core-shell configurations but have a segregated alternating layered shell pattern (e.g. A-B-A).

Layered (Janus-type) structures are segregated, maximising homometallic bonding (e.g. A–A, B–B), while minimising heterometallic (e.g. A–B) bonding. Mixed structures, on the other hand, tend to maximise heterometallic (e.g. A–B) bonding. These mixed nano alloys can either

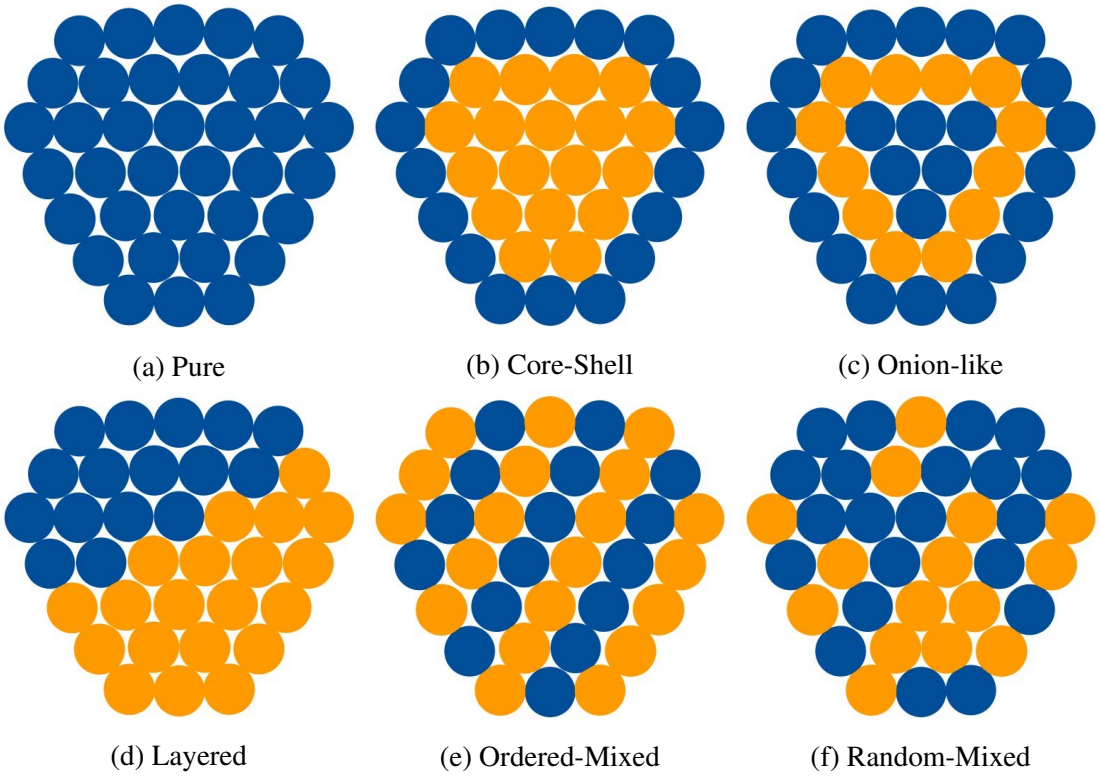

(a) Pure (b) Core-Shell (c) Onion-like

(d) Layered (e) Ordered-Mixed (f) Random-Mixed

Figure 1.6: Schematic representation of some possible mixing patterns.

possess ordered or randomly mixed patterns. The mixing pattern adopted by a cluster will be determined by a number of factors:

- bond strength
- surface energy
- atomic size
- charge transfer
- binding strength to ligands and surfactant molecules

The relative strengths of A–A, B–B and A–B bonds play an important role in the formation of different mixing patterns [101, 103]. If the homometallic A–A or B–B bonds are stronger, segregation will be favoured, with the element forming the stronger bond typically occupying core positions. If hetrometallic A–B bonds are favoured over homometallic bonding, the clusters will preferentially form mixed configurations. When comparing surface energies, the metal

with the lower energy will tend to occupy surface sites. Strain effects are induced by an atomic size mismatch, where larger atoms will tend to occupy surface sites. For elements with differing electronegitivities, the more electronegative atom will tend to occupy surface positions but extensive charge transfer will favour ordered mixing. Finally, for passivated clusters, ligands can lead to surface stabilisation of the more strongly binding metal.

1.8 Clusters in Catalysis

As discussed in Section 1.5.2, the ORR takes place at the PEFC cathode. It is well established that the ORR is structurally sensitive [111, 112], meaning certain facets will be more active than others, as a result of differing adsorption strengths of e.g. OH, on the different sites. It is found that activity on Pt(hkl) surfaces is as follows: (111) $>$ (110) $>$ (100) in KOH solution [113], (110) $>$ (111) $>$ (100) in $HClO_4$ solution [111] and (100) $>$ (110) $>$ (111) in H_2SO_4 [114]. For PEFC electrocatalytic applications, there has been extensive interest in the (111) facet, where under PEM operating conditions, the (111) facet exhibits weaker Pt–O binding when compared to other facets, leading to an improvement in activity [115]. When investigating potential electrocatalysts with a cluster based model, it is possible to perform calculations on clusters with multiple facets in order to study this structural sensitivity. Figure 1.7 shows a representation of the (111) and (100) facets, as well as an octahedral and cube-octahedral cluster, which vary in the number of (111) and (100) facets present. Through utilising a model cluster system it is not only possible to investigate different facets, but also a large number of possible sites on a single system. These can include atop, bridge and hollow sites both at the centre and at the edge of any facet.

Through modelling slab or cluster systems, it is possible to gain an understanding of the ORR kinetics and how these are altered when changes are made to the system e.g. formation of an alloy. Through performing density functional theory (DFT) calculations, it is possible to investigate free energy changes during the ORR. Two reaction steps are rate-limiting (greatest positive free energy), these being the first electron and proton transfer to form OOH^* (ΔG_1)

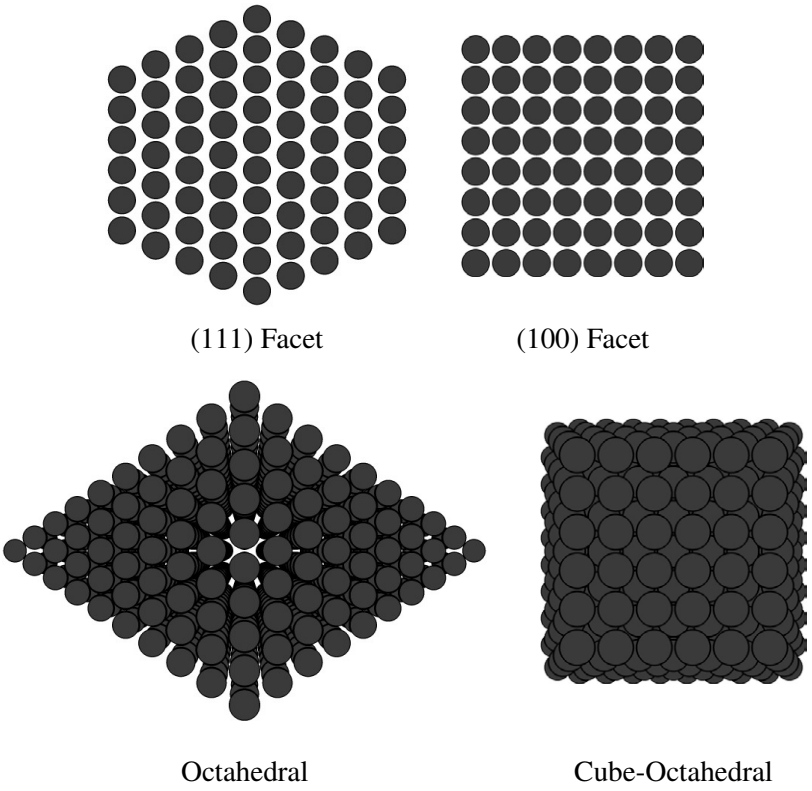

Figure 1.7: Schematic of the (111) and (100) facets, as well as octahedral and cube-octahedral clusters, where the octahedral cluster exhibits only (111) facets and the cube-octahedral cluster exhibits both (111) and (100) facets.

and the final transfer desorbing OH to form H_2O (ΔG_2) [41]. Therefore, the reaction rate of the ORR is dependent on the magnitudes of ΔG_1 and ΔG_2, which are in turn related to the stability of OOH and OH on the metallic surface. The stability of OOH and OH interactions with the metallic surface scale with one another, meaning that more general trends can be deduced from studies of single adsorbates.

1.9 Summary

This thesis focuses on investigations of the PEFC electrocatalyst with the aim of improving catalytic activity and reducing the overall cost of the fuel cell. This is to be achieved through the theoretical investigation of Pt-based alloys. Through theoretical screening of potential alloys it is possible to identify key features in order to select intelligently the ideal system. To achieve these goals, a number of characteristics have been studied for model systems, utilising density functional theory methodology.

In Chapter 2, the general methodologies employed throughout this work are discussed, with specific parameters and chapter specific methodologies being described in each chapter. In Chapter 3, discussions of structural searches of sub-nanometre clusters, utilising the GA-DFT methodology, are presented. In Chapter 4, results from chemisorption studies on pure Pt and PtTi nanoalloy clusters are shown, studying changes in the *d*-band density of states on alloying. O_2 dissociation studies on pure Pt and PtTi nanoalloys are presented in Chapter 5. Further O_2 dissociation studies for all *d*-block M@Pt core-shell clusters are presented in Chapter 6. Finally, conclusions are drawn in Chapter 7.

Chapter 2

Methodology

2.1 Modelling Transition Metal Clusters

The potential energy of a nanoparticle can be represented on a potential energy surface (PES) of a system [116]. The PES is represented in terms of the atomic coordinates, which has $3N$ degrees of freedom as the potential energy does not change on translation or rotation of the cluster in space. Therefore, the PES is only dependent on the cluster's internal coordinates and a PES with $3N + 1$ dimensions is found, where the extra dimension is the potential energy. A local minimum on the PES is defined as a point where all gradients are zero and in which any displacement will lead to higher potential energy configurations. There are a high number of local minima on the PES, the lowest of which is the global minimum (GM). As well as minima, there exist transition states, saddle points which are minima in all dimensions but one. Finally, there are higher-order saddle points, which are minimum in all dimensions but n, where $n > 1$. A representation of the PES can be seen in Figure 2.1.

Calculations can be performed to investigate the PES, although simulations of nanoclusters present complex issues, especially when modelling transition metals. Several techniques have been employed to compute quickly and accurately the physical and chemical properties of nanoclusters with a range of compositions and sizes. The technique used is generally determined by a combination of the desired property and the size and composition of the cluster. For exam-

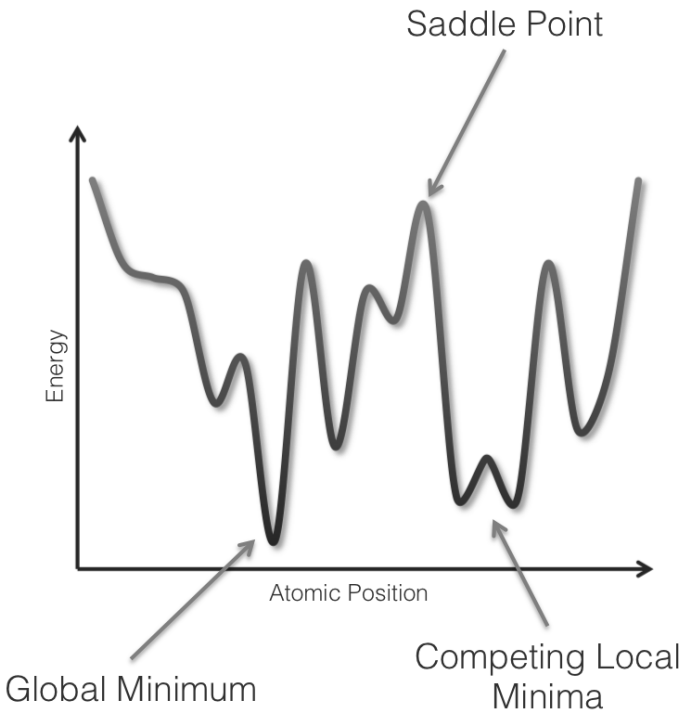

Figure 2.1: Schematic of a basic PES.

ple, search algorithms can be used to find low energy structures for pure and alloyed systems of between a few and several hundred atoms. Common search techniques include basin-hopping algorithms, stochastic-search methods and genetic algorithms coupled with an empirical potential e.g. Gupta, Sutton-Chen and Murrell-Mottram [117–119].

Genetic algorithms (GAs) are search methods for function minimisation, which are based on principles akin to natural evolution. The algorithm utilises operators analogous to those observed in nature (mating, mutation and natural selection) to explore the multidimensional PES [120]. Empirical potentials, such as those mentioned above, can be used to search for low energy structures on the PES although they tend to favour 3D structures with high symmetry. This may be relatively accurate for clusters with sizes of more than 20 atoms, however certain smaller clusters tend to favour 2D structures [121], making the use of empirical potentials for small systems questionable.

Ab initio simulations, which are able to treat electrons explicitly, have been used to compute successfully structural properties of transition metal clusters. DFT calculations have been acknowledged as one of the best methods for performing relatively accurate simulations on

metallic clusters [122]. DFT can generally describe the PES more accurately than empirical potentials and so is able to predict the likely low energy structures of small nanoclusters. Aside from structural searches, the explicit treatment of electrons is required for any investigation of potential electrocatalysts, where the interactions of reactants and products with the cluster surface are largely dependent on electronic effects.

2.2 Quantum Mechanics

The Schrödinger equation is shown in its simplest form, in Equation 2.1, for a single particle of mass m, moving in a one dimensional box. The Schrödinger equation determines how the wavefunction (ψ) of the particle evolves over time, where the wave function describes the state of the system.

$$-\frac{\hbar}{2m}\frac{d^2\psi}{dx^2} + V(x) = E\psi \tag{2.1}$$

where $\hbar$ is the reduced Planck's constant ($\hbar = h/2\pi$), the potential energy, V is dependent on the position, x, of the particle and time, t. The Schrödinger equation is expanded for multi-particle systems as in Equation 2.2.

$$\hat{H}\Psi\left(\vec{r}_1, \vec{r}_2, \ldots \vec{r}_N, \vec{R}_1, \vec{R}_2, \ldots \vec{R}_m\right) = E\Psi\left(\vec{r}_1, \vec{r}_2, \ldots \vec{r}_N, \vec{R}_1, \vec{R}_2, \ldots \vec{R}_M\right) \tag{2.2}$$

where $\hat{H}$ is the Hamiltonian operator of the system, an operator which generates the energy, E of a wavefunction for a certain eigenstate, Ψ. The wavefunction of the eigenstate is dependent on the positions of the electrons ($\vec{r}_1, \vec{r}_2, \ldots \vec{r}_N$) as well as the nuclei ($\vec{R}_1, \vec{R}_2, \ldots \vec{R}_M$). The Hamiltonian is a sum of five parts, shown in Equation 2.3; these terms account for the kinetic energy of each electron ($\hat{T}_e$) and nucleus ($\hat{T}_n$), the electrostatic interaction energy between two electrons ($\hat{V}_{ee}$) and nuclei ($\hat{V}_{nn}$) and the interaction energy between an electron and atomic nucleus ($\hat{V}_{en}$), respectively.

$$\hat{H} = \hat{T}_e + \hat{T}_n + \hat{V}_{ee} + \hat{V}_{nn} + \hat{V}_{en} \tag{2.3}$$

The kinetic energy of the the electrons and nuclei are defined as in Equations 2.4 and 2.5, respectively.

$$\hat{T}_e = -\sum_{i}^{N} \frac{\hbar^2}{2m_e} \nabla^2 (r_i) \tag{2.4}$$

$$\hat{T}_n = -\sum_{A}^{M} \frac{\hbar^2}{2M_A} \nabla^2 (R_A) \tag{2.5}$$

The mass of the electron is m_e while the mass of the nucleus is M_A, ∇^2 is given by:

$$\nabla^2 = \frac{\partial^2}{\partial x^2} + \frac{\partial^2}{\partial y^2} + \frac{\partial^2}{\partial z^2}$$

Coulombic repulsion for electrons and nuclei is treated by Equations 2.6 and 2.7, whilst Coulombic attraction between electrons and nuclei is treated in Equation 2.8.

$$\hat{V}_{ee} = \sum_{i}^{N} \sum_{j>i}^{N} \frac{e^2}{4\pi\varepsilon_0 |r_i - r_j|} \tag{2.6}$$

$$\hat{V}_{nn} = \sum_{A}^{M} \sum_{B>A}^{M} \frac{Z_A Z_B e^2}{4\pi\varepsilon_0 |R_A - R_B|} \tag{2.7}$$

$$\hat{V}_{en} = -\sum_{A}^{M} \sum_{i}^{N} \frac{Z_A e^2}{4\pi\varepsilon_0 |R_A - r_i|} \tag{2.8}$$

In Equations 2.6–2.8, e is the charge of an electron, Z is the atomic number of the nucleus and ε_0 is the vacuum permittivity. The Hamiltonian can be simplified to the form shown in Equation 2.9 when expressed in atomic units, with the electron mass m_i, charge e, the reduced Planck's constant $\hbar$ and vacuum permittivity $4\pi\varepsilon_0$ set to unity. In this form, energy is given in hartrees (1 hartree = 27.21 eV) and length in bohr (1 bohr = 0.53 Å).

$$\hat{H} = -\frac{1}{2}\sum_{i}^{N} \nabla^2 (r_i) - \frac{1}{2}\sum_{A}^{M} M_A \nabla^2 (R_A) + \sum_{i}^{N}\sum_{j>i}^{N} \frac{1}{r_{ij}} + \sum_{A}^{M}\sum_{B>A}^{M} \frac{Z_A Z_B}{R_{AB}} - \sum_{A}^{M}\sum_{i}^{N} \frac{Z_A}{r_{iA}} \tag{2.9}$$

When performing calculations, both the positions of the nucleui and the electrons must be clearly defined. Atomic nuclei are much heavier than individual electrons, with each proton or

neutron having more than 1800 times the mass of an electron. It is, therefore, assumed that electrons respond more quickly to changes in their surroundings than the nuclei. It is possible to firstly solve the equations for electron motion with the atomic nuclei in fixed positions (described as fixed point charges) and to later move the nuclei in the potential field generated by the electrons. The separation of the electronic (Ψ_e) and nuclear (Ψ_n) components of the wavefunction is know as the Born-Oppenheimer approximation, shown in Equation 2.10.

$$\Psi\left(r,R\right)=\Psi_e\left(r,\{R\}\right)\Psi_n\left(\{R\}\right) \tag{2.10}$$

Here, each wavefunction is calculated with respect to the nuclear coordinates $\{R\}$. When the nuclear components of the Hamiltonian are removed to calculate electronic motion, the Schrödinger equation is solved for the electrons only, as in Equation 2.11.

$$\hat{H}_e=-\frac{1}{2}\sum_{i}^{N}\nabla^2\left(r_i\right)+\sum_{i}^{N}\sum_{j>i}^{N}\frac{1}{r_{ij}}-\sum_{A}^{M}\sum_{i}^{N}\frac{Z_A}{r_{iA}}$$

where:

$$\hat{H}_e\Psi\left(r,\{R\}\right)=E_e\Psi\left(r,\{R\}\right) \tag{2.11}$$

Finally, it is possible to add nuclear energies ($\hat{T}_n+\hat{V}_{nn}$) to the electronic energy ($\hat{H}_e$) to give an approximation of the total system energy ($\hat{H}=\hat{H}_e+\hat{T}_n+\hat{V}_{nn}$).

It is important to note that, in order to completely describe an electron, the spin must be specified as well as the spatial coordinates. Electrons are indistinguishable fermions, particles with half-integer spin. The electronic wavefunction represents the probability of electron's occupying a point in space, although the Pauli principle states that only one fermion can occupy a particular quantum state at any given time. However, it is possible for multiple fermions to have the same spatial probability distribution. As electrons are indistinguishable, if any two electrons are interchanged, the respective spatial probability distribution must not alter. The electronic wavefunction must therefore be antisymmetric with respect to the interchange of

spatial and spin coordinates of any two electrons, as in Equation 2.12.

$$\Psi\left(\vec{r}_1, \vec{r}_2 \ldots \vec{r}_i, \vec{r}_j \ldots \vec{r}_N\right) = -\Psi\left(\vec{r}_1, \vec{r}_2 \ldots \vec{r}_i, \vec{r}_j \ldots \vec{r}_N\right) \tag{2.12}$$

Whilst there are a number of *ab initio* methods available to study molecules and clusters (e.g. Møller-Plasset perturbation theory and coupled cluster methods), these methods have limitations because of the computational difficulty of performing accurate calculations with large basis sets. This becomes particularly problematic when performing calculations on a large number of atoms or on systems with a large number of electrons e.g. transition metals. The calculations described in this thesis were performed primarily using Density Functional Theory, DFT, a method by which the electronic states of atoms, molecules, and materials are described in terms of the three-dimensional electronic density of the system.

2.3 Density Functional Theory

DFT is based on a reformulation of the Schrödinger equation, which rests on two mathematical theorems of Hohenberg and Kohn [123] as well as derivation of a set of equations by Kohn and Sham [124].

2.3.1 Hohenberg-Kohn Theorem

The first Hohenberg-Kohn theorem states that an electronic ground-state wavefunction is determined completely by the ground-state electron density. Electron density uniquely determines the positions and charges of the nuclei, which is sufficient to determine the Hamiltonian. Coulombic attraction between electrons and nuclei ($\hat{V}_{en}$) is considered a response of the electrons to a constant external potential ($\hat{V}_{ext}$). The Hamiltonian can therefore be written as in Equation 2.13.

$$\hat{H} = -\frac{1}{2}\sum_{i}^{N}\nabla^2\left(r_i\right) + \sum_{i}^{N}\sum_{j>i}^{N}\frac{1}{r_{ij}} + \sum_{i}^{N}\hat{V}_{ext} \tag{2.13}$$

Where:

$$\hat{V}_{ext} = -\sum_{A}^{M} \frac{Z_A}{r_{iA}}$$

This can be expressed as in Equation 2.14.

$$\hat{H} = \hat{F} + \hat{V}_{ext} \tag{2.14}$$

Where:

$$\hat{F} = \hat{T}_e + \hat{V}_{ee}$$

The electronic kinetic energy, $\hat{T}_e$, and Coulombic repulsion of two electrons, $\hat{V}_{ee}$, is dependent on only the electron density, meaning that $\hat{F}$ is the same for all N-electron systems. The Hamiltonian is therefore dependent on only the number of electrons, N, and the external potential, $\hat{V}_{ext}$. The first Hohenberg-Kohn theorem results from the fact that $\hat{V}_{ext}$ is a functional of the electron density, $\rho(r)$, where the ground state electron density, $\rho(r_0)$,as in Equation 2.15, can be used to calculate any ground state property for an N-electron system.

$$N = \int \rho_0(\vec{r})\, d\vec{r} \tag{2.15}$$

The first Hohenberg-Kohn theorem shows that it is possible to solve the ground state Hamiltonian by calculating the electron density with three spatial variables instead of 3N variables for the wavefunction. This reduces the complexity of solving the Hamiltonian for 100 Pd atoms, from 23,000 dimensions to just 3.

Whilst the first Hohenberg-Kohn theorem shows that a functional for the electron density of any system exists, it does not specify the form of that function. The second Hohenberg-Kohn theorem states that the functional of the electron density, $E[\rho]$, that minimises the energy of the system, is the true electron density corresponding to the ground state energy ($E[\rho_0] = E_0$). As the exact form is unknown, the variational principle can be used to approximate the functional form of the ground state electron density. Equation 2.16 is used to find the ground state energy

of a trial density, $\tilde{\rho}(r)$.

$$E_0 \leq E(\tilde{\rho}) = T[\tilde{\rho}] + E_{ee}[\tilde{\rho}] + E_{en}[\tilde{\rho}] \tag{2.16}$$

Any trial density, $\tilde{\rho}(r)$, defines its own Hamiltonian, $\tilde{\hat{H}}$, and wavefunction, $\tilde{\Psi}$. The solution for the Hamiltonian is described by this trial wavefunction, generated from the true external potential, V_{ext}, as in Equation 2.17.

$$\left\langle \tilde{\Psi} \left| \hat{H} \right| \tilde{\Psi} \right\rangle = T[\tilde{\rho}] + V_{ee}[\tilde{\rho}] + \int \tilde{\rho}(\vec{r}) V_{ext} d\vec{r} = E[\tilde{\rho}] \geq E_0[\rho_0] = \left\langle \Psi_0 \left| \hat{H} \right| \Psi_0 \right\rangle \tag{2.17}$$

2.3.2 Kohn-Sham Equations

Kohn and Sham derived a set of equations to describe the Hohenberg-Kohn theorem in terms of the single-electron orbitals. These collectively define the electron density, $\rho(r)$, for an N-electron system. The Kohn-Sham equations express the ground state energy as in Equation 2.18, for single-electron orbitals, $\{\psi_i\}(r)$. The form of some of the functionals are known exactly, $E_{exact}[\{\psi_i\}]$ although no explicit form of the exchange correlation functional, $E_{xc}[\{\psi_i\}]$, can be defined.

$$E[\{\psi_i\}] = E_{exact}[\{\psi_i\}] + E_{xc}[\{\psi_i\}] \tag{2.18}$$

The electron kinetic energy, the Coulomb interactions between the electrons and the nuclei and the Coulomb interactions between pairs of electrons are all known functionals, as in Equation 2.19.

$$\begin{aligned} E_{exact}[\{\psi_i\}] = &- \sum_i^N \int \psi_i^*(\vec{r}) \left(\frac{\hbar}{2m_e} \nabla^2 \right) \psi_i(\vec{r}) \, d\vec{r} + \int \rho(\vec{r}) V_{ext} d\vec{r} \\ &+ \frac{e^2}{2} \int \int \frac{\rho(\vec{r}) \rho\left(\vec{r'}\right)}{\left| \vec{r} - \vec{r'} \right|} d\vec{r} d\vec{r'} \end{aligned} \tag{2.19}$$

The exchange-correlation functional is a correction required to account for the electron-electron approximations made as a result of the non-interacting nature of the Kohn-Sham equations. The exchange interaction alters the energy when electronic wavefunctions overlap, where the

Pauli exclusion principle states the wavefunction is antisymmetric. The correlation correction accounts for the fact that Coulomb correlation, which describes the correlation between the spatial position of electrons due to their Coulomb repulsion, is not accounted for.

The electron density is constructed over the particle indices, as in Equation 2.20.

$$\rho\left(\vec{r}\right) = \sum_{i}^{N} \left|\psi_i\left(\vec{r}\right)\right|^2 \tag{2.20}$$

The energy of the single electron Kohn-Sham orbital, ε_i, is constructed as in Equation 2.21.

$$\left(-\frac{\hbar}{2m_e}\nabla^2 + V_{KS}\left(\vec{r}\right)\right)\psi_i\left(\vec{r}\right) = \varepsilon_i\psi_i\left(\vec{r}\right) \tag{2.21}$$

where the Kohn-Sham potential is:

$$V_{KS} = e^2 \int \frac{\rho\left(\vec{r'}\right)}{\left|\vec{r} - \vec{r'}\right|} d\vec{r'} + V_{ext}\left(\vec{r}\right) + V_{xc}\left(\vec{r}\right)$$

and the exchange-correlation potential is:

$$V_{xc}\left(\vec{r}\right) = \frac{\delta E_{xc}\left[\rho\right]}{\delta\rho\left(\vec{r}\right)}$$

The Kohn-Sham equations are solved in a self-consistent fashion with the following steps:

- Define an initial, trial electron density, $\tilde{\rho}\left(\vec{r}\right)$.
- Solve the Kohn-Sham equations using the trial electron density to find the single electron wavefunctions, $\psi_i\left(\vec{r}\right)$, as in Equation 2.21.
- Using Equation 2.20 an improved set of orbitals are calculated for the electron density.
- Repeat the above steps until convergence is reached, when Equation 2.18 is used to calculate the total energy of the system.

Electronic configurations of atoms are described as wavefunctions, which are the set of basis

functions that describe the atomic or molecular orbitals. There are two main ways in which to define these orbitals, the linear combination of atomic orbitals (LCAO) and planewave methods.

2.3.3 Basis Sets

In the LCAO method, it is assumed that the number of molecular orbitals is equal to the number of atomic orbitals included in the linear expansion, where each orbital, ϕ_i, is defined as in Equation 2.22.

$$\phi_i = \sum_{r}^{N} c_{ri}\eta_i \tag{2.22}$$

where, for a total of N functions, the contribution of each function, η, is described by a coefficient, c. The atomic orbitals are either Slater-type orbitals (STOs), hydrogen-like wavefunctions that are known analytically, or Gaussian-type orbitals (GTOs). GTOs typically require a greater number of functions to achieve accuracy similar to that of STOs, as they exhibit an incorrect density at the nucleus and decay too rapidly at distances away from the nucleus. However, GTOs are commonly used due to the Gaussian product theorem, where the product of two GTOs is a finite sum of Gaussians centred on a point along the axis connecting them, which leads to a reduction in computational expense compared to STOs. One LCAO based code has been utilised in the work reported here, this being the NWChem Quantum Chemistry package [125].

Plane waves are functions as in Equation 2.23.

$$\eta^{PW} = e^{i\vec{k}\vec{r}} \tag{2.23}$$

The wave-vector $\vec{k}$ is related to the momentum ($\vec{p} = \hbar\vec{k}$) of the electron. These functions are not based around a nucleus, but are instead extended throughout the complete space defined by periodic boundary conditions. A finite number of plane wave functions are used, below a certain cutoff energy, although a large number of these functions are required to achieve reasonable accuracy. Plane wave basis sets are used in combination with pseudopotentials, where the plane waves are used to describe only the valance electrons. Core electrons are concentrated around the atomic nuclei, resulting in large wavefunction and density gradients that are not well

described by a plane wave basis set unless a very high energy cutoff is used. Two plane wave codes have been used in the work reported here, Quantum Espresso [126] and the Vienna Ab initio Simulation Package (VASP) [127–130].

2.3.4 Exchange-Correlation Functionals

In DFT, the ground state is found by minimising the energy of an energy functional, which is achieved by finding a self-consistent solution to a set of single electron equations. To solve the Kohn-Sham equations, the exchange-correlation function, $E_{xc}\left[\{\psi_i\}\right]$, must be defined. However, the exact form of the exchange-correlation functional is not known, aside from in one case. In the situation of the uniform electron gas, the electron density is constant at all points in space so that $\rho\left(\vec{r}\right)$ is constant. Whilst this assumption is not valid for systems where, e.g., variations in electron density define chemical bonds, it is possible to set the exchange-correlation potential at each position to be the known exchange-correlation potential from the uniform electron gas at the electron density for a given position, as in Equation 2.24.

$$V_{xc}^{LDA}\left(\vec{r}\right) = V_{xc}^{electron\ gas}\left[\rho\left(\vec{r}\right)\right] \tag{2.24}$$

This is known as the local density approximation (LDA), as only the local density is used to define the approximate exchange-correlation functional. The LDA functional assumes that all electrons are spin-paired. An extension of LDA to account for unpaired electrons is called the local spin density approximation (LSDA), as in Equation 2.25.

$$V_{xc}^{LSDA}\left(\vec{r}\right) = V_{xc}\left[\rho_\alpha\left(\vec{r}\right), \rho_\beta\left(\vec{r}\right)\right] \tag{2.25}$$

The majority of calculations performed in this thesis utilise a different functional to estimate exchange-correlation. For this functional, the local electron density and the local gradient of the electron density is used; this approach is known as the generalized gradient approximation

(GGA), as in Equation 2.26.

$$V_{xc}^{GGA}\left(\vec{r}\right) = V_{xc}\left[\rho_{\alpha}\left(\vec{r}\right), \rho_{\beta}\left(\vec{r}\right), \nabla\rho_{\alpha}\left(\vec{r}\right), \nabla\rho_{\beta}\left(\vec{r}\right)\right] \tag{2.26}$$

There are many GGA functionals as there are many ways in which the gradient of the electron density can be included in a GGA functional. Two popular GGA functionals are those of Perdew-Wang 1991 (PW91) and Perdew-Becke-Ernzerhof (PBE).

2.4 Charge Analysis

Throughout this thesis a number of methods have been used to analyse charge transfer. These are the Mulliken [131, 132], Löwdin [133–135] and Bader [136–139] methods. Mulliken has been noted to produce questionable results when analysing charge transfer in non-organic systems [140]. It is therefore noted that this technique is not ideal for the majority of systems studied but is included in some cases for comparative purposes. Mulliken population analysis provides a method for determining partial atomic charges, which has been widely used, although there are a number of weaknesses. Mulliken analysis divides overlap populations equally between the two corresponding orbital populations (atoms of a bond), although its results tend to vary with basis set and it yields unnatural values in a number of cases.

The approach of Mulliken also leads to a weakness arising from the fact that it employs a non-orthogonal basis set; this problem is overcome by Löwdin population analysis, where atomic orbitals are transformed to an orthogonal basis set. This avoids the problem of violating the Pauli exclusion principle but also means there is no longer the arbitrary division of shared electrons. However, as with Mulliken analysis, this method is also dependent on the basis set being used.

The Bader method is based on the study of the charge density topology. This method subdivides the molecular volume into regions based on the spatial distribution of the electron density function in terms of its critical points, the points at which the gradient of the density is equal to zero. Each subsection belongs to a particular nucleus, while each atomic volume contains

a certain number of electrons, used to assign atomic charges. The Löwdin and Bader methods have been used extensively to study transition metal clusters but the magnitude of the resulting charges has been found to vary for different systems. It is therefore suggested that the charge analysis gives the direction of charge transfer, as opposed to absolute physical charges.

2.5 Energetic Analysis

A number of common calculations are performed throughout this thesis, which have been described here. To assess cluster binding energies per atom, Equation 2.27 is used.

$$E_b = \frac{1}{N}\left(A_m B_n - (m \times A) - (n \times B)\right) \tag{2.27}$$

where N is the total number of atoms, $A_m B_n$ is the total electronic energy of the cluster, and A and B are the total electronic energies of the single atoms. Cluster distortion energies are calculated using Equation 2.28, where the single point energies of distorted species are denoted by *.

$$\Delta E(A_n B_m) = A_n B_m - A_n B_m^* \tag{2.28}$$

In order to assess the chemisorption strength of small molecules, the adsorption energy (E_{ads}) is used, as defined in Equation 2.29.

$$E_{ads} = E_{AB} - (E_A + E_B) \tag{2.29}$$

E_{AB} is the energy of the cluster with the molecule adsorbed, E_A is the energy of the relaxed cluster and E_B is the energy of the relaxed molecule. The interaction energy (E_{int}) is used to calculate the adsorption strength accounting for distortions as defined in Equation 2.30.

$$E_{int} = E_{AB} - (E_A^* + E_B^*) \tag{2.30}$$

Adsorbate distortion energies are calculated using Equation 2.31.

$$\Delta E(O_2) = E_{O_2} - E^*_{O_2} \tag{2.31}$$

Chapter 3

BCGA-DFT Structural Searches on Subnanometre Clusters

3.1 Introduction

Structural searches have been performed on sub-nanometre clusters using the Birmingham Cluster Genetic Algorithm (BCGA) coupled with DFT to perform the structural minimisations. Structural searches have traditionally been performed with an empirical potential (EP) but these are known to give questionable results for sub-nanometre clusters. Small clusters can have planar conformations, whilst empirical potentials tend to favour 3D structures. The computational expense associated with BCGA-DFT searches is very limiting, in this chapter clusters up to 10 atoms in size have been studied. Previous investigations have revealed a number of different growth patterns of small Pt clusters, as well as disagreement over the size at which the lowest energy structure changes from 2D to 3D [141–144]. For example, whilst Sebetci found 3D cluster geometries to be favourable as low as Pt_4 using the Becke, three-parameter, Lee-Yang-Parr (B3LYP) exchange correlation (*xc*) functional [145], Bhattacharyya and Majumder predicted the 2D-3D transition to occur between Pt_9 and Pt_{10} using the projected augmented wave (PAW) method implementation for the Perdew Wang 91 (PW91) *xc* functional [146].

Whilst some theoretical studies have been reported on pure Ti clusters [147, 148], to our

knowledge, little has been performed on Pt clusters doped with early transition metals. This is likely to be, in part, a result of the unreliability of coupling EPs for very different transition metals where electronic effects play an important role. Here, we use a novel Genetic Algorithm (GA) coupled with Density Functional Theory (DFT) approach to search for Pt clusters with 2–6 atoms. We then investigate the effects of doping with the early transition metals Ti and V. The aim of this study is to identify minimum energy structures for clusters that would not be reliably described by EPs. Promise has also been shown by Pt nanoalloys with other early transition metals, including Ti and V, for catalytic applications [100, 149–152].

3.2 Methodology

The GA-DFT approach has been successfully employed to study a range of systems [121, 153, 154]. This method uses the BCGA [120, 155] coupled with the PWscf plane wave DFT code in the quantum chemistry package Quantum-Espresso [126]. An initial generation is produced by randomly placing atoms in a sphere of size $1.1 \cdot N^{1/3} \cdot r_0$. In this case, r_0 is set to be the A–A bond distance for a monometallic system or the averaged A–B bond length for a bimetallic system. The atoms are then transferred to a centre of mass coordinate system and placed in the centre of the unit cell. The cell is set to be large enough that, when minimised, the clusters are non-interacting.

The cluster is then locally relaxed until convergence is achieved. In the case that the convergence criteria are not met, a new random structure is generated. After all members of the generation have been minimised, the energetically lowest members are selected and taken forward. These energetically favourable members of the population are mated and mutated to form novel structures for the next generation. This process, as presented in Figure 3.1, is repeated until the energy of the lowest lying isomer is considered to have converged.

Using the GA-DFT method, it is possible to search accurately the PES of the system being studied. Following the structural search, re-minimisations are performed on all unique structures, using the quantum chemistry code NWChem [125]. As well as re-minimising, other

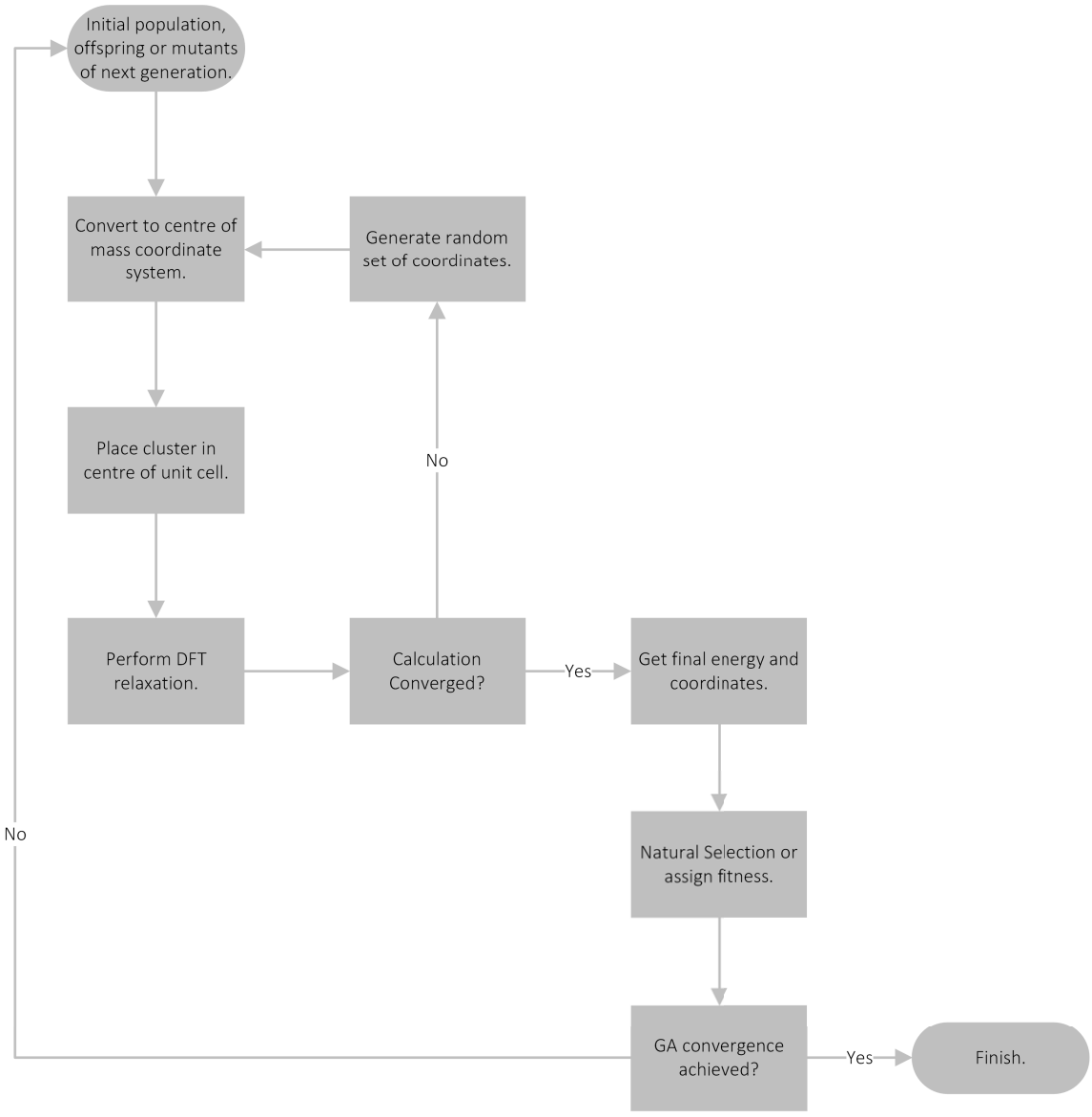

Figure 3.1: Schematic for the GA-DFT approach implemented within the BCGA.

properties have also been studied using NWChem, e.g. spin effects, investigating multiplicities up to the nonet. Since there is no guarantee that the structures generated using this approach are actually local minima rather than transition states or higher rank saddle points, following the structural search a frequency analysis is performed. Frequency analysis was performed using NWChem after re-minimisation for varying multiplicities. For the lowest lying isomers, Bader charge analysis is performed. Bader charge analysis is utilised to elucidate general trends in charge transfer. This quantitatively suggests the direction of charge transfer, although values are not suggested to be physically accurate.

In the study presented here, the GA search was performed with a population size of 10 clusters and termination upon convergence was set at five generations. This means that if the energy of the lowest energy cluster per generation was within 0.01 eV for five generations, convergence was said to have been achieved. All GA-DFT simulations were performed using the PWscf plane wave DFT code in the quantum chemistry package Quantum-Espresso 4.3.2. The PWscf calculations were performed using ultrasoft Perdew-Burke-Ernzerhof (PBE) xc functional, accounting for 12 ($3s^2$, $3p^6$, $3d^2$, $4s^2$), 13 ($3s^2$, $3p^6$, $3d^3$, $4s^2$) and 10 ($5d^9$, $6s^1$) valence electrons for Ti, V and Pt, respectively. Scalar relativistic corrections were employed for all pseudopotentials, while the Pt potential also contains non-linear core correction and Ti and V potentials contain semi-core states.

A kinetic energy (E_k) cutoff for the wavefunctions of 55.0 Ry was used, and the supercell dimensions were taken to be sufficiently large to remove the possibility of interactions with neighbouring clusters, however not so large as to be detrimental to calculation speed. When performing structural searches, E_k cutoff for the charge density was set at 500.0 Ry. The convergence threshold for self consistency was also set at 10^{-5} Ry, whilst Marzari-Vanderbilt Gaussian smearing was set at 0.002 Ry.

Following the initial structural searches, further structural relaxation and frequency analysis was performed using the DFT code in the quantum chemistry package NWChem 6.1. This analysis was performed using the PBE *xc* functional and spherical Gaussian-type orbital triple-zeta (TZVP) basis sets. All electron calculations were performed on Ti and V atoms while an

Table 3.1: Cleri and Rosato Gupta parameters for Pt-Pt interactions. [156]

	Pt-Pt
A (eV)	0.298
ξ (eV)	2.695
p	10.612
q	4.004
r0 (Å)	2.775

effective core potential (accounting for 60 electrons) was employed for Pt. To allow for some comparisons with the traditional GA-EP search, the Gupta potential has been utilised with the Cleri and Rosato parameters presented in Table 3.1.

3.3 Dimers

A number of dimers was studied, including pure M_2 (M = Ti, V, Pt) and alloyed Pt-M (M = Ti, V), the results of which can be seen in Tables 3.2 and 3.3 for the pure and alloyed dimers, respectively. In all cases, the energies are given relative to the lowest energy structures found for the lowest spin state (singlet or doublet). When analysing the results for the pure dimers, several trends become apparent. Firstly, for the Ti, V and Pt dimers, triplet states are found to be energetically favourable, with higher multiplicities generally being less favourable than the singlet.

When comparing bond lengths, increasing the spin multiplicity generally results in bond elongation for the Ti and V dimers. The bond lengths for Pt_2 remain relatively constant, even for the high spin multiplicities, although the energetic penalty paid to access these higher spin states is greater than for Ti_2 and V_2. For the Pt-M dimers, a triplet or quartet is found to be energetically favourable for PtTi and PtV, respectively, with higher multiplicities being less favourable than singlet or doublet states. All Pt-M bond lengths are greater than in the corresponding M_2 dimers, though smaller than the Pt_2 dimer. Once again, as the multiplicity is increased the bond length also increases.

Results for Pt_2 are in good agreement with experimental and theoretical work. Experimental studies have determined a Pt-Pt bond length of 2.33 Å [157], close to the 2.34 Å calculated for

Table 3.2: Relative energies (E_{rel}) and bond lengths for the pure dimers M_2, for varying spin multiplicities (2S+1).

M	2S+1	E_{rel} (eV)	M-M (Å)
	1	0.00	1.93
	3	-0.23	1.90
Ti	5	-0.05	1.97
	7	0.13	2.39
	9	0.50	2.37
	1	0.00	1.74
	3	-0.23	1.74
V	5	0.25	1.73
	7	0.89	1.89
	9	0.64	2.52
	1	0.00	2.34
	3	-0.30	2.34
Pt	5	0.17	2.32
	7	2.58	2.36
	9	5.18	2.34

Table 3.3: Relative energies (E_{rel}) and bond lengths for the heteronuclear Pt-M dimers at varying spin multiplicities (2S+1).

M	2S+1	E_{rel} (eV)	Pt-M (Å)
	1	0.00	2.12
	3	-0.47	2.13
Ti	5	0.48	2.40
	7	1.81	2.68
	9	4.14	2.90
	2	0.00	2.14
	4	-0.35	2.18
V	6	0.37	2.39
	8	1.55	2.66
	10	3.76	2.83

the lowest energy Pt dimer. This is also in good agreement with other DFT studies, which have predicted the triplet state to be the lowest in energy [158]. It has been found that DFT calculations tend to underestimate the Ti_2 and V_2 bond lengths [159]. Our calculated dimer bond lengths are 1.90 and 1.74 Å for Ti_2 and V_2, respectively, compared with experimental values of 1.94 and 1.78 Å [160, 161].

3.4 Structural Searches

3.4.1 Platinum Clusters

The results of the structural searches performed with the PWscf code, for varying sizes and compositions, are presented here. Initially, the results of GA-DFT searches are compared to a GA-EP-Gupta search to demonstrate the poor reliability of the EPs in producing GM structures at small sizes, the results of which can be seen in Table 3.4. Whilst the Gupta potential favours 3D morphologies for all but Pt_3 (which cannot form a 3D structure), the GA-DFT method favours 2D structures in all cases for PBE pseudopotentials. The structures generated by the Gupta-GA search are found through the GA-DFT search, although these structures are found to be higher in energy. This demonstrates the importance of utilising DFT geometry minimisation for small clusters.

Whilst the GM structures are discussed later, a far greater number of low energy isomers can be explored, such as those shown in Figures 3.2–3.5. The QE GA-DFT search generates a number of locally stable minima which are then reoptimised at varying spin multiplicities with NWChem. Two structures are found for Pt_3, although the linearity of structure 2 varies depending on multiplicity. Structure 1 locally minimises at all multiplicities, resulting in a range of relative energies, depending on the spin state. However, structure 2 only locally minimises for multiplicities 1–5, but there is little variation in the relative energies.

The Pt_4 clusters in Figure 3.3 are ordered by their energetic favourability according to the GA search, where structure 1 is found to be most energetically favourable and structure 6 least favourable. It is found that all structures generated through the GA search, locally minimise for

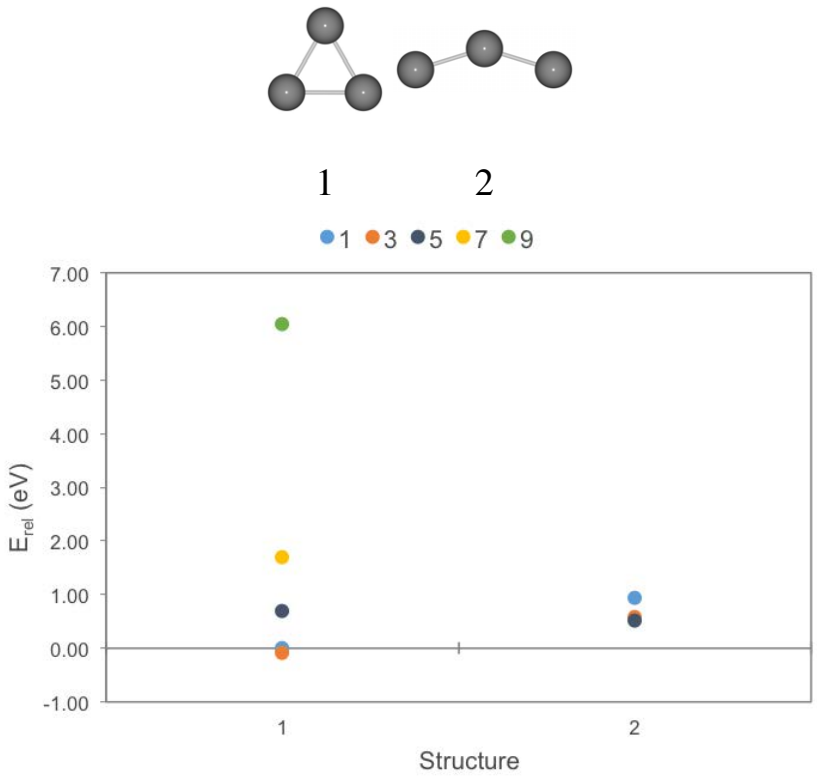

Figure 3.2: Relative energies for Pt_3 structures generated from GA-DFT search at varying multiplicities. All energies relative to the singlet structure 1, the GM calculated from the PWscf calculation. Missing data points indicate that there was structural rearrangement during the subsequent local relaxation.

Table 3.4: Comparison between GM structures obtained for the Gupta-GA and PBE-GA methods.

Gupta	DFT
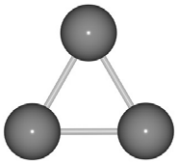	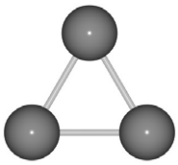
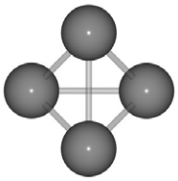	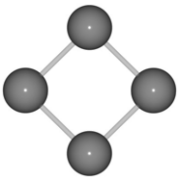
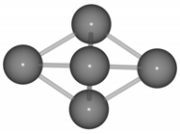	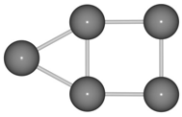
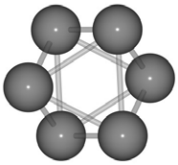	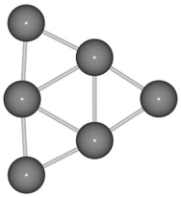

at least one multiplicity when reoptimised with NWChem. However, a slight structural rearrangement of cluster 4 occurs. The GA search located a slightly distorted structure (4^a) which locally minimised to the C_{2v} butterfly structure (4^b) when relaxed with NWChem. This structural rearrangement makes the C_{2v} butterfly cluster more energetically competitive, bringing the energy in line with that of structure 1 at a multiplicity of 1.

The majority of structures generated from the GA search are planar (or "bent"), aside from structure 2, the T_d tetrahedron, which is also the structure generated by the GA-Gupta-EP search. Structures with low coordinated Pt atoms tend to be higher in energy than those greater coordination of Pt atoms. For structure 1, reoptimisation at multiplicities of 1–7 result in very similar relative energies. When the multiplicity is increased to 9 and the structure relaxed, the relative energy increases significantly ($\sim$2.50 eV). For other structures, there is a greater spread of relative energies when varying spin multiplicity, although multiplicities of 7 and 9 result in less energetically favourable structures. Finally, relaxations with multiplicities of 3 and 5 result

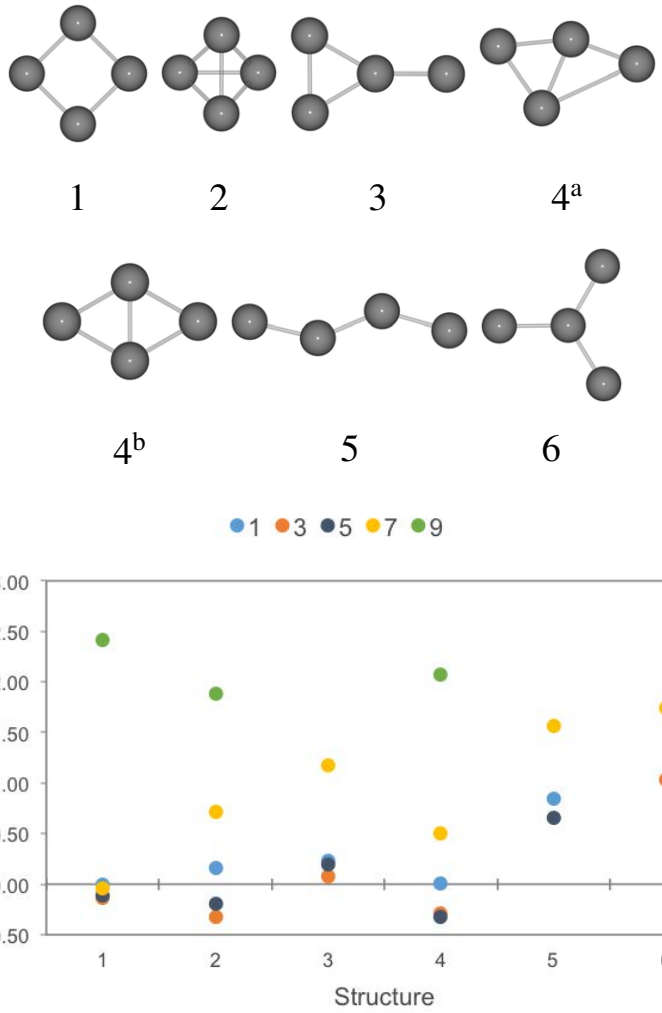

Figure 3.3: Relative energies for Pt_4 structures generated from GA-DFT search at varying multiplicities. All energies relative to the singlet structure 1, the GM calculated from the PWscf calculation. Missing data points indicate that there was structural rearrangement during the subsequent local relaxation.

in lower energy structures than the singlet in all cases.

Pt_5 clusters generated from the GA search are shown in Figure 3.4. It is seen that whilst there are similar energetic penalties for unfavourable structures or multiplicities (<3.0 eV) of Pt_5 compared to Pt_4, there is greater variation of the relative energies with varying spin. Once again, high spin multiplicites of 7 or 9 tend to result in energetically unfavourable structures, although the septet is competitive in the cases of structures 1, 2 and 5. Once again, a large number (8 out of the 11) of planar or "bent" structures are found. Clusters with low coordinated Pt atoms typically account for the high energy structures. Structure 4 also has a low coordinated Pt atom, although upon local minimisation at varying spin, this structure is found to be less favourable than structures 5 and 6. In general, moving from structure 1 to 11 results in an increase in relative energy. This suggests that there is broad agreement between the NWChem and QE results, although the inclusion of spin in the NWChem results does complicate this trend slightly.

Whilst spin had a significant effect on the energy of Pt_5 structures, it has less of an effect on Pt_6. From Figure 3.5, it is shown that there is far less energetic variation on inclusion of spin. There is general agreement between the relative energies from the GA search and the local relaxations with varying spin. Once again the nonet is generally found to result in significantly higher energies than the other states. This suggests that for the pure Pt clusters, a spin multiplicity of 9 is sufficient to capture the energetically competitive structures.

Structure 20 was not located during the initial GA search and instead was found through a rearrangement of the nonet structure 13. Nine of the Pt_6 structures were non-planar, meaning that whilst the majority were still planar or "bent", a greater proportion were 3D structures when compared to Pt_4 and Pt_5. This is to be expected, as the system size increases, moving towards a 3D GM, a greater proportion of 3D structures are going to be found. As with other sizes, initially planar structures are favoured, followed by a number of 3D structures. Finally, high energy structures (predominantly planar) with low-coordinated Pt atoms are found.

The energetically favourable structures for the pure Pt clusters can be seen in Figure 3.6, with their relative energies displayed in Table 3.5: energetically competitive structures are also

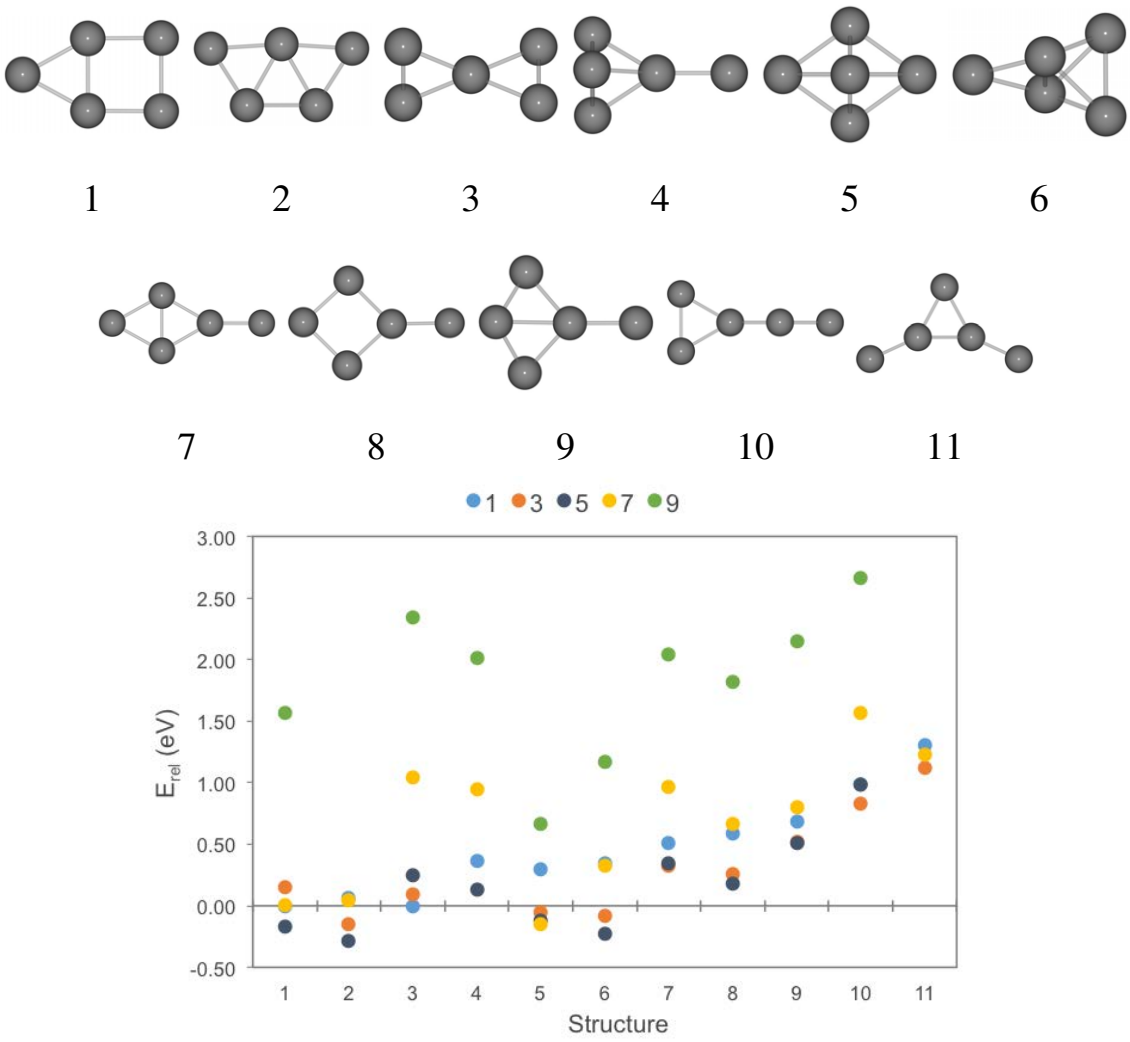

Figure 3.4: Relative energies for Pt_5 structures generated from GA-DFT search at varying multiplicities. All energies relative to the singlet structure 1, the GM calculated from the PWscf calculation. Missing data points indicate that there was structural rearrangement during the subsequent local relaxation.

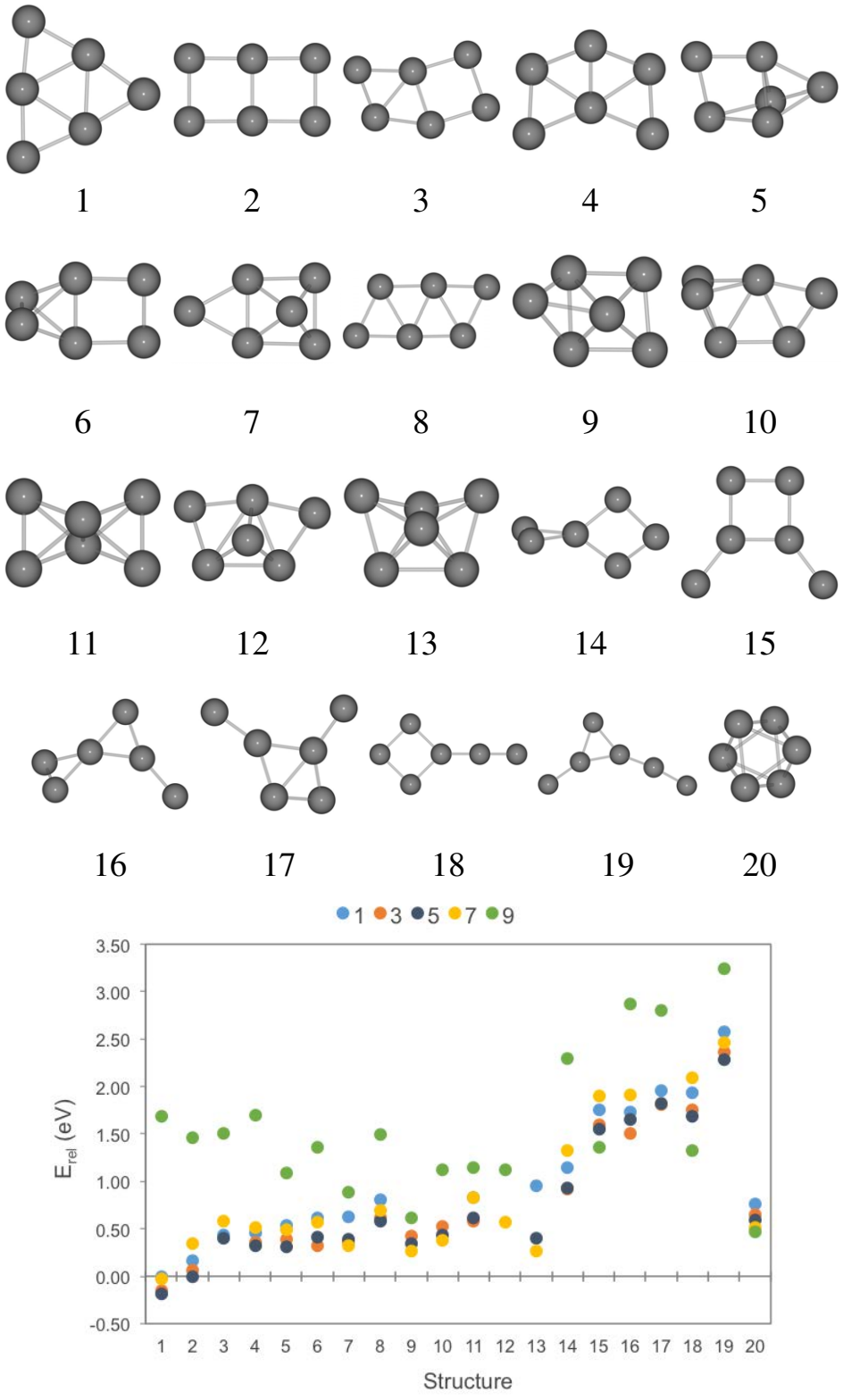

Figure 3.5: Relative energies for Pt_6 structures generated from GA-DFT search at varying multiplicities. All energies relative to the singlet structure 1, the GM calculated from the PWscf calculation. Missing data points indicate that there was structural rearrangement during the subsequent local relaxation.

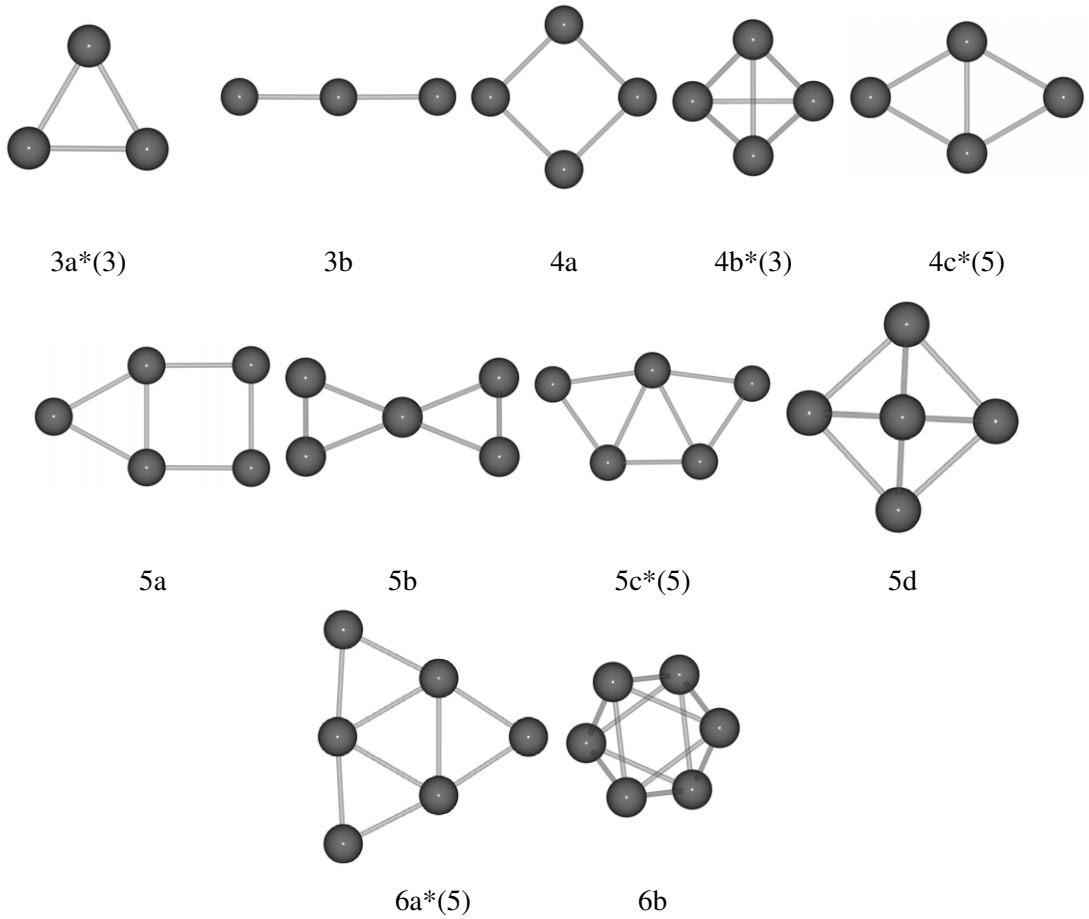

Figure 3.6: Low energy structures found for pure Pt clusters, from Pt_3 to Pt_6, with varying spin. GM clusters for all sizes are specified (*). Numbers in brackets show at which spin multiplicity the GM is found.

displayed for a more complete discussion. In previous discussions of small Pt clusters, it has been noted that results do not always converge on the same structures, with different studies finding different global minimum (GM) clusters. It has been suggested that this is a result of the use of different pseudopotentials, basis sets, *xc* functionals and energy cutoffs [141].

GM clusters are discussed with respect to the minimum energy cluster for a given size. It was expected that the 3-atom clusters would preferentially form triangular D_{3h} structures (*3a*). For all spin multiplicities other than 5 this was found to be the case. However, for a spin multiplicity of 5, the linear conformation (*3b*) was 0.2 eV lower in energy than the triangular structure. The GM is still found for the triangular D_{3h} structure at the triplet state, with a Pt-Pt-Pt angle of 60.0°, although there is little difference between the singlet and triplet energies.

Table 3.5: Relative energies (E_{rel}) and average bond distances for the low energy Pt_3 to Pt_6 clusters (shown in Figure 3.6), with varying spin multiplicities (2S+1).

2S+1	Cluster	E_{rel} (eV)	Pt-Pt Å
		Pt_3	
1	3a	0.00	2.47
3	3a	-0.09	2.50
5	3b	0.51	2.37
7	3a	1.69	2.51
9	3a	6.04	2.50
		Pt_4	
1	4a	0.00	2.46
1	4c	0.01	2.52
3	4b	-0.32	2.60
3	4c	-0.29	2.53
5	4c	-0.32	2.52
7	4a	-0.04	2.45
9	4b	1.88	2.61
		Pt_5	
1	5a	0.00	2.48
1	5b	0.00	2.47
3	5c	-0.15	2.53
5	5c	-0.29	2.54
7	5d	-0.15	2.58
9	5d	0.66	2.62
		Pt_6	
1	6a	0.00	2.53
3	6a	-0.15	2.53
5	6a	-0.19	2.54
7	6a	-0.03	2.54
9	6b	0.47	2.64

For Pt_4 clusters there is competition between the triplet T_d tetrahedron (*4b*) and the quintet C_{2v} butterfly (*4c*), though this structure is only 30 meV higher in energy than the tetrahedron in the triplet state. For Pt_5, the GM is found to be the C_2 W-shaped cluster (*5c*) in the quintet state. This is found to be at least 0.14 eV more stable than other isomers. Finally, the quintet triangular D_{3h} structure (*6a*) is found to be the GM for Pt_6.

Whilst for Pt_3, there is little advantage in increasing the spin multiplicity, for the larger clusters, higher spin states (up to septet) are favoured. For the nonet states, relatively large energetic penalties are observed for all the pure Pt clusters, though this penalty decreases with increased cluster size. From the results obtained in this study, no clear 2D/3D transition can be identified. Whilst the 3 and 6 atom GM are predicted to be planar (D_{3h}) triangles, other structures identified as GM tend to have more deformed (twisted, or puckered) structures. For the Pt_2 dimer, there was little change in the Pt-Pt bond length with changing spin. This trend is continued for Pt_3 and Pt_4. However, for the larger cluster sizes, the average bond length increases with increasing spin.

As mentioned previously, small differences in the computational methodology can result in differences in the predicted GM structures. The methodology employed in this work differs from others [141–146], with the use of a LCAO-based DFT code, TZVP basis set and PBE XC for the final energetic analysis. All structures noted in previous studies were located in the GA-DFT search, although in some cases different energetic ordering was observed.

3.4.2 Platinum-Titanium Clusters

3.4.2.1 Singly Doped Clusters

The full range of clusters generated for Pt_2Ti to Pt_5Ti are shown in Figures 3.7–3.10. As with Pt_3, two structures are found for Pt_2Ti, with a preference for maximising Pt–Ti bonds. Five structures are found from the GA search for Pt_3Ti, all of which are planar or "bent", shown in Figure 3.8. However, of the five structures, structure 4 is not locally stable when optimised with NWChem. During the relaxation, the structure distorts with the low coordinated Pt atom

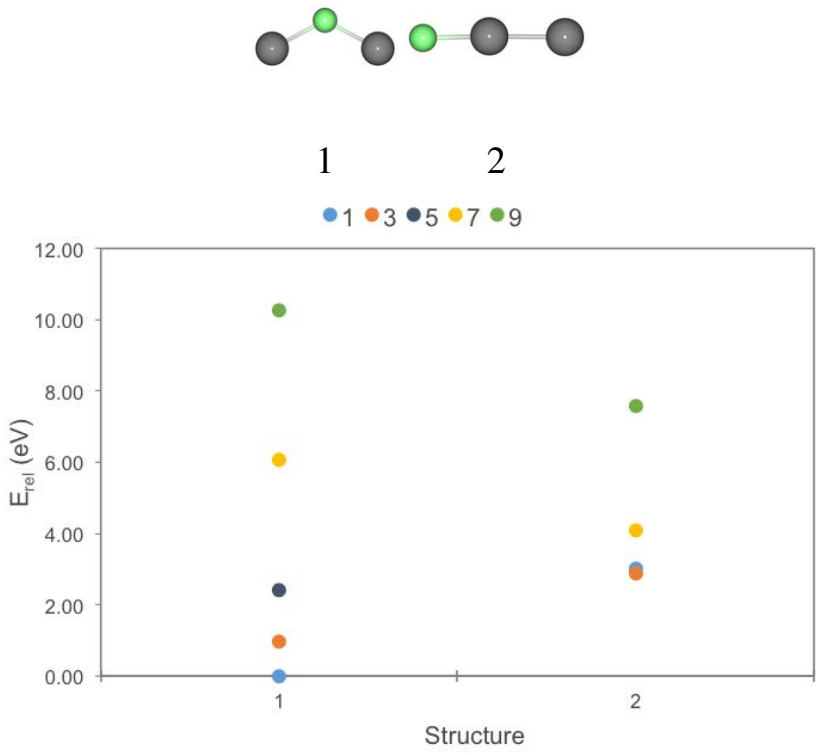

Figure 3.7: Relative energies for Pt_2Ti structures generated from GA-DFT search at varying multiplicities. All energies relative to the singlet structure 1, the GM calculated from the PWscf calculation. Missing data points indicate that there was structural rearrangement during the subsequent local relaxation.

bonding to the Ti to form structure 1. When compared to the pure Pt clusters, it is found that there are far greater energetic penalties associated with less favourable spin states. The typical variation in relative energies is below 2.5 eV for Pt_4, whereas for Pt_3Ti, the relative energies can be as high as 5.0 eV. It is found that maximising Pt–Ti bonding leads to more energetically favourable structures. The singlet structure 5 is $\sim$3.0 eV higher in energy than structures 1 and 2.

Similar trends to those found for Pt_3Ti are also observed for Pt_4Ti, as can be seen in Figure 3.9. There are once again significant energetic penalties associated with the higher spin states. Pt–Ti bonding is maximised, resulting in low energy structures, this can easily be achieved at the expense of Pt–Pt bonding. This leads to only three out of the seven structures being planar or "bent", with the majority being 3D. There is generally little competition between varying

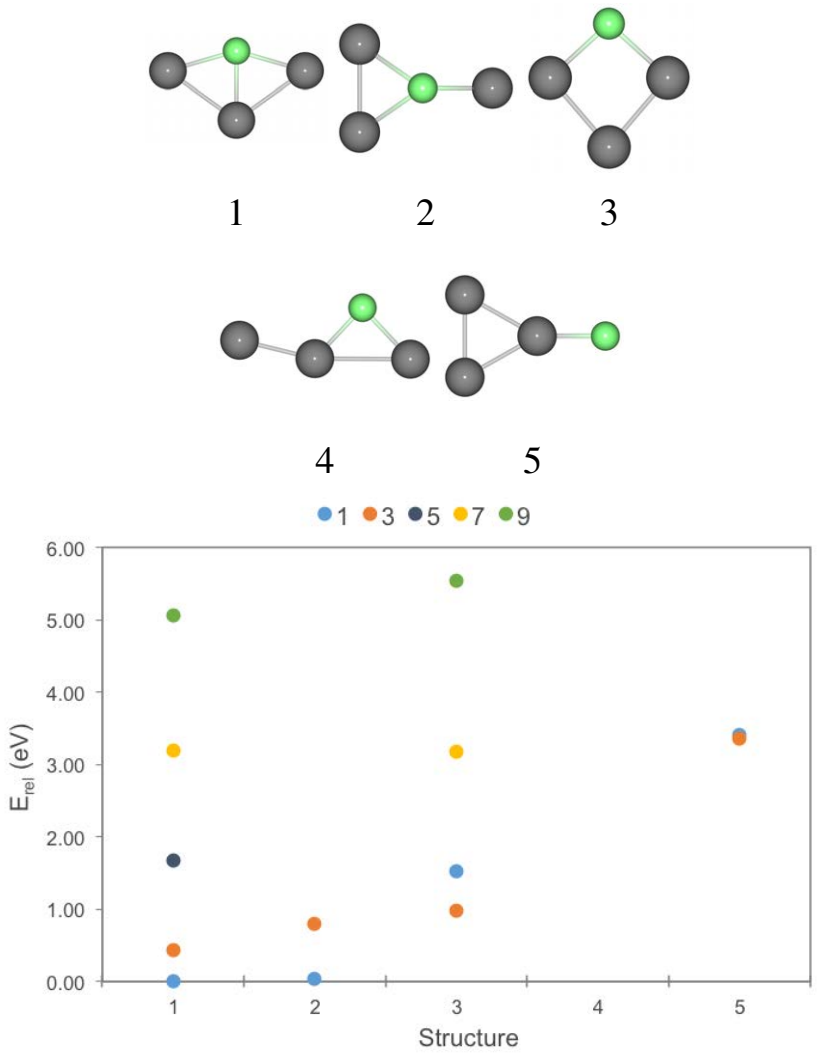

Figure 3.8: Relative energies for Pt_3Ti structures generated from GA-DFT search at varying multiplicities. All energies relative to the singlet structure 1, the GM calculated from the PWscf calculation. Missing data points indicate that there was structural rearrangement during the subsequent local relaxation.

spin states, with higher multiplicities leading to less favourable structures. This is contrary to Pt_5, where significant variation can be seen for different multiplicities and structures.

Structures found for Pt_5Ti are displayed in Figure 3.10. It is found that only five of the 16 structures are planar or "bent", while the majority of structures discovered for Pt_5Ti are 3D. When compared to the majority of Pt_6 clusters being planar, this suggests that doping Pt clusters with a single Ti atom favours a move towards 3D structures. It is also seen that with the increased Pt:Ti ratio, there is a reduction in the energetic penalties associated with higher spin states. Whilst energetic penalties can be as large as 5.0 eV for Pt_3Ti or Pt_4Ti, it is found that energetic penalties are no higher than $\sim$4.0 eV for Pt_5Ti. There is also more variation in competition between singlet and triplet multiplicities. For Pt_5Ti half the structures are found to be lower in energy than the singlet. This suggests that for higher Pt:Ti ratios, higher spin states may start to become more favourable.

The lowest lying structures for the singly doped PtTi clusters are listed in Table 3.6, corresponding to the structures in Figure 3.11. For Pt_2Ti, the open bent C_{2v} structure (*3a*) is favourable for the singlet state, with a Pt-Ti-Pt angle of 124.6°. The bonding angle is reduced in the triplet state, to 79.6°, producing the closed C_{2v} triangle structure (*3b*) with a Pt-Pt bond, 0.96 eV higher in energy than the singlet. The closed triangle remains the lowest energy structure for the quintet and septet states. The cluster then opens up again (*3c*) for the nonet state, producing a more linear cluster.

Different energetic trends are observed for the Pt_3 and Pt_2Ti clusters. The GM is a triplet state for Pt_3 and a singlet state when doped with a single Ti atom. Energetic penalties are observed for higher spin multiplicities compared to the singlet state. These penalties are found to be larger for Pt_2Ti than Pt_3.

For Pt_3Ti, the GM is a singlet, with the C_{2v} kite (*4a*) and C_s Y-shape (*4b*) isomers being energetically competitive. Significant energetic penalties are associated with increasing spin multiplicity, in contrast to Pt_2Ti and Pt_4. For Pt_4, the triplet and quintet states produce competitive GM structures, with even the septet state being 40 meV more favourable than the singlet. Once doped with a single Ti atom, this behaviour changes, making the higher spin multiplies

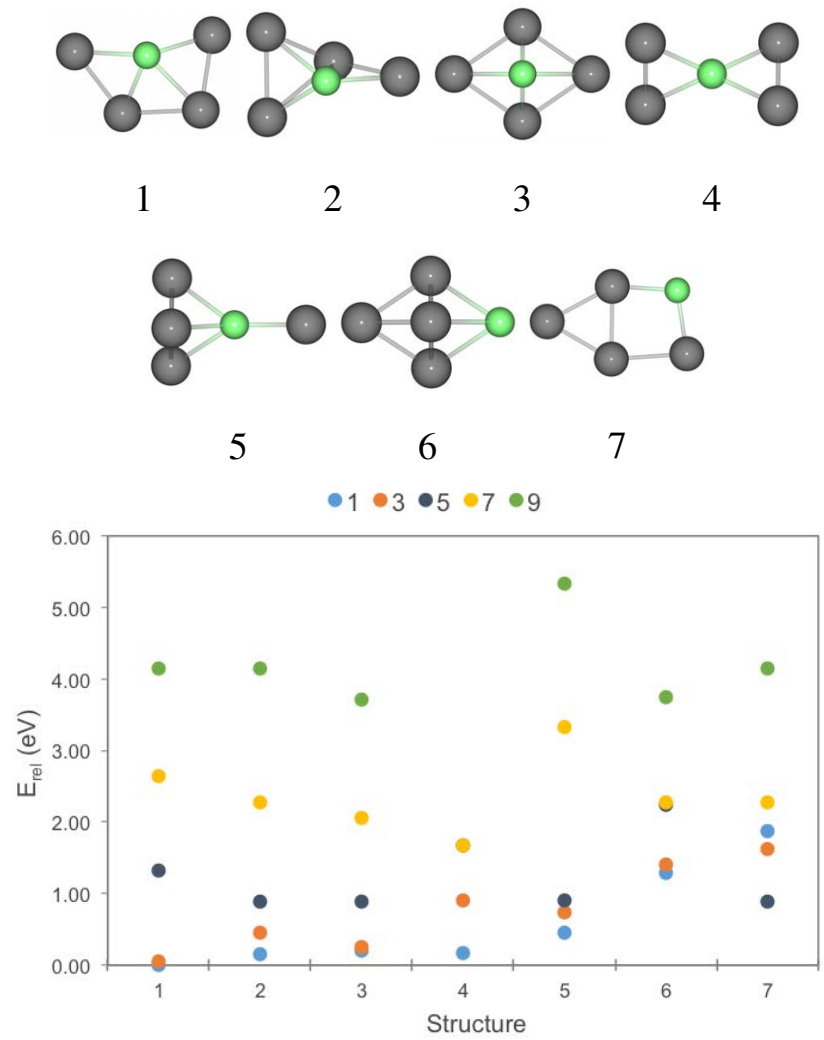

Figure 3.9: Relative energies for Pt_4Ti structures generated from GA-DFT search at varying multiplicities. All energies relative to the singlet structure 1, the GM calculated from the PWscf calculation. Missing data points indicate that there was structural rearrangement during the subsequent local relaxation.

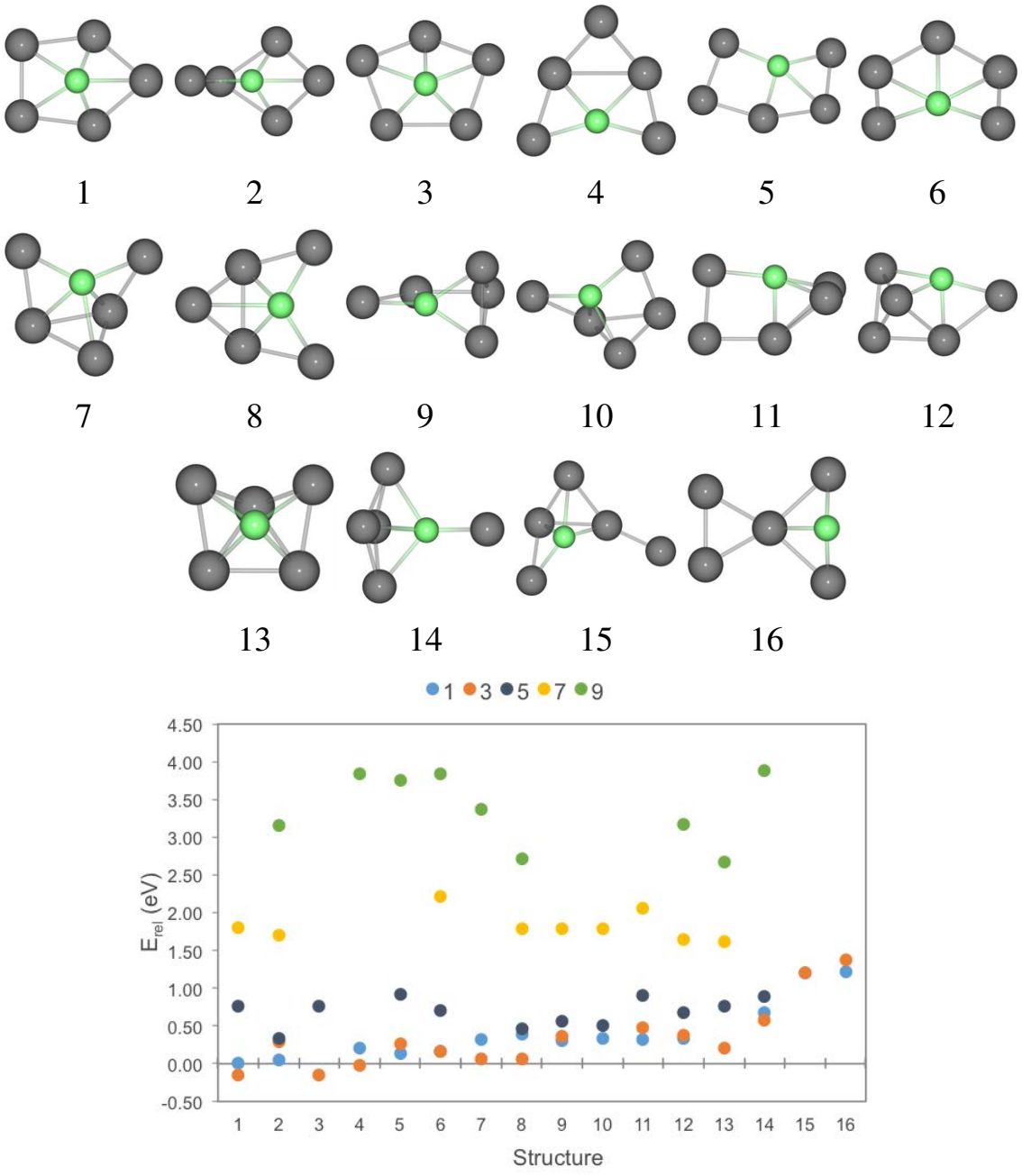

Figure 3.10: Relative energies for Pt_5Ti structures generated from GA-DFT search at varying multiplicities. All energies relative to the singlet structure 1, the GM calculated from the PWscf calculation. Missing data points indicate that there was structural rearrangement during the subsequent local relaxation.

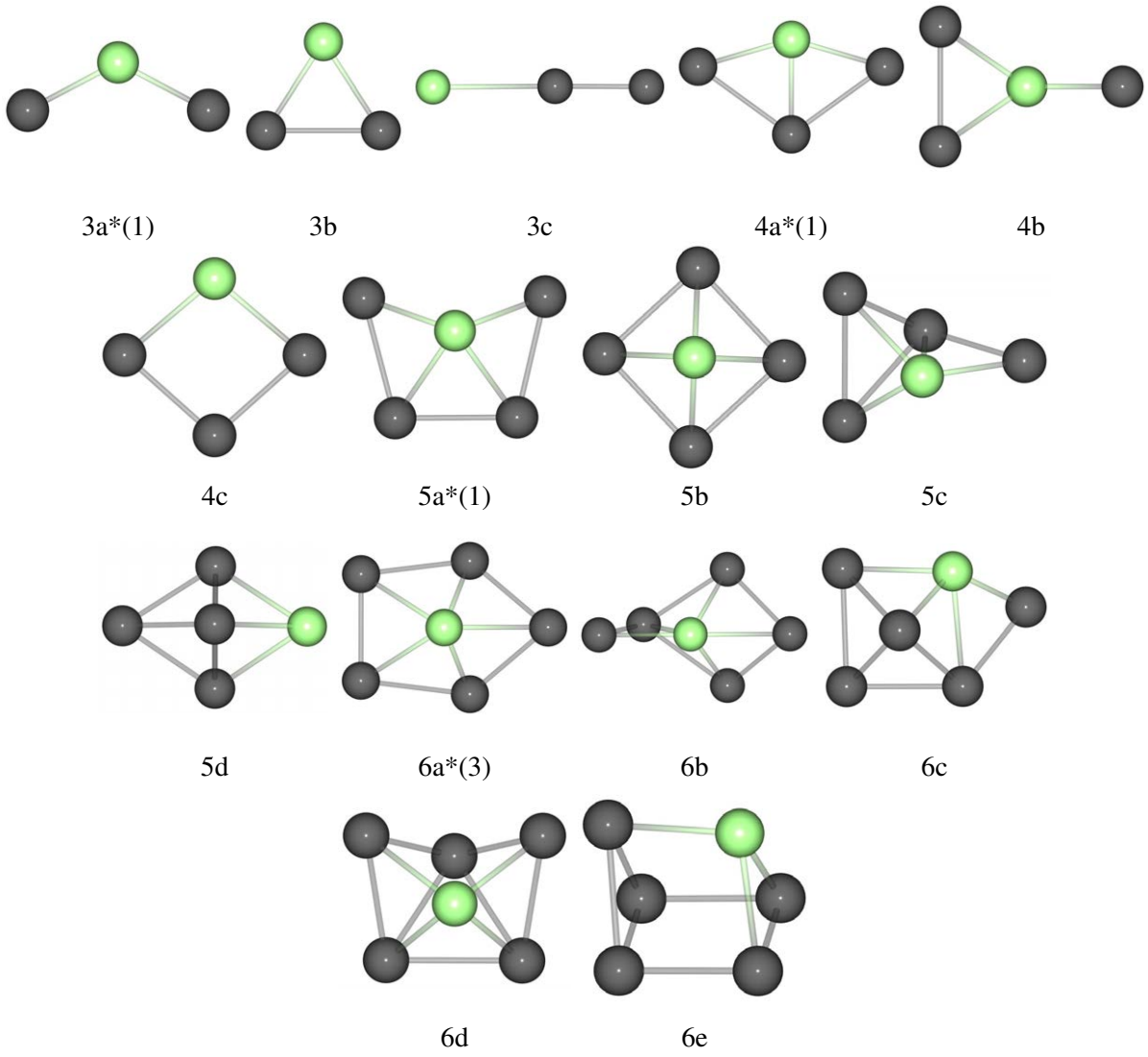

Figure 3.11: Low energy structures found for $Pt_{x-1}Ti$ clusters, from Pt_2Ti_1 to Pt_5Ti_1, with varying spin multiplicities. GM clusters for all sizes are specified (*). Numbers in brackets show at which spin multiplicity the GM is found.

Table 3.6: Relative energies (E_{rel}), average bond lengths and average Bader charges for singly doped PtTi clusers (shown in Figure 3.11), for varying spin multiplicities (2S+1).

2S+1	Cluster	E_{rel} (eV)	Pt-Pt (Å)	Pt-Ti (Å)	Ave. Pt Charge |e|	Ave. Ti Charge |e|
			Pt_2Ti			
1	3a	0.00	-	2.14	-0.68	1.41
3	3b	0.96	2.83	2.21	-0.52	1.10
5	3b	2.42	2.59	2.38	-0.46	0.58
7	3b	4.09	2.40	2.62	-0.32	0.70
9	3c	7.58	2.31	3.10	-0.06	0.10
			Pt_3Ti			
1	4a	0.00	2.70	2.26	-0.44	1.28
1	4b	0.03	2.56	2.27	-0.45	1.45
3	4a	0.43	2.77	2.25	-0.45	1.37
5	4a	1.67	2.57	2.41	-0.39	1.23
7	4c	3.18	2.48	2.43	-0.29	0.98
7	4a	3.19	2.47	2.62	-0.30	1.01
9	4a	5.06	2.56	2.70	-0.24	0.83
			Pt_4Ti			
1	5a	0.00	2.63	2.35	-0.36	1.51
3	5a	0.05	2.60	2.35	-0.35	1.46
5	5b	0.89	2.62	2.43	-0.32	1.36
5	5c	0.89	2.68	2.38	-0.32	1.28
7	5b	2.06	2.65	2.49	-0.31	1.24
9	5b	3.72	2.60	2.65	-0.24	1.07
9	5d	3.75	2.64	2.57	-0.24	1.13
			Pt_5Ti			
1	6a	0.00	2.62	2.42	-0.29	1.60
1	6b	0.05	2.65	2.41	-0.29	1.44
3	6a	-0.15	2.61	2.42	-0.29	1.43
5	6b	0.34	2.62	2.43	-0.29	1.43
7	6b	1.62	2.65	2.47	-0.27	1.42
7	6c	1.65	2.60	2.43	-0.28	1.54
9	6d	2.67	2.63	2.53	-0.23	1.20
9	6e	2.68	2.58	2.45	-0.24	1.19

unfavourable. The septet state is 3.18 eV higher in energy than the singlet Pt_3Ti.

Once again, for Pt_4Ti the GM is found for the singlet state. A W-shape structure (*5a*) with no symmetry is found to be the GM, a similar structure to that of Pt_5. However, once again higher spin multiplies incur an energetic penalty compared to the singlet state, although not as much as for Pt_3Ti.

Unlike the three, four and five atom clusters, the triplet state is found to be most favourable for Pt_5Ti. This results in the triplet C_s twisted pentagonal structure (*6a*) as the most energetically favourable structure. For larger cluster sizes, the energetic penalties associated with higher spin states is reduced. For Pt_5Ti it is then found that the Ti doped clusters behave more like the pure Pt clusters, with higher spin states (triplet) becoming more favourable.

As a result of charge transfer, the lowest energy homotops tend to maximise the number of Pt-Ti bonds, with Ti atoms in the most highly-connected sites. As with the pure Pt clusters, the GM isomers identified for $Pt_{x-1}Ti$ are planar, or "bent-planar" structures for cluster sizes 3–6. As the multiplicity is increased, there is generally little change in the average Pt-Pt bond length, though there is a slight increase in the average Pt-Ti bond lengths.

When analysing the Bader charges, significant charge transfer is seen from the Ti, which becomes highly positive (as high as +1.60), to the Pt atoms, which become negative. As expected, on increasing the cluster size, the Pt generally becomes slightly less negatively charged, whilst the Ti generally becomes slightly more positively charged. There is a decrease in charge transfer as the spin multiplicity is increased. The average Pt charge is 0.25 less negative and Ti is an average 0.64 less positive.

3.4.2.2 Doubly Doped Clusters

The range of doubly doped PtTi clusters can be found in Figures 3.12–3.15, for $PtTi_2$ to Pt_4Ti_2, respectively. The energetic penalties associated with higher spin states are reduced with respect to Pt_2Ti clusters, which have penalties as high as $\sim$10.0 eV. Only two structures were located from the GA search for Pt_2Ti_2, as shown in Figure 3.13. This is significantly fewer local minima than for Pt_4 or Pt_3Ti, where 6 and 5 minima were located, respectively. Structure 3 was not

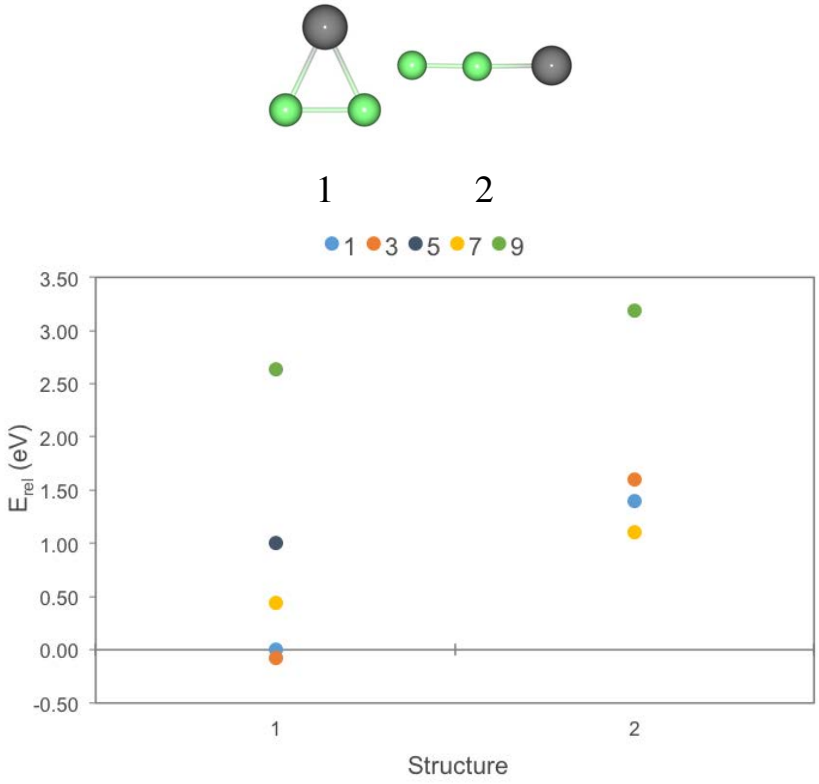

Figure 3.12: Relative energies for $PtTi_2$ structures generated from GA-DFT search at varying multiplicities. All energies relative to the singlet structure 1, the GM calculated from the PWscf calculation. Missing data points indicate that there was structural rearrangement during the subsequent local relaxation.

located from the GA search but was found through a distortion of structure 2 at high spins. Structure 3 is not stable for the singlet or triplet states, which explains why it was not located by the search. However, there is a strong preference for formation of the Ti–Ti dimer, with no structures being located where the Ti atoms were not bound to one another.

Structures from the GA search for Pt_3Ti_2 are shown in Figure 3.14. Only structures 1–4 were located through the GA; the rest were found through distortions when performing local geometry relaxations, and these new structures were then further optimised for multiplicities of 1–9. Of the nine structures investigated, only the first three are locally stable at the singlet, the multiplicity at which the GA search was performed. Higher spin states lead to more stable structures, with fewer distortions being observed for nonet state compared to any other. However, none of these structures are competitive with the singlet structure 1, at any multiplicity.

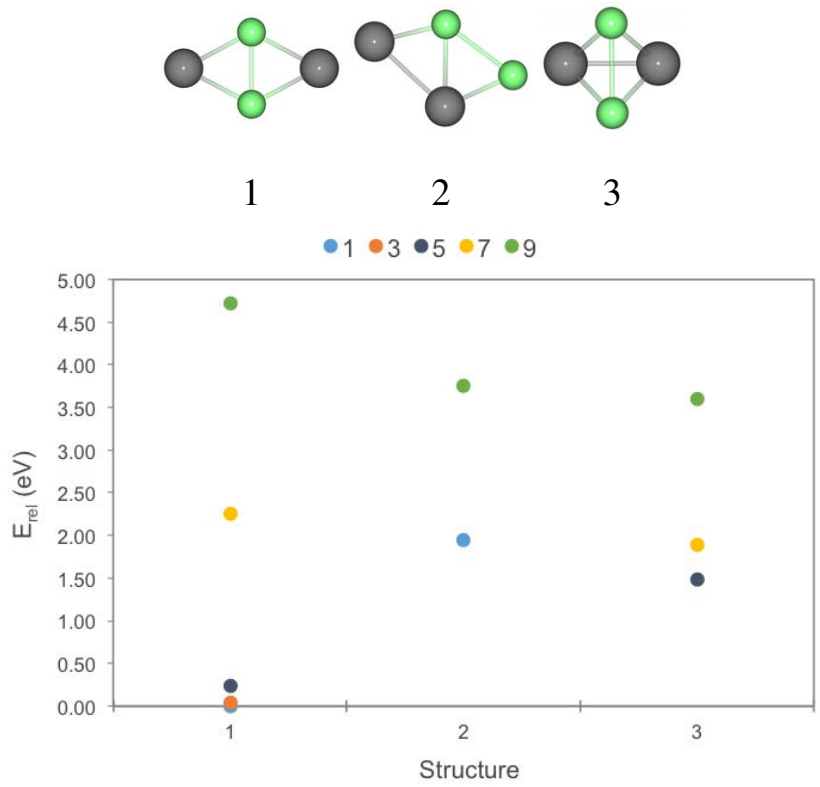

Figure 3.13: Relative energies for Pt_2Ti_2 structures generated from GA-DFT search at varying multiplicities. All energies relative to the singlet structure 1, the GM calculated from the PWscf calculation. Missing data points indicate that there was structural rearrangement during the subsequent local relaxation.

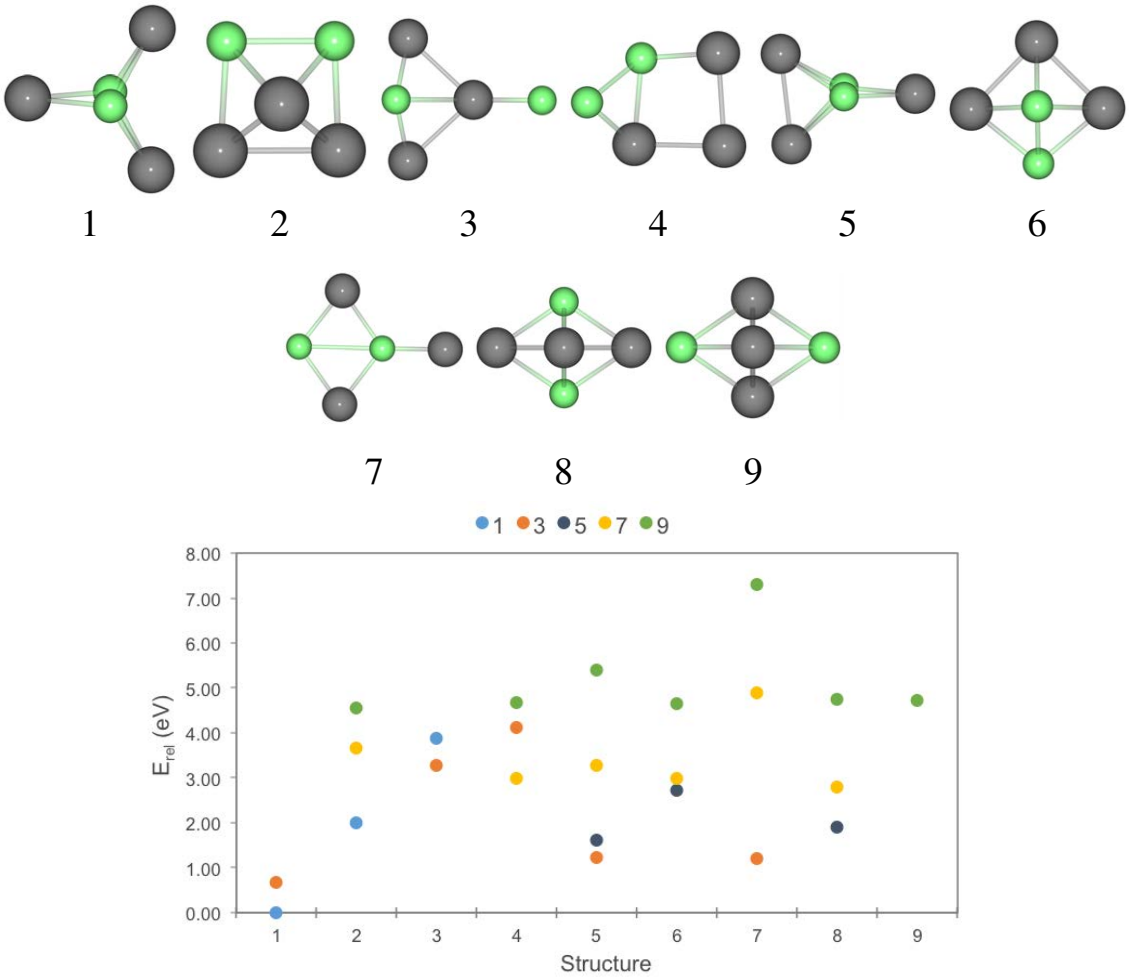

Figure 3.14: Relative energies for Pt_3Ti_2 structures generated from GA-DFT search at varying multiplicities. All energies relative to the singlet structure 1, the GM calculated from the PWscf calculation. Missing data points indicate that there was structural rearrangement during the subsequent local relaxation.

Once again formation of the Ti–Ti dimer fragment is generally favourable.

Structures from the GA search for Pt_4Ti_2 are shown in Figure 3.15. Only structures 1–7 were located by the search, with the remaining structures found through distortions during locally minimisations at higher spin states. This is similar to the Pt_3Ti_2 system, where distortions of a relatively large number of clusters at higher spin states lead to new structures being observed. Local relaxations performed on the pure Pt and singly doped PtTi clusters resulted in few distortions leading to significant structural rearrangement. For the doubly doped PtTi clusters this is much more common, although in every case, the GM is located through the GA search. Furthermore, none of the new structures found through structural rearrangements of the

Table 3.7: Relative energies (E_{rel}), average bond lengths and average Bader charges for doubly doped PtTi clusters (shown in Figure 3.16), for varying multiplicities (2S+1).

2S+1	Cluster	E_{rel} (eV)	Pt-Pt (Å)	Pt-Ti (Å)	Ti-Ti (Å)	Ave. Pt Charge |e|	Ave. Ti Charge |e|
				$PtTi_2$			
1	3a	0.00	-	2.42	2.09	-0.85	0.52
3	3a	-0.08	-	2.43	2.12	-0.85	0.41
5	3a	0.09	-	2.45	2.03	-0.88	0.47
7	3a	0.44	-	2.18	2.28	-0.95	0.56
9	3a	2.63	-	2.45	2.38	-0.68	0.38
				Pt_2Ti_2			
1	4a	0.00	-	2.42	2.19	-0.89	0.85
3	4a	0.04	-	2.43	2.26	-0.91	1.00
5	4a	0.23	-	2.41	2.53	-0.89	0.87
7	4b	1.89	2.71	2.45	2.54	-0.73	0.69
9	4b	3.60	2.51	2.59	2.46	-0.60	0.66
				Pt_3Ti_2			
1	5a	0.00	-	2.41	2.30	-0.79	1.27
3	5a	0.68	-	2.39	2.55	-0.79	1.23
5	5b	1.63	2.67	2.43	2.65	-0.76	1.08
7	5c	2.80	2.70	2.48	2.73	-0.68	1.01
9	5d	4.56	2.63	2.49	2.36	-0.46	0.76
				Pt_4Ti_2			
1	6a	0.00	-	2.37	2.74	-0.86	1.25
3	6b	0.51	2.62	2.35	2.65	-0.63	1.41
5	6c	1.24	2.60	2.48	2.60	-0.61	1.30
7	6d	2.34	2.60	2.51	2.65	-0.60	1.28
9	6e	3.95	2.65	2.54	2.41	-0.42	0.91

original GA structures are stable at the singlet. In general it is found that as the spin multiplicity is increased, the structures become less energetically favourable. For the vast majority of structures, 3D geometries are located, with only two planar or bent structures being found. These two more planar structures are also the only two structures where a Ti–Ti bond is not formed. There is also a general preference for maximising Pt–Ti bonding.

The lowest lying structures for doubly doped PtTi clusters are listed in Table 3.7, corresponding to the structures in Figure 3.16. The closed C_{2v} triangle (*3a*) is found preferentially for all multiplicites for the $PtTi_2$ clusters. Unlike for Pt_2Ti, the GM is found for the triplet state, with a Ti-Pt-Ti angle of 51.7°. For $PtTi_2$ relatively small energy penalties are found for higher

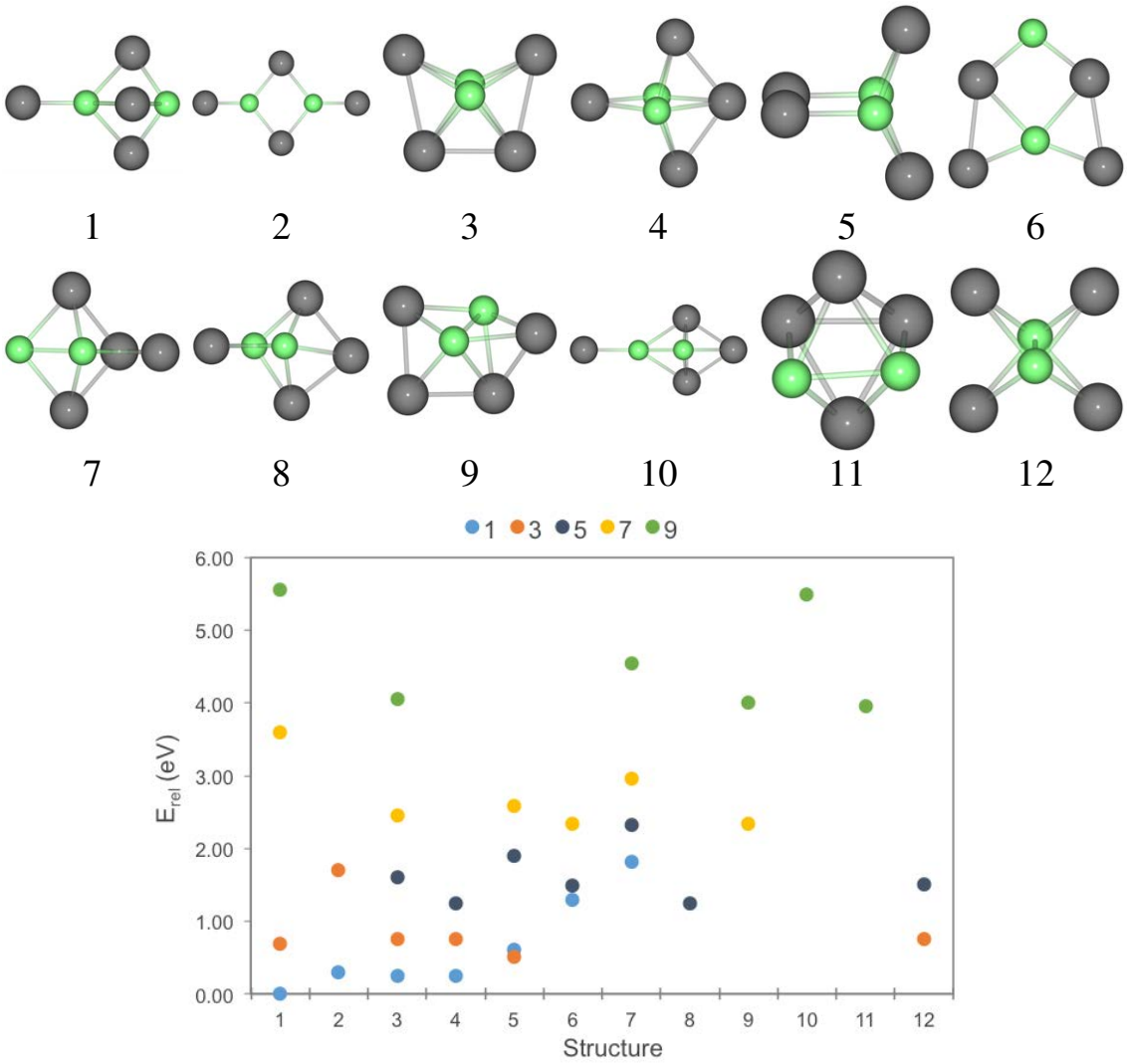

Figure 3.15: Relative energies for Pt_4Ti_2 structures generated from GA-DFT search at varying multiplicities. All energies relative to the singlet structure 1, the GM calculated from the PWscf calculation. Missing data points indicate that there was structural rearrangement during the subsequent local relaxation.

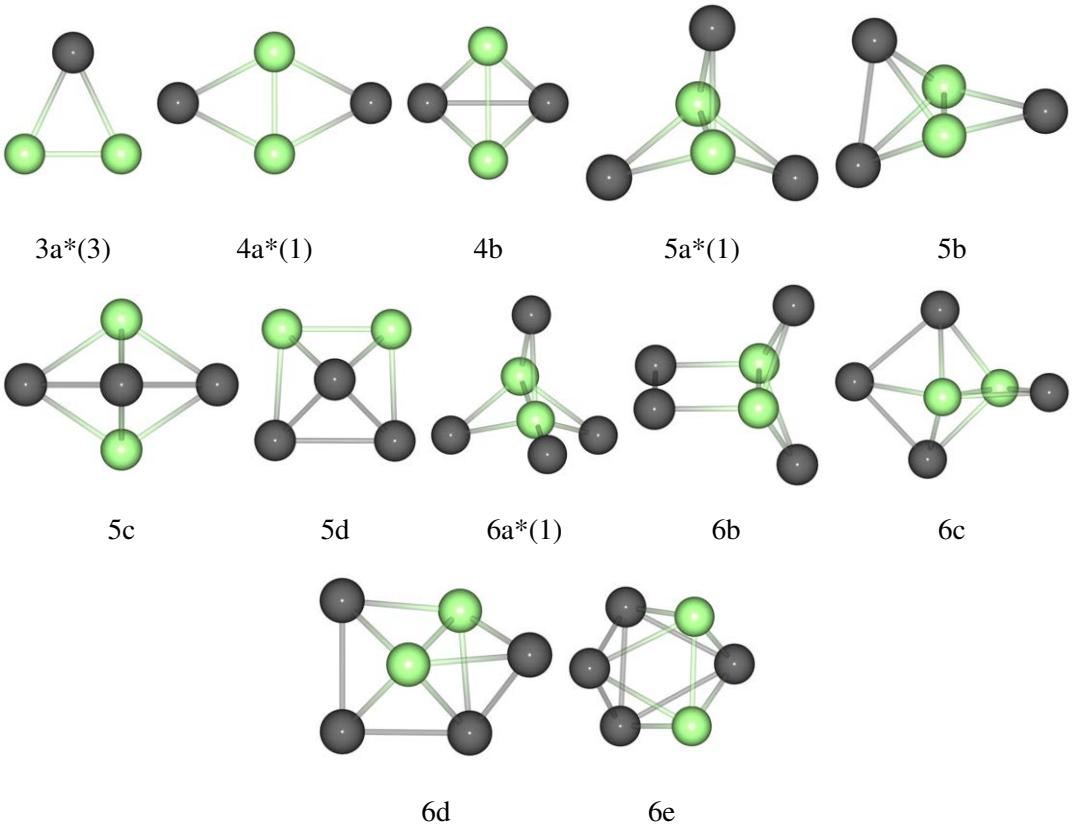

Figure 3.16: Low energy structures found for $Pt_{x-2}Ti_2$ clusters, from $PtTi_2$ to Pt_4Ti_2, with varying spin multiplicities. GM clusters for all sizes are specified (*). Numbers in brackets show at which spin multiplicity the GM is found.

spin states.

This situation is different for the larger doubly doped clusters, with the GM being found for the singlet state in all cases. The observed bonding motifs suggest preferential formation of Ti-Ti bonds, followed by Pt-Ti bonding, and it appears that greater Pt-Pt bonding results in less favourable structures. For the C_{2v} butterfly Pt_2Ti_2 GM structure (*4a*), there are no Pt-Pt bonds. The C_{2v} tetrahedron structure (*4b*) with a single Pt-Pt bond is only found to be locally stable at higher spin multiplicities (5–9).

The singlet D_{3h} structure (*5a*) is found to be the GM for Pt_3Ti_2. The lowest energy homotop again favours Ti-Ti and Pt-Ti bonding, with Pt-Pt bonding found to be unfavourable, with the same being true for the singlet C_{3v} structure (*6a*), which is the GM for Pt_4Ti_2. With increasing cluster size, the energetic penalty associated with increasing the spin multiplicity initially increases, although it decreases again for Pt_4Ti_2. The lowest penalties (and the triplet state GM) are found for the three atom clusters, with the largest penalties associated with the five atom clusters. It is expected that as the cluster size increases and the Pt/Ti ratio increases, higher spin states will again be lower in energy (as with Pt_5Ti), although this is not seen in the 3–6 atom range.

For the 3–5 atom clusters, growth occurs with additional Pt atoms bonding to a central Ti_2 unit. This minimises Pt-Pt interactions, whilst maximising Pt-Ti interactions. Following filling of the Ti-Ti bridge positions, additional Pt atoms favour bonding to the Ti top sites, as in Pt_4Ti_2. The lack of Pt-Pt bonding makes it difficult to draw conclusions from the average Pt-Pt bond lengths. However, in general, as the spin multiplicity increases, the Pt-Ti bond length increases. The same appears to be true for the average Ti-Ti bond length. For Pt_4Ti_2, as the spin is increased the average Ti-Ti bond length generally decreases. The doubly doped PtTi clusters, have a distinct 2D/3D transition between Pt_2Ti_2 and Pt_3Ti_2.

The Bader charge analysis demonstrates significant charge transfer from Ti to Pt. Once again, as the spin is increased, the charge transfer decreases, though there is less change in charge transfer with changing cluster size, compared to the singly doped PtTi clusters.

3.4.3 Platinum-Vanadium Clusters

3.4.3.1 Singly Doped Clusters

The range of singly doped PtV clusters is shown in Figures 3.17–3.20, for Pt_2V to Pt_5V, respectively. For Pt_2V, the same two structures are found as for Pt_2Ti, which are shown in Figures 3.17 and 3.7, respectively, although the energetic penalties associated with unfavourable spin stares are reduced for the PtV clusters compared to the PtTi clusters. The structures generated for Pt_3V are displayed in Figure 3.18, with structures 1–6 generated by the GA search. Structure 7 was not stable for the singlet and was found through a distortion of structure 1 when relaxed at high spin states. However, structure 2 was generated by the GA search, although it was not locally stable when relaxed with NWChem. There is a general preference for maximising Pt-V bonding. The singlet structure 5 is relatively low in energy, although it is unstable at higher multiplicities.

Pt_4V structures generated by the GA search are shown in Figure 3.19. Structures 1–5 were located by the initial search, with the remainder being found through structural rearrangements during the local geometry optimisation. The GA search located planar or bent structures, which are energetically favourable at low spin states. However, at higher spin states, the 3D structures are typically favoured. Maximising Pt–V bonding typically results in low energies.

For Pt_5V, structures 1–9 shown in Figure 3.20, were found by the GA. The remaining five structures were located through structural rearrangements during local geometry relaxations. Once again, the structures located through structural rearrangements tend to not be stable at the singlet. For Pt_5V, there is a greater mix of planar and 3D structures, when compared to Pt_4V, with no clear preference for one over the other. As with Pt_4V, there is a preference for maximising Pt–V bonding, with particularly high energies for structures 7, 8 and 9. There is also a general trend that as the spin multiplicity increases, the energy increases.

The lowest lying structures for the singly doped PtV clusters are given in Table 3.8, corresponding to the structures shown in Figure 3.21. From the energetic analysis, in all cases a spin multiplicity of 2 (the lowest possible) is favoured. This differs from the monometallic and

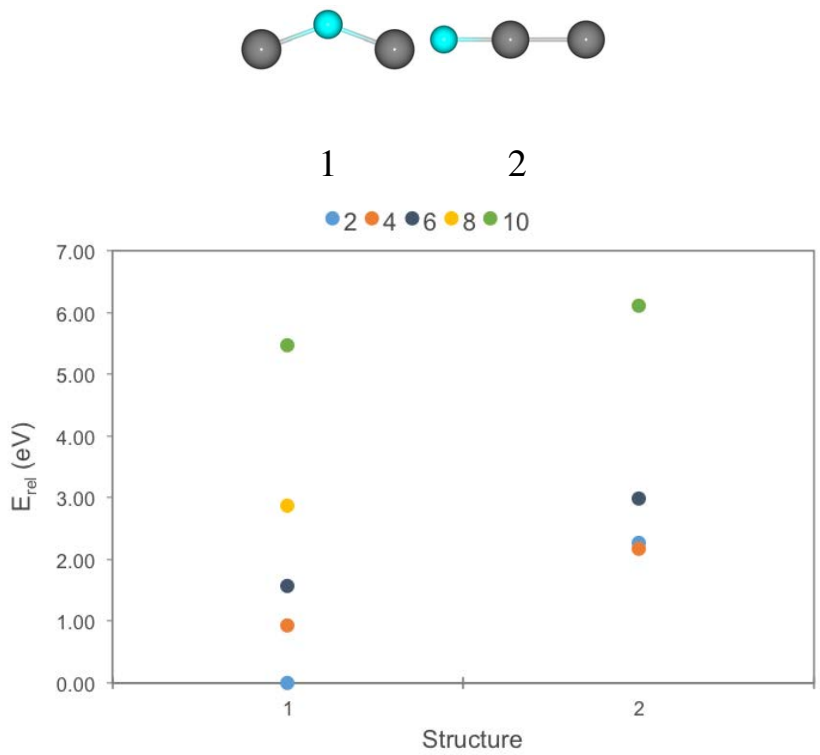

Figure 3.17: Relative energies for Pt_2V structures generated from GA-DFT search at varying multiplicities. All energies relative to the singlet structure 1, the GM calculated from the PWscf calculation. Missing data points indicate that there was structural rearrangement during the subsequent local relaxation. It should be noted that the Pt-V-Pt angle of structure 1 varies with changing multiplicity.

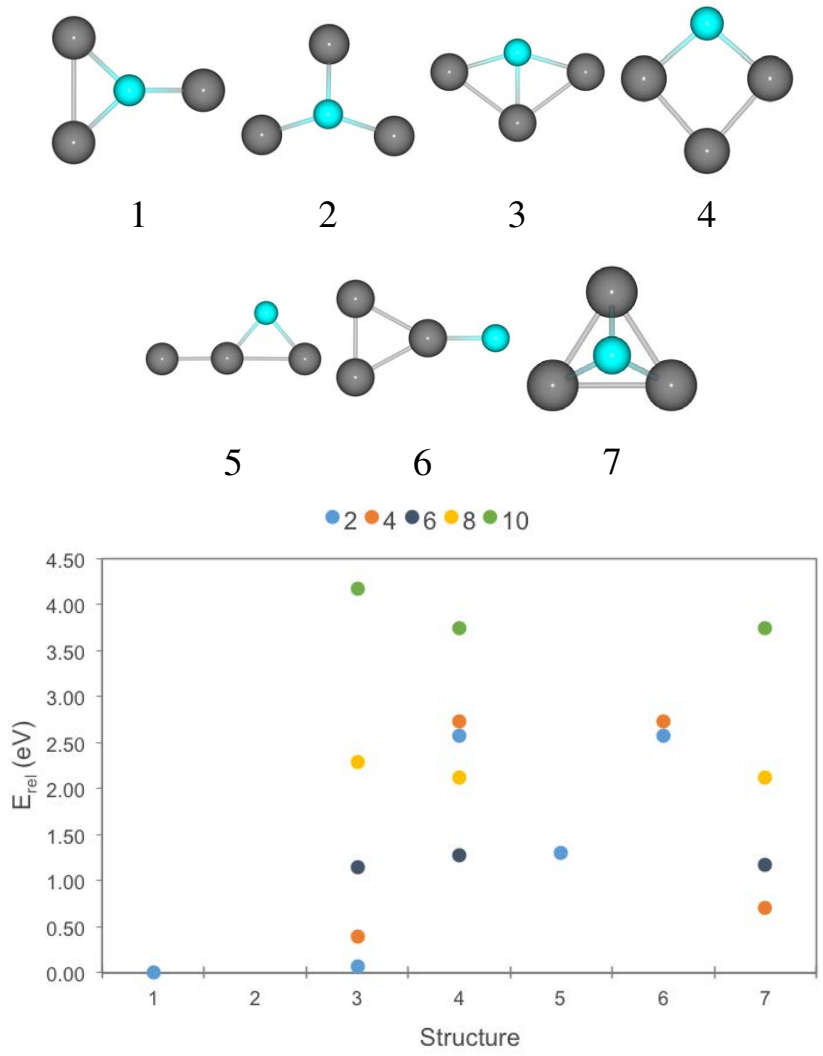

Figure 3.18: Relative energies for Pt_3V structures generated from GA-DFT search at varying multiplicities. All energies relative to the singlet structure 1, the GM calculated from the PWscf calculation. Missing data points indicate that there was structural rearrangement during the subsequent local relaxation.

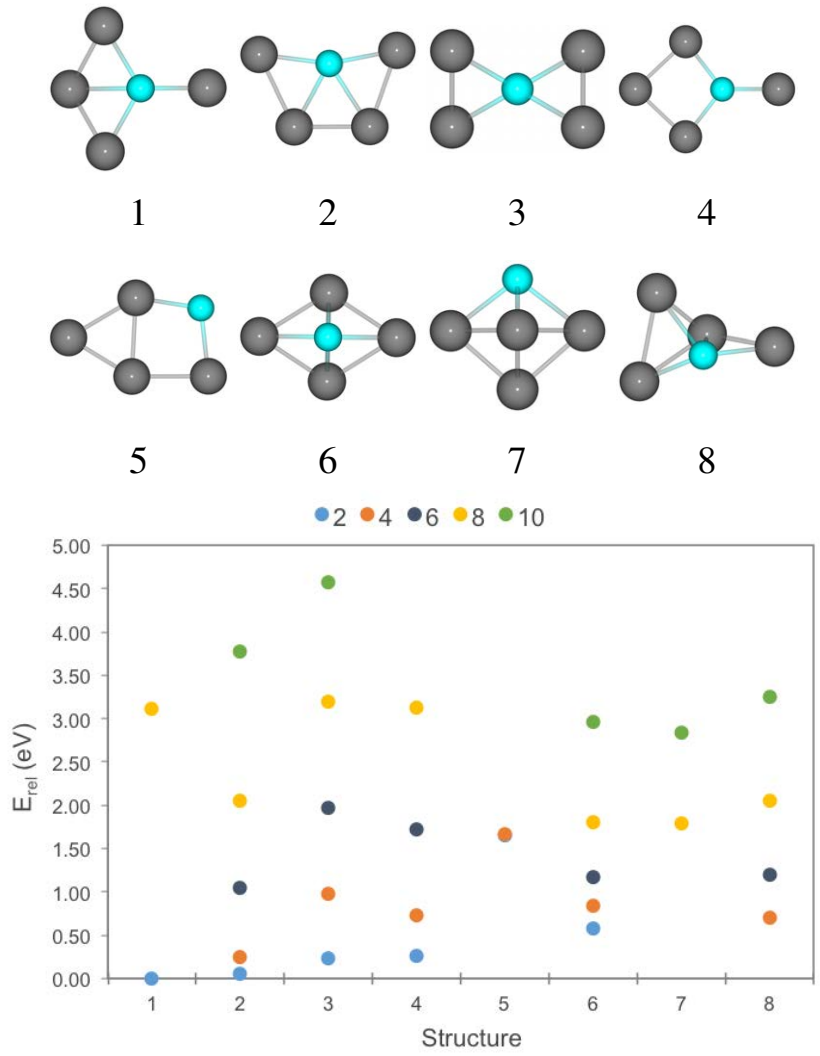

Figure 3.19: Relative energies for Pt_4V structures generated from GA-DFT search at varying multiplicities. All energies relative to the singlet structure 1, the GM calculated from the PWscf calculation. Missing data points indicate that there was structural rearrangement during the subsequent local relaxation.

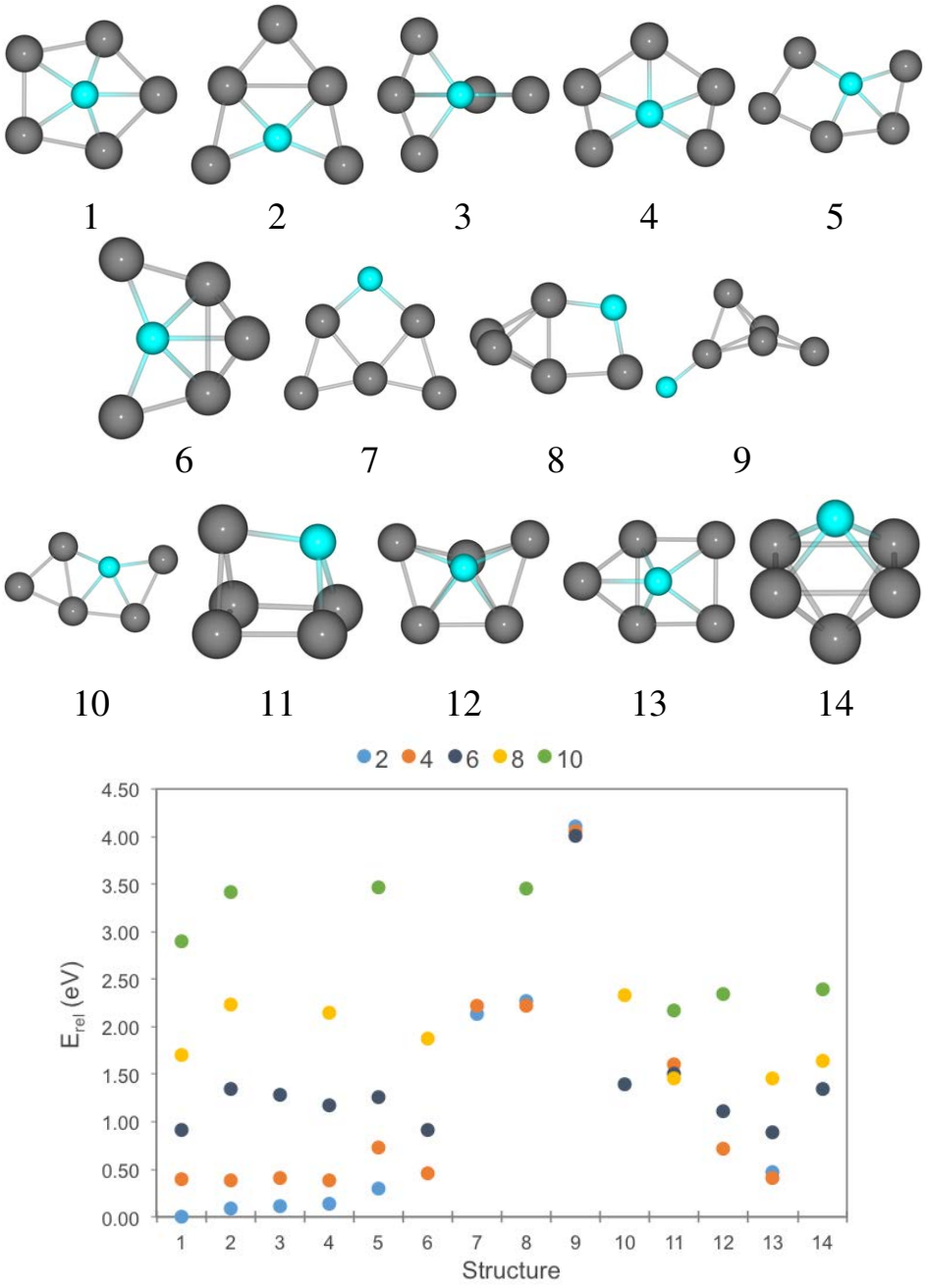

Figure 3.20: Relative energies for Pt_5V structures generated from GA-DFT search at varying multiplicities. All energies relative to the singlet structure 1, the GM calculated from the PWscf calculation. Missing data points indicate that there was structural rearrangement during the subsequent local relaxation.

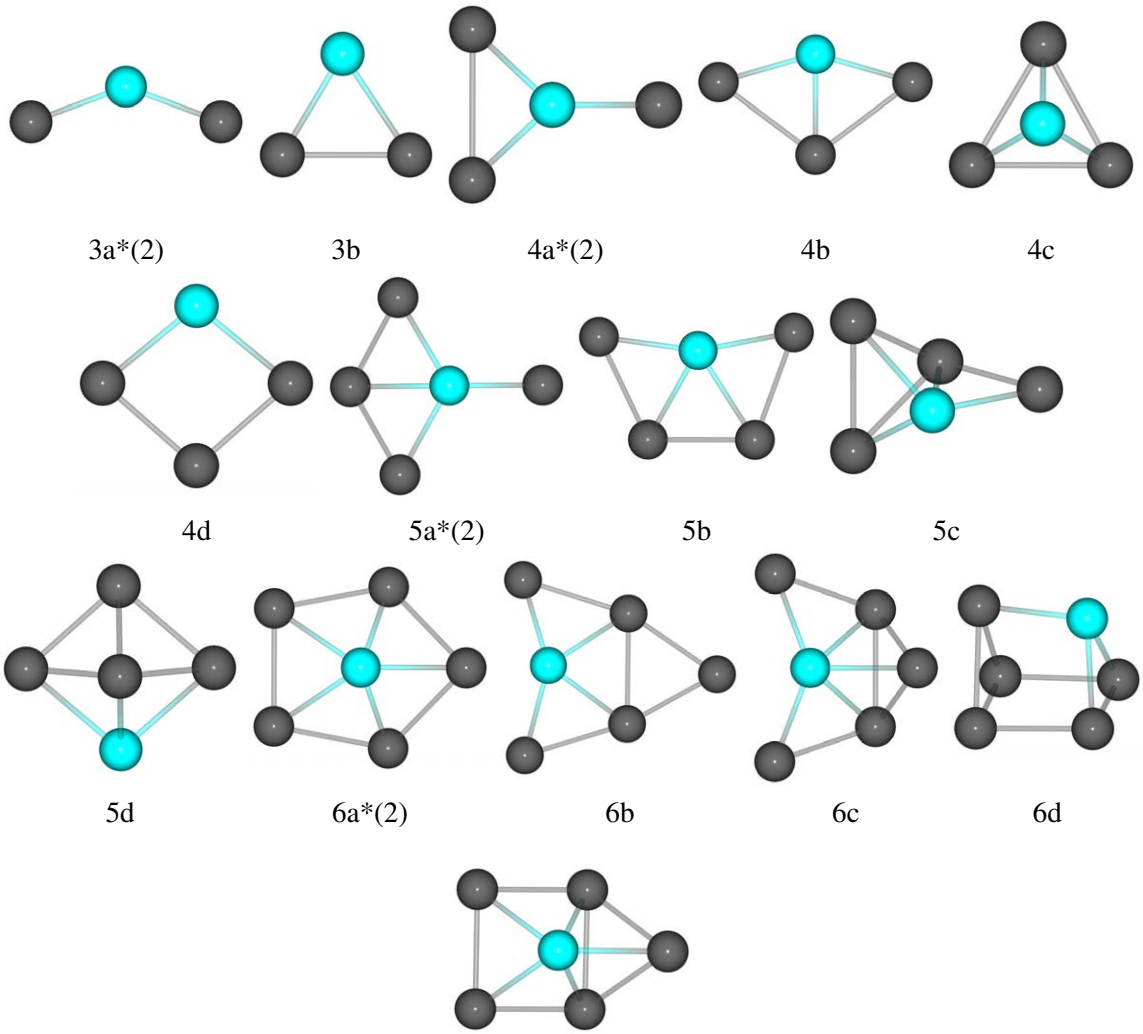

Figure 3.21: Low energy structures found for singly doped $Pt_{x-1}V$ clusters, from Pt_2V_1 to Pt_5V_1, with varying spin multiplicities. GM clusters for all sizes are specified (*). Numbers in brackets show at which spin multiplicity the GM is found.

Table 3.8: Relative energies (E_{rel}), average bond lengths and average Bader charges for the singly doped PtV clusters (shown in Figure 3.21), with varying spin multiplicities (2S+1).

2S+1	Cluster	E_{rel} (eV)	Pt-Pt (Å)	Pt-V (Å)	Ave. Pt Charge |e|	Ave. V Charge |e|
			Pt_2V			
2	3a	0.00	-	2.13	-0.60	0.69
4	3a	0.94	-	2.21	-0.48	1.01
6	3b	1.58	2.55	2.39	-0.41	0.79
8	3b	2.87	2.41	2.60	-0.27	0.37
10	3a	5.46	-	2.66	-0.12	0.36
			Pt_3V			
2	4a	0.00	2.89	2.16	-0.41	1.12
2	4b	0.07	2.70	2.25	-0.37	1.12
4	4b	0.40	2.58	2.33	-0.35	1.09
6	4b	1.15	2.52	2.45	-0.32	0.82
6	4c	1.17	2.71	2.35	-0.36	1.16
8	4c	2.12	2.63	2.50	-0.29	0.82
8	4d	2.12	2.48	2.42	-0.28	0.90
10	4c	3.75	2.56	2.70	-0.19	0.61
10	4d	3.75	2.43	2.60	-0.19	0.71
			Pt_4V			
2	5a	0.00	2.59	2.27	-0.33	1.43
2	5b	0.06	2.71	2.25	-0.31	1.27
4	5b	0.25	2.59	2.34	-0.31	1.32
6	5b	1.05	2.53	2.44	-0.26	1.08
8	5b	2.05	2.49	2.56	-0.25	1.16
8	5c	2.05	2.58	2.44	-0.27	1.07
10	5d	2.84	2.60	2.54	-0.21	0.87
			Pt_5V			
2	6a	0.00	2.67	2.32	-0.27	0.96
4	6b	0.31	2.57	2.35	-0.25	1.38
6	6a	0.91	2.56	2.47	-0.23	1.00
6	6c	0.92	2.62	2.41	-0.26	1.34
6	6b	0.93	2.53	2.45	-0.23	1.23
8	6d	1.46	2.58	2.36	-0.20	1.20
8	6e	1.46	2.61	2.49	-0.22	0.93
10	6d	2.17	2.56	2.49	-0.18	1.09

alloyed dimers, where the triplet or quartet states were the most stable. Furthermore, as the cluster size increases, the energetic penalty associated with higher spin states decreases.

For Pt_2V, the bent C_{2v} open triangle (*3a*) is the GM, with a Pt-V-Pt angle of 139.3°. Pt-Pt bonding is not observed for the GM doublet states. This is similar to the Pt_2Ti cluster, where Pt-Pt bonding is also not observed for the GM singlet state. Differences between the singly doped PtTi and PtV clusters are observed for the four and five atom clusters.

The doublet bent C_s Y-shape cluster (*4a*) is found to be the GM for Pt_3V, compared with the C_{2v} kite structure GM of Pt_3Ti. The doublet bent C_s top-capped rhombus structure (*5a*) is found to be the GM for Pt_4V, compared with the W-shaped structure for Pt_4Ti. These differences suggest that Pt-Pt bonding is less favourable for PtV clusters than PtTi clusters, although it appears to be more favourable than for the doubly doped PtTi clusters. A similar C_s twisted pentagonal structure (*6a*) is found to be the GM for both Pt_5V (doublet) and Pt_5Ti (triplet).

As with the singly doped PtTi clusters, GM planar and "bent-planar" structures are predicted for the singly doped PtV clusters for 3–6 atoms. When comparing the average Pt-Pt bond lengths, few trends are apparent, with variation being structure dependent. However, more evident trends are observed for Pt-V bonding, where the Pt-V bond length generally increases with increasing spin.

The Bader charge analysis reveals that once again there is significant charge transfer from the V, becoming positive, to the Pt, becoming negative. As the spin is increased, generally the charge transfer decreases as for PtTi clusters, though there is generally less charge transfer than in PtTi.

3.4.3.2 Doubly Doped Clusters

The range of doubly doped PtV clusters are shown in Figures 3.22–3.25, for PtV_2 to Pt_4V_2, respectively. For PtV_2, the same two structures are found as for $PtTi_2$, which are shown in Figures 3.22 and 3.12, respectively. Furthermore, the energetic penalties associated with unfavourable spin states are similar for the PtV_2 and $PtTi_2$ clusters. The structures generated by the GA search for Pt_2V_2 are shown in Figure 3.22. Structure 4 was found through a distortion of structure 1,

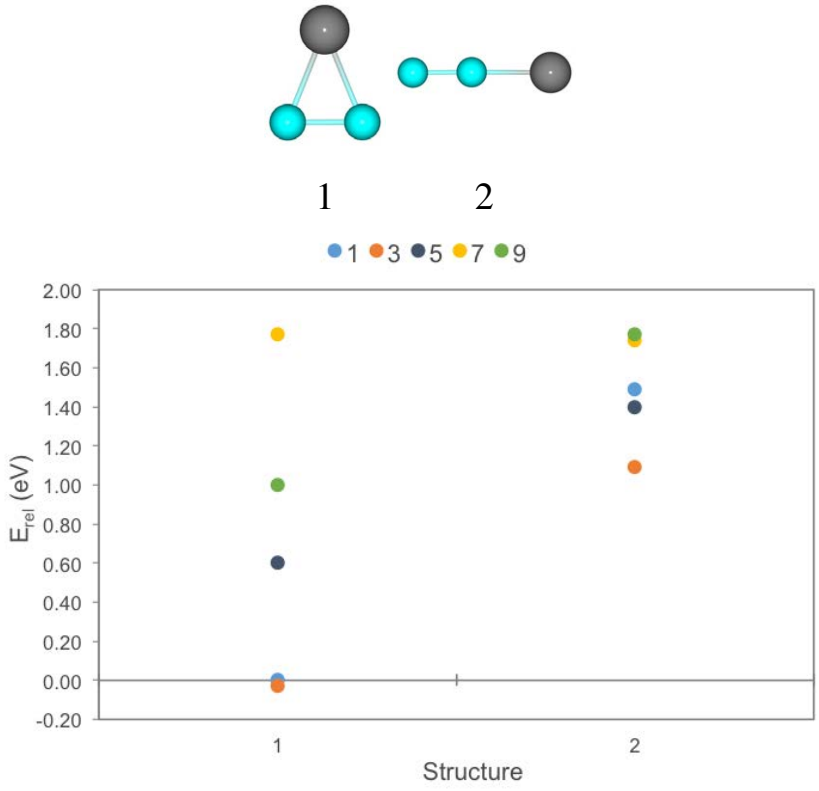

Figure 3.22: Relative energies for PtV_2 structures generated from GA-DFT search at varying multiplicities. All energies relative to the singlet structure 1, the GM calculated from the PWscf calculation. Missing data points indicate that there was structural rearrangement during the subsequent local relaxation.

but was only stable at the nonet state. In all cases a V–V bond is formed and maximising Pt–V bonding results in lower energies. Structure 4 also maximises Pt–V bonding, but is unstable at low spin multiplicities where 3D structures are destabilised.

Pt_3V_2 structures generated from the GA search are shown in Figure 3.24, where structures 1–7 are located by the search and the remainder through structural rearrangements during local relaxation. As with the other systems studied, the structures located by rearrangements are not local minima for the singlet state. A mixture of planar and 3D structures are identified, with no clear trend for preferences of one over the other, although the majority of structures are 3D. As for the smaller clusters, V–V bonding, as well as maximising Pt–V bonding results in favourable structures. Structures 6 and 7 are found to be particularly high in energy, although similar energies are found for the singlet state. A V–V bond is not formed for structure 6, while

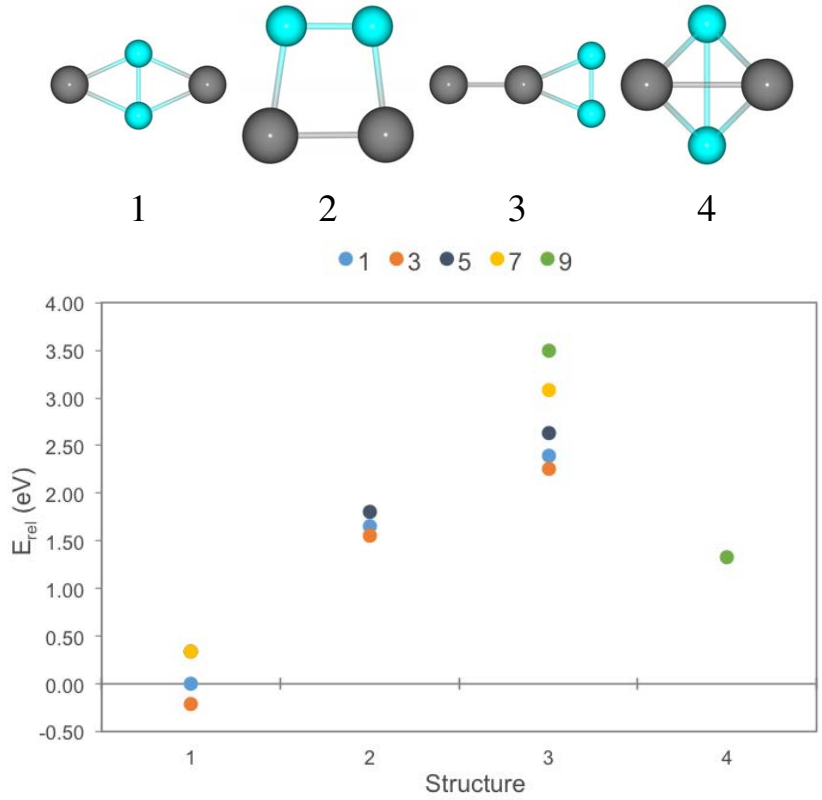

Figure 3.23: Relative energies for Pt_2V_2 structures generated from GA-DFT search at varying multiplicities. All energies relative to the singlet structure 1, the GM calculated from the PWscf calculation. Missing data points indicate that there was structural rearrangement during the subsequent local relaxation.

Table 3.9: Relative energies (E_{rel}), average bond lengths and average Bader charges for the doubly doped PtV clusters (shown in Figure 3.26), for varying multiplicities (2S+1).

2S+1	Cluster	E_{rel} (eV)	Pt-Pt (Å)	Pt-V (Å)	V-V (Å)	Ave. Pt Charge |e|	Ave. V Charge |e|
				Pt_1V_2			
1	3a	0.00	-	2.41	1.80	-0.68	0.21
3	3a	-0.03	-	2.43	1.79	-0.74	0.33
5	3a	0.60	-	2.45	1.76	-0.77	0.30
7	3b	1.74	-	2.15	2.46	-0.71	0.27
7	3a	1.77	-	2.45	1.97	-0.71	0.46
9	3b	1.00	-	2.15	2.49	-0.83	0.60
				Pt_2V_2			
1	4a	0.00	-	2.38	1.95	-0.74	0.77
3	4a	-0.21	-	2.41	1.91	-0.75	0.62
5	4a	0.34	-	2.40	2.19	-0.83	0.86
7	4a	0.34	-	2.39	2.70	-0.81	0.86
9	4b	1.33	2.77	2.44	2.80	-0.70	0.62
				Pt_3V_2			
1	5a	0.00	-	2.39	2.01	-0.67	0.99
3	5a	-0.31	-	2.40	2.02	-0.69	1.14
5	5a	0.15	-	2.39	2.47	-0.70	1.06
7	5b	0.49	2.70	2.44	2.53	-0.66	0.76
9	5c	1.51	2.70	2.47	3.06	-0.59	0.89
9	5d	1.56	2.62	2.45	2.68	-0.54	0.83
				Pt_4V_2			
1	6a	0.00	2.86	2.33	2.33	-0.55	1.15
3	6b	-0.08	-	2.34	2.58	-0.56	1.19
5	6c	0.33	2.60	2.37	2.61	-0.53	0.96
7	6d	0.62	2.58	2.44	2.52	-0.51	1.07
9	6e	1.35	2.63	2.44	2.72	-0.51	1.10

there is very little Pt–V bonding in structure 7 compared with e.g. structure 1.

Structures found for Pt_4V_2 are shown in Figure 3.25. Structures 1–12 were found by the GA search, whilst 13–16 were found through structural rearrangements during local relaxations. For Pt_4V_2, the majority of clusters are 3D. The formation of the V–V bond, with maximised Pt–V bonding, generally results in lower energy structures. Where singlet and triplet states are locally stable, the triplet tends to be more energetically favourable. This differs from the Pt_4Ti_2 system, where in general the singlet is lower in energy.

The lowest lying structures for doubly doped PtV clusters are listed in Table 3.9, correspond-

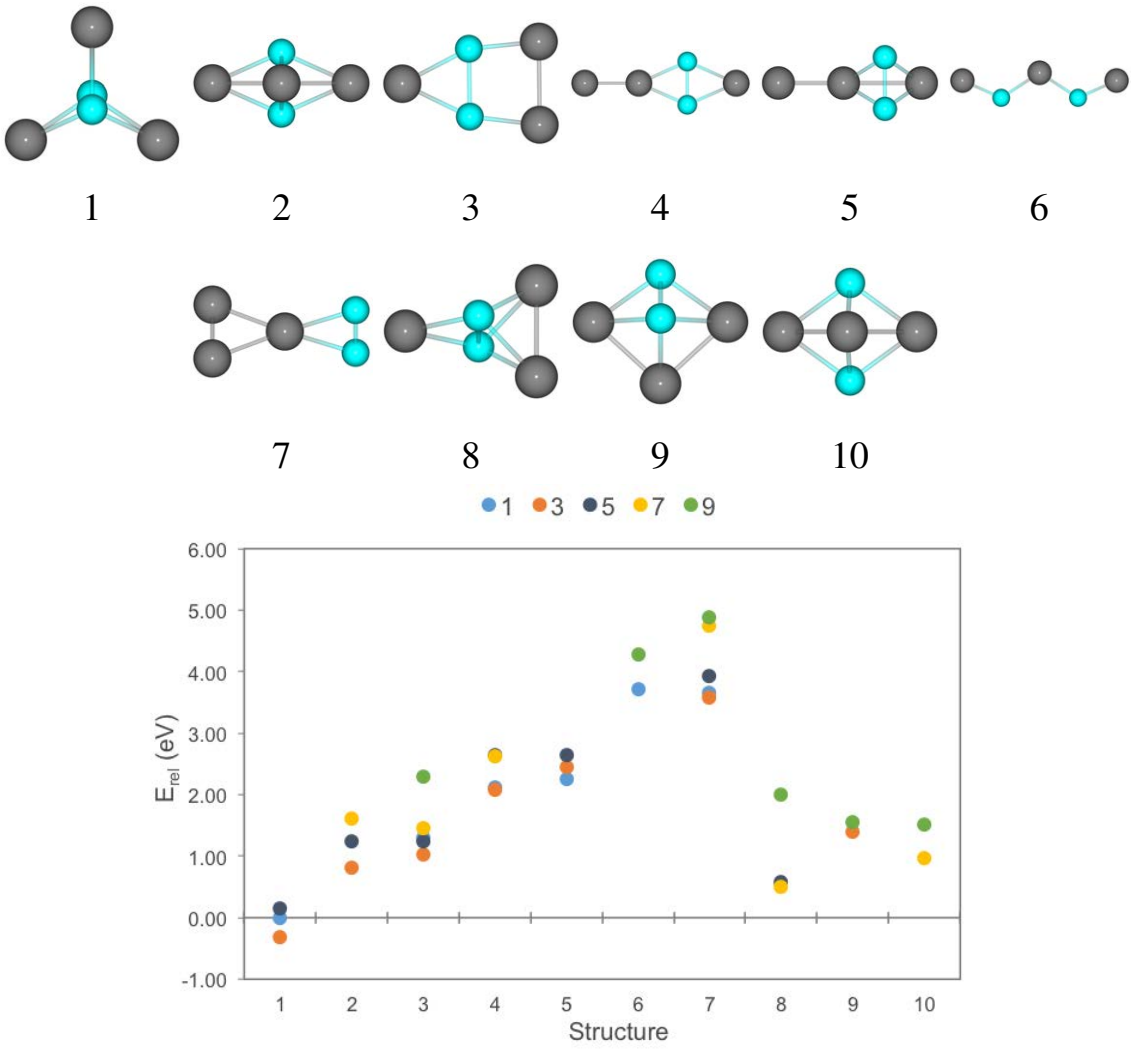

Figure 3.24: Relative energies for Pt_3V_2 structures generated from GA-DFT search at varying multiplicities. All energies relative to the singlet structure 1, the GM calculated from the PWscf calculation. Missing data points indicate that there was structural rearrangement during the subsequent local relaxation.

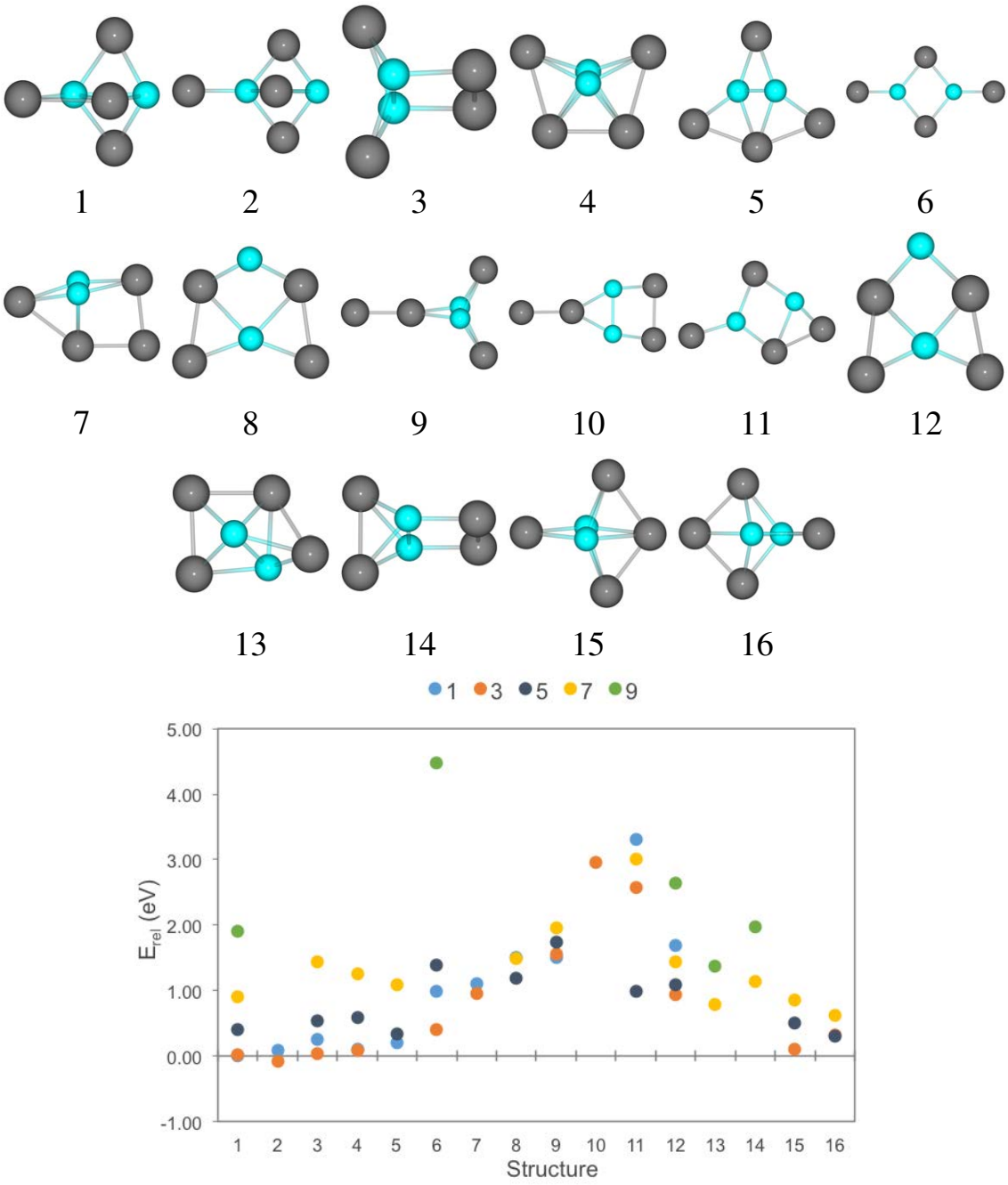

Figure 3.25: Relative energies for Pt_4V_2 structures generated from GA-DFT search at varying multiplicities. All energies relative to the singlet structure 1, the GM calculated from the PWscf calculation. Missing data points indicate that there was structural rearrangement during the subsequent local relaxation.

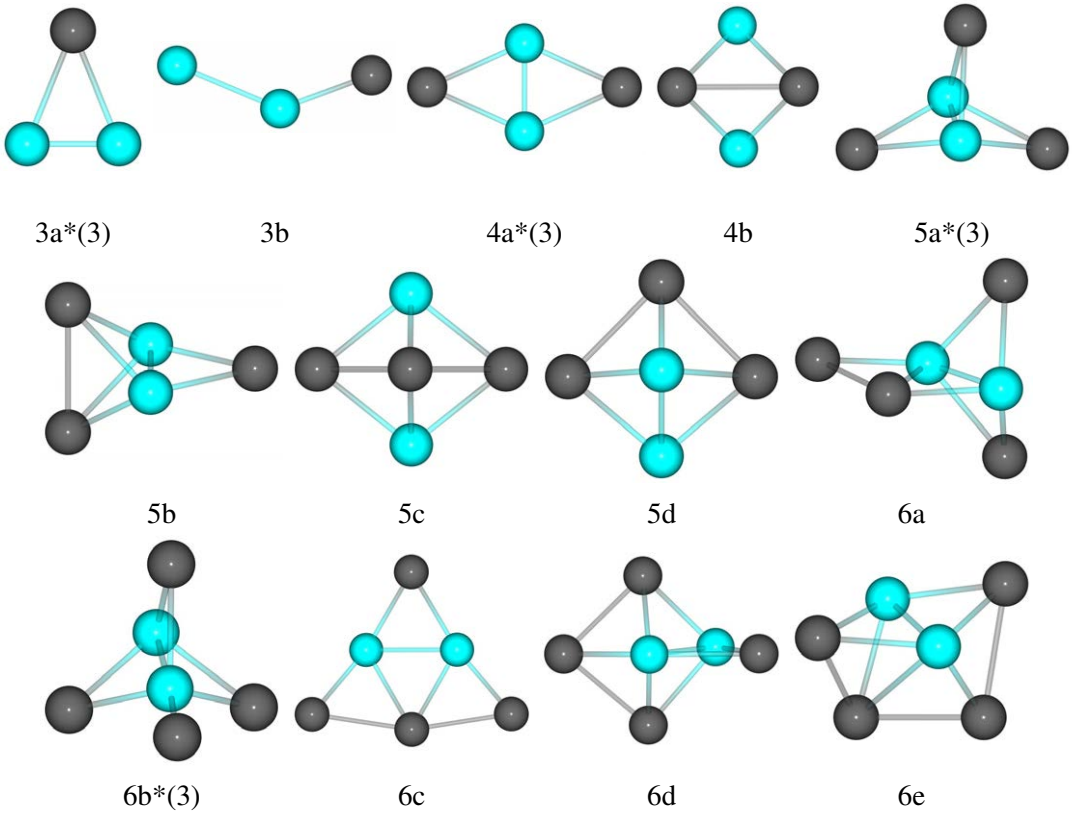

Figure 3.26: Low energy structures found for $Pt_{x-2}V_2$ clusters, from Pt_1V_2 to Pt_4V_2, with varying spin multiplicities. GM clusters for all sizes are specified (*). Numbers in brackets show at which spin multiplicity the GM is found.

ing to the structures in Figure 3.26. In contrast to the singly doped clusters, GM structures for the doubly doped clusters are all triplets. This is similar to the dimers, where the triplet and quartet states (for V_2 and PtV, respectively) are lowest in energy. Furthermore, energetic penalties associated with higher spin states are reduced compared to the singly doped clusters.

The GM structures for the doubly doped PtV clusters are similar to those for doubly doped PtTi clusters. The 3-atom closed C_{2v} triangle (*3a*), with a Ti-Pt-Ti angle of 43.3°, 4-atom bent C_{2v} rhombus (*4a*), 5-atom D_{3h} (*5a*) and 6-atom C_{3v} (*6b*) structures are identified as GM for $Pt_{x-2}V_2$ clusters. As mentioned previously, cluster growth leads to maximisation of V-V and Pt-V bonding and minimisation of Pt-Pt bonding. Once again, due to the low number of Pt-Pt bonds, it is hard to draw trends from the average Pt-Pt bond lengths. Average Pt-V and V-V bond lengths show that generally, as the spin increases, so do the bond lengths. As for PtTi, the doubly doped PtV clusters exhibit a distinct 2D/3D transition. This occurs between the 4-atom bent C_{2v} rhombus and 5-atom D_{3h} structures.

Once again, there is generally reduced charge transfer for the PtV clusters, compared with the PtTi clusters. Furthermore, for the doubly doped PtV clusters, there is greater overall charge transfer to the Pt and a reduction in the positive charges on the V atoms, compared to the singly doped PtV clusters. A general reduction in the amount of charge transfer is also seen as the spin is increased, as for the other systems. However, PtV_2 is anomalous, as an increase in charge transfer is observed as the spin is increased. Generally as the cluster size increases, the average Pt negative charge decreases (as there are a greater number of Pt atoms), whilst the average positive charge on the V atoms increases.

3.5 Conclusions

From the results presented in this study, it is apparent that, whilst spin has a significant effect on pure Pt clusters, varying effects are found for the doped PtTi and PtV clusters. Favourable energies are observed up to the septet state for pure Pt clusters. GM structures are found to be planar or "bent-planar" for Pt cluster sizes 3–6. However, partial spin quenching is observed

when Pt clusters are doped with Ti or V.

Increasing the spin of PtTi clusters generally results in higher energies. The triplet state is favourable for Pt_5Ti and $PtTi_2$; however, the GM structures are singlets for all other PtTi clusters studied. For the singly doped clusters, again planar and "bent-planar" structures are located as the GM for the 3–6 atom clusters. For the doubly doped PtTi clusters, initially more planar structures are favoured, however the GM for 5–6 atom structures adopt 3D conformations.

The GM structures for 3–6 atom singly doped PtV clusters are all doublets. However, the doubly doped clusters, all have triplet GM. As for the PtTi clusters, planar and "bent-planar" structures are found for the 3–6 atom singly doped PtV clusters, although different GM structures are proposed for the 4–5 atom clusters. Similar GM structures are found for the PtV and PtTi clusters, exhibiting the same 2D/3D transition between the 4- and 5-atom clusters.

Chapter 4

Chemisorption Studies on PtTi Clusters

4.1 Introduction

As mentioned in Section 1.5.2, it has been suggested that OH bonds particularly strongly to the Pt surface during the oxygen reduction reaction (ORR) at the cathode. It is also known that CO bonds strongly to the Pt surface during the hydrogen oxidation reaction (HOR) at the anode when impure hydrogen streams are used. To study the effects of alloying, adsorption searches are performed and compared for varying sizes and compositions. The ultimate aim is to reduce the adsorption energy of the OH or CO species. The initial study focuses on investigating chemisorption at different facet sites on the cluster, as well as comparisons between monometallic and bimetallic Pt/Ti clusters.

In the second part of the study, to understand better the reasons for the changes in adsorption energies, electronic density of states (DOS) analysis was performed. The average energy of the *d*-band (*d*-band centre) was linked to the adsorption properties of small molecules investigated in the initial studies. Adsorption energies are dependent upon the filling of the *d*-band, where the occurrence of more unoccupied *d*-states allows for stronger binding of small molecules. Therefore, an upshift in the *d*-band centre toward the Fermi energy (E_F) gives rise to stronger binding; conversely, a downshift, away from the E_F, results in weaker binding arising from greater filling of high-lying *d*-states [162,163]. It would be beneficial for the alloyed Pt-majority

clusters to exhibit a downshift in the *d*-band centre compared to the pure Pt cluster.

4.2 Methodology

Most calculations were performed using the PWscf plane wave DFT code in the quantum chemistry package Quantum-Espresso 4.2.1 [126]. The PWscf calculations were performed using the ultrasoft Perdew-Wang (PW91) *xc* functional, accounting for 10 ($5d^9$, $6s^1$), 12 ($3s^2$, $3p^6$, $3d^2$, $4s^2$), 4 ($2s_2$, $2p_2$), 6 ($2s_2$, $2p_4$) and 1 ($1s_1$) valence electrons for Pt, Ti, C, O and H, respectively. Scalar relativistic corrections have been employed for all pseudopotentials, as well as non-linear core correction for Pt and Ti. A kinetic energy (E_k) cutoff for the wavefunctions of 26.0 Ry was used, and the E_k cutoff for the charge density (ρ) was set at 208.0 Ry as ultrasoft pseudopotentials were used; furthermore, Fermi-Dirac smearing was used with Gaussian smearing of 0.007 Ry. The quantum chemistry package NWChem 6.0 [125] was used to analyse the electron density and calculate atomic charges employing the Löwdin and Mulliken methods. A separate program was used to analyse the atomic charges with the Bader method [137].

The DOS was analysed in terms of average band centre as well as band width. The energy of the *d*-band centre (ε_d) is given by Equation 4.1.

$$\varepsilon_d = \frac{\int \rho E \quad dE}{\int \rho \quad dE} \tag{4.1}$$

where ρ is the *d*-band density, E is the *d*-band energy, and ρdE is the number of *d*-states. The root-mean-squared *d*-band width (W_d) is given by Equation 4.2.

$$W_d = \sqrt{\frac{\int \rho E^2 dE}{\int \rho \quad dE}} \tag{4.2}$$

When calculating ρ_d and W_d for a specific fraction of a cluster (e.g., the core or shell atoms), Equations 4.1 and 4.2 were applied for the relevant subset of atoms, i.e., by summing over atoms in the appropriate fraction of the cluster.

4.3 Results and Discussion

4.3.1 Model System

Simulations have been carried out on TO clusters of varying sizes and compositions. Complete TO structures are obtained for 38, 79, 116, 140, 201, 260, etc. atoms [164], where the odd-numbered TOs are atom-centred and the even-numbered TOs have a central M_6 octahedral core. A more detailed overview of cluster sizes can be found in Table 4.1. The diagonal shows the sizes of complete true TO clusters, the top right section results in more cube-octahedral (CO) type structures, while the bottom left section results in more octahedral (Oh) type structures. Upper right CO-type clusters have a greater proportion of (100) facets whilst bottom left Oh clusters have a greater number of (111) facets. The magic numbers can be calculated using Equation 4.3.

$$N_{TO}(n,m) = \frac{(n+2m+1)}{3}[2(n+2m+1)^2+1] - m(m+1)(2m+1) \tag{4.3}$$

N is the total number of atoms for the cluster, which consists of n/m atomic shells. For example, the 309-atom CO-type cluster consists of four atomic shells, on a single core atom, or an additional shell on the 147-atom cluster.

Table 4.1: Magic numbers for producing TO, CO and Oh type clusters. Those highlighted in red represent complete TO clusters. Those in green represent magic numbers for CO type clusters and those in blue, Oh type clusters.

n \ m	0	1	2	3	4	5	6	7	8	9	10	11	12	
0	1	13	55	147	309	561	923	1415	2057	2869	3871	5083	6525	CO
1	6	38	116	260	490	826	1288	1896	2670	3630	4796	6188	7826	
2	19	79	201	405	711	1139	1709	2441	3355	4471	5809	7389	9231	
3	44	140	314	586	976	1504	2190	3054	4116	5396	6914	8690	10744	
4	85	225	459	807	1289	1925	2735	3739	4957	6409	8115	10095	12369	
5	146	338	640	1072	1654	2406	3348	4500	5882	7514	9416	11608	14110	
6	231	483	861	1385	2075	2951	4033	5341	6895	8715	10821	13233	15971	
7	344	664	1126	1750	2556	3564	4794	6266	8000	10016	12334	14974	17956	
8	489	885	1439	2171	3101	4249	5635	7279	9201	11421	13959	16835	20069	
9	670	1150	1804	2652	3714	5010	6560	8384	10502	12934	15700	18820	22314	
10	891	1463	2225	3197	4399	5851	7573	9585	11907	14559	17561	20933	24695	
11	1156	1828	2706	3810	5160	6776	8678	10886	13420	16300	19546	23178	27216	
12	1469	2249	3251	4495	6001	7789	9879	12291	15045	18161	21659	25559	29881	
	Oh													TO

Initial calculations are performed on the 38-atom TO cluster, that being the smallest complete TO. For bimetallic 38-atom PtTi clusters, three high symmetry model structures were studied based on the TO: "core-shell", "hex" and "centroid" configurations have been simulated, as shown in Figure 4.1. Calculations performed on the larger cluster sizes were restricted to the core-shell configurations, rather than exploring a wider range of chemical ordering patterns. However, with cluster sizes >79-atoms it is possible to also investigate "onion-like" structures.

The 79-atom clusters have a complete core-shell structure at the $A_{60}B_{19}$ composition, although it is also possible to study the $A_{68}B_1$ composition for this atom-centred cluster. $A_{78}B_{38}$ and $A_{110}B_6$ compositions result in complete core-shell structures for the 116-atom clusters, with shells composed of one and two layers of species A, respectively. The 140-atom cluster has complete core-shell structures at $A_{96}B_{44}$ and $A_{134}B_6$ as well as an onion structure for $A_{102}B_{38}$ ($A_{96}B_{38}A_6$). The $A_{122}B_{79}$ and $A_{182}B_{19}$ compositions result in complete core-shell structures for the 201-atom clusters. The $A_{141}B_{60}$ ($A_{122}B_{60}A_{19}$) composition is an onion structure, although it is possible to create an $A_{140}B_{61}$ ($A_{122}B_{60}A_{18}B_1$) onion structure as the cluster is atom-centred.

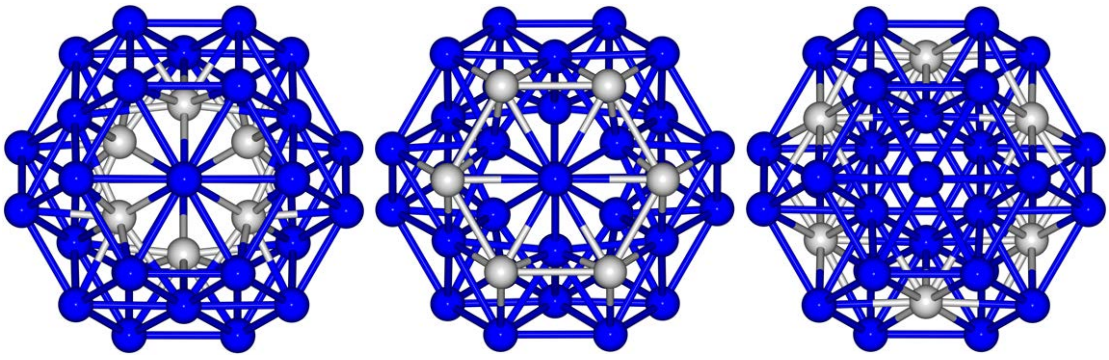

(a) Core-Shell (b) Hex (c) Cent

Figure 4.1: $Pt_{32}Ti_6$ core-shell, hex and centroid TO configurations.

The TO conformation was studied as a model of the face-centred cubic (FCC) bulk structure; the TO structure also allows the study of both (111) and (100) facets on a single cluster. The purpose of computing these structures was to allow the study of adsorption of relevant molecules onto various cluster surfaces whilst retaining a constant composition, and investigat-

ing the effects of mixing and segregation. The core-shell structure provides a pure surface for adsorption, the hex structure simulates a segregated cluster and the centroid is a mixed configuration. For comparative purposes, the core-shell, hex and centroid structures were modelled with a constant $A_{32}B_6$ composition. This composition was chosen as it produces a complete core-shell arrangement (6 core and 32 shell atoms) whilst still allowing the hex and centroid geometries to be easily constructed [165].

It was observed that the presence of the titanium in the $Pt_{32}Ti_6$ core-shell TO structure leads to a "hollow" core after relaxation. The core titanium atoms had a bond length of around 3.29 Å for the TO structure calculated by PWscf compared with $\sim$2.7 Å for pure Ti_{38}. Furthermore, distortion of the $Pt_{32}Ti_6$ hex TO was also observed, producing Ti–Ti bond lengths of over 3.36 Å. The increased Ti–Ti bond lengths for the hex structure likely arise from the fact that the Ti atoms have fewer constraints on the surface of the cluster. In the core positions the atoms are unable to expand as much as surface atoms because of the presence of the Pt shell. No distortion of the $Pt_{32}Ti_6$ centroid TO structure was observed, suggesting that there is sufficient distance between Ti atoms to alleviate the cause of cluster distortion. As this bond increase is only present for the minority-Ti structures it is believed that charge effects could be responsible. If the Ti atoms gain sufficient positive charge then Ti–Ti repulsion could account for the structural distortion.

In order to test this, various forms of charge analysis were performed on all structures. Löwdin, Mulliken and Bader charges were calculated to allow comparisons to be made. The calculated charges for core-shell $Pt_{32}Ti_6$ and Pt_6Ti_{32} clusters are listed in Table 4.2. It was expected that platinum, with an electronegativity of 2.28 on the Pauling scale, would gain electron density, becoming more negatively charged compared with the titanium (1.54 on the Pauling scale). Löwdin analysis resulted in the expected trend, the platinum atoms gain extra electron density to become slightly negative, thus the titanium atoms are slightly positive. Compositional effects were observed showing Ti charges in the minority Ti system to be more positive than in the majority-Ti system. This same trend was observed for Pt, with less negatively charged Pt atoms in the Pt-rich system compared to the minority-Pt system.

Table 4.2: Average Bader, Löwdin and Mulliken charges of Pt and Ti for 38-atom core-shell clusters.

	$Pt_{32}Ti_6$		Pt_6Ti_{32}	
	Pt	Ti	Pt	Ti
Bader	-0.22	1.23	-1.44	0.05
Löwdin	-0.05	0.25	-0.36	0.07
Mulliken	0.44	-2.35	-1.33	0.25

The Bader charge analysis agreed with the Löwdin analysis, especially for the Pt-rich clusters. Mulliken charges disagreed with the Löwdin and Bader results for the Pt-rich clusters, suggesting that platinum became positive and titanium negative, although they generally agreed with Löwdin for the Ti rich clusters. We note, that Mulliken population analysis is known to be unreliable when calculating charges for transition metal systems [140]. It was found that the average difference in charge density from the neutral atom for Löwdin analysis was up to ± 0.5 |e| compared with unrealistically high values of up to ± 1.9 and ± 2.4 |e| for Bader and Mulliken, respectively.

There was generally little distortion observed in the Pt_6-Ti_{32} TO structures, although a distortion was observed for the centroid structure. This distortion is most likely because the configuration is not stable rather than because of the charge effects observed for Pt_{32}-Ti_6. The Ti_{38} TO structure, when optimised, resulted in distortion tending towards an icosahedral (Ico) structure instead of TO. This shows that the presence of platinum stabilises the TO structure in the core-shell and hex conformations, though not for the centroid conformation. This indicates that it is the Pt–Pt interactions which stabilise majority-Ti TO structures.

When the $Pt_{32}Ti_6$ structures are optimised using PWscf, the core-shell conformation is the most stable isomer and the distorted hex the least stable. For Pt_6Ti_{32}, whilst the core-shell isomer is the least stable, the distorted centroid isomer is the most stable, as seen in Figure 4.2. Both the distorted centroid and hex isomers are more stable than the $Pt_{32}Ti_6$ core-shell isomer. Although, the core-shell $Pt_{32}Ti_6$ is more stable than the Pt_6Ti_{32} structure, all of the Ti-rich clusters are more stable than both the $Pt_{32}Ti_6$ centroid and hex isomers. It is beneficial to have a Pt skin covering the underlying alloyed metal for use in PEFC electrocatalysts [166–169]. It is encouraging that the core-shell isomer is found to be the lowest lying of the Pt-rich structures investigated.

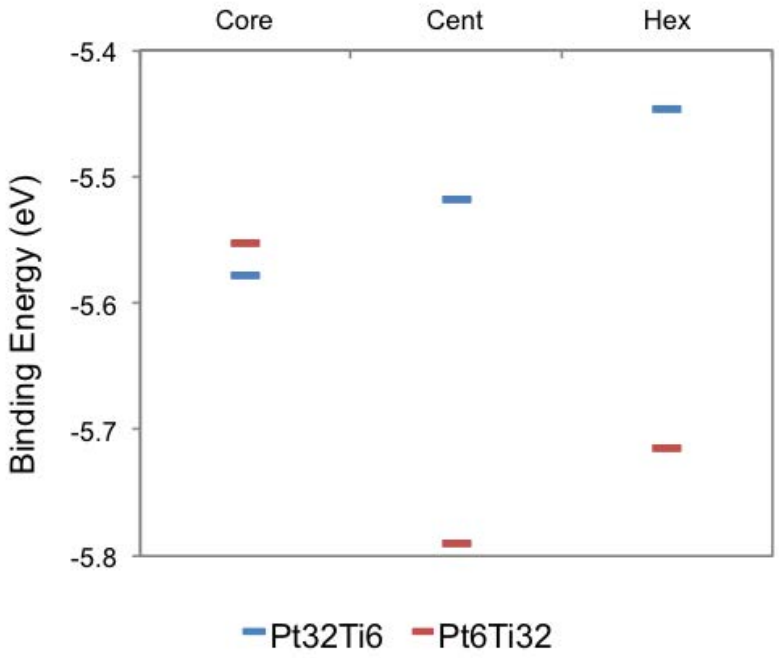

Figure 4.2: Binding energies of the $Pt_{32}Ti_6$ and Pt_6Ti_{32} clusters with chemical ordering as depicted in Figure 4.1.

In the study of larger cluster sizes, calculations have been restricted to high symmetry core-shell and onion-like configurations, rather than exploring a wider range of chemical ordering patterns similar to those investigated for the 38-atom clusters. The 79-atom clusters have a complete core-shell structure at the $A_{60}B_{19}$ composition, although it is also possible to study the $A_{68}B_1$ composition for this atom-centred cluster. $A_{78}B_{38}$ and $A_{110}B_6$ compositions result in complete core-shell structures for the 116-atom clusters, with shells composed of one and two layers of species A, respectively. The 140-atom cluster has complete core-shell structures at $A_{96}B_{44}$ and $A_{134}B_6$ as well as an onion structure for $A_{102}B_{38}$ ($A_{96}B_{38}A_6$). The $A_{122}B_{79}$ and $A_{182}B_{19}$ compositions result in complete core-shell structures for the 201-atom clusters. The $A_{141}B_{60}$ ($A_{122}B_{60}A_{19}$) composition is an onion structure, although there is the possibility of creating an $A_{140}B_{61}$ ($A_{122}B_{60}A_{18}B_1$) onion structure as the cluster is atom-centred.

Once again, cluster binding energies (E_b^{clust}) are used to give an indication of the relative cluster stability. More negative energies suggest that the structure is more stable than those with less negative energies. Figure 4.3 shows the binding energies associated with pure and alloyed

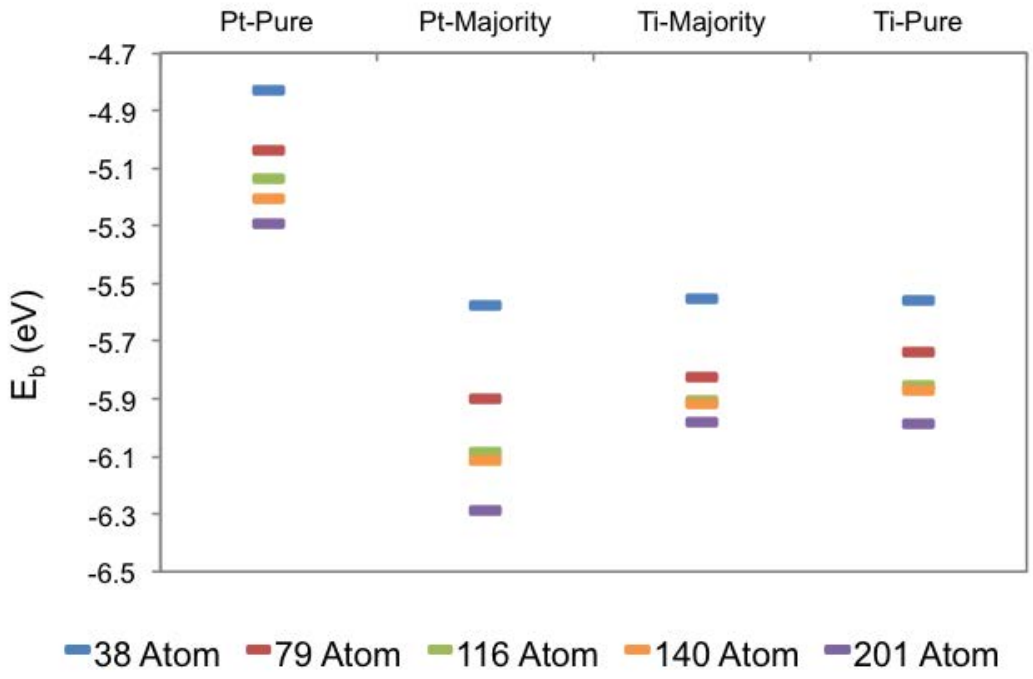

Figure 4.3: Binding energies (E_b) calculated for pure Pt and Ti and bimetallic Pt-Ti monolayered core shell clusters, studying compositional as well as size effects.

core-shell TO structures for varying sizes and compositions. This shows that the most negative binding energies, thus the most stable structures, are obtained for the Pt-majority core-shell clusters, with the least negative, least stable structures obtained for the pure Pt clusters. There is also a noticeable shift to more negative binding energies as size increases. This is because the larger clusters studied in this work have increased average atomic coordination numbers than the small 38-atom clusters. The stability of the Pt-majority core-shell isomer is advantageous for PEFCs as they benefit from a Pt shell on which the ORR and HOR can take place.

Figure 4.4 shows the calculated binding energies for all 140 and 201-atom cluster compositions investigated. This reveals that the Pt-rich core-shell and onion structures had very similar stabilities. For the Ti-rich clusters, the onion structure is slightly more stable than both core-shell structures. The Pt-rich clusters remain most favourable for the onion or monolayered core-shell composition. It can also be seen that the bilayer Pt shell ($Pt_{134}Ti_6$ and $Pt_{182}Ti_{19}$) clusters are less stable than for the Pt-rich monolayer and onion structures. For the Ti-rich clusters, the bilayer conformation is slightly more favourable than the monolayer. This suggests that the

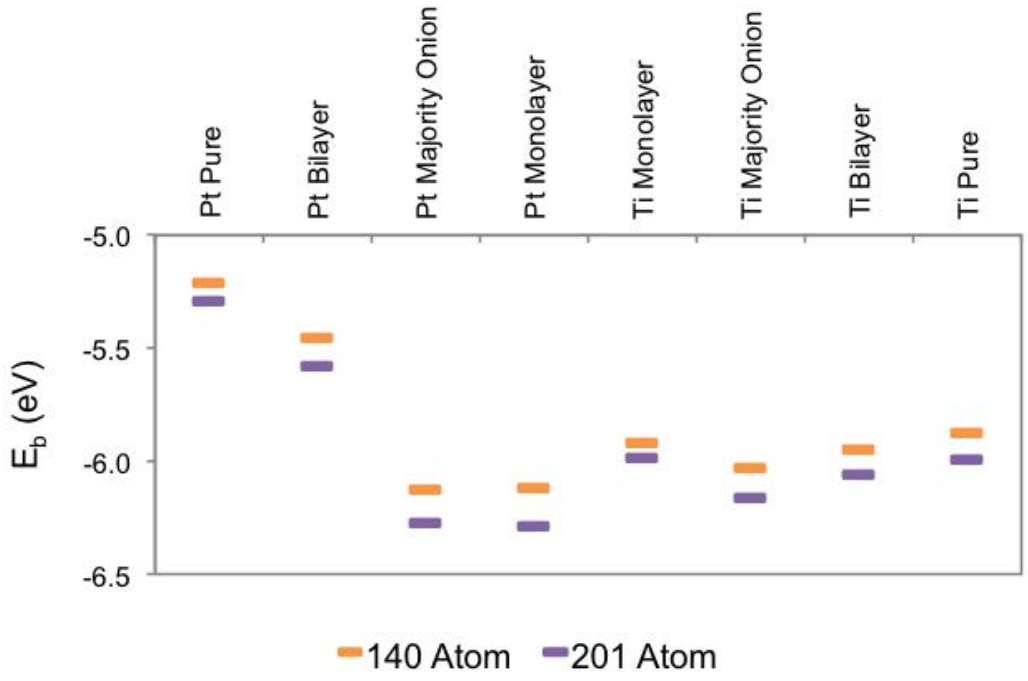

Figure 4.4: Binding energies (E_b) calculated for the onion and bilayered core shell structures for the 140- and 201-atom clusters.

larger Pt core induces more strain within the clusters, making them slightly less stable.

4.3.2 Adsorption Search

A study of OH and CO adsorption onto cluster surfaces was performed, with a view to investigating how structure and composition can affect bonding energies. There are eight non-symmetrically equivalent sites on the surface of the 38-atom TO cluster for consideration. These consist of two atop, three bridge and three hollow sites, shown in Figure 4.5. When setting up the initial geometries, approximate Pt–O and Pt–C bond lengths were used.

$Pt_{32}Ti_6$ TO core-shell clusters were studied and compared with the pure Pt_{38} TO cluster. Adsorption energies were calculated of single hydroxyl molecules adsorbed onto specific sites for comparisons between pure and bimetallic clusters. This involved investigating both the (111) and (100) faces as well as the bridge, hollow and atop sites.

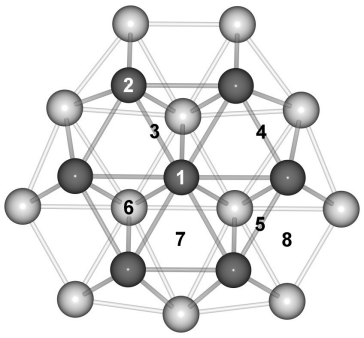

1 A(1,1)
2 A(0,1)
3 B(1,1)
4 B(1,2)
5 B(0,1)
6 H(1,1)
7 H(1,2)
8 H(0,1)

Figure 4.5: Adsorption sites for 38-atom TO clusters, showing atop (A), bridge (B) and hollow (H) sites. In the case of, e.g. A(x,y), x denotes either the (100) where x = 0 or (111) where x = 1 facets.

4.3.2.1 Hydroxyl Adsorption

The PWscf results, shown in Figure 4.6, revealed slightly weaker hydroxyl binding to the bimetallic cluster $Pt_{32}Ti_6$ than to pure Pt_{38}. Migration of the OH molecule to the edge-bridge-(100) site was observed for the bimetallic $Pt_{32}Ti_6$ cluster. This is most likely because the edge-bridge-(100) site produces the strongest interaction energy for the $Pt_{32}Ti_6$ cluster. Migration was also observed from the hollow-(111)/(111) to the edge-bridge-(111) site. Although the edge-bridge-(111) site is not particularly low in energy, this migration most likely results from the hollow-(111)/(111) site's being higher in energy with a relatively simple path between the two sites.

For the pure Pt_{38} cluster, migration of the hydroxyl molecule from the hollow-(100) to the edge-bridge-(100) site occurred. Once again, the edge-bridge-(100) site was found to result in strongest OH binding for the pure cluster. The calculated interaction energy difference between the edge-bridge-(100) sites for the $Pt_{32}Ti_6$ and Pt_{38} clusters is only 0.02 eV. This indicates little difference in ORR kinetics at this site for bimetallic PtTi and pure Pt nanoparticles.

For both the pure and bimetallic clusters, the atop-(111) site was the least stable. The bimetallic $Pt_{32}Ti_6$ cluster gave rise to weaker interaction energies than the pure Pt_{38} cluster. This resulted in a slightly larger interaction energy difference of $\sim$0.5 eV. Other binding sites lead to weaker binding of OH to the bimetallic cluster with energy differences around 0.2 eV. Whilst there may not be a noticeable improvement in the ORR kinetics associated with the

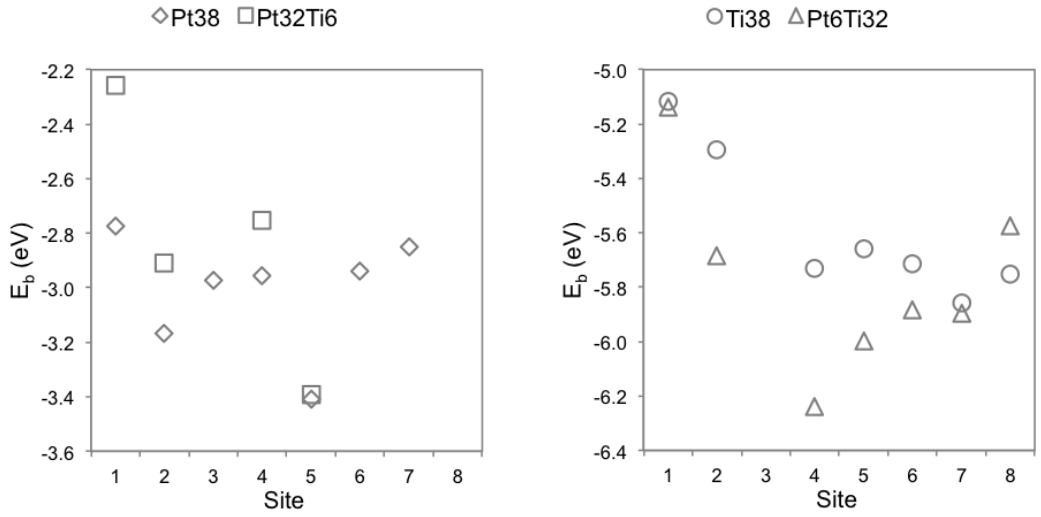

(a) Pt-Rich

(b) Ti-Rich

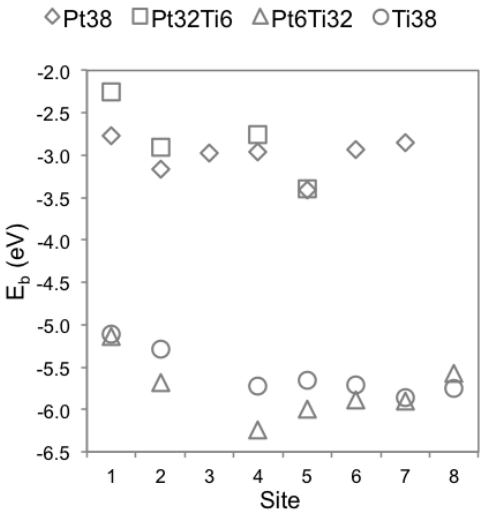

(c) Compare

Figure 4.6: Binding energy of hydroxyl adsorption on (i) Pt_{38} and $Pt_{32}Ti_6$ (Core-Shell) TO, (ii) Ti_{38} and Pt_6Ti_{32} (Core-Shell) TO and (iii) a comparisson between Pt_{38}, $Pt_{32}Ti_6$, Pt_6Ti_{32} and Ti_{38} (Core-Shell) TO, on the sites shown in Figure 4.5. Missing data points indicate migration of hydroxyl during optimisation, leading to an interconversion of isomers.

site of strongest binding, the edge-bridge-(100), other sites may exhibit slight improvements. After these initial studies, the bimetallic Pt_6Ti_{32} TO core-shell and pure Ti_{38} TO clusters were examined, although these structures are not ideal for use in a PEFC because of strong Ti–O bonds. As mentioned, when performing the geometry optimisations of the Ti_{38} TO structure, the cluster distorted slightly. However, it was still possible to investigate the same site as previously shown in Figure 4.5. PWscf calculations revealed that binding OH to the Ti surface resulted in stronger interaction energies than for both bimetallic $Pt_{32}Ti_6$ and pure Pt_{38} clusters. When studying the resulting hydroxylated Pt_6Ti_{32} TO core-shell structures it was possible to see Pt-Ti bond stretching associated with the OH binding site.

As for the Pt-rich core-shell cluster, the weakest site of binding on the majority-Ti core-shell structure was the atop-(111). The same was not true for the site of strongest binding, the edge-bridge-(111) site for the majority-Ti cluster, compared to the edge-bridge-(100) site for the Pt-rich cluster. The edge-bridge-(100) site still remains preferable over many of the others investigated in the majority-Ti case. Far less OH migration was observed for the majority-Ti cluster, with the only site of migration being from the cent-bridge-(111) to the edge-bridge-(111) site.

Calculations on the pure Ti cluster revealed, in general, weaker binding of the OH when compared with the majority-Ti cluster. As for the other systems studied, the site with the weakest interaction energy was the atop-(111), with the site of strongest binding found to be the hollow-(111)/(111). This is different from all other systems, although the deformation of the TO structure led to distortion of the hollow-(111)/(111) site which is likely to have resulted in the stronger interaction energy. Once again the only migration observed was away from the cent-bridge-(111), this time to the hollow-(111)/(100). The interaction energy associated with the edge-bridge-(111) site of the majority-Ti cluster relative to the hollow-(111)/(111) of the pure Ti cluster is approximately 0.4 eV.

The Pauling electronegativities of O, Pt and Ti are in the order, O (3.44) $<$ Pt (2.28) $<$ Ti (1.54). In the previous charge calculations on core-shell $Pt_{32}Ti_6$, the Pt shell became slightly negatively charged and the Ti core became slightly positive. For the Pt_6Ti_{32} core-shell cluster,

the Pt core becomes negative and the Ti shell positive. Considering the electronegativities above, the oxygen in the hydroxyl molecule will be negatively charged. This means that it will exhibit stronger binding to the slightly positively charged Ti shell than to either the neutral Pt, or Ti for the pure clusters, or the negatively charged Pt shell for the Pt-rich bimetallic cluster. The average interaction energy associated with the Pt-rich clusters is calculated to be $\sim$2.6 eV weaker than those for the majority-Ti clusters.

4.3.2.2 Carbon Monoxide Adsorption

For studies of CO adsorption, the same sites are compared as those for OH adsorption, with the results shown in Figure 4.7. From Figure 4.7a, we observe that edge-bridge-(100) is the site of strongest binding of CO on the pure Pt_{38} cluster. This disagrees with experimental and theoretical data, which show atop sites on the (111) facet exhibiting strongest CO binding (a common problem when calculating at the DFT level). Instead, the atop-111 site is found to have the weakest binding to the CO molecule, although because of the size of the clusters being studied, this is not a true (111) facet site. Migration is observed from the hollow-(100) to the edge-bridge-(100) site for the pure Pt_{38} cluster, differing from the migration observed for OH from the hollow-(111)/(111) site.

Once again, the bimetallic $Pt_{32}Ti_6$ core-shell cluster exhibits weaker CO binding than the pure Pt_{38} cluster. For the $Pt_{32}Ti_6$ bimetallic core-shell cluster, the strongest CO binding site was again calculated to be the edge-bridge-(100). There was significant migration to this site, from the cent-bridge-(111), hollow-(100) and hollow-(111)/(100) site. Comparing the interaction energy difference between the edge-bridge-(100) site of the bimetallic and pure clusters revealed an energy difference of $\sim$0.2 eV. The site of weakest binding for the $Pt_{32}Ti_6$ core-shell cluster was again the atop-(111) site. The interaction energy difference between the pure and bimetallic clusters for the atop-(111) site was larger ($\sim$1.1 eV). From the previous studies of charge distribution, the centroid site of the (111) facet gained more electron density than other sites on the Pt shell. This resulted in the CO molecule at the atop-(111) site binding to a very negative Pt atom, which suggests why the site may be so unfavourable when comparing the bimetallic to

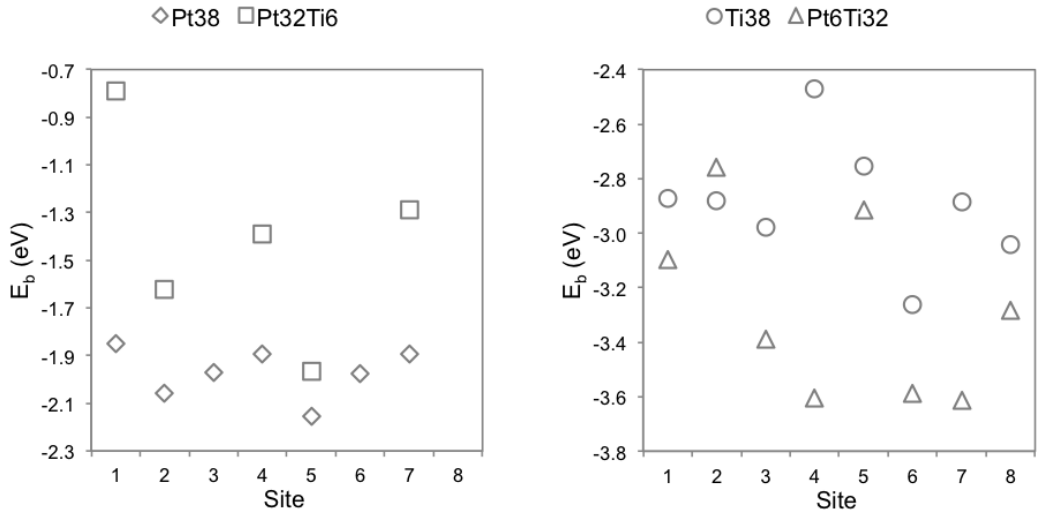

(a) Pt-Rich

(b) Ti-Rich

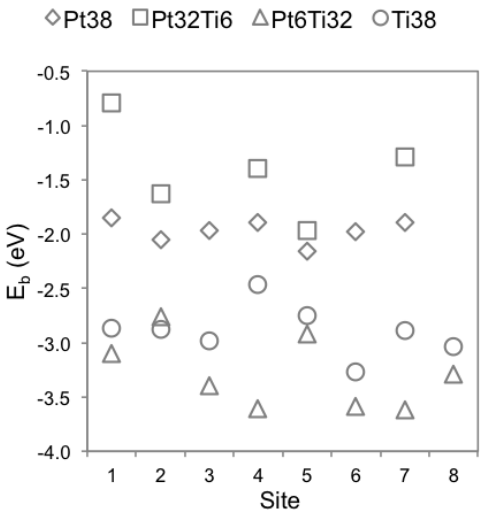

(c) Compare

Figure 4.7: Binding energy of carbon monoxide adsorption on (i) Pt_{38} and $Pt_{32}Ti_6$ (Core-Shell) TO, (ii) Ti_{38} and Pt_6Ti_{32} (Core-Shell) TO and (iii) a comparison between Pt_{38}, $Pt_{32}Ti_6$, Pt_6Ti_{32} and Ti_{38} (Core-Shell) TO, on the sites shown in Figure 4.5. Missing data points indicate migration of carbon monoxide during optimisation, leading to an interconversion of isomers.

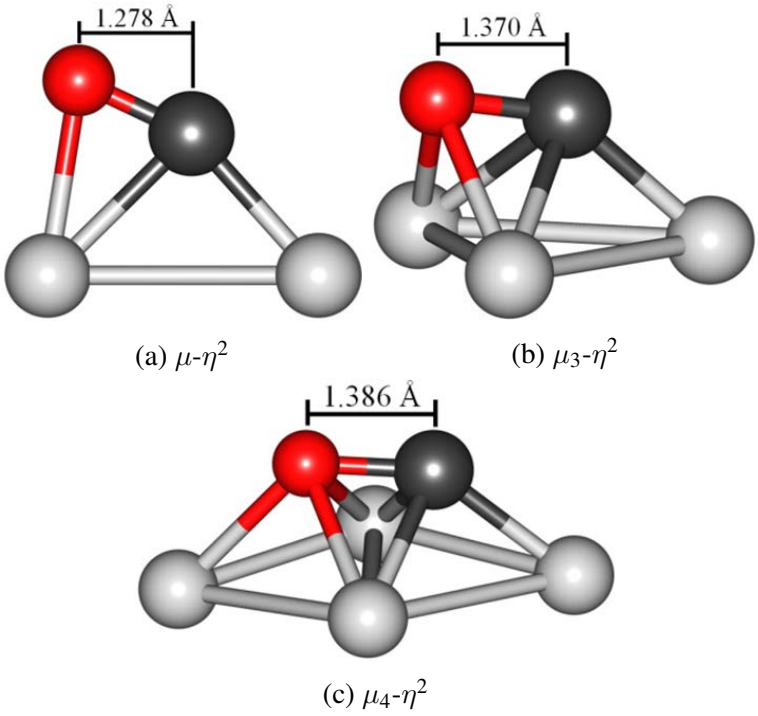

(a) μ-η^2 (b) μ_3-η^2

(c) μ_4-η^2

Figure 4.8: Observed bonding motifs of Ti–CO. Carbon monoxide bond lengths (Å) are shown. Atoms are coloured as follows: Ti - Silver, C - Black, O - Red.

the pure cluster.

When simulating CO adsorption on the pure Ti_{38} and bimetallic core-shell Pt_6Ti_{32} clusters, unusual CO binding motifs were observed, as seen in Figure 6.4. Ti bonding to both the carbon and oxygen, in a side-on (η^2) fashion, instead of forming an axial (η^1) bond to only the carbon, was observed for the Ti-rich systems. The mode of coordination to the metal surface is denoted μ_x, where x ranges from 1 to 4. Ti still favourably binds to carbon initially; if attempting to bond to the oxygen first, bond destabilisation occurs, preventing binding of CO to the cluster. This is also observed when adsorbing CO on a Pt surface. From the previous calculations it is possible to see strong Ti–O bonding which is likely to favour this side-on bonding.

The bimetallic Pt_6Ti_{32} clusters exhibited, in general, stronger binding to CO than the pure Ti_{38} clusters, as seen in Figure 4.7b. The two structures resulting in the strongest interaction energies for the bimetallic and pure clusters are the μ_4-η^2 motifs seen in Figure 4.8c. The site resulting in the weakest interaction energy is the μ-η^2 motif seen in Figure 4.8a for both the bimetallic and pure clusters. Bond distances are also displayed in Figures 4.8a–4.8c. These

reveal slightly longer C–O bond lengths when adsorbed in this η^2 fashion, compared with axial atop, bridge and hollow sites. The C–O bond length associated with these η^1 sites is approximately 1.1 Å. Whilst C–O bond elongation corresponds to weakening of the C–O bond, overall molecular stability is achieved through the increased interaction with the cluster surface observed for the η^2 coordinated systems. Comparisons of the interaction energy for the majority-Ti clusters shows average stronger binding by approximately 1.3 eV when compared with the Pt-rich clusters. It is likely that the stronger interaction energies arise from the increased interaction (via Ti–O bonding) with the Ti surface.

It is noted that for the 38-atom TO clusters the presence of a Ti shell produced significantly stronger interactions with OH and CO molecules. This would inhibit the ORR; in other words, the electrocatalyst would be less efficient than pure Pt. Also, the electrocatalyst would be more susceptible to CO poisoning, thus leading to more blocking of active sites on the catalyst surface. When studying the larger clusters, emphasis is placed on the energetically favourable bimetallic Pt-rich clusters, although Ti-rich clusters are also investigated for completeness. Comparisons are made with the currently used pure Pt clusters to establish any advantages which may occur due to alloying.

4.3.3 Electronic Effects

4.3.3.1 Density of States

DOS calculations have been performed to determine the *d*-band characteristics for varying TO cluster sizes and compositions. Following geometry optimisation, a projected DOS (PDOS) analysis was performed on the bare clusters. In conjunction with the PDOS calculations, Löwdin charge analysis on the various structures was also performed to give an indication of electron transfer within the cluster. This allows us to link charge effects to changes in the PDOS, which is discussed later. Unless otherwise stated, when quoting PDOS values, only the outer shell of atoms is considered. The values are not divided to give data per atom; the values are for the entire outer shell. This is because it is at the outer layer of atoms that the electrochemical

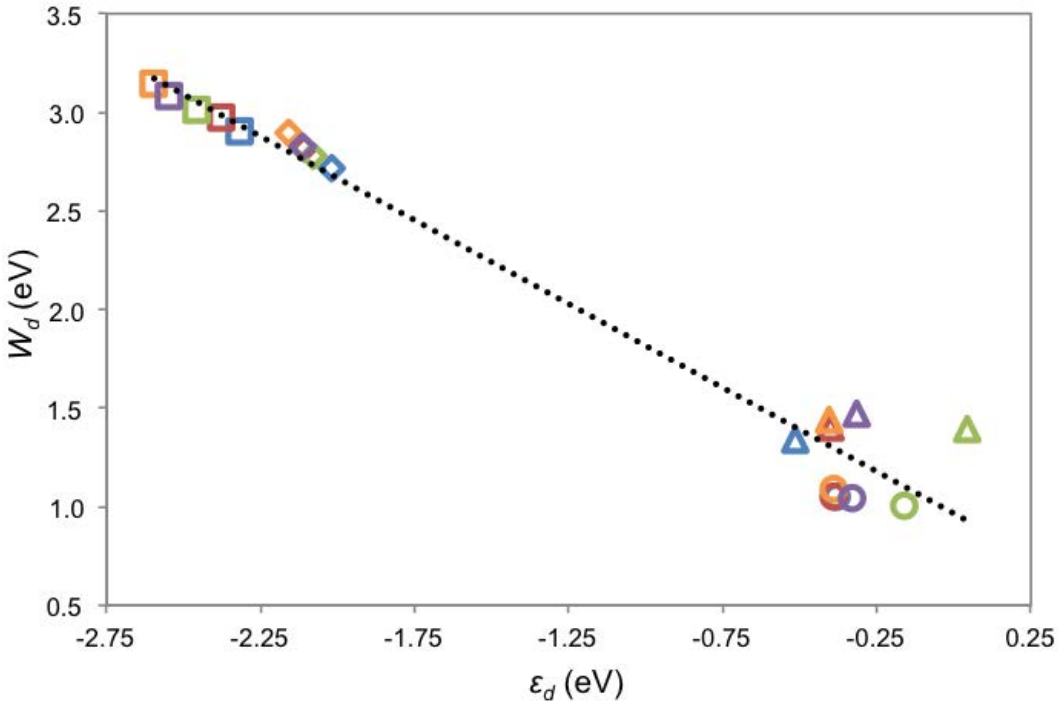

Figure 4.9: Relationship between d-band centre (ε_d) and d-width (W_d) for the 38 (blue), 79 (red), 116 (green), 140 (orange), and 201 (purple) atom pure Pt (diamond), Pt-rich monolayer (square), Ti-rich monolayer (triangle), and Ti pure (circle) clusters. The data has a least squares regression (R^2) fitness of 0.96.

reactions will occur, so changes in shell properties can have significant effects on the catalytic activity of a cluster. Averaging over the entire outer shell removes variations due to site specific changes, e.g., centroid or edge sites gaining greater charge.

Figure 4.9 shows a plot of d-band centre (ε_d) and d-width (W_d) for the 38, 79, 116, 140, and 201-atom clusters, for which the raw data can be found in Table 4.3. As expected, this reveals the trend that a more negative d-band centre coincides with an increase in d-band width. As a result of constant d-band occupancy, the d-band centre shifts to more negative values (relative to the Fermi energy (E_F)) as a consequence of the wider d-band. If the d-band were to become more narrow, this would result in the d-band centre shifting to a more positive value. The d-band centre of the pure and majority-Pt clusters are found to be more negative than for the pure and majority-Ti clusters. This is because Pt has nine d-band valence electrons while Ti has only two.

The d-band centre of the bimetallic Pt-rich clusters is also found to be slightly more negative

Table 4.3: Calculated values of Fermi Energy (E_F), *d*-band centre (ε_d), *d*-width (W_d), and average charge of various clusters (data for outer shell atoms) as well as OH and CO adsorption energies.

N	Chemical Ordering	Pt_n	E_F (eV)	ε_d (eV)	W_d (eV)	Shell Charge ($\|e\|$)	E_{ads} (eV) OH	CO
38	pure	0	-2.75	-0.38	1.05	+0.03	-5.12	-2.87
38	monolayer	6	-2.71	-0.51	1.34	+0.06	-5.14	-3.10
38	monolayer	32	-4.59	-2.32	2.91	-0.02	-2.26	-0.79
38	pure	38	-4.95	-2.02	2.72	+0.02	-2.78	-1.85
79	pure	0	-2.48	-0.39	1.05	+0.03	-5.85	-3.48
79	monolayer	19	-2.40	-0.40	1.40	+0.07	-5.96	-3.25
79	monolayer	60	-3.98	-2.38	2.98	-0.03	-2.44	-1.08
79	pure	79	-4.35	-2.11	2.82	+0.02	-2.79	-1.77
116	pure	0	-2.14	-0.16	1.01	+0.04	-6.05	-3.29
116	monolayer	38	-1.95	0.04	1.39	+0.09	-6.15	-3.53
116	monolayer	78	-3.44	-2.46	3.01	-0.04	-2.38	-1.04
116	pure	116	-3.80	-2.08	2.78	+0.02	-2.79	-1.80
140	pure	0	-1.83	-0.39	1.09	+0.03	-6.11	-3.25
140	monolayer	44	-1.73	-0.41	1.44	+0.08	-5.26	-3.78
140	monolayer	96	-3.04	-2.60	3.15	-0.04	-2.54	-0.92
140	pure	140	-3.49	-2.16	2.89	+0.02	-2.69	-1.61
201	pure	0	-1.19	-0.33	1.04	+0.04	-5.12	-3.46
201	monolayer	79	-1.00	-0.32	1.47	+0.10	-6.07	-1.74
201	monolayer	122	-2.26	-2.55	3.09	-0.05	-2.34	-0.71
201	pure	201	-2.64	-2.12	2.83	+0.02	-2.64	-1.52

than for the pure Pt clusters. This trend is observed for all cluster sizes, suggesting that the formation of a Ti@Pt cluster results in broadening of the *d*-band. Although the Ti@Pt bimetallic system has fewer electrons than the pure Pt system, the Ti levels are located higher in energy than those of Pt (as Ti is more electropositive than Pt) and so broadening occurs upon alloying. This broadening then results in the observed downshift in *d*-band centre. It is also possible to see size effects with, in general, a slight downshift in *d*-band centre and a broadening of the *d*-width as the cluster size increases.

The relationship between *d*-band centre and *d*-width for the Ti-rich and pure Ti clusters is less regular. Pt@Ti bimetallic clusters have slightly broader *d*-widths than the pure Ti clusters. This can again be explained by considering the effect of alloying with Pt. The Pt *d*-band character is found below that for the Ti *d*-band. Upon alloying with Pt, broadening occurs due to

interactions of the lower Pt *d*-band character with the higher Ti *d*-band. For the pure Ti and Ti-rich clusters size effects seem to have little effect on *d*-band characteristics. The lack of correlation between ε_d and W_d for the pure Ti and Ti-rich clusters is most likely a result of structural effects. Contraction of Ti–Ti bonds would result in a downshift of the *d*-band centre, while elongation would lead to an upshift.

The relationship between the *d*-band character for Pt and Ti at the 116 cluster size can be seen in Figure 4.10. This clearly demonstrates that, upon alloying Pt with Ti, the *d*-band levels below E_F are generally dominated by the Pt orbitals; conversely, the levels above the E_F tend to be dominated by Ti. This likely results from two effects: charge transfer and orbital overlap. Charge transfer resulting in donation of electron density from Ti to Pt will lead to filling of the higher *d*-band states, causing an increase in E_F and a consequent downward shift of the *d*-band centre related to E_F. It is likely that orbital overlap will increase as a result of interactions between the Pt and Ti, resulting in broadening of the *d*-band and thus a downshift in *d*-band centre.

Through the study of larger clusters, it is also possible to investigate compositional effects in more detail. The 38-atom clusters allows for four high symmetry configurations: two pure and two core-shell – as does the 79-atom cluster if changes to the single central atom are ignored. The larger 116-atom cluster allows for the study of six high-symmetry structures: two pure and four core-shell. The 140 and 201-atom clusters allow for the generation of further structures: two pure, four core-shell, and two onion. A breakdown of the *d*-band characteristics for these larger clusters is given in Table 4.4.

The bimetallic $Pt_{78}Ti_{38}$ cluster has a more negative *d*-band centre than the pure Pt_{116} cluster. The $Pt_{110}Ti_6$ cluster has a slightly less negative *d*-band centre than the pure Pt_{116} cluster. Splitting the cluster into layers (inner core, outer core, and shell) reveals the reason for this. For the pure Pt_{116} cluster the ordering of the *d*-band centre, with ascending negativity, is inner core (Pt) $>$ outer core (Pt) $>$ shell (Pt), with a difference of 0.69 eV between the outer core and the shell. The $Pt_{110}Ti_6$ cluster has altered ordering because of the presence of the Ti core to: outer core (Pt) $>$ shell (Pt) $>$ inner core (Ti). There is a slightly larger difference between the outer core

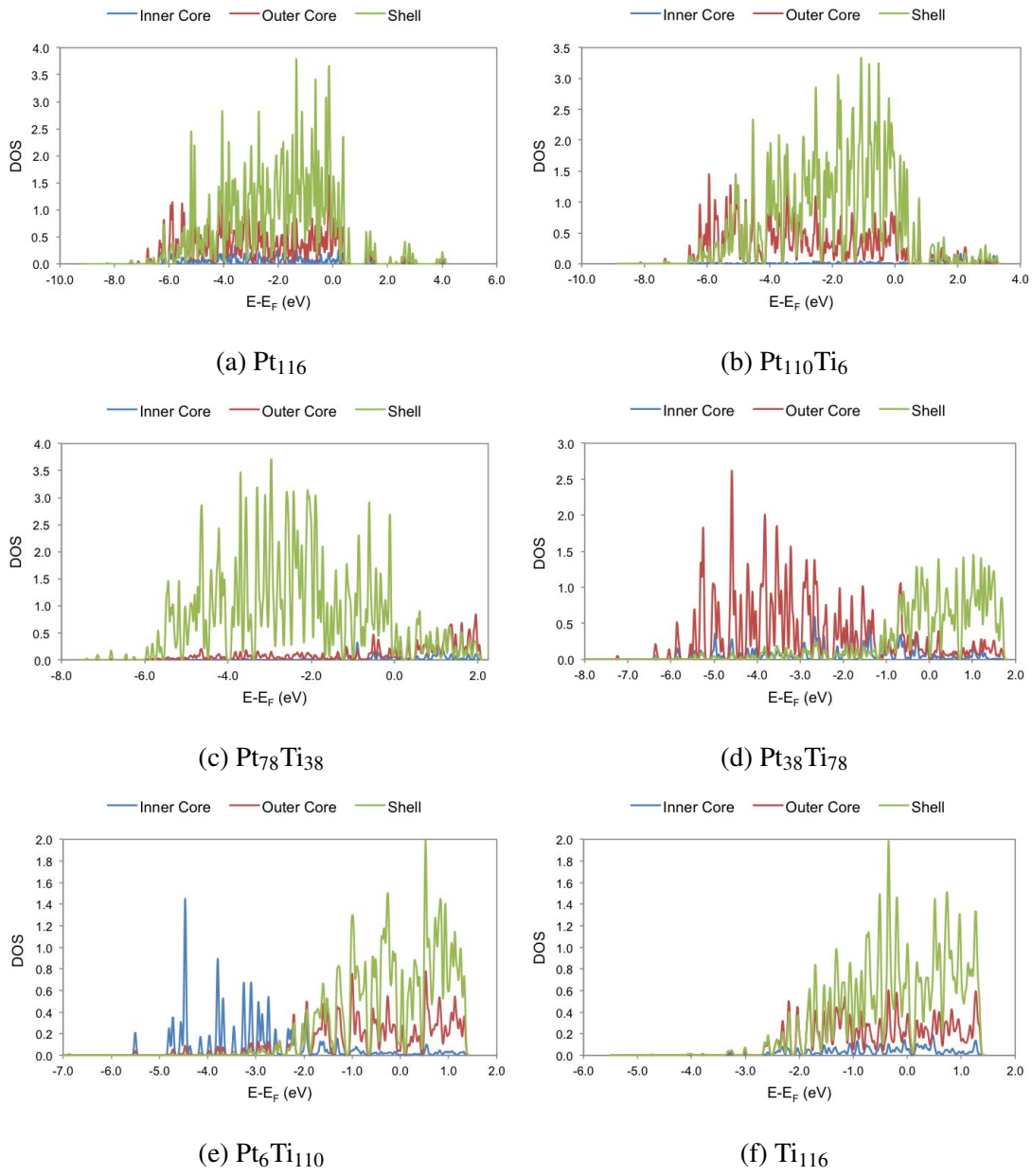

(a) Pt_{116} (b) $Pt_{110}Ti_6$

(c) $Pt_{78}Ti_{38}$ (d) $Pt_{38}Ti_{78}$

(e) Pt_6Ti_{110} (f) Ti_{116}

Figure 4.10: Relationship between *d*-band character for (i) Pt_{116}, (ii) $Pt_{110}Ti_6$, (iii) $Pt_{78}Ti_{38}$, (iv) $Pt_{38}Ti_{78}$, (v) Pt_6Ti_{110} and (vi) Ti_{116}. *d*-band PDOS is evaluated for fractions of the clusters, comparing the inner core, outer core, and shell. This demonstrates that the higher orbitals, closer to the Fermi energy (E_F), have predominantly Ti character, whereas the lower-lying orbital are mostly Pt in character.

Table 4.4: Calculated Values of *d*-band centre (ε_d) and *d*-width (W_d) for Pure, Monolayer, Bilayer, and Onion Compositions at Varying Sizes Showing the Relationship between Cluster Inner Core, Outer Core, and Shell Atoms total.

N	Chemical Ordering	Pt_n	ε_d (eV)			W_d (eV)		
			inner core	outer core	shell	inner core	outer core	shell
116	pure	0	-0.46	-0.52	-0.16	1.18	1.25	1.01
116	bilayer	6	-3.08	-0.54	-0.11	3.38	1.43	0.99
116	monolayer	38	-2.19	-2.97	0.04	2.87	3.45	1.39
116	monolayer	78	0.14	-0.22	-2.46	1.25	2.12	3.01
116	bilayer	110	0.54	-2.93	-2.01	2.48	3.69	2.68
116	pure	116	-2.90	-2.78	-2.08	3.65	3.56	2.78
140	pure	0	-0.44	-0.55	-0.39	1.16	1.26	1.09
140	bilayer	6	-3.40	-0.70	-0.31	3.70	1.46	1.05
140	onion	38	-0.82	-3.47	-0.35	2.18	3.86	1.39
140	monolayer	44	-2.54	-3.42	-0.41	3.12	3.84	1.44
140	monolayer	96	0.04	-0.26	-2.60	1.22	2.10	3.15
140	onion	102	-3.23	-0.24	-2.60	3.65	2.17	3.17
140	bilayer	134	0.50	-2.86	-2.15	2.41	3.60	2.86
140	pure	140	-2.73	-2.58	-2.16	3.48	3.36	2.89
201	pure	0	-0.54	-0.64	-0.33	1.20	1.31	1.04
201	bilayer	19	-3.19	-0.71	-0.28	3.54	1.57	1.04
201	onion	60	-0.55	-3.44	-0.29	1.91	3.83	1.42
201	monolayer	79	-2.50	-3.31	-0.32	3.11	3.76	1.47
201	monolayer	122	0.04	-0.29	-2.55	1.25	2.04	3.09
201	onion	141	-3.17	-0.33	-2.64	3.59	2.19	3.18
201	bilayer	182	0.64	-2.93	-2.07	2.35	3.66	2.74
201	pure	201	-2.73	-2.72	-2.12	3.48	3.51	2.83

and shell of 0.92 eV in this case. This shows that the Pt *d*-band broadening occurs most significantly at the Pt-Ti interface; in the $Pt_{110}Ti_6$ case the outer core is able to shield the shell from the same broadening effects as with the $Pt_{78}Ti_{38}$ cluster. Chen *et al.* [170] reported experimental results showing favourable ORR properties when Pt forms a near monolayer on the underlying nonprecious metal. This supports the results presented here, where the most significant changes in *d*-band character happen at the Pt-Ti interface. The same trend can be seen for the larger clusters in all cases.

The relationship between *d*-band centre, *d*-width, and composition for the Ti-rich clusters is slightly more complex. The pure Ti_{116} and the bimetallic Pt_6Ti_{110} clusters have similar *d*-band centres. This suggests that the six inner core Pt atoms in the bimetallic Pt_6Ti_{110} cluster have

little effect on the shell because of the shielding effects of the outer core. For the pure Ti_{116} cluster the *d*-band centre ordering, with ascending negativity is outer core (Ti) > inner core (Ti) > shell (Ti). For the bimetallic Pt_6Ti_{110} the ordering is inner core (Pt) > outer core (Ti) > shell (Ti). However, the shell of the bimetallic $Pt_{38}Ti_{78}$ cluster has a slightly positive *d*-band centre coupled with a larger *d*-width; the ordering in this case is outer core (Pt) > inner core (Pt) > shell (Ti). A narrowing of the *d*-width and a slight upshift in *d*-band centre were expected to result from interactions between the Pt core and Ti shell. There is a broadening of the *d*-band and a dramatic upshift in *d*-band centre to a slightly positive value. This suggests that charge transfer from the Ti shell to the Pt core leads to a positive *d*-band centre. The same trends are true for the larger clusters.

The 140 ($A_{96}B_{38}A_6$) and 201 ($A_{122}B_{60}A_{19}$) atom onion clusters result in the cluster shells having similar *d*-band centres to those for the $A_{96}B_{44}$ and $A_{122}B_{79}$ clusters. For the $Pt_{96}Ti_{38}Pt_6$ and $Pt_{122}Ti_{60}Pt_{19}$ clusters, the *d*-band centre ordering, with ascending negativity, is inner core (Pt) > shell (Pt) > outer core (Ti). For the $Ti_{96}Pt_{38}Ti_6$ and $Ti_{122}Pt_{60}Ti_{19}$ clusters, the *d*-band centre ordering, with ascending negativity, is outer core (Pt) > inner core (Ti) > shell (Ti). This is in line with the previously investigated core-shell structures, showing large changes in *d*-band centre at the Pt-Ti interface.

A search of the literature shows that the bulk Pt surface has a calculated *d*-band centre of -2.44 eV while bulk Pt_3Ti has a calculated *d*-band centre of -3.16 eV. [171] This demonstrates the trend of a downshift in *d*-band centre when Pt is alloyed with Ti, also suggesting weaker adsorption of e.g. OH to the bulk Pt_3Ti system compared with the pure Pt bulk. These results fit well with the trends observed in this study; as the cluster size increases, tending toward the bulk, the *d*-band centre becomes more negative. For the pure Pt clusters, the *d*-band centre ranges from -2.02 eV (38-atom) to -2.16 eV (140-atom). For the monolayered bimetallic Pt-rich clusters, the *d*-band centre ranges from -2.32 eV (38-atom) to -2.60 eV (140-atom).

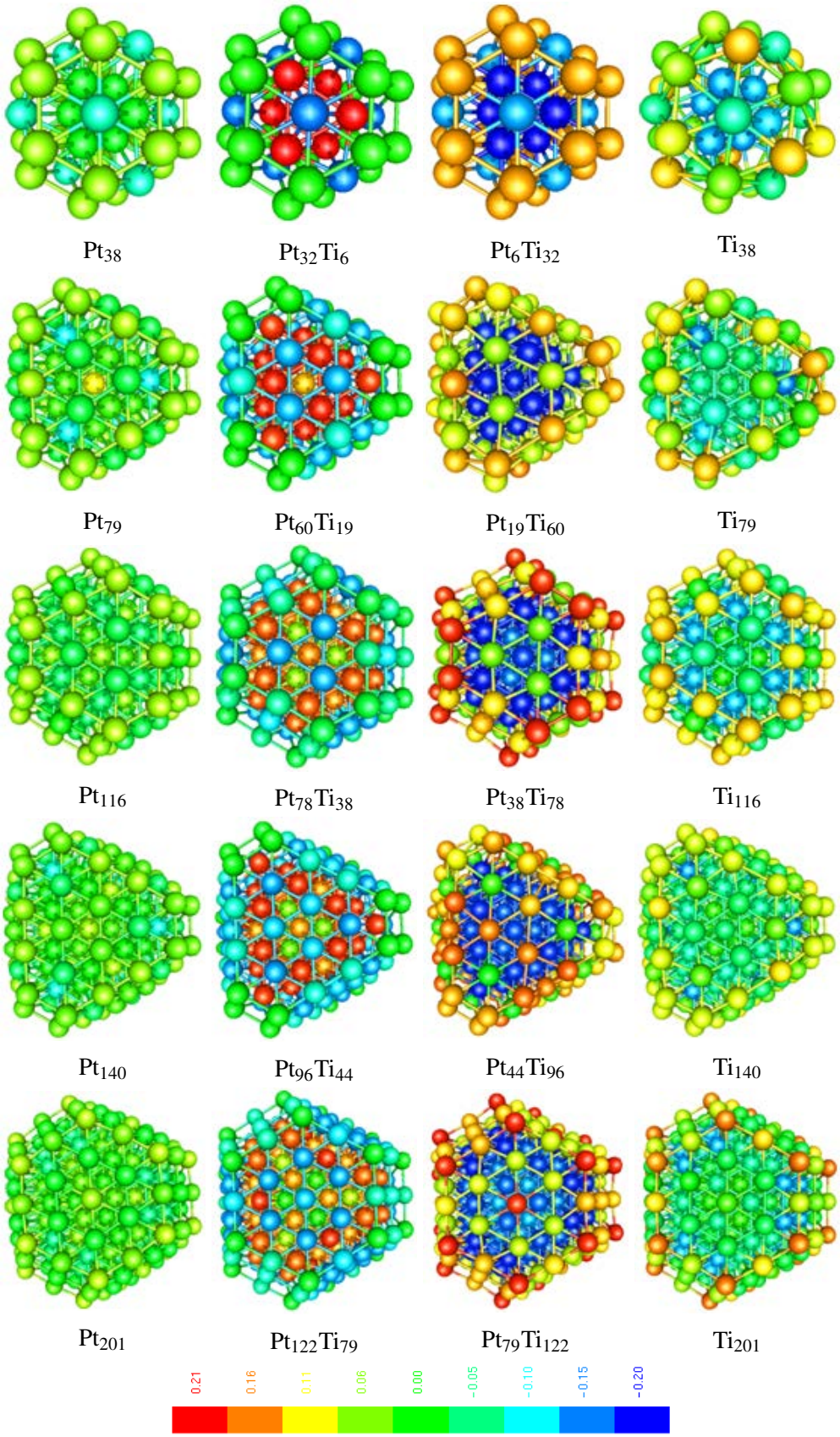

Figure 4.11: Charge density plots showing net atomic charges, with negative charge in blue and positive charge in red. The scale remains constant across varying compositions and sizes.

4.3.3.2 Charge Analysis

The results of the Löwdin charge analysis are shown in Figure 4.11, giving composition, average outer shell charge, and a colour-coded image of the charge distribution. This shows the charges on clusters of constant size, plotted on the same scale, to investigate how the charge changes with composition. This clearly demonstrates that most clusters have an outer shell with an average positive charge, apart from the Ti@Pt core-shell structures. The shell of the Ti-majority clusters becomes significantly more positive than other compositions. This shows that alloying Pt and Ti results in a loss of electron density from the electropositive Ti atoms and a gain of charge density by the electronegative Pt atoms. It also shows that for the pure clusters there is slight donation from the shell to the core of the cluster.

It is expected that loss of electron density results in a downshift of the E_F and a narrowing of the DOS. This is coupled with the previously discussed observation that a narrowing of the *d*-band would result in an upshift in the *d*-band centre. The overall charge of the clusters remains neutral (with only the core or shell atoms gaining charge) and the DOS is plotted with respect to the E_F. This normalisation results in only narrowing or broadening of the *d*-band: changes in atomic charge have an observable effect on the *d*-band centre.

This is clearly demonstrated through studying charged Pt_{38} TO clusters. The DOS characteristics were studied for the entire cluster as electron density was altered for the whole system. The neutral cluster was compared with $Pt_{38}{}^{x}$ clusters where x = -2, -1, +1, and +2. Figure 4.12a shows the relationship between the E_F and *d*-band centre, demonstrating that changes in the E_F due to charge have no effect on the *d*-band centre. Instead, the *d*-band centre changes, because of broadening or narrowing of the *d*-band, as seen in Figure 4.12b. It is apparent that as the cluster becomes more positive, the E_F decreases, the *d*-width decreases and there is an upshift in the *d*-band centre energy, the reverse is found for negative clusters.

Changes in charge distribution are plotted in Figure 4.12c. The figure shows the average number of electrons in the *s*-, *p*-, and *d*-bands. The partial charges are normalised to the values calculated for the neutral cluster. A negative value indicates gain of electrons and positive values represent loss of electrons. When the cluster becomes negative, the *p*-band gains more

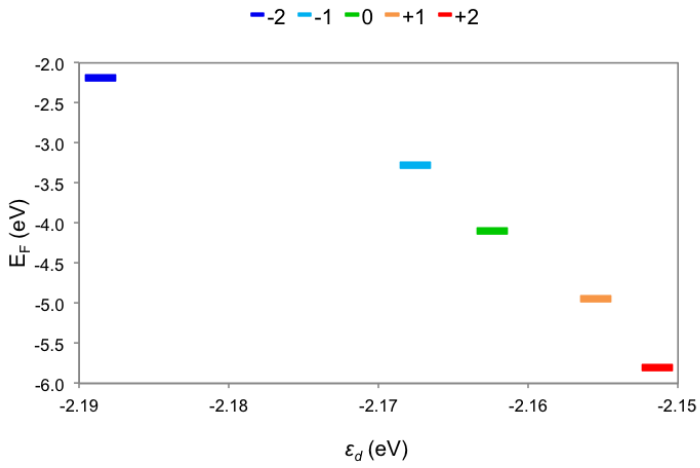

(a)

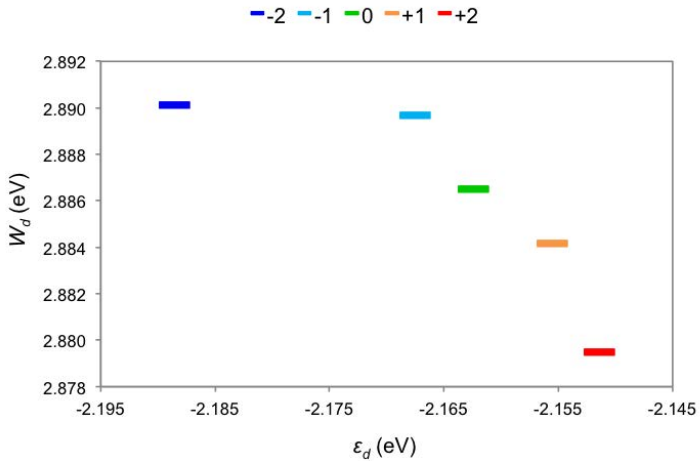

(b)

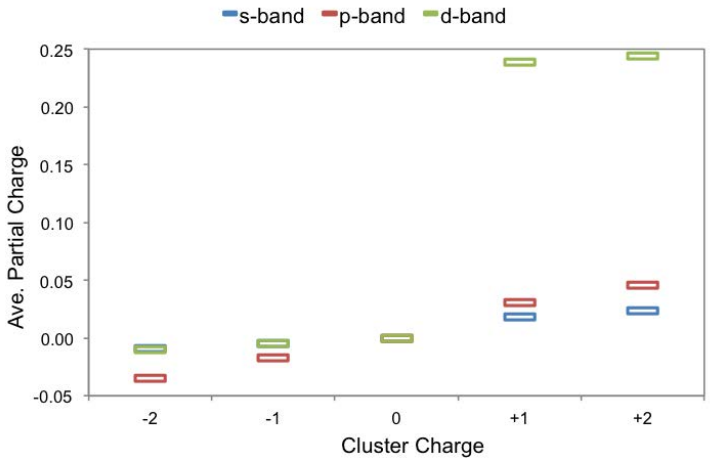

(c)

Figure 4.12: Effect of altering the cluster charge on the (i) Fermi energy (E_F), (ii) d-width (W_d) and (iii) band filling with relation to the d-band centre (ε_d).

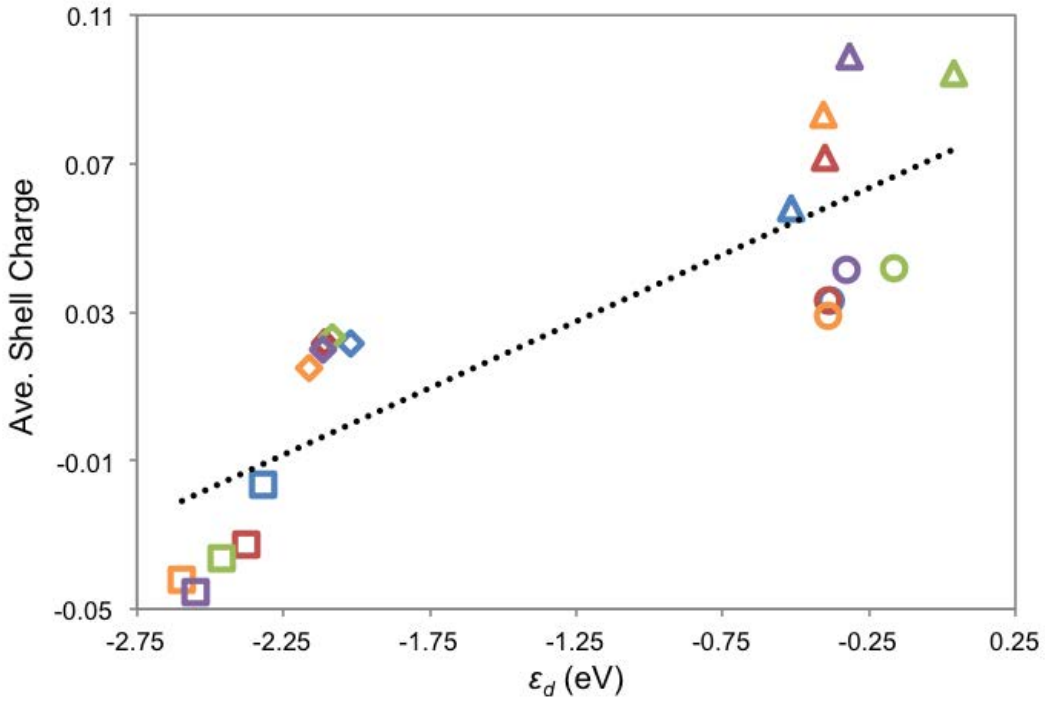

Figure 4.13: Relationship between *d*-band centre (ε_d) and charge for the 38 (blue), 79 (red), 116 (green), 140 (orange), and 201 (purple) atom pure Pt (diamond), Pt-rich (square), Ti-rich (triangle), and Ti pure (circle) clusters. The data has a R^2 fitness of 0.71.

electron density than the *s*- or *d*-bands. Conversely, when the the cluster becomes positive, it is the *d*-band that loses the most electron density.

Figure 4.13 shows the relationship between charge and *d*-band centre for various cluster sizes with varying compositions. For the Pt-rich clusters, a loss of charge density results in the *d*-band centre becoming more negative. Also, as the cluster size increases, there is greater transfer of negative charge to the outer shell. The same is not true for the Ti-rich clusters, where gain of positive charge results in a downshift in the *d*-band centre. This is likely because of structural effects, (e.g., bond strain) cancelling out the various charge effects through opposing changes in *d*-band characteristics.

4.3.3.3 Chemisorption Studies

In the second set of chemisorption studies, calculated adsorption energies are linked to previously discussed DOS values. This enables an indication of how changes in the composition and size of clusters affects adsorption energies brought about by changes in the electronic structure

of the cluster. The adsorption energies reported in Table 4.3 are for the atop-(111) facet site only. It should be noted that this site is not actually the most favourable for these types of systems. In the study on the smaller 38-atom clusters (see Section 4.3.2), it was found that the site of strongest binding (the edge-bridge site between the (111) and (100) facets) demonstrated little difference between absorption on the pure or bimetallic clusters. When comparing adsorption energies for the other sites, more significant differences were observed. As the cluster size increases, the number of strongly binding edge-bridge sites decreases relative to the other sites where differences in the adsorption energies were observed. It was thought that the atop-(111) site would be most suitable to allow relevant comparisons between the pure and bimetallic clusters. This site also has the advantage of being a locally stable binding site; no barrierless migration from the site was observed in the previous study of the 38-atom clusters.

Figure 4.14a shows the OH adsorption energy decreasing, as the *d*-band centre became more negative, shifting down relative to the E_F. This trend is generally observed across varying cluster sizes and compositions suggesting a close relationship between the calculated *d*-band centre and the adsorption energy which has been extensively discussed in the literature. [171–173] This explains the slight weakening of OH adsorption on the bimetallic Pt-rich clusters compared with other cluster compositions. The *d*-band centre characteristics help to explain the differences in binding energy for the pure and bimetallic clusters investigated in this study. Stronger binding is observed for the pure Pt clusters compared with the bimetallic Pt-rich clusters. This can be attributed to the downshift observed in *d*-band centre when comparing the pure with the bimetallic. This downshift results from filling of orbitals in the Pt shell through donation of *d*-band density from the Ti core.

The adsorption energy associated with CO bonding has also been studied in order to assess the susceptibility of the electrocatalyst to CO poisoning. From the previous studies (in Section 4.3.2), it was found that reducing the Pt–C bond strength results in a reduced susceptibility to CO poisoning. [174] This study is aimed at establishing the strength with which a CO molecule binds to the cluster surface. The previous investigations demonstrated unusual CO bonding to the Ti-rich clusters, where both the C and O are bound to the Ti surface. This is once again

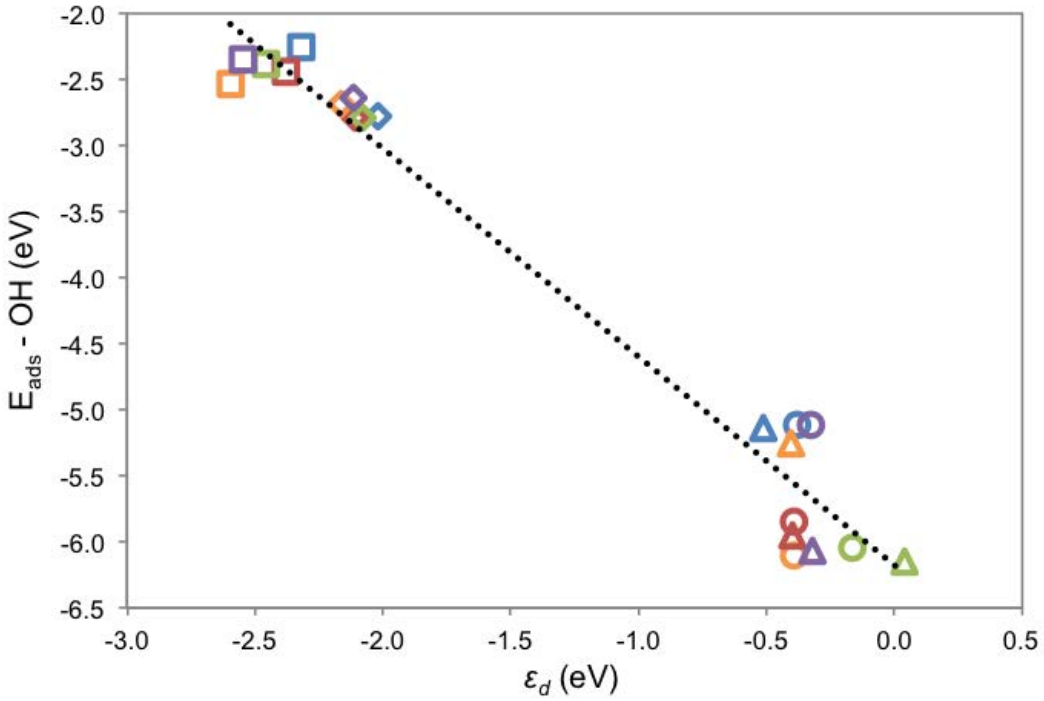

(a)

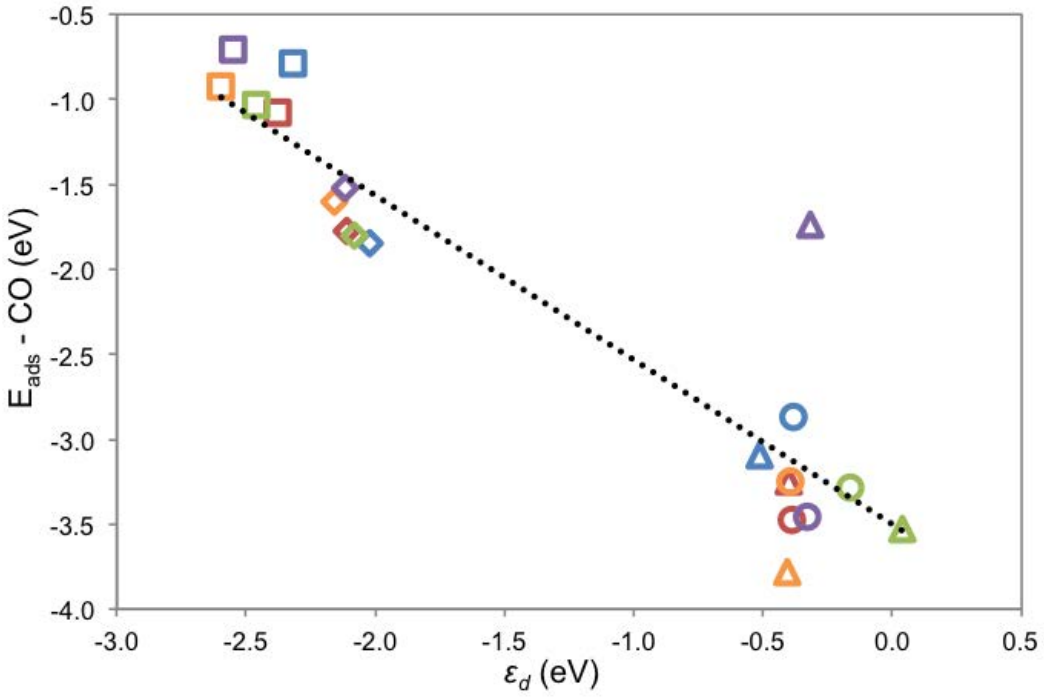

(b)

Figure 4.14: Relationship between d-band centre (ε_d) and (i) OH adsorption energy as well as (ii) CO adsorption for the 38 (blue), 79 (red), 116 (green), 140 (orange), and 201 (purple) atom pure Pt (diamond), Pt-rich (square), Ti-rich (triangle), and Ti pure (circle) clusters to the atop-(111) site. The R^2 fitness of the OH and CO adsorption data is 0.71 and 0.84, respectively.

observed for the larger cluster sizes. This unusual binding motif results in stronger CO bonding than would be observed for the more common axial binding motif, with M-C binding only. As previously mentioned, this binding motif was attributed to the particularly strong Ti–O bonds that formed.

The Blyholder model [175] is commonly used to describe CO bonding to metal surfaces through a donor-acceptor mechanism. Bonding occurs with electron transfer from the highest filled (5σ) molecular orbital of the CO, to unoccupied metal orbitals and back-donation from the occupied metal orbitals to the lowest unfilled ($2\pi^*$) orbital of the CO. Hammer *et al* proposed a quantitative model for relating changes in the CO chemisorption energy to shifts in the energy of the *d*-band centre [176], as in Equation 4.4.

$$\Delta E_{d-hyb} = \frac{-2\left(1-f\right)\beta_{5\sigma}^{2}}{\left|\varepsilon_{d}-\varepsilon_{5\sigma}\right|} - 2f\frac{\beta_{2\pi}^{2}}{\left|\varepsilon_{2\pi}-\varepsilon_{d}\right|} + 2\left(1+f\right)\gamma_{5\sigma}\beta_{5\sigma}^{2} + 2f\gamma_{2\pi}\beta_{2\pi}^{2} \tag{4.4}$$

In Equation 4.4, the first two terms account for attractive interactions, while the second two are repulsive terms. For transition metals, the *d*-band couples much more strongly to the $2\pi^*$ orbital than the 5σ orbital. It is therefore possible to simplify this expression and describe M–CO interactions as in Equation 4.5 [177].

$$\Delta E_{d-hyb} \approx -2f\frac{\beta_{2\pi}^{2}}{\left|\varepsilon_{2\pi}-\varepsilon_{d}\right|} + 2f\gamma_{2\pi}\beta_{2\pi}^{2} \tag{4.5}$$

When the *d*-band is narrow and the *d*-band centre (ε_d) is small, the attractive term dominates. For a wide *d*-band, with a corresponding downshift in the *d*-band centre, resulting in a large ε_d, the first attractive term is smaller meaning meaning the second repulsive term will have a greater effect.

Results for CO adsorption energies are presented in Figure 4.14b. A similar trend is observed for CO adsorption as with OH adsorption. As the *d*-band centre upshifts towards E_F, the adsorption energy becomes more negative resulting in stronger binding, in agreement with Equation 4.5. This suggests electronic effects contribute significantly to the weaker binding energy of CO to the bimetallic Pt-rich cluster compared with other compositions. The CO

adsorption energy for the $Pt_{79}Ti_{122}$ cluster is significantly higher in energy than for the other Ti-rich clusters. This is because the calculation reaches convergence with the CO still in the axial position. When setting up all chemisorption calculations, a slightly longer M-CO bond length was generated for the initial structure. The idea behind this was to avoid favouring the planar binding motif. In all other calculations, the M-CO bond length reduced throughout the geometry optimisation cycles until the oxygen was close enough to the cluster surface that a switchover between the axial and planar geometries occurred. While this did not occur for the $Pt_{79}Ti_{122}$ cluster, with the oxygen remaining too far away from the Ti surface, it does demonstrate the significantly stronger binding exhibited by the CO in the planar conformation compared with the axial conformation.

4.4 Conclusions

In this study, DFT calculations have indicated that bimetallic core-shell $Pt_{32}Ti_6$ clusters exhibit slightly weaker hydroxyl binding compared with pure Pt_{38} clusters. Weaker Pt–O bonding has been linked to improved ORR kinetics in PEFCs as discussed previously. This suggests that alloying Pt with Ti may provide small improvements to the PEFC electrocatalyst reactivity. If Ti were to form the cluster skin, the Ti–O bond would be significantly stronger. Hydroxyl binding is found to be stronger for the bimetallic Pt_6Ti_{32} cluster than the pure Ti_{38} cluster, most likely because of charge effects.

The same trend can be seen for CO, with weaker binding to core-shell $Pt_{32}Ti_6$ than to the pure Pt cluster and stronger binding to the majority-Ti clusters. CO binding to the bimetallic Pt_6Ti_{32} cluster was found to be stronger than to the pure Ti_{38} cluster. This probably results from the unusual binding motifs observed, involving Ti–O as well as Ti–C binding. This suggests that the $Pt_{32}Ti_6$ core-shell clusters should provide reduced susceptibility to CO poisoning. This is particularly useful at the anode where CO poisoning is a prevalent problem.

The initial study focused on 38-atom TO clusters, whilst later work investigated size effects for the bimetallic PtTi system. It should be noted that the $Pt_{32}Ti_6$ clusters contain roughly 85%

Pt and 15% Ti. This would not lead to a dramatic reduction in Pt loading. As cluster size increases, there is a significant decrease in Pt content for the core-shell TO nanoparticles. For example, the 1.7 nm 201-atom TO cluster with a complete $Pt_{122}Ti_{79}$ core-shell structure results in 61% Pt and 39% Ti loading. Larger sized nanoparticles would lead to further reductions in Pt content. This demonstrates that significant reductions can be made in Pt loading for core-shell TO nanoparticles compared with the 38-atom clusters investigated in the initial study. This also demonstrates that the clusters can result in significant reductions in cost when compared with the Pt_3Ti bulk system.

From the results presented in the DOS study, it was found that compositional and size effects can have a significant effect on the *d*-band properties of the PtTi nanoparticles. Shifts are observed in the *d*-band centre when comparing pure and bimetallic clusters, with downshifts observed for the Pt-rich bimetallic clusters compared with the pure clusters. For Pt-rich clusters, this downshift has been previously noted in other systems such as bulk Pt_3Ti. In this study, when comparing the nanoparticles to the bulk system, this shift seems to vary with size and composition.

Changes in the *d*-band centre are ascribed to changes in electron density, with electron donation from Ti to Pt. This accounts for the downshift observed for the shell of the Pt-rich cluster with donation from the Ti core to the Pt shell, resulting in greater filling of the *d*-band. These changes in *d*-band characteristics were found to have an effect on the binding energies of OH and CO. It was also shown that where a downshift in *d*-band centre occurs, leading to more occupied orbitals, this results in weaker binding. An upshift in *d*-band centre, suggesting more unoccupied orbitals, results in stronger binding. This suggests that while the bulk Pt_3Ti system results in a slightly weaker Pt–O bond than would be desired, nanoparticles may result in slightly stronger binding. From the calculations performed here, it is possible to see that while slightly stronger adsorption is observed compared with the bulk system, weaker binding is observed compared with the pure Pt clusters. This means that the nano PtTi alloy system should present advantages over both bulk Pt_3Ti and pure Pt nanoparticles.

Chapter 5

Oxygen Dissociation on Pt and Ti@Pt Nanoparticles

5.1 Introduction

In the work presented in this chapter, oxygen dissociation is studied for pure Pt clusters as well as core-shell Ti@Pt clusters. As stated in Section 1.5.2, oxygen dissociation is one of the initial stages of the ORR. The studies presented in Chapter 4 have demonstrated the potential for the alloyed PtTi system to form improved PEFC electrocatalysts for anodic and cathodic reactions. Whilst it has been suggested that the rate limiting step in the ORR is due to particularly strong Pt–OH bonding, it is a necessity that the formation of any alloyed system does not have too much of a detrimental effect on other stages of the ORR.

Initially focusing on 38-atom clusters, barrier-free dissociation is observed for the Pt_{38} cluster on the (111) surface. However, dissociation barriers are observed for the (100) surface as well as both (111) and (100) surfaces on the $Pt_{32}Ti_6$ cluster. This behaviour is explained through an in depth study of cluster stability and is further investigated for larger clusters.

5.2 Methodology

5.2.1 Nudged Elastic Band

The nudged elastic band (NEB) method is a technique commonly used to calculate reaction pathways. This is achieved through relaxation of an estimated pathway to find the minimum energy path (MEP) between known initial and final states. A number of intermediate images along the reaction path are optimised with each image finding the lowest energy possible while maintaining equal spacing to neighbouring images. This constrained optimisation is achieved by adding spring forces along the band, between images and by projecting out the component of the force resulting from the potential perpendicular to the band.

An elastic band with $N-1$ images can be denoted by $[R_0, R_1, R_2, ..., R_N]$, where the end points, R_0 and R_N, are fixed and given by the energy minima corresponding to the initial and final states, the vector R_i has the Cartesian coordinates of the atoms for image i. The $N-1$ intermediate images are subject to projected forces and adjusted by the optimisation algorithm to find the MEP.

$$F_i^{NEB} = F_i^{s\parallel} + F_i^{g\perp} \tag{5.1}$$

$F_i^{s\parallel}$ are spring forces acting along the local tangent to the path $\hat{\tau}_i$, where k is the spring constant used to keep the images equally spaced along the path.

$$F_i^s|_{\parallel} = k\left(|R_{i+1} - R_i| - |R_i - R_{i-1}|\right)\hat{\tau}_i \tag{5.2}$$

$F_i^{g\perp}$ is the true force arising from the potential which acts perpendicular to the path.

$$F_i^{g\perp} = F_i - (F_i \cdot \hat{\tau}_i)\hat{\tau}_i \tag{5.3}$$

Convergence is reached when all images lie on on a steepest descent (SD) path.

5.2.2 Dimer Method

In some simple systems, reaction endpoints can be guessed and the nudged elastic band can be used to find reaction pathways. In more complex systems, it has been shown that reactions often take place via unexpected mechanisms. The dimer method is designed to deal with this problem by searching for saddle points corresponding to unknown reaction mechanisms. The dimer method is a min-mode following method that allows any initial configuration to be used as a starting point to search for a nearby saddle point. The method can also search in random directions for a saddle point when starting from a minimum basin.

In the dimer method, the gradients g_1 and g_2 of the "dimer", two close-lying points (x_1 and x_2) of distance 2Δ on the PES, are calculated. With the dimer direction $\tau = (x_1 - x_2)/2$, the dimer is rotated around its midpoint, against gradients g_1 and g_2. With $\hat{\tau} = \tau/|\tau|$ the rotational force F_R is equivalent to a torque of $T = -\tau \times (g_1 - g_2)$.

$$F_R = -(g_1 - g_2) + [(g_1 - g_2) \cdot \hat{\tau}]\hat{\tau} \tag{5.4}$$

When F_R is minimised, the dimer aligns along the eigenmode of the Hessian with the lowest eigenvalue, thus the softest vibrational mode. This results in a minimisation of the dimer end points and the curvature of the energy surface along τ. Once rotational convergence has been achieved, the dimer is translated to maximise the energy with respect to τ and to minimise the energy in all directions perpendicular to it. Translational force is calculated with g_0 being the gradient at the dimer midpoint.

$$F_T = -g_0 + 2(g_0 \cdot \hat{\tau})\hat{\tau} \tag{5.5}$$

Alternating rotational and transitional steps are taken, assuming F_R finds the global softest mode, iterative translations along F_T allow for convergence on first order saddle points.

5.2.3 Computational Details

Calculations were performed using the Vienna Ab initio Simulation Package (VASP) 5.2 [127–130]. The $5d^9$, $6s^1$ of Pt, $3d^3$, $4s^1$ of Ti and $2s^2$, $2p^4$ of O were treated as valence electrons, while the ionic cores have been represented by the projected augmented wave (PAW) method [178, 179]. Electronic exchange and correlation were described using the generalised gradient approximation (GGA) using the Perdew Wang 91 (PW91) formula [180, 181]. The Methfessel-Paxton smearing method has been used with a width of 0.1 eV and an energy cutoff of 415.0 eV was employed. All clusters were placed in the centre of a large enough supercell to ensure sufficient separation between periodic images, the Γ point is used to sample the Brillouin Zone. Atoms were then relaxed according to the calculated atomic forces, with convergence criteria for energies and forces required to be better than 1.0×10^{-4} eV/atom and 0.02 eV/Å, respectively. Electron spin is restricted to the lowest possible multiplicity, as spin unrestricted calculations resulted in little difference at considerable computational expense.

Geometry optimisations were performed using the standard VASP code. Dissociation pathways were investigated using the VTST implementation of the VASP code, by first generating an approximate pathway using the Nudged Elastic Band (NEB) method [182], as described in Section 5.2.1, with further refinements achieved using the Dimer method [183], as described in Section 5.2.2. Bader charges [136] were calculated using the standard VASP code, with analysis performed using the Bader code [184] also from the Henkelmen Group.

5.3 Results and Discussion

5.3.1 Bulk Pt

Large metal nanoparticles are often approximated in computational studies of catalysts by infinite slab models of (111) surfaces [185]. Hence, the study starts with the investigation of O_2 dissociation on slabs. There are four non-symmetry equivalent sites on the surface of the infinite (111) slab, the atop, bridge, *fcc* and *hcp* sites. It is found that the bridge and *fcc* sites are

energetically competitive, the E_b for O_2 at the bridge site being -0.87 eV, while it is -0.86 eV for the *fcc* position. This is in good agreement with experimental and theoretical studies, which have found both sites favourable for O_2 chemisorption [186–190]. The *hcp* site is 0.1 eV higher in energy than the *fcc* site (at -0.76 eV), while migration occurs when locally minimising O_2 at the atop position, resulting in O_2 bonding to the more favourable *fcc* site.

For the Pt(111) system, the oxygen molecule is initially adsorbed on a three-fold *fcc* hollow site, before dissociating, resulting in each O atom being bound to *fcc* hollow sites. The dissociation barrier on the Pt(111) slab is found to be 0.45 eV, in agreement with other calculations, which find a barrier of between 0.4 and 0.6 eV, presented in the literature [191–195] as well as experimental studies. [196] An O–O distance of 2.10 Å is found at the transition state (TS) structure; this compares to an O–O distance of 1.40 Å for the initial state (IS) and 1.24 Å in the gas phase O_2. Significant elongation of the O–O bond suggests a late transition state. The average Pt–Pt bond lengths in the *fcc* sites below the adsorbate for the IS, TS and final state (FS) structures are close: 2.94, 2.98 and 2.97 Å, respectively. However, the average Pt–Pt bond length for the pure Pt(111) surface is found to be 2.82 Å for the fcc hollow. This shows slight elongation of the Pt–Pt bond length when O_2 is adsorbed, by ≤ 0.15 Å. This is reflected in the relatively low RMSD values of 0.03, 0.05 and 0.05 Å, respectively, for IS, TS and FS structures. It was expected that a shortening of the Pt–O bond would be observed, corresponding to increased interactions with the Pt surface as O_2 dissociates. Indeed, average Pt–O bond lengths are 2.14, 1.95 and 2.05 Å for the IS, TS and FS, respectively.

The distortion energy of the bulk slab ($\Delta E(Pt_{surf})$) is found to be 0.17, 0.25 and 0.39 eV for the IS, TS and FS, respectively. Greater distortion of the surface is generally expected as the system progresses from the IS to the FS due to greater Pt–O interactions and a reduction in O–O interactions. $\Delta E(O_2)$ values calculated for the IS, TS and FS are 0.64, 5.72 and 6.34 eV, respectively. The average charge on the Pt atoms directly below O_2 are +0.18, +0.34 and +0.29 |e| for the IS, TS and FS, respectively, while overall average charges on O_2 are -0.34, -0.57 and -0.76 |e| for the IS, TS and FS, respectively. For all states, electron density is withdrawn from Pt by O, with increased charge transfer as the system progresses from the IS to the FS. There is

greater Pt charge transfer when comparing the TS to the FS because O_2 is bonded to one 3-fold *fcc* hollow site in the TS and two in the FS.

The PtTi(111) alloyed system was also considered with a model (which has been studied before [171]) where the second layer of the slab was set as Ti and the top three layers (Pt - Ti - Pt) were allowed to fully relax. During the geometry optimisation, however, it shows instability and surface and subsurface layers can no longer be identified as (111). In order to study a more realistic model of the PtTi(111) alloyed system, Ti@Pt nanoparticles were considered, with Ti cores, where the effect of edges, larger flexibility, etc. can be taken into account. Three model clusters have been studied, consisting of 38, 79 and 116 metal atoms.

5.3.2 38-Atom Clusters

5.3.2.1 Oxygen Adsorption

On the surface of the 38-atom TO cluster there are eight symmetry inequivalent sites for a pure surface composition of the monometallic and alloyed core-shell clusters, shown in Figure 5.1. Adsorption studies of atomic and molecular oxygen were performed on all non-symmetry equivalent sites. E_b values were then calculated, the results of which can be found in Table 5.1. Two possible bonding orientations were studied for O_2 adsorption, axial and planar. The axial configuration has O_2 bound to the surface through one O atom. The planar configuration is bound parallel to the surface, where the adsorbate position is defined in the following by the position of the middle of the O–O bond. It was found that the planar conformation is favourable in all cases, hence only those values are listed in Table 5.1.

For the pure Pt_{38} cluster, three-fold hollow positions 6 and 7 on the (111) facets, as well as the edge bridge position 5 between the (111) and (100) facets are the most stable for adsorption of atomic oxygen, -5.21, -5.12 and -5.12 eV, respectively. Interestingly, on $Pt_{32}Ti_6$, three-fold hollow positions are no longer locally stable and move to bridge sites (4 and 5). Position 5 is the most stable site, with an E_b value of -4.78 eV, a decrease of 0.34 eV with respect to the same position on the pure Pt_{38} cluster.

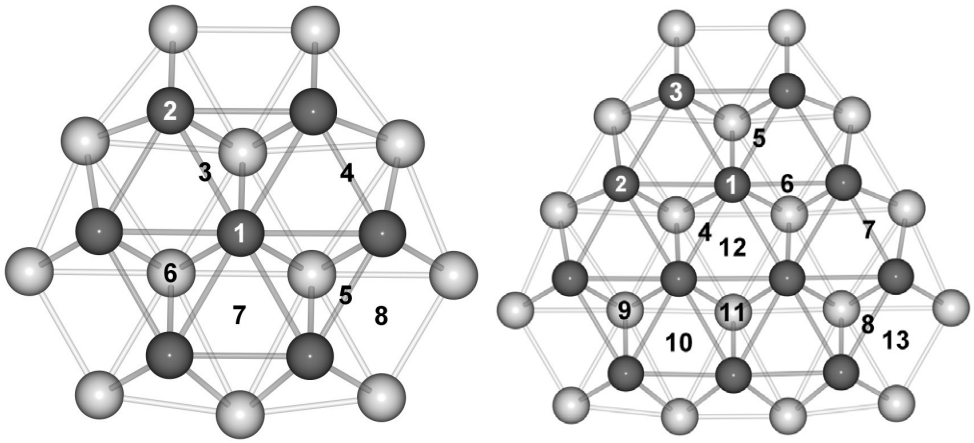

Figure 5.1: Top view of the surface (dark grey) and subsurface (light grey) metal atoms at a (111) facet sites on the 38 (left) and 79 (right) atom TO clusters.

Table 5.1: Calculated binding energies (E_b) for atomic and molecular oxygen on all non-symmetry equivalent sites of the 38-atom clusters, shown in Figure 5.1. Missing values are the result of oxygen migration to other sites during relaxation, as labelled. All energies are given in eV.

Site	Position	Pt_{38}–O	Pt_{38}–O_2	$Pt_{32}Ti_6$–O	$Pt_{32}Ti_6$–O_2
1	top	-4.17	-0.51	- [a]	- [b]
2	top	-4.48	-0.77	-4.16	-0.59
3	bridge	- [b]	-1.66	- [a]	-0.57
4	bridge	-4.72	-1.67	-4.39	-1.02
5	bridge	-5.12	-2.01	-4.78	-1.75
6	*hcp*	-5.21	-1.84	- [c]	-0.73
7	*fcc*	-5.12	-1.80	- [a]	-0.37
8	4-fold hollow	-4.79	- [c]	-4.25	- [c]

[a] Adsorbate migration to position 4.
[b] Adsorbate migration to position 6.
[c] Adsorbate migration to position 5.

For O_2 adsorption, position 5, the edge-bridge site between (111) and (100) facets is most stable on both Pt_{38} and $Pt_{32}Ti_6$, E_b values are -2.01 and -1.75 eV, respectively. Hollow positions 6 and 7 are next in stability, -1.84 and -1.80 eV, on Pt_{38}, while on $Pt_{32}Ti_6$ other bridge positions are more favourable. Edge-bridge sites are also found to be positions of favourable O_2 bonding in other studies. Step sites on Pt(111) surfaces have been reported to result in particularly stable oxygen bonding. [197, 198] Furthermore, studies of Pt TO clusters has revealed favourable bonding at the edge-bridge sites. [199] Calculations on the Pt(100) surface have favoured bonding to bridge sites, in line with the results presented here. [200] As with the previous OH and CO adsorption studies [201, 202], weaker bonding for O_2 and O is calculated for the bimetallic Ti@Pt cluster when compared with the pure Pt cluster.

It was expected that oxygen dissociation will occur preferentially at sites with higher E_b values, where oxygen is most likely to adsorb on the surface of the cluster. Due to the small size of the cluster, it would be relatively easy for molecular oxygen to dissociate and migrate to any of the other seven sites, or an equivalent site in a different location on the surface. It was therefore assumed that dissociation will also likely result in atomic oxygen being adsorbed on the most energetically favourable sites. The energetic ordering of adsorption for molecular oxygen was similar to that of atomic oxygen, making the proposed dissociation pathways relatively straightforward.

The most stable sites, the edge site 5, as well as hollow sites 6 and 7 were studied. For each pathway, O_2 dissociation proceeds from one site to an adjacent position at an equivalent site (e.g. O_2 bound to position 5 dissociates to atomic oxygen bound to separate 5 sites). Data for each dissociation pathway are presented in Table 5.2. In each case, distortion energies of the cluster and O_2 at each step of the dissociation pathway are presented.

5.3.2.2 Distortion and Interaction Energies

Representations of the minimised geometries for the IS, TS and FS can be found in Figures 5.2–5.7. Studies of the IS show that the distortion energy values ($\Delta E(Pt_{n-m}Ti_m)$) associated with Pt_{38} clusters are higher than those for the $Pt_{32}Ti_6$ clusters. The distortion energies associ-

Table 5.2: Values for cluster ($\Delta E(Pt_{n-m}Ti_m)$) and oxygen ($\Delta E(O_2)$) deformation energies, root mean squared displacements (RMSD) of the cluster, interaction energies (E_{int}), binding energies (E_b) and barriers for O_2 dissociation ($\Delta E^{\neq}$). The ratios of distortion energy to RMSD ($\Delta E(Pt_{n-m}Ti_m)/RMSD$) are also presented. Site numbering is introduced in Figure 5.1. All energy values are given in eV, RMSD in Å.

Initial State	$\Delta E(Pt_{n-m}Ti_m)$	RMSD	$\Delta E(Pt_{n-m}Ti_m)/RMSD$	$\Delta E(O_2)$	E_{int}	E_b	$\Delta E^{\neq}$
Pt_{38}-5	0.42	0.09	4.67	0.58	-3.02	-2.01	
$Pt_{32}Ti_6$-5	0.37	0.07	5.29	0.49	-2.62	-1.76	
Pt_{38}-6	0.45	0.19	2.37	1.05	-3.34	-1.84	
$Pt_{32}Ti_6$-6	0.12	0.03	4.00	0.73	-1.59	-0.74	
Pt_{38}-7	0.53	0.19	2.79	1.36	-3.68	-1.79	
$Pt_{32}Ti_6$-7	0.34	0.06	5.67	0.69	-1.40	-0.38	
Pt(111) Slab	0.17*	0.03	5.67*	0.64	-1.67	-0.86	
Transition State							
Pt_{38}-5	0.39	0.08	4.88	4.64	-6.72	-1.68	0.32
$Pt_{32}Ti_6$-5	0.62	0.10	6.20	4.89	-6.62	-1.11	0.62
Pt_{38}-6	0.48	0.19	2.53	2.75	-5.03	-1.80	0.04
$Pt_{32}Ti_6$-6	0.80	0.11	7.27	2.69	-3.90	-0.41	0.34
Pt_{38}-7	0.54	0.19	2.84	1.83	-4.16	-1.79	0.00
$Pt_{32}Ti_6$-7	0.44	0.07	6.29	5.29	-5.50	0.24	0.62
Pt(111) Slab	0.25*	0.05	5.00*	5.72	-6.41	-0.43	0.45
Final State							
Pt_{38}-5	0.58	0.10	5.80	6.27	-9.87	-3.02	
$Pt_{32}Ti_6$-5	0.35	0.06	5.83	6.36	-9.06	-2.36	
Pt_{38}-6	0.65	0.11	5.91	6.29	-10.32	-3.39	
$Pt_{32}Ti_6$-6	0.38	0.06	6.33	6.79	-10.13	-2.95	
Pt_{38}-7	0.92	0.22	4.18	6.28	-10.07	-2.87	
$Pt_{32}Ti_6$-7	0.86	0.10	8.60	6.79	-10.17	-2.51	
Pt(111) Slab	0.39*	0.05	7.80*	6.34	-9.12	-2.39	

* Values for $\Delta E(Pt_{surf})$.

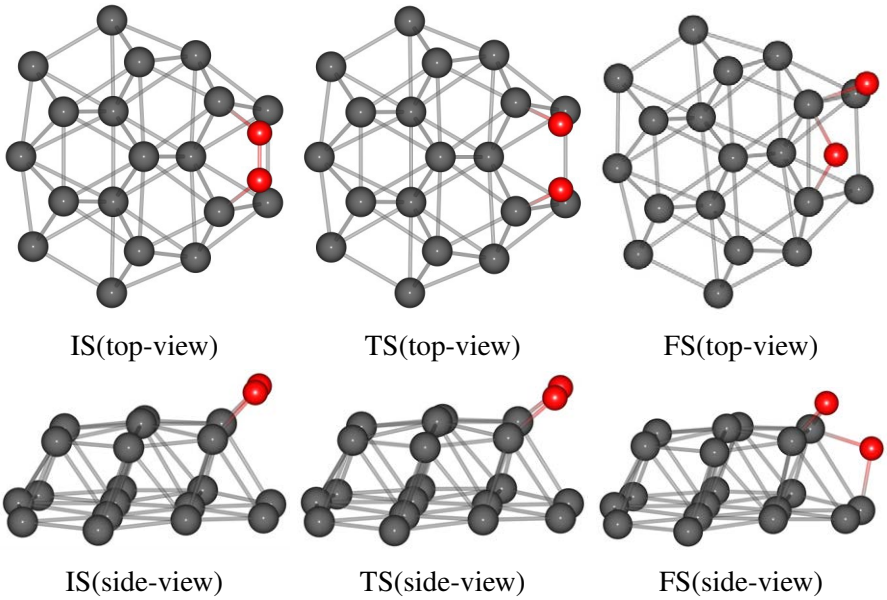

Figure 5.2: IS, TS and FS structures for O_2 dissociation on Pt_{38}, when O_2 is located at position 5. Only the top two layers of metal atoms are shown.

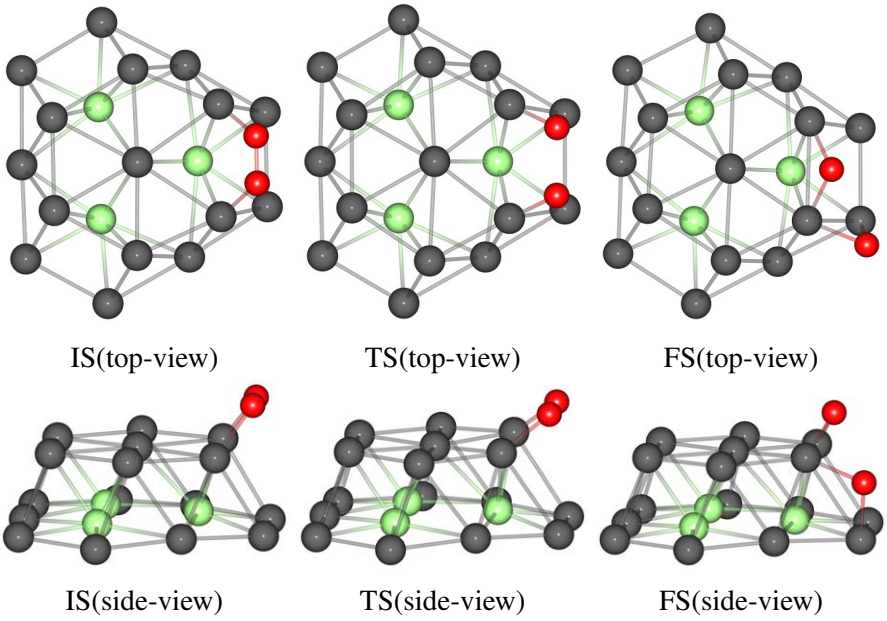

Figure 5.3: IS, TS and FS structures for O_2 dissociation on $Pt_{32}Ti_6$, when O_2 is located at position 5. Only the top two layers of metal atoms are shown.

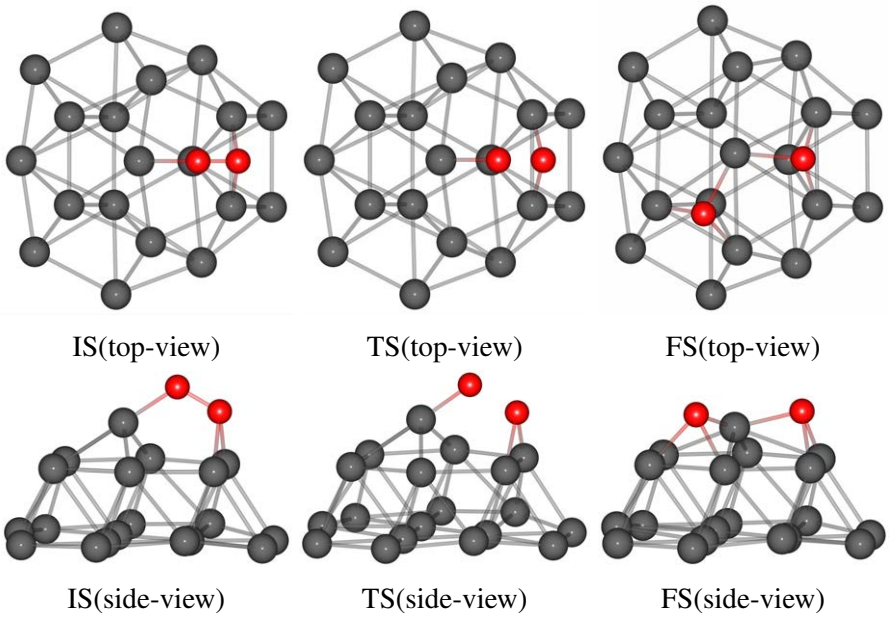

Figure 5.4: IS, TS and FS structures for O_2 dissociation on Pt_{38}, when O_2 is located at position 6. Only the top two layers of metal atoms are shown.

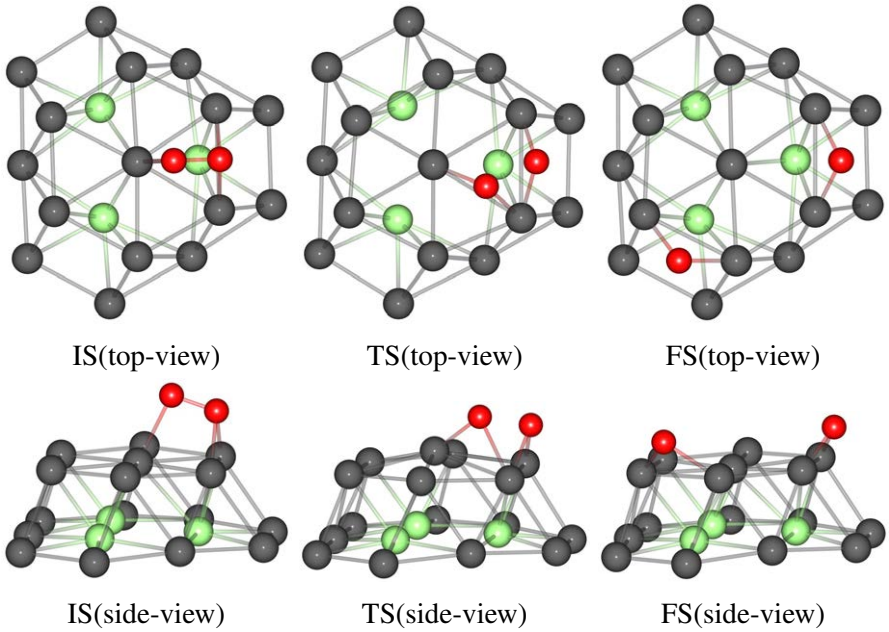

Figure 5.5: IS, TS and FS structures for O_2 dissociation on $Pt_{32}Ti_6$, when O_2 is located at position 6. Only the top two layers of metal atoms are shown.

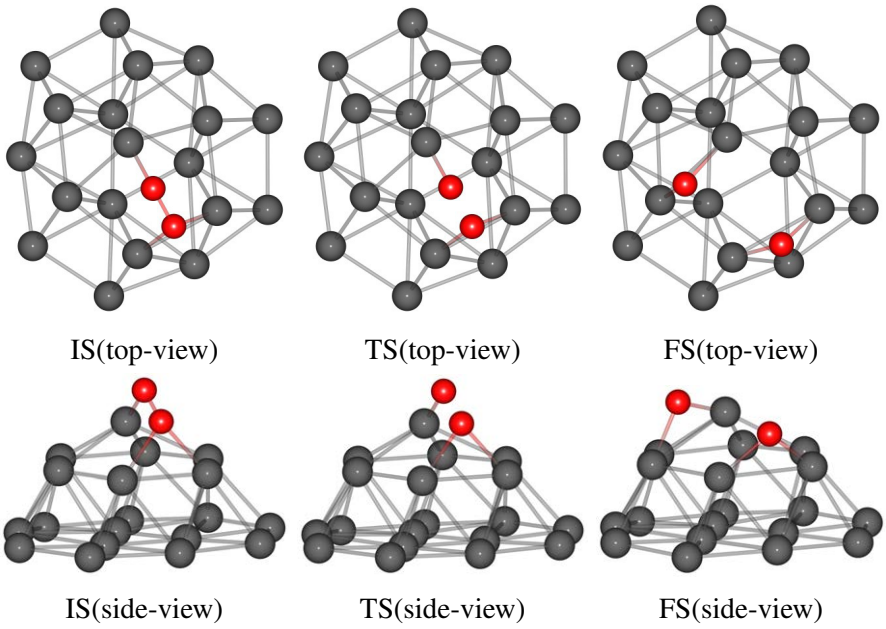

Figure 5.6: IS, TS and FS structures for O_2 dissociation on Pt_{38}, when O_2 is located at position 7. Only the top two layers of metal atoms are shown.

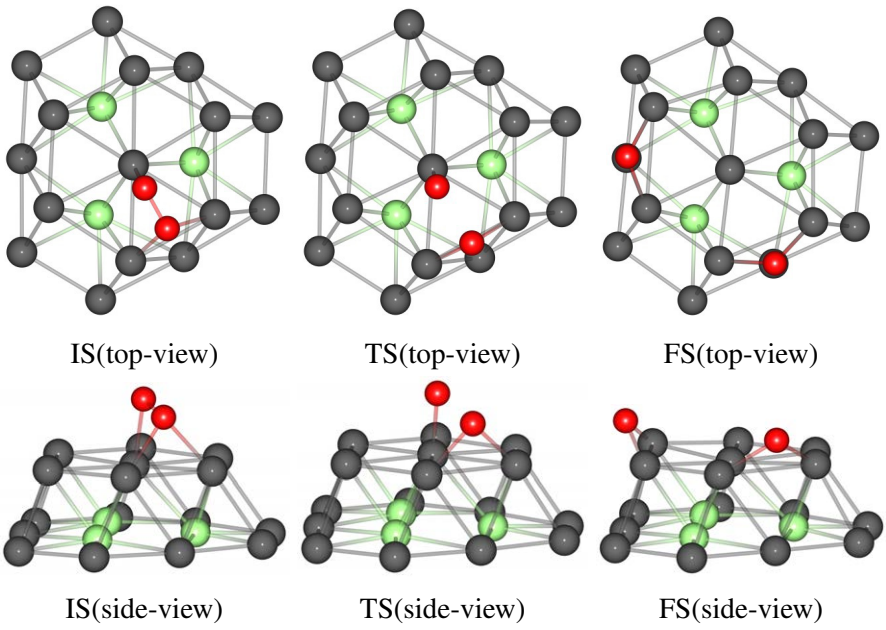

Figure 5.7: IS, TS and FS structures for O_2 dissociation on $Pt_{32}Ti_6$, when O_2 is located at position 7. Only the top two layers of metal atoms are shown.

ated with both clusters are also found to be greater than those for the pure slab, in most cases. O_2 distortion energies ($\Delta E(O_2)$) show greater distortions of the O_2 molecule adsorbed on Pt_{38} compared with $Pt_{32}Ti_6$ for the IS structures. However, as mentioned previously, larger in magnitude adsorption energies are observed for the Pt_{38} clusters than for the $Pt_{32}Ti_6$ clusters. This suggests that the increased interaction energy of O_2 with the Pt surface of the pure cluster, overcomes the distortion energies to a greater extent than for the bimetallic clusters. Furthermore, the stronger Pt–O binding will likely aid in distorting both oxygen and the Pt_{38} cluster to a greater degree than the $Pt_{32}Ti_6$ cluster. $\Delta E(O_2)$ values calculated for the bulk system are found to be greater than those on the (100) facet of both clusters but these are smaller than on the (111) facet. The greater distortions on the cluster (111) facets than those on the slab probably result from the increased binding energies on the clusters.

Distortion energies in the TS structures show, in general, that there is a greater distortion energy associated with the $Pt_{32}Ti_6$ clusters. The one exception is where distortion occurs on site 7 of the $Pt_{32}Ti_6$ cluster, because different types of TS structures are possible. In this case, a "straight" dissociation pathway is located over the central atop position (site 1) of the $Pt_{32}Ti_6$ cluster. For dissociation on site 6, however, a more curved pathway is preferred, avoiding the atop position and instead progressing over the hollow sites of the alloyed cluster. However, the fact that the distortion energies for the $Pt_{32}Ti_6$ clusters are significantly higher than for the Pt_{38} clusters suggests that the presence of the Ti core in the alloyed cluster stabilises (makes more rigid) the Pt shell. Nevertheless, the alloyed cluster is still distorted by the adsorbate. In all cases, the cluster distortion energies are greater than that of the slab, suggesting that the slab is significantly harder to distort than both clusters at the TS, leading to little change in the slab structure. Similarly to IS, data for the FS show the distortion energies associated with the Pt_{38} clusters are higher than those for the alloyed $Pt_{32}Ti_6$ clusters in all cases. Once again, there are generally greater distortion energies associated with the clusters than the slab. This was found to be the case also for positions 5 and 6.

For the pure Pt clusters, the IS and TS have similar distortion energies and the FS is found to have slightly greater distortion energies. This is consistent with atomic oxygen's having a

greater effect on the Pt surface than the single O_2 molecule. For the $Pt_{32}Ti_6$ clusters, it is found that the TS generally has greater distortion energies than the IS or FS. The exception to this is dissociation occurring at position 7, where a relatively small distortion energy is found at the TS compared to a relatively high energy at the FS. In summary, this energetic ordering suggests that at sites 5 and 6 greater distortions occur at the TS, not the FS as with the pure Pt clusters.

RMSD of the metal atoms are also listed in Table 5.2 but it is important to note that O_2 distortions are not accounted for. These indicate the geometric distortion of the metal particle as a result of adsorption of the O_2 molecule. Data on distortions to specific facets of the cluster are described later. For RMSD analysis, the geometry of the distorted cluster, with O_2 removed, is compared to the geometry of the relaxed gas phase cluster, with higher values suggesting greater distortion. For the Pt_{38} clusters, there is a larger RMSD associated with O_2 adsorption on the (111) facet, compared to the (100) facet, an average of 0.19 and 0.09 Å, respectively. For the $Pt_{32}Ti_6$ clusters, there is less difference between O_2 adsorption on the (111) and (100) facets, 0.03 – 0.11 Å vs. 0.06 – 0.10 Å. Furthermore, it is found that smaller RMSD values for the bimetallic clusters can lead to greater distortion energies than for the pure Pt clusters. This shows that even though there is less overall distortion, there is a greater energetic cost associated with it for the $Pt_{32}Ti_6$ clusters. This is expected, as the Pt_2 dimer binding energy is found to be -4.11 eV, which is destabilised over both the PtTi and Ti_2 dimers, -6.08 and -5.34 eV, respectively. Compared with the values calculated for the bulk system ($<$0.05 Å), there are significantly greater RMSD values associated with the Pt_{38} clusters and marginally greater values for the $Pt_{32}Ti_6$ cluster.

$\Delta E(Pt_{n-m}Ti_m)/RMSD$ has been calculated, showing the energy needed to achieve RMSD of 1.00 Å. An average of 1.71, 3.17 and 1.63 eV $Å^{-1}$ more energy is required to distort the $Pt_{32}Ti_6$ cluster than the Pt_{38} cluster at the IS, TS and FS, respectively. This demonstrates the significant energy barriers that need to be overcome in order to distort the $Pt_{32}Ti_6$ cluster compared to the Pt_{38} cluster.

A high dissociation barrier ($\Delta E^{\neq}$) is found for site 5, on the (100) facet of the $Pt_{32}Ti_6$ cluster, 0.62 eV, this being approximately twice that of the pure Pt_{38} cluster, 0.32 eV (Table 5.2). When

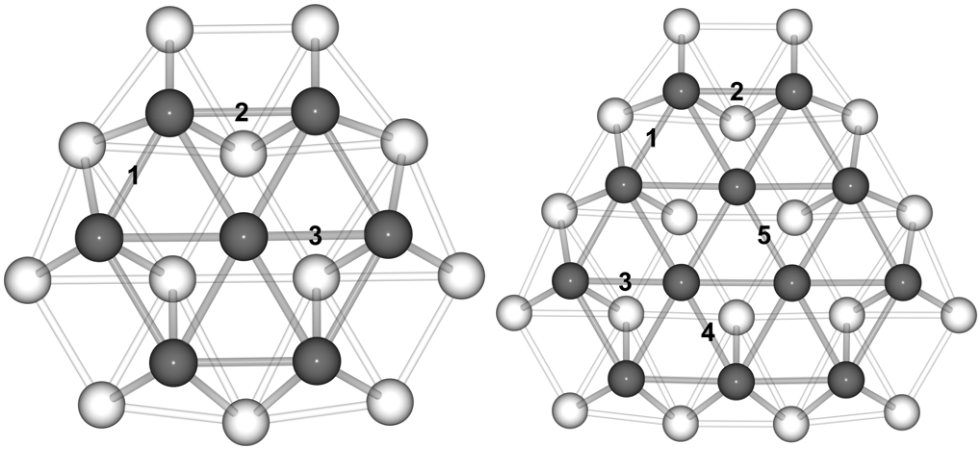

Figure 5.8: Bond numbering on the 38 (left) and 79-atom (right) TO clusters.

considering the (111) facet of the $Pt_{32}Ti_6$ cluster, the dissociation barriers for sites 7 and 5 are equal, 0.62 eV, while for site 6 the barrier, 0.34 eV, is about half that of the other two sites. The Pt_{38} cluster is found to exhibit barrier-free dissociation on the (111) facet, which dramatically differs from the 0.45 eV barrier found on the Pt(111) slab. On the (100) facet of the Pt_{38} cluster (site 5), comparable dissociation barriers are found to site 6 on the $Pt_{32}Ti_6$ cluster.

5.3.2.3 Geometric Analysis

Analysis of the system geometries can be found in Table 5.3. O–O bonds, in general, are shorter for the IS adsorption on the (100) facet. However, at the TS, generally shorter bond lengths are associated with the (111) facet. When studying the average Pt–O bond length, as the system moves from the IS to the TS, the average bond length gets smaller. The average Pt–Pt bond lengths are found to be 2.65, 2.70 and 2.70 Å for bond types 1 to 3, respectively for the bare Pt_{38} cluster, while for the bare $Pt_{32}Ti_6$ cluster, the corresponding Pt–Pt bond lengths are slightly larger, 2.69, 2.71 and 2.74 Å for sites 1 to 3, respectively.

Once oxygen is adsorbed on the (100) facet of the Pt_{38} cluster, significant elongation of bond type 2 by up to 0.54 Å is observed, although there is less overall distortion of the cluster geometry. Following oxygen adsorption on the (100) facet, the average distortion of the Pt–Pt bonds calculated from the data in Table 5.3 is 0.43, 0.53 and 0.78 Å for sites 5, 6 and 7 on the Pt_{38} cluster, respectively. When O_2 is adsorbed on the (111) facet, there is a slight elongation of

Table 5.3: Data for oxygen - oxygen distances (O–O), average platinum - oxygen bond lengths (Pt–O), average platinum - platinum bond lengths (Pt–Pt) for specific bonds defined in Figure 5.8 and distances from the octahedral core to the central (111) atom in the y-direction (Pt-X^{centre}). Average Pt–Pt bond lengths are calculated for those atoms directly below the adsorbed O_2 molecule. The type of the bond is shown in brackets according to Figure 5.8.

	O–O			Pt–O			Pt–Pt			Pt-X^{centre}		
	IS	TS	FS	IS	TS	FS	IS	TS	FS	IS	TS	FS
Pt_{38}-5	1.39	1.92	2.89	1.95	1.82	1.95	3.24[2]	3.20[2]	2.94[2]	-	-	-
$Pt_{32}Ti_6$-5	1.37	1.96	3.02	1.98	1.83	1.98	3.26[2]	3.28[2]	2.93[2]	-	-	-
Pt_{38}-6	1.45	1.66	3.32	2.07	2.00	2.07	2.64[2]	2.65[2]	2.69[2]	3.27	3.26	2.95
							3.43[3]	3.44[3]	2.93[3]			
$Pt_{32}Ti_6$-6	1.41	1.66	5.43	2.21	2.13	1.98	2.92[2]	3.02[2]	2.94[2]	2.19	2.72	2.08
							2.74[3]	3.04[3]				
Pt_{38}-7	1.49	1.55	3.42	2.05	2.02	1.94	2.68[1]	2.69[1]	2.95[1]	3.27	3.26	3.35
							3.54[3]	3.55[3]	2.98[3]			
$Pt_{32}Ti_6$-7	1.40	2.03	5.47	2.19	1.99	1.95	2.78[1]	2.93[1]	3.06[1]	2.12	2.23	2.11
							2.78[3]	2.79[3]				

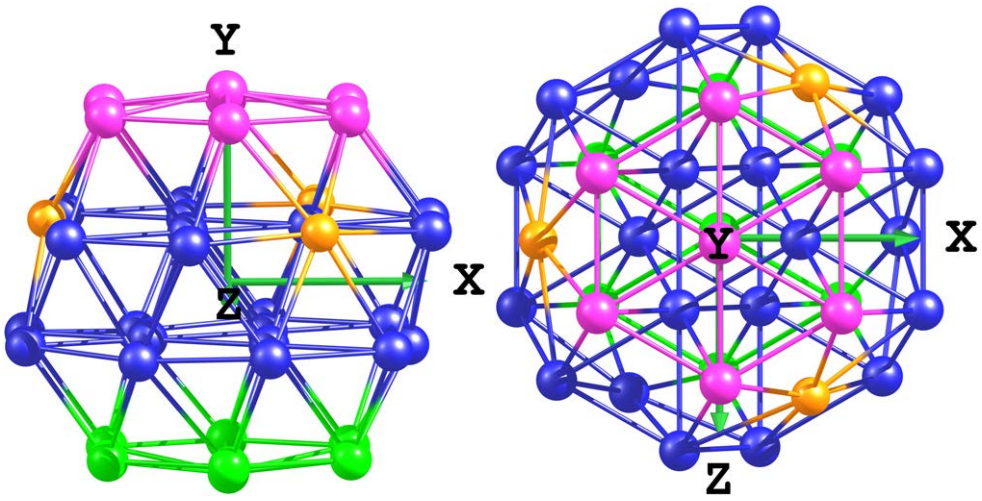

Figure 5.9: Splitting the cluster into top and bottom portions to analyse relevant movement of the plane defined to measure distortions. Pink atoms are at the top of the cluster, whilst green are at the bottom. The plane passes through the centre of the adjoining (111) surfaces to that at which the O_2 is adsorbed, in this case depicted by the orange atoms.

bond type 1 by up to 0.29 Å, although not as much as for bond type 3 by up to 0.85 Å, which is significantly elongated. There is generally a slight contraction in the bond length of type 2 by up to 0.06 Å. This suggests that the majority of the distortion that occurs when O_2 is adsorbed on the (111) facet of the Pt_{38} cluster is due to changes in the bond length of type 3, bonding to the central (111) atom. For the $Pt_{32}Ti_6$ cluster significant elongation is observed of bond type 2 by up to 0.57 Å, when O_2 is adsorbed on site 5 of the (100) facet. However, there is considerably less distortion of the other bond types when O_2 is adsorbed on the (111) facet, the maximum distortion observed being $\leq$0.37 Å.

Pt-X^{centre} values were only calculated for dissociations on the (111) facet. From the values presented, there are few well-defined trends when comparing initial, transition and final states. However, the point of these values is to demonstrate the differences between the Pt_{38} and $Pt_{32}Ti_6$ clusters. Pt-X^{centre} was calculated by defining a plane through the cluster, parallel to the (111) facet on which oxygen is adsorbed and then measuring Pt distortions along the y-axis from that plane. The plane passes through the central atoms of the (111) surfaces surrounding the facet on which the O_2 is adsorbed, as shown in Figure 5.9.

Following O_2 adsorption, Pt-X^{centre} distances are presented in Table 5.4. This reveals small distortions, $\leq$ 0.14 and $\leq$ 0.08 Å for the Pt_{38} and $Pt_{32}Ti_6$ clusters, respectively, measuring

Table 5.4: Pt-X^{centre} distances relative to those of the bare clusters. Positive values show atoms being drawn out of the plane, leading to elongation of the cluster in the y-direction, whilst negative values show compression of the cluster in the y-direction. All values are given in Å.

	IS		TS		FS	
	Top	Bottom	Top	Bottom	Top	Bottom
Pt_{38}-6	0.83	0.13	0.82	0.14	0.51	0.14
$Pt_{32}Ti_6$-6	-0.12	0.07	0.42	0.04	-0.23	0.08
Pt_{38}-7	0.83	0.00	0.82	0.00	0.91	0.00
$Pt_{32}Ti_6$-7	-0.18	0.03	-0.07	0.04	-0.19	0.02

distances from the plane to the bottom of the cluster. More significant changes are seen at the top of the cluster, ≤ 0.91 and ≤ 0.42 Å for the Pt_{38} an $Pt_{32}Ti_6$ clusters, respectively. Furthermore, it is found that there is considerably stronger distortion of the Pt_{38} cluster, with the atop central (111) atom being pulled out of the plane. The relationship between Pt-X^{centre} and distortion barriers can be seen in Figure 5.10 for the IS and TS.

5.3.2.4 Bader Charge Analysis

Previously studied charge transfer between Pt and Ti atoms within alloyed systems [202] is discussed in Chapter 4. For reference, the electronegativities of Pt, Ti and O are 2.28, 1.54 and 3.44 on the Pauling scale, respectively. For the bare clusters, there is significant electron donation from Ti to Pt, which likely results in the strong core-shell interactions that stabilise the Pt surface. The average charges for the $Pt_{32}Ti_6$ cluster are found to be -0.36 and +1.94 |e| for Pt and Ti, respectively. Following this, an analysis was performed of the effect of the adsorbate on the atomic charges, as shown in Table 5.5.

When O_2 is adsorbed on the surface of the pure Pt_{38} cluster, the Pt atoms on which the oxygen is adsorbed have a positive charge +0.22 — +0.31 |e|. It is generally found on Pt_{38} and $Pt_{32}Ti_6$ clusters, that the Pt becomes more positively charged as the system moves from the initial to final states, while the O atoms become more negatively charged at the same time. Furthermore, more positive Pt charge values are observed for O_2 adsorption on the (100) facet. This charge transfer is found to be comparable between the slab and cluster models. In the case of the $Pt_{32}Ti_6$ cluster Pt has positive and negative charges depending on the state of the system,

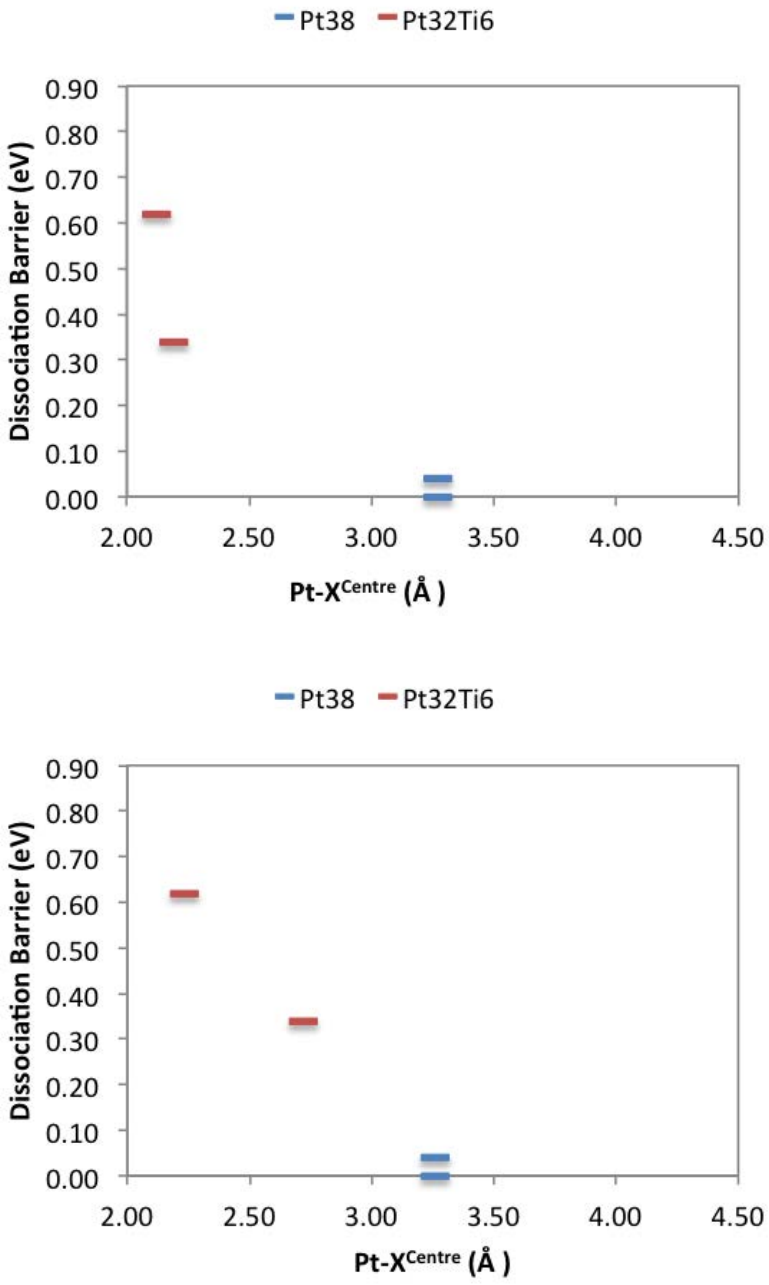

Figure 5.10: Plot of Pt-X^{centre} against dissociation barrier at the TS for 38-atom clusters.

Table 5.5: Average charges (|e|) of the initial (IS), transition (TS) and final (FS) state structures of O_2 dissociation on the 38-atom clusters.

	Pt Charges[a]			Ti Charges[b]			O Charges		
	IS	TS	FS	IS	TS	FS	IS	TS	FS
Pt_{38}-5	0.31	0.46	0.45	-	-	-	-0.33	-0.51	-0.74
$Pt_{32}Ti_6$-5	0.04	0.22	0.21	1.97	1.97	1.88	-0.34	-0.55	-0.75
Pt_{38}-6	0.22	0.29	0.28	-	-	-	-0.39	-0.47	-0.76
$Pt_{32}Ti_6$-6	-0.22	0.02	0.11	1.95	1.87	1.94	-0.38	-0.50	-0.79
Pt_{38}-7	0.25	0.26	0.33	-	-	-	-0.43	-0.45	-0.74
$Pt_{32}Ti_6$-7	-0.23	-0.10	0.09	1.95	1.93	1.94	-0.37	-0.58	-0.76

[a]Pt atoms interacting directly with O atoms.
[b]Ti atoms interacting directly with O bound Pt atoms.

slightly positive (+0.04 |e|) when O_2 is adsorbed on the (100) facet and negative on the (111) facet (-0.22 — -0.23 |e|). At the same time, charges on the Ti atoms, which are remote from the adsorbates, do not change notably. They also do not change when the system progresses from IS to FS. Not surprisingly, the charges on the oxygen atoms get significantly more negative as the system progresses from the initial to the final states. This charge seems unaffected by the site at which oxygen is adsorbed, or whether it is the pure or alloyed cluster. Hence, one can conclude that O atoms have local effects on the withdrawal of electron density from the closest Pt atoms only. When O_2 is adsorbed on the (111) facet of the alloyed $Pt_{32}Ti_6$ nanoparticle, Pt is found to have a negative charge at the initial state and a positive charge at the final state, while on the (100) facet, the Pt atoms are positive for all states.

5.3.2.5 Conclusions

There are several conclusions that can be drawn from the 38-atom system. It is evident that there are significant differences in the Pt_{38} and $Pt_{32}Ti_6$ systems, not only in adsorption energies but also in the way dissociation proceeds. Larger dissociation barriers are observed for the $Pt_{32}Ti_6$ system. This is to be expected because oxygen is more weakly adsorbed onto the Pt surface of the alloyed cluster, hence the O–O bond is less activated and it takes more energy to dissociate the O_2 molecule. Furthermore, for the Pt_{38} cluster, a higher dissociation barrier is observed for the (100) facet whereas for $Pt_{32}Ti_6$ there are similar barriers on the (111) and (100)

facets. Once again, this coincides with the larger values of adsorption energies associated with the (111) facet for the Pt_{38} system and the (100) facet for the $Pt_{32}Ti_6$ system.

Finally, barrier-free dissociation is observed on the (111) facet of the Pt_{38} cluster, which appears to result from significant distortions of the facet. There are greater energetic costs associated with distorting the $Pt_{32}Ti_6$ cluster, compared with the Pt_{38} cluster (Table 5.2), although according to the cluster geometries there is greater distortion of the Pt_{38} cluster. This suggests that the presence of the octahedral Ti core in the $Pt_{32}Ti_6$ cluster stabilises the Pt shell and makes the structure more rigid, while the Pt_{38} nanoparticle is more flexible and the surface Pt atoms become more easily distorted, hence more reactive. When compared to the Pt(111) bulk system, the barrier for O_2 dissociation is found to be 0.45 eV; however, very little distortion of the (111) surface is observed. This supports the suggestion that it is the distortion of the (111) facet on the cluster that leads to barrier-free dissociation.

5.3.3 79-Atom Clusters

5.3.3.1 Oxygen Adsorption

Following the calculations on 38-atom clusters, studies progressed to larger 79-atom TO clusters, considering the pure Pt_{79} and core-shell $Pt_{60}Ti_{19}$ systems. On the surface of the 79-atom TO cluster there are 13 non-symmetry equivalent sites for a pure surface composition, depicted in Figure 5.1. As with the 38-atom clusters, studies of these 13 sites were performed, looking at atomic and molecular oxygen. Binding energies are listed in Table 5.6.

For the pure Pt_{79} cluster, the hollow site on the (111) facet is no longer as favourable as the edge-bridge sites on the (100) facet for O_2 and O adsorption. However, the site resulting in strongest bonding is the edge-bridge site of the (111) facet, labelled as site 7. For the $Pt_{60}Ti_{19}$ cluster, in all cases, the edge-bridge site on the (100) facet results in strongest bonding. This was also the case for $Pt_{32}Ti_6$.

In a similar fashion to the 38-atom system, O_2 dissociation has been investigated at various sites on the (111) and (100) facets of the 79-atom clusters (8, 9, 10 and 11 in Figure 5.1).

Table 5.6: Calculated binding (E_b) energies for atomic and molecular oxygen on the various sites of the 79-atom clusters. Values which have not been presented are the result of oxygen migration to other sites during relaxation, as labelled. All energies are given in eV.

Site	Position	Pt_{79}–O	Pt_{79}–O_2	$Pt_{60}Ti_{19}$–O	$Pt_{60}Ti_{19}$–O_2
1	top	-[a]	-[b]	-2.69	-[a]
2	top	-[c]	-0.41	-[c]	-0.41
3	top	-4.36	-0.71	-4.24	-[d]
4	bridge	-[e]	-1.07	-[f]	-0.09
5	bridge	-[g]	-1.45	-[c]	-0.77
6	bridge	-[g]	-1.21	-[c]	-0.68
7	bridge	-5.04	-1.83	-4.60	-1.15
8	bridge	-4.94	-1.81	-4.93	-1.85
9	*hcp*	-4.93	-1.13	-[d]	-0.71
10	*fcc*	-4.98	-1.39	-[c]	-0.69
11	*hcp*	-4.74	-0.99	-3.79	-0.63
12	*fcc*	-4.93	-0.88	-3.32	0.07
13	4-fold hollow	-4.83	-[d]	-4.56	-[d]

[a] Adsorbate migration to position 9.
[b] Adsorbate migration to position 5.
[c] Adsorbate migration to position 7.
[d] Adsorbate migration to position 8.
[e] Adsorbate migration to position 12.
[f] Adsorbate migration to position 11.
[g] Adsorbate migration to position 10.

Due to the increased size of the (111) facet, it is no longer beneficial to allow dissociation pathways from a certain site to an identical adjacent site, as this would span the entire facet. Following dissociation, any further barriers observed would be due to migration of the oxygen atoms over the surface, which was not the aim of this study. Therefore, for the 79-atom clusters, the pathways on the (111) facet terminate at the central site 12. As with the 38-atom clusters, dissociation on the edge-bridge site of the (100) facet proceeds from position 8 to two adjacent 8 sites.

The central positions on the (111) facet were also investigated, the hollow site 12 for the Pt_{79} cluster and site 4 on $Pt_{60}Ti_{19}$. However, relatively weak O_2 binding energies, particularly on the $Pt_{60}Ti_{19}$ cluster, are associated with these sites. Hence, finding TS for O_2 dissociation proved difficult on these sites. The terrace site is unlikely to be active for oxygen dissociation due to the weaker Pt–O interactions associated with this position. On the 79-atom clusters, the central three-fold hollow site is surrounded by more favourable edge hollow and bridge sites. This means that it is far more likely that O_2 dissociation will occur at the edge sites of the facet, where stronger Pt–O bonding is observed. Furthermore, low-coordinated edge sites are able to distort to a greater extent (see below) than the central three-fold hollow site, hence facilitating lower barriers to O_2 dissociation.

5.3.3.2 Distortion and Interaction Energies

Representations of the minimised geometries for the IS, TS and FS can be found in Figures 5.11–5.18. Table 5.7 shows distortion energies for the cluster and oxygen as well as interaction, binding energies and dissociation barriers. The IS studies revealed slightly greater energetic penalties (by an average of 0.11 eV) associated with distorting the Pt_{79} cluster compared to the $Pt_{60}Ti_{19}$ cluster. This same trend is observed for the FS, with greater distortion energies located for the Pt_{79} cluster. These trends were also found for the smaller 38-atom clusters. However, the trends for the TS structures differ from those for the 38-atom clusters. For the 79-atom clusters, sites 8 and 11 result in greater distortion energies associated with the alloyed $Pt_{60}Ti_{19}$, whilst for sites 9 and 10, greater distortion energies are associated with Pt_{79}.

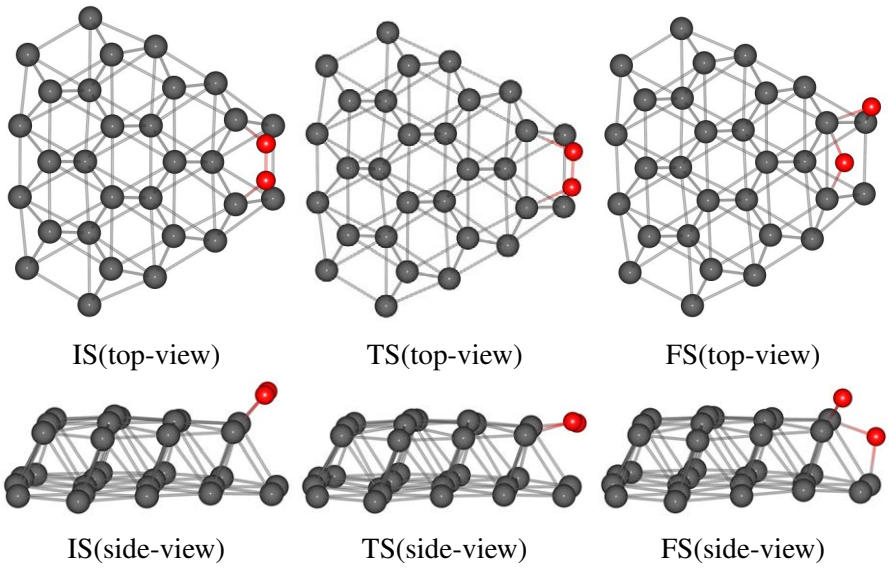

Figure 5.11: IS, TS and FS structures for O_2 dissociation on Pt_{79}, when O_2 is located at position 8. Only the top two layers of metal atoms are shown.

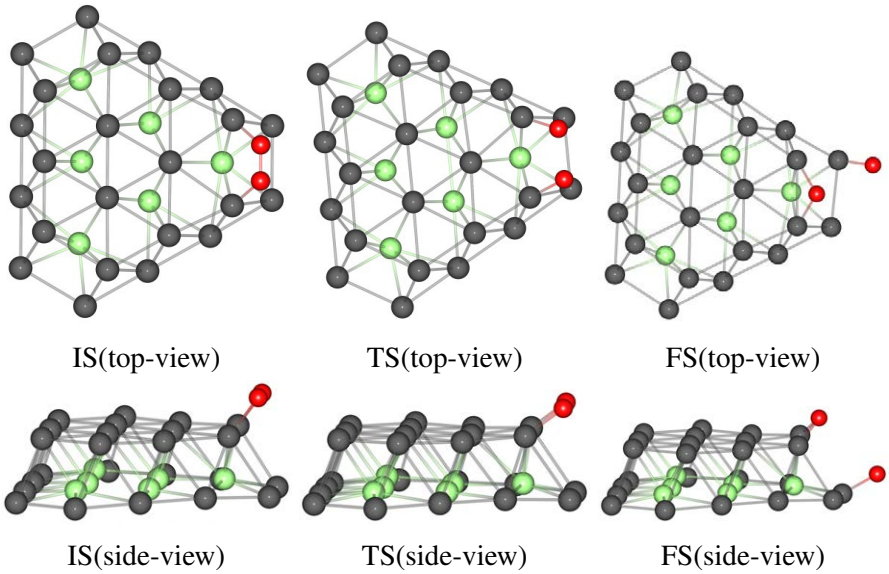

Figure 5.12: IS, TS and FS structures for O_2 dissociation on $Pt_{60}Ti_{19}$, when O_2 is located at position 8. Only the top two layers of metal atoms are shown.

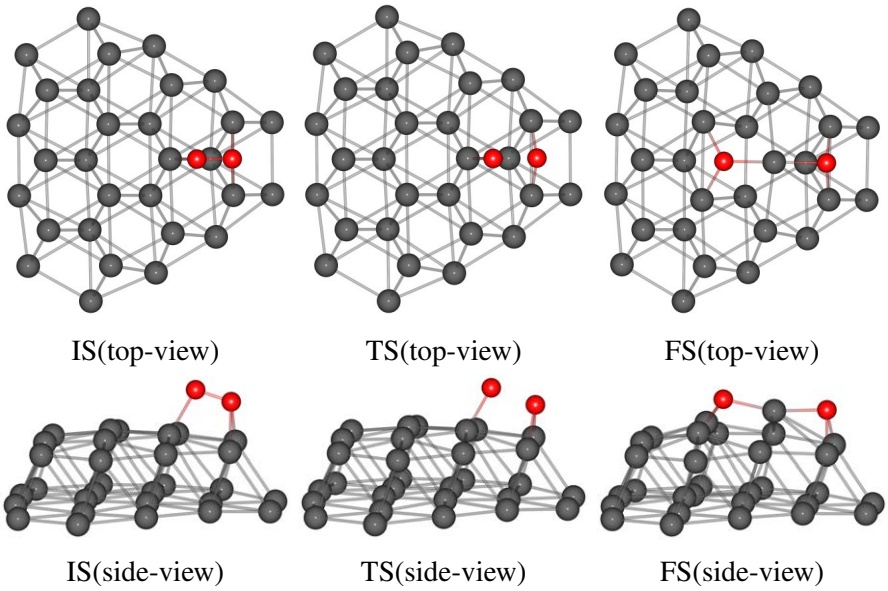

Figure 5.13: IS, TS and FS structures for O_2 dissociation on Pt_{79}, when O_2 is located at position 9. Only the top two layers of metal atoms are shown.

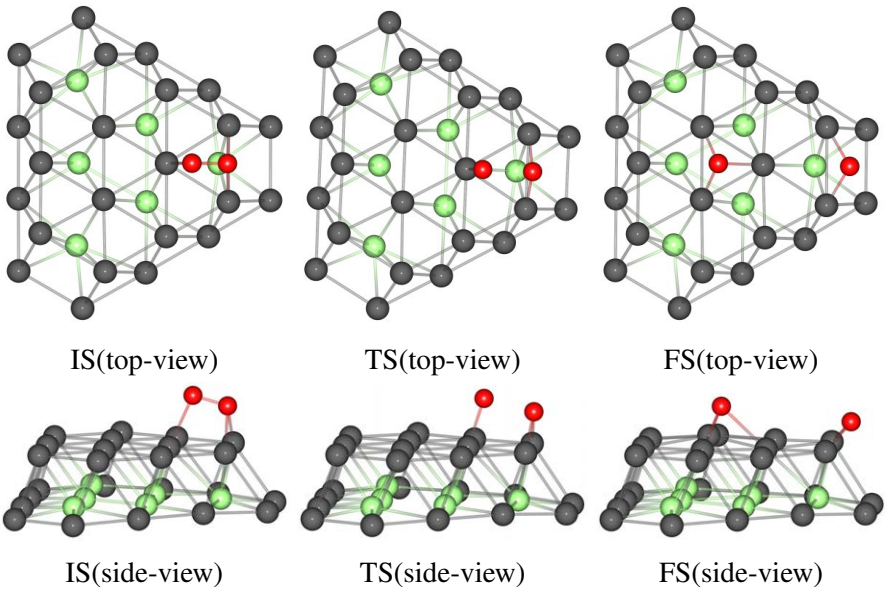

Figure 5.14: IS, TS and FS structures for O_2 dissociation on $Pt_{60}Ti_{19}$, when O_2 is located at position 9. Only the top two layers of metal atoms are shown.

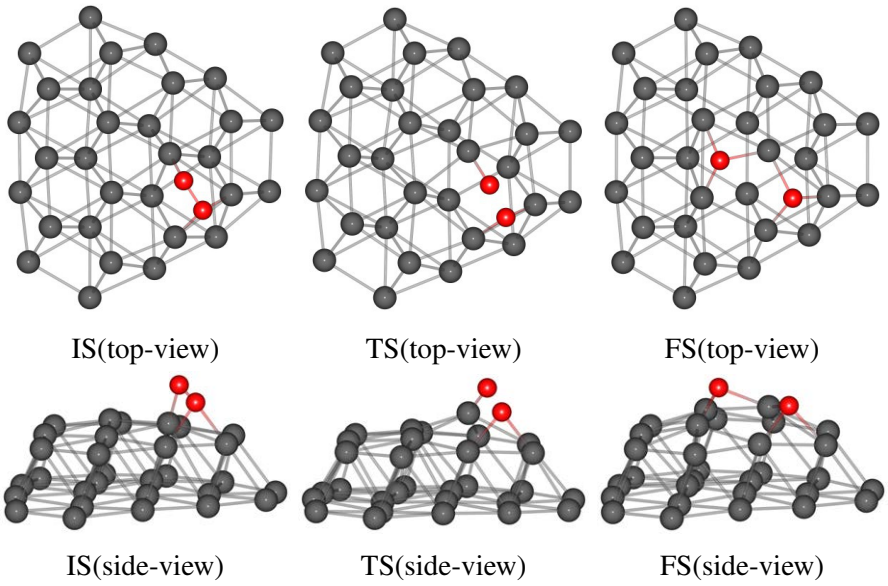

Figure 5.15: IS, TS and FS structures for O_2 dissociation on Pt_{79}, when O_2 is located at position 10. Only the top two layers of metal atoms are shown.

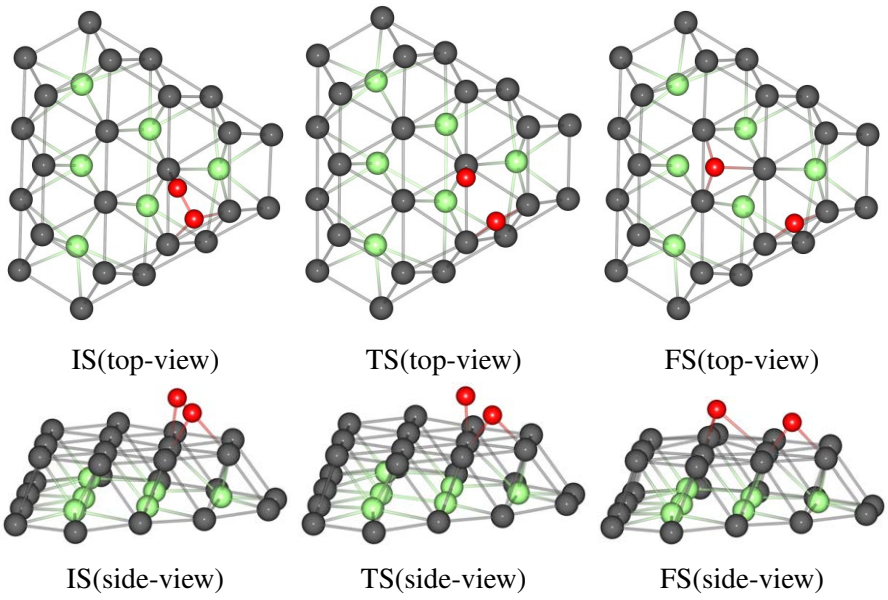

Figure 5.16: IS, TS and FS structures for O_2 dissociation on $Pt_{60}Ti_{19}$, when O_2 is located at position 10. Only the top two layers of metal atoms are shown.

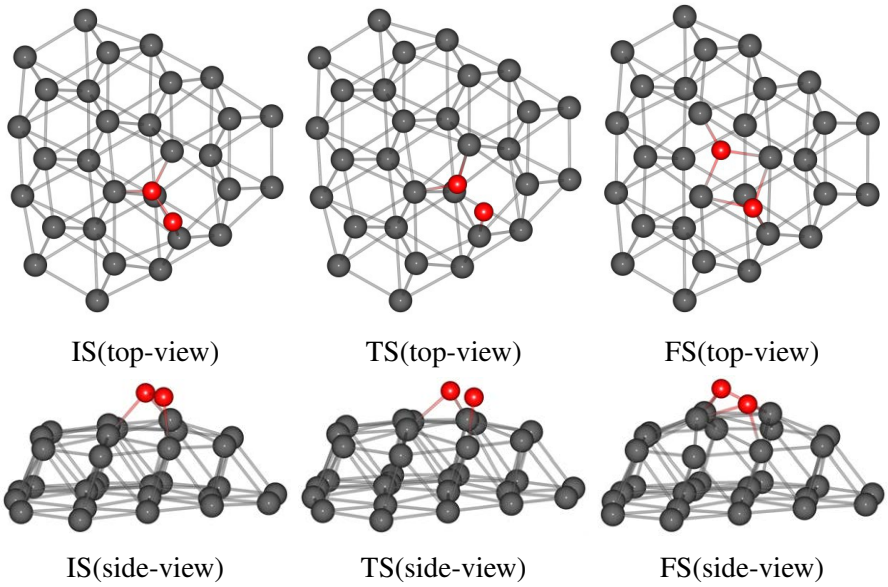

Figure 5.17: IS, TS and FS structures for O_2 dissociation on Pt_{79}, when O_2 is located at position 11. Only the top two layers of metal atoms are shown.

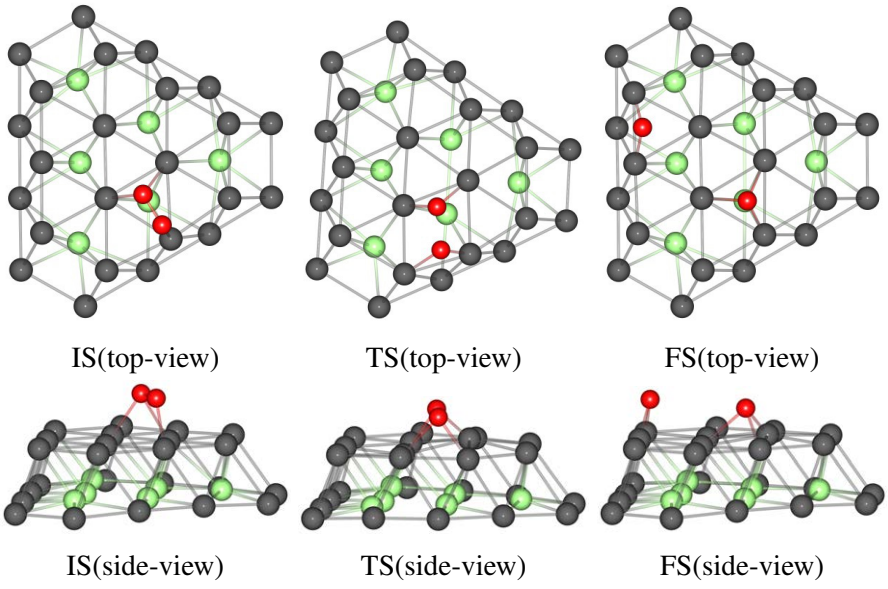

Figure 5.18: IS, TS and FS structures for O_2 dissociation on $Pt_{60}Ti_{19}$, when O_2 is located at position 11. Only the top two layers of metal atoms are shown.

As with Pt_{38}, there are greater distortion energies associated with the FS compared to the IS or TS. This once again suggests that the strongly interacting atomic oxygen has a greater ability to distort the Pt_{79} surface. For $Pt_{60}Ti_{19}$, there are greater distortion energies associated with the TS and FS compared to the IS. RMSD analysis demonstrates that for the Pt_{79} cluster, there is generally least structural distortion when O_2 is adsorbed on position 9 on the (111) facet. Although, there is little difference between positions 8 on the (100) facet and 9 on the (111) facet, there is significant distortion of Pt_{79} when oxygen is adsorbed on sites 10 and 11. As with the 38-atom clusters, there is greater distortion of the pure Pt clusters, compared to the alloyed ones. For $Pt_{60}Ti_{19}$, there is generally little difference between the RMSD for the cases when O_2 is adsorbed on (111) and (100) facets, suggesting again that Ti@Pt structures are more rigid as a result of the strong interaction between Ti core and Pt shell.

When comparing the (111) and (100) facets, it is found that the Pt_{79} cluster distortion energy associated with site 8 on the (100) facet is greater than that for site 9 on the (111) facet of the Pt_{79} IS structure (Table 5.7). However, the distortion energy becomes equal at the TS and is 0.95 eV greater on site 9 for the FS structure. For sites 10 and 11 on the (111) facet, the distortion energy is greater than for site 8 in all cases. The $\Delta E(Pt_{79})$ values for sites 9, 10 and 11 correlate with the differences between the dissociation barriers between sites. The smallest $\Delta E(Pt_{79})$ value is for site 9 which also has the largest barrier, whilst site 10 has the largest $\Delta E(Pt_{79})$ value and smallest barrier. There is less correlation between cluster distortion energies, surface sites and dissociation barriers for the $Pt_{60}Ti_{19}$ system.

$\Delta E(Pt_{n-m}Ti_m)/RMSD$ has also been calculated for the 79-atom clusters. An average of 1.62, 4.05 and 0.64 eV $Å^{-1}$ more energy is required to distort the $Pt_{60}Ti_{19}$ cluster than the Pt_{79} cluster at the IS, TS and FS, respectively. This further demonstrates the significant energy barriers that need to be overcome in order to distort the $Pt_{60}Ti_{19}$ cluster compared to the Pt_{79} cluster.

Oxygen distortion values for the IS are greater for the Pt_{79} system than the $Pt_{60}Ti_{19}$ system, in all cases. However, at the TS, significantly greater distortion energies are associated with the $Pt_{60}Ti_{19}$ clusters. This suggests that, initially, when oxygen is adsorbed on the surface of the Pt_{79}

Table 5.7: Cluster ($\Delta E(Pt_{n-m}Ti_m)$) and oxygen ($\Delta E(O_2)$) deformation energies, root mean squared displacements (RMSD) of the cluster, interaction energies (E_{int}), binding energies (E_b) of O_2 and barrier of O_2 dissociation ($\Delta E^{\neq}$). The ratios of distortion energy to RMSD ($\Delta E(Pt_{n-m}Ti_m)/RMSD$) are also presented. All energy values are given in eV, RMSD in Å.

Initial State	$\Delta E(Pt_{n-m}Ti_m)$	RMSD	$\Delta E(Pt_{n-m}Ti_m)/RMSD$	$\Delta E(O_2)$	E_{int}	E_b	$\Delta E^{\neq}$
Pt_{79}-8	0.31	0.08	3.88	0.58	-2.69	-1.80	
$Pt_{60}Ti_{19}$-8	0.27	0.05	5.40	0.49	-2.60	-1.84	
Pt_{79}-9	0.13	0.06	2.17	0.80	-2.05	-1.12	
$Pt_{60}Ti_{19}$-9	0.12	0.02	6.00	0.71	-1.51	-0.68	
Pt_{79}-10	0.37	0.10	7.10	0.95	-2.71	-1.40	
$Pt_{60}Ti_{19}$-10	0.32	0.05	6.40	0.65	-1.64	-0.67	
Pt_{79}-11	0.50	0.13	3.85	0.88	-2.37	-0.99	
$Pt_{60}Ti_{19}$-11	0.17	0.03	5.67	0.47	-1.23	-0.59	
Pt(111) Slab	0.17*	0.03	5.67*	0.64	-1.67	-0.86	
Transition State							
Pt_{79}-8	0.22	0.10	2.20	0.78	-2.46	-1.46	0.34
$Pt_{60}Ti_{19}$-8	0.33	0.05	6.60	5.31	-6.81	-1.18	0.66
Pt_{79}-9	0.22	0.08	2.75	3.69	-4.81	-0.91	0.21
$Pt_{60}Ti_{19}$-9	0.15	0.03	5.00	5.02	-5.25	-0.08	0.60
Pt_{79}-10	0.73	0.18	4.06	2.23	-4.45	-1.49	0.00
$Pt_{60}Ti_{19}$-10	0.45	0.06	7.50	5.41	-5.86	0.00	0.69
Pt_{79}-11	0.45	0.15	3.00	1.14	-2.54	-0.95	0.05
$Pt_{60}Ti_{19}$-11	0.91	0.10	9.10	3.08	-3.82	0.17	0.77
Pt(111) Slab	0.25*	0.05	5.00*	5.72	-6.41	-0.43	0.45
Final State							
Pt_{79}-8	0.43	0.09	4.78	6.33	-9.50	-2.74	
$Pt_{60}Ti_{19}$-8	0.33	0.05	6.60	6.28	-8.91	-2.30	
Pt_{79}-9	1.38	0.16	8.63	6.28	-10.57	-2.91	
$Pt_{60}Ti_{19}$-9	0.40	0.05	8.00	6.79	-8.69	-1.50	
Pt_{79}-10	1.21	0.14	8.64	6.30	-10.47	-2.96	
$Pt_{60}Ti_{19}$-10	0.52	0.05	10.40	6.28	-7.92	-1.13	
Pt_{79}-11	1.41	0.16	8.81	5.94	-9.68	-2.33	
$Pt_{60}Ti_{19}$-11	0.42	0.05	8.40	6.79	-8.87	-1.66	
Pt(111) Slab	0.39*	0.05	7.80*	6.34	-9.12	-2.39	

* Values for $\Delta E(Pt_{surf})$.

cluster, because of the stronger Pt–O interactions, the O_2 molecule is distorted to a greater extent than on the alloyed system, where weaker bonding is observed. However, at the TS, on the more weakly bound $Pt_{60}Ti_{19}$ system, greater distortion of the O_2 molecule is required, compared to the Pt_{79} system. This greater distortion requires more energy and can rationalise larger dissociation barriers on Ti@Pt compared to the pure Pt nanoparticle. The same discussion is also valid for Pt_{38} and $Pt_{32}Ti_6$ nanoparticles. O_2 distortion energies correlate with the corresponding O–O distances. Furthermore, the smaller difference in the O–O distances between the IS and TS for the Pt_{79} clusters compared to $Pt_{60}Ti_{19}$ clusters show that TS are "earlier" on Pt_{79}. Earlier TS are known to have lower barriers, which is found to be the case in this study.

Very similar dissociation barriers on the (100) facet are located for the 79- and 38-atom clusters (Tables 5.2 and 5.7). The dissociation barriers for the alloyed clusters (0.62 and 0.66 eV for the $Pt_{32}Ti_6$ and $Pt_{60}Ti_{19}$ clusters, respectively) are about twice those of the pure clusters (0.32 and 0.34 eV for the Pt_{38} and Pt_{79} clusters, respectively). However, for the dissociation barriers located on the (111) facet the relationship becomes a little more complicated.

For the Pt_{38} cluster, barrier-free dissociation was observed on sites 6 and 7 on the (111) facet. For the Pt_{79} cluster, once again almost barrier-free dissociation is located on sites 10 and 11. However, a dissociation barrier of 0.21 eV is found for dissociation on site 9. When comparing binding energies at sites 9 and 11, there is a small difference of 0.12 eV. Probably this difference is not simply a matter of different Pt–O bonding strengths but is related more to differences in the sites. Sites 9 and 11 are *hcp* whilst site 10 is *fcc*. This suggests that the difference in dissociation barriers is probably a consequence of the neighbouring surfaces to which the sites are adjacent. Whilst site 9 is neighbouring a (100) facet, sites 10 and 11 are both neighbouring (111) facets, implying that the adjacent (100) facet distorts less than an adjacent (111) facet and results in the small dissociation barrier for site 9 on the Pt_{79} cluster (see Pt-X^{centre} values in Table 5.8). Finally, dissociation barriers on the (111) facet of the $Pt_{60}Ti_{19}$ clusters are similar to that of the (100) facet. Here again, correlation between barriers and Pt-X^{centre} values is found since Pt-X^{centre} values are also similar at both types of facets.

5.3.3.3 Geometric Analysis

Again, it appears that the more easily distorted shell on the Pt_{79} cluster results in the observed barrier-free dissociation. Similar measurements to those performed for the 38-atom clusters, to quantify differences in distortions, are compiled in Table 5.8. Roughly comparable O–O bond lengths are observed for all initial states on the 79-atom clusters, 1.39 – 1.44 Å for the pure Pt_{79} nanoparticle and 1.37 – 1.41 Å for $Pt_{60}Ti_{19}$. At the TS, there are significantly shorter O–O bond lengths associated with the Pt_{79} cluster compared to those for the $Pt_{60}Ti_{19}$ clusters, 1.42 – 1.79 Å vs 1.71 – 2.05 Å. Studying Pt–O bond lengths reveals a similar trend to those for the 38-atom clusters, where in general, shorter bond lengths are observed as the system progresses from the initial to the transition state.

The Pt–Pt bond lengths for the bare Pt_{79} cluster are 2.66, 2.73, 2.70, 2.75, 2.68 Å for bond types 1 to 5, respectively (Figure 5.8). For site 8 on the (100) facet, significant distortion (by an average of 0.33 Å) of bond type 2 is observed. However, for the initial and transition states this is unsurprising as O_2 is interacting with the one bond. Therefore, although there is significant elongation of bond type 2, there is less overall distortion of the cluster. Bond types 3 and 4 are distorted (by an average of 0.42 and 0.56 Å, respectively) to the greatest extent for O_2 adsorption on the (111) facet. The elongation of bonds surrounding the hollow sites at which oxygen is adsorbed on the (111) facet leads to greater overall distortions of the cluster.

The Pt–Pt bond lengths of the alloyed $Pt_{60}Ti_{19}$ cluster are 2.68, 2.84, 2.73, 2.75 and 2.73 Å for bond types 1 to 5, respectively. Once again, significant elongation of bond type 2 is observed on the (100) facet when O_2 is adsorbed, 0.34 Å, although as with the Pt_{79} cluster, little overall distortion of the cluster is observed, $\leq$0.10 Å. There is far less distortion of other bond types when studying dissociation on the (111) facet. This is expected as there appears to be far less distortion of the overall cluster geometries upon adsorbing O_2.

Pt-X^{centre} values for the bare pure Pt_{79} cluster are 3.15 and 6.29 Å for the top and bottom of the cluster, respectively. For the bare $Pt_{60}Ti_{19}$ cluster, these values are 3.02 and 6.05 Å. Once again, there is considerable distortion of the Pt_{79} cluster when O_2 is adsorbed on the (111) facet, with Pt-X^{centre} distances elongated by up to 1.07 Å (Table 5.9). There is less distortion of the IS

Table 5.8: Data for oxygen - oxygen distances (O–O), average platinum - oxygen bond lengths (Pt–O), average platinum - platinum bond lengths (Pt–Pt) for specific bonds defined in Figure 5.8 and distances from the octahedral core to the central (111) atom in the y-direction (Pt-X^{centre}). Average Pt–Pt bond lengths are calculated for those atoms directly below the adsorbed O_2 molecule. The type of the bond is shown in brackets according to Figure 5.8.

	O–O			Pt–O			Pt–Pt			Pt-X^{centre}		
	IS	TS	FS	IS	TS	FS	IS	TS	FS	IS	TS	FS
Pt_{79}-8	1.39	1.42	2.98	1.96	2.01	1.95	3.18[2]	3.03[2]	2.96[2]	-	-	-
$Pt_{60}Ti_{19}$-8	1.37	2.03	3.87	1.98	1.84	1.92	3.27[2]	3.22[2]	3.04[2]	-	-	-
Pt_{79}-9	1.42	1.79	3.94	2.14	2.00	2.02	2.77[2]	2.83[2]	2.78[2]	3.21	3.30	4.22
							2.80[3]	2.84[3]	2.93[3]			
									3.11[5]			
$Pt_{60}Ti_{19}$-9	1.41	1.98	5.03	2.22	2.02	2.10	2.91[2]	2.89[2]	2.97[2]	2.96	3.00	2.95
							2.76[3]	2.76[3]	2.77[5]			
Pt_{79}-10	1.44	1.60	3.17	2.08	2.00	2.04	2.72[1]	2.72[1]	2.74[1]	4.01	4.01	3.93
							3.54[3]	3.54[3]	3.12[3]			
							3.53[4]	3.54[4]	3.19[4]			
									2.98[5]			
$Pt_{60}Ti_{19}$-10	1.40	2.05	3.75	2.18	1.99	2.02	2.69[1]	2.72[1]	2.70[1]	2.92	2.96	2.91
							2.85[3]	2.77[3]	2.75[5]			
							2.90[4]	2.91[4]				
Pt_{79}-11	1.43	1.47	2.53	2.09	2.09	2.07	3.24[4]	3.30[4]	3.08[4]	3.41	3.39	3.90
							2.73[5]	2.76[5]	3.11[5]			
$Pt_{60}Ti_{19}$-11	1.37	1.71	4.89	2.33	2.13	2.09	2.90[4]	2.71[1]	2.71[1]	2.94	3.11	2.91
							2.68[5]	2.71[3]	2.85[4]			
								3.09[4]				
								2.76[5]				

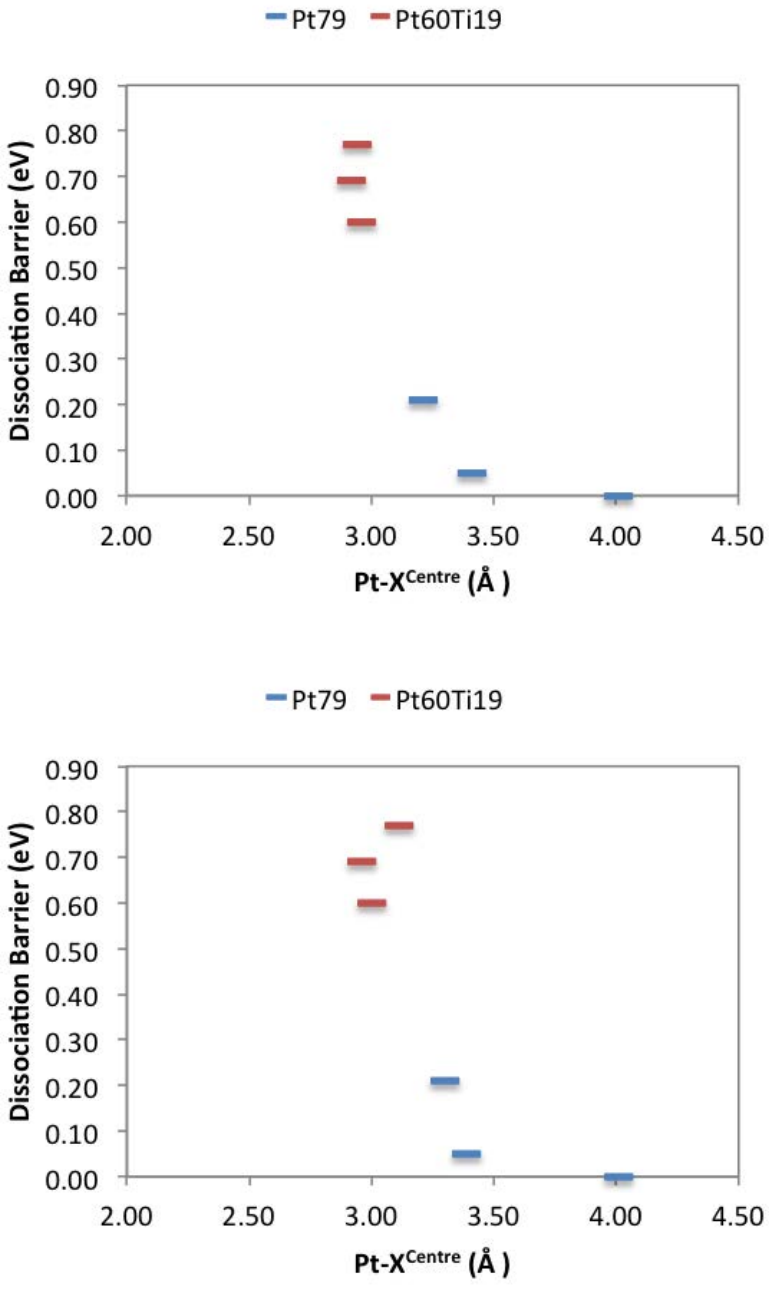

Figure 5.19: Plot of Pt-X^{centre} against dissociation barrier at the IS (left) TS (right).

Table 5.9: Pt-X^{centre} values relative to the bare clusters. Positive values show atoms being drawn out of the plane, leading to elongation of the cluster in the y-direction, whilst negative values show compression of the cluster in the y-direction. All values are given in Å.

	IS		TS		FS	
	Top	Bottom	Top	Bottom	Top	Bottom
Pt_{79}-9	0.06	-0.07	0.15	-0.11	1.07	-0.12
$Pt_{60}Ti_{19}$-9	-0.06	0.01	-0.02	0.01	-0.07	-0.01
Pt_{79}-10	0.86	0.05	0.86	0.04	0.78	-0.11
$Pt_{60}Ti_{19}$-10	-0.11	0.00	-0.06	0.00	-0.11	-0.01
Pt_{79}-11	0.26	-0.13	0.24	-0.19	0.75	-0.10
$Pt_{60}Ti_{19}$-11	-0.08	0.00	0.09	-0.02	-0.11	-0.01

(111) facet (Pt-X^{centre} - 0.06 Å) associated with site 9, where a small dissociation barrier of 0.21 eV is observed. Less distortion is also observed for the $Pt_{60}Ti_{19}$ clusters, with generally even a slight contraction in the Pt-X^{centre} values. More detailed analysis of the changes in Pt-X^{centre} can be found in Table 5.9, once again showing little deviation in distances from the plane to the bottom of the cluster. The relationship between Pt-X^{centre} and dissociation barriers can be seen in Figure 5.19 for the IS and TS, again allowing for further comparisons between the 38- and 79-atom clusters.

5.3.3.4 Bader Charge Analysis

Charge analysis was performed, the results of which are given in Table 5.10. The charges for the bare $Pt_{60}Ti_{19}$ cluster are -0.45 and +1.43 for Pt and Ti atoms, respectively. For the pure Pt_{79} cluster, similar to the Pt_{38} case, a positive charge is found on the Pt atoms interacting with the oxygen. These charges generally get more positive as the system progresses from the initial to final state. Again, this coincides with the charge on the oxygen becoming more negative.

For the $Pt_{60}Ti_{19}$ clusters, the charges on the Pt atoms bonded to oxygen generally become less negative as the system progresses from the initial to final state. Only for dissociation on the (100) facet are the Pt atoms positively charged for both the transition and final states. In all cases, the Ti atoms remain positive, generally gaining greater positive charge than Ti atoms in the bare $Pt_{60}Ti_{19}$ nanoparticle. This is consistent with electron donation from Ti to Pt which in turn donates to O, following the increase in electronegativity. The situation here differs from

Table 5.10: Average charges (|e|) of the initial, transition and final states of O_2 dissociation on the 79-atom clusters.

	Pt Charges[a]			Ti Charges[b]			O Charges		
	IS	TS	FS	IS	TS	FS	IS	TS	FS
Pt_{79}-8	0.28	0.25	0.44	-	-	-	-0.33	-0.38	-0.74
$Pt_{60}Ti_{19}$-8	-0.03	0.19	0.11	1.87	1.86	1.83	-0.33	-0.59	-0.74
Pt_{79}-9	0.20	0.29	0.32	-	-	-	-0.36	-0.51	-0.83
$Pt_{60}Ti_{19}$-9	-0.28	-0.16	-0.16	1.59	1.62	1.47	-0.37	-0.58	-0.74
Pt_{79}-10	0.27	0.30	0.33	-	-	-	-0.37	-0.46	-0.78
$Pt_{60}Ti_{19}$-10	-0.26	-0.12	-0.14	1.38	1.50	1.49	-0.36	-0.60	-0.78
Pt_{79}-11	0.24	0.24	0.41	-	-	-	-0.37	-0.40	-0.79
$Pt_{60}Ti_{19}$-11	-0.39	-0.22	-0.15	1.25	1.35	1.47	-0.34	-0.50	-0.78

[a]Pt atoms interacting directly with O atoms.
[b]Ti atoms interacting directly with O bound Pt atoms.

that on the $Pt_{32}Ti_6$ cluster, where the charge on the Ti atoms does not change appreciably when an O_2 molecule is adsorbed. This is likely a result of the greater Ti:Pt ratio in the 79-atom clusters. The greater ratio of Ti:Pt in the $Pt_{60}Ti_{19}$ clusters results in similarly negative charges on the Pt atoms but smaller positive charges on the Ti atoms. This will mean that more charge can be drawn from the Ti core as the system progresses to the FS, which would not be possible for the $Pt_{32}Ti_6$ clusters.

5.3.3.5 Conclusions

For most of the investigated features of the the larger 79-atom clusters, it is possible to see similar trends to the 38-atom clusters. This implies that the present trends can be generalised also to somewhat larger nanoparticles, approaching the size of particles present in common experimental catalytic studies. For the pure Pt_{79} clusters, essentially barrier-free dissociation barriers are observed on the (111) facet for sites 10 and 11. This coincides with significant distortions of the (111) facet. However, for site 9, less distortion of the (111) facet is observed and a small dissociation barrier of 0.21 eV is found. This difference is attributed to stabilisation effects of the neighbouring (100) facet. As with the 38-atom cluster, a similar dissociation barrier of 0.34 eV is found at site 8, for the Pt_{79} and site 5 for the Pt_{38} models, on the less distorted (100) facet. Once again, dissociation barriers are observed for all sites on the $Pt_{60}Ti_{19}$

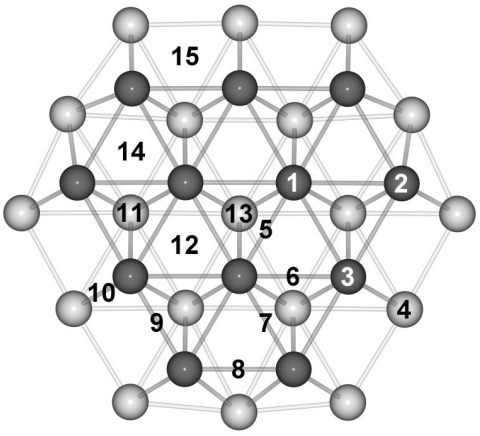

Figure 5.20: Top view of the surface (dark grey) and subsurface (light grey) metal atoms at a (111) facet sites on the 116-atom TO clusters.

cluster, which are attributed to a notably more structurally rigid outer Pt shell when the Ti core is present.

5.3.4 116-Atom Clusters

5.3.4.1 Oxygen Adsorption

Whilst the Pt_{79} cluster showed similar trends to the Pt_{38} cluster, further site dependent trends were observed for the larger cluster that were not present on the limited (111) facet of the 38-atom cluster. Therefore, one further cluster size was studied for the pure Pt system; the PtTi system was not investigated in this instance as the system does not show promise for fast O_2 dissociation. On the surface of the 116-atom TO cluster there are 15 non-symmetry equivalent sites which are depicted in Figure 5.20. The results of atomic and molecular oxygen adsorption on Pt_{116} are presented in Table 5.11.

Atomic oxygen is preferentially adsorbed to site 9, the edge-bridge position between the (111) and (100) facets, with a binding energy of -5.02 eV. This is in agreement with the studies on the Pt_{79} cluster. Whilst the atomic oxygen preferentially binds to the *hcp* hollow site (by $\geq$0.09 eV compared to edge-bridge sites) on the 38-atom cluster, favourable binding is observed to the edge-bridge position between two (111) facets (by $\geq$0.06 eV compared to hollow sites). This shows there is competition between atomic oxygen adsorption on the edge-bridge and

Table 5.11: Calculated binding energies (E_b) for atomic and molecular oxygen on all non-symmetry equivalent sites of the 116-atom cluster, shown in Figure 5.20. Values not presented are the result of oxygen migration to other sites during relaxation, as labelled. All energies are given in eV.

Site	Position	Pt_{116}–O	Pt_{116}–O_2
1	top	- [a]	- [b]
2	top	-4.26	-0.66
3	top	-3.92	- [c]
4	top	-3.58	- [d]
5	bridge	- [e]	-0.83
6	bridge	- [f]	-0.93
7	bridge	- [a]	-1.17
8	bridge	-4.92	-1.87
9	bridge	-5.02	-1.68
10	bridge	-4.76	-1.34
11	*hcp*	-4.66	-0.99
12	*fcc*	-4.65	-0.88
13	*hcp*	-4.42	-0.68
14	*fcc*	-4.79	-1.07
15	4-fold hollow	- [c]	- [d]

[a] Adsorbate migration to position 14.
[b] Adsorbate migration to position 13.
[c] Adsorbate migration to position 9.
[d] Adsorbate migration to positions 9 and 10.
[e] Adsorbate migration to position 12.
[f] Adsorbate migration to position 11.

hollow sites on the 38- and 79-atom clusters. However, on the 116-atom cluster, the edge-bridge site between the (111) and (100) facets are found to be $\geq$0.23 eV when compared to the hollow positions. This shows that, as the cluster size increases, there is a move away from the hollow sites being favoured towards the edge bridge sites. The exact edge-bridge position also varies as seen when comparing the 79-atom cluster, where the edge-bridge position between two (111) facets is favourable, to the 116-atom cluster, where the edge-bridge site between the (111) and (100) facets is favourable.

O_2 is preferentially adsorbed at position 8, the edge-bridge site between the two (111) facets. This is in agreement with results obtained for the 79-atom cluster, although it is found that the edge-bridge site between the (111) and (100) facets is favourable for Pt_{38}. The edge-bridge site is found to be $\geq$0.17 eV lower in energy than hollow sites on the 38-atom cluster, suggesting more site preference for O_2 binding when compared with atomic oxygen. This is also seen for the 79- and 116-atom clusters, where the preference for binding to edge-bridge sites over hollow sites is $\geq$0.70 and $\geq$0.80 eV, respectively. This also shows size dependence, where the energy difference between the edge-bridge and hollow sites increases as cluster size increases.

Once again, O_2 dissociation is investigated for sites on both the (111) and (100) facets. For the 116-atom cluster, bridge sites 8, 9 and 10 have been investigated as well as hollow sites 11, 12 and 14. As with the 79-atom clusters, O_2 dissociation proceeds from an initial site and terminates at the central hollow position on the (111) facet (site 13). Any further migration of the atomic oxygen to other positions on the cluster would lead to small barriers associated with moving between different sites but would have little importance. As with the 79-atom cluster, the central hollow site of the (111) facet was also investigated, although found to be unfavourable for O_2 dissociation, which is likely due to the small O_2 binding energies.

5.3.4.2 Distortion and Interaction Energies

Representations of the minimised geometries for the IS, TS and FS can be found in Figure 5.21–5.26. For Pt_{116} a greater range of facet sites were studied, these included similar (111) hollow sites to those investigated previously (positions 11, 12, 13 and 14) but also a greater range of

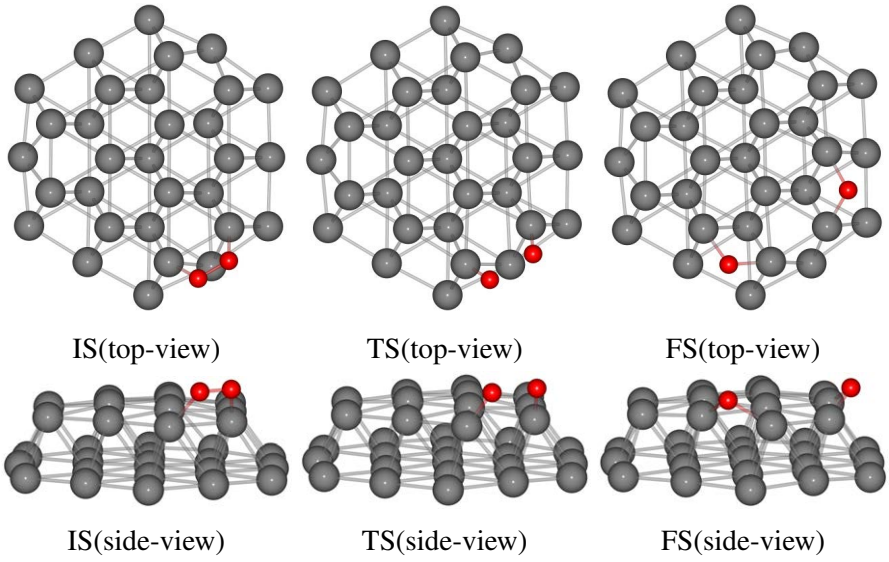

Figure 5.21: IS, TS and FS structures for O_2 dissociation on Pt_{116}, when O_2 is located at position 8. Only the top two layers of metal atoms are shown.

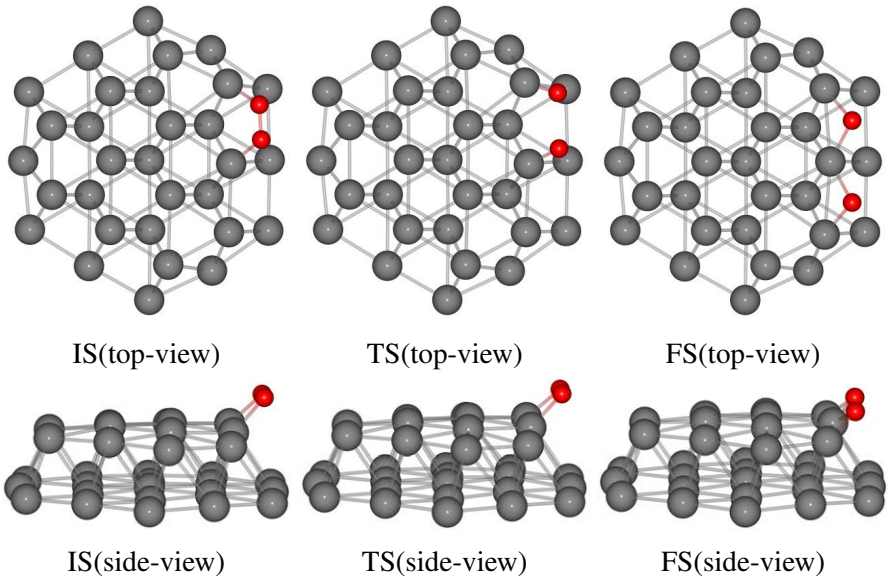

Figure 5.22: IS, TS and FS structures for O_2 dissociation on Pt_{116}, when O_2 is located at position 9. Only the top two layers of metal atoms are shown.

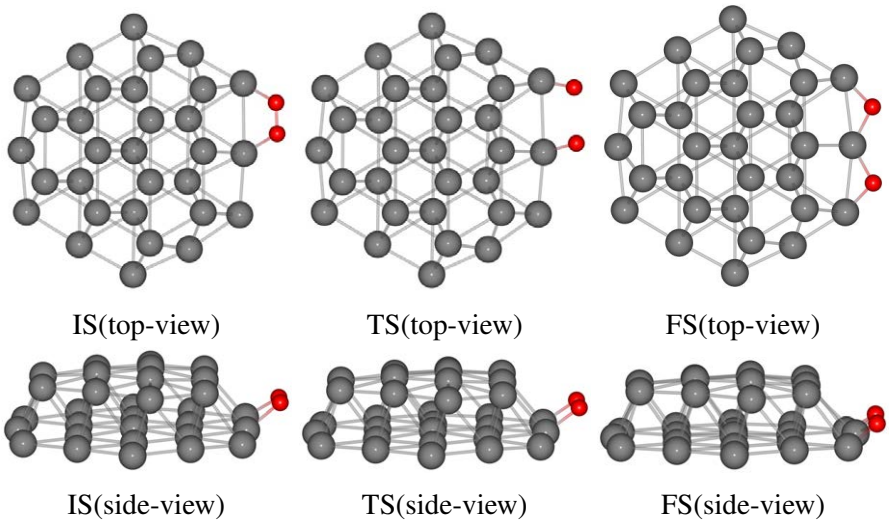

Figure 5.23: IS, TS and FS structures for O_2 dissociation on Pt_{116}, when O_2 is located at position 10. Only the top two layers of metal atoms are shown.

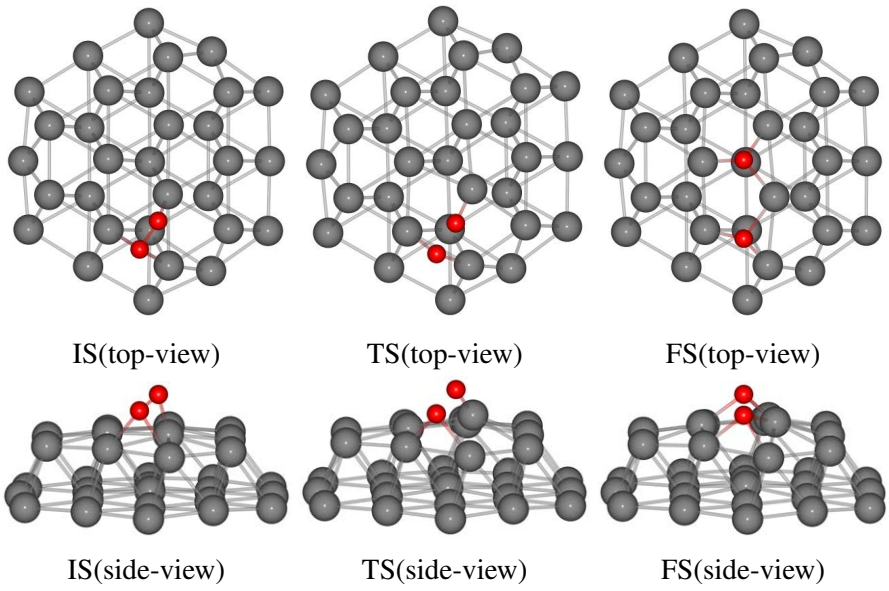

Figure 5.24: IS, TS and FS structures for O_2 dissociation on Pt_{116}, when O_2 is located at position 11. Only the top two layers of metal atoms are shown.

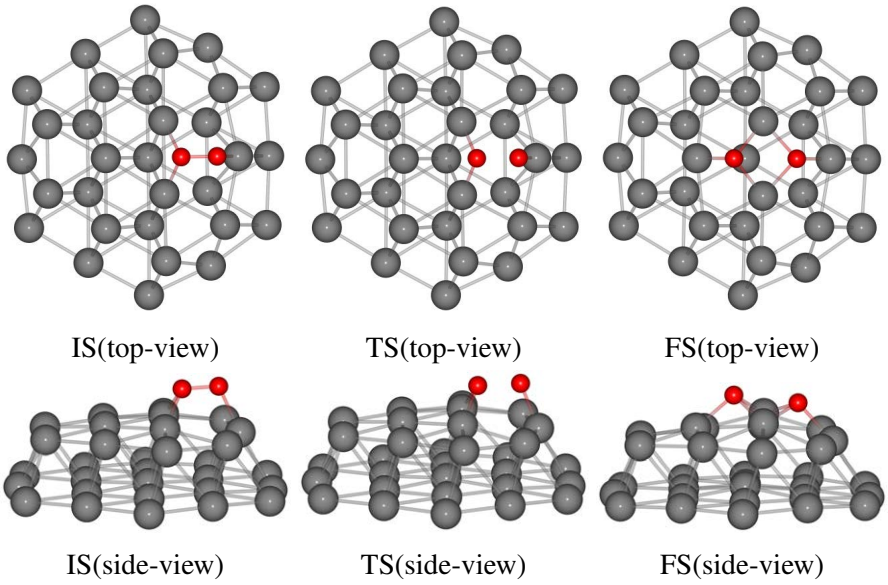

Figure 5.25: IS, TS and FS structures for O_2 dissociation on Pt_{116}, when O_2 is located at position 12. Only the top two layers of metal atoms are shown.

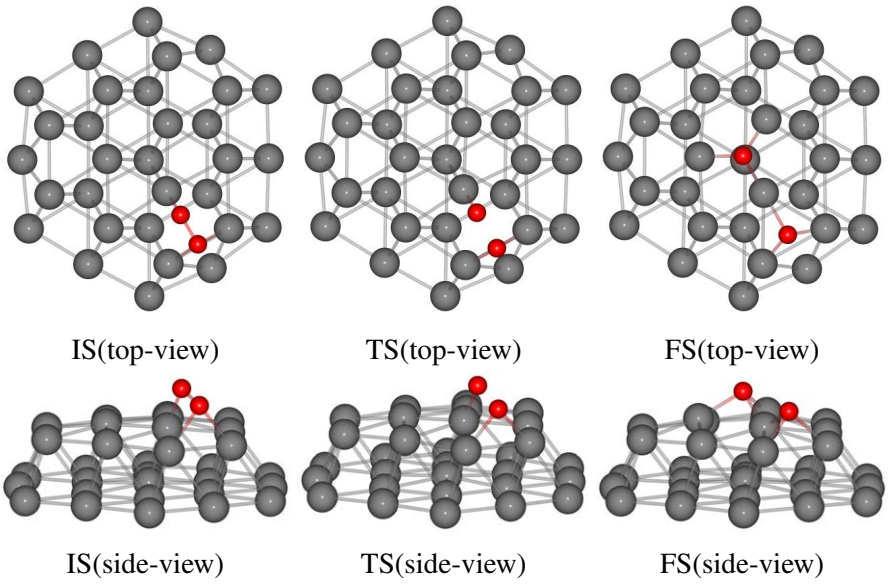

Figure 5.26: IS, TS and FS structures for O_2 dissociation on Pt_{116}, when O_2 is located at position 14. Only the top two layers of metal atoms are shown.

bridge sites (positions 5, 6, 7, 8, 9, and 10). As with the 79-atom cluster, the (111) hollow site at the centre of the (111) facet, position 13, is found to exhibit weak Pt–O binding. This means that the attempted O_2 dissociation studies were not successful, where the O_2 molecule migrates away from the facet position, towards a more favourable one, instead of dissociating.

For bridge positions 5, 6 and 7, once again relatively low binding energies are found for these sites. Instead of O_2 dissociation barriers being located for these positions, small barriers are found for O_2 migration to a preferential e.g. hollow site. This suggests that, where possible, O_2 migrates to favourable binding sites prior to dissociation. Details for the positions at which dissociation barriers were located are found in Table 5.12.

For Pt_{116} it is found that, as with the smaller clusters, there are very low dissociation barriers for hollow positions 11, 12 and 14, at 0.08, 0.07 and 0.14 eV, respectively. Although the barrier at position 14 is slightly higher than those for 11 and 12, it is significantly lower than that of the bulk ($\sim$0.40 eV). Furthermore, it is comparable with that of position 9 on Pt_{79}, which was found to be 0.21 eV. Whilst position 9 on Pt_{79} is the *hcp* hollow site adjacent to a (100) facet, position 14 on Pt_{116} is the *fcc* hollow site adjacent to another (111) facet site. There are few similarities between the two sites that could lead to this slightly higher dissociation barrier aside from the fact that they are both adjacent to the "short" edge of the (111) facet. On Pt_{79}, there are two hollow positions adjacent to (111) facets and only one adjacent to the (100) facets. For Pt_{116} there are two hollow sites adjacent to the (100) facets but only one adjacent to the (111) facets. It is therefore likely that the facets on the "short" edge are slightly more difficult to distort, with the bridge bond between facets being more ridged. However, as the central atoms of the (111) facet are more flexible, favourable distortions of the (111) facet are still possible, leading to these slightly higher dissociation barriers compared to other hollow positions on the (111) facet, but still lower than the Pt slab.

Studies of the IS reveal few trends in the cluster distortion energies observed upon adsorption of O_2. Compared to other positions, there is a small distortion energy for Pt_{116} when O_2 is adsorbed on position 8, the edge-bridge between two (111) facets. When compared to the Pt slab, sites 8, 11 and 14 have similar distortion energies ($\leq$ 0.07 eV difference). For Pt_{38}, none

Table 5.12: Cluster ($\Delta E(Pt_{n-m}Ti_m)$) and oxygen ($\Delta E(O_2)$) deformation energies, root mean squared displacements (RMSD) of the cluster, interaction energies (E_{int}), binding energies (E_b) of O_2 and barrier of O_2 dissociation ($\Delta E^{\neq}$). The ratios of distortion energy to RMSD ($\Delta E(Pt_{n-m}Ti_m)/RMSD$) are also presented. All energy values are given in eV, RMSD in Å.

Initial State	$\Delta E(Pt_{n-m}Ti_m)$	RMSD	$\Delta E(Pt_{n-m}Ti_m)/RMSD$	$\Delta E(O_2)$	E_{int}	E_b	$\Delta E^{\neq}$
Pt_{116}-8	0.10	0.02	5.14	0.70	-2.67	1.87	
Pt_{116}-9	0.38	0.05	7.66	0.56	-2.63	1.68	
Pt_{116}-10	0.34	0.04	8.49	0.51	-2.19	-1.34	
Pt_{116}-11	0.20	0.03	6.81	0.84	-2.03	-0.99	
Pt_{116}-12	0.65	0.06	10.84	0.91	-2.43	-0.88	
Pt_{116}-14	0.23	0.03	7.80	0.91	-2.21	-1.07	
Pt(111) Slab	0.17*	0.03	5.67*	0.64	-1.67	-0.86	
Transition State							
Pt_{116}-8	0.21	0.04	5.13	5.15	-6.91	-1.56	0.32
Pt_{116}-9	0.47	0.07	6.78	5.58	-7.33	-1.27	0.41
Pt_{116}-10	0.44	0.06	7.33	5.84	-6.92	-0.64	0.69
Pt_{116}-11	0.84	0.08	10.55	2.35	-4.11	-0.91	0.08
Pt_{116}-12	0.72	0.07	10.23	2.81	-4.33	-0.80	0.07
Pt_{116}-14	0.41	0.04	10.18	3.35	-4.69	-0.93	0.14
Pt(111) Slab	0.25*	0.05	5.00*	5.72	-6.41	-0.43	0.45
Final State							
Pt_{116}-8	0.53	0.04	13.37	9.65	-13.41	-3.23	
Pt_{116}-9	0.52	0.05	10.43	9.31	-12.77	-2.94	
Pt_{116}-10	0.65	0.06	10.84	9.35	-12.50	-2.50	
Pt_{116}-11	1.03	0.08	12.92	9.22	-12.56	-2.30	
Pt_{116}-12	1.37	0.09	15.28	8.20	-11.36	-1.78	
Pt_{116}-14	0.72	0.06	12.08	9.49	-12.41	-2.19	
Pt(111) Slab	0.39*	0.05	7.80*	6.34	-9.12	-2.39	

* Values for $\Delta E(Pt_{surf})$.

of the cluster distortion energies are close to that of the slab ($\geq$ 0.25 eV difference). For Pt_{79}, site 9 is 0.04 eV lower in energy than the slab; however, other sites are $\geq$ 0.14 eV higher in energy. This shows the cluster system trending towards the slab model as cluster size increases. The greatest distortion energy is found for position 12, although the distortion energies for the various sites are generally in line with those for the 38- and 79-atom clusters of $\leq$ 0.50 eV.

At the TS, position 8 once again has the lowest cluster distortion energy associated with it. The cluster distortion energy for site 8 is similar to that of the slab: 0.21 and 0.25 eV, respectively. However, all other sites have significantly higher distortion energies associated with them, 0.44–0.84 eV. The greatest distortion energies are found for positions 11 and 12 which are indicative of the low O_2 dissociation barriers. The cluster distortion energy for site 14 is found to be similar to those of positions 9 and 10, although a significantly lower O_2 dissociation barrier is found for 14 than for 9 and 10. It should be noted that the dissociation barrier for position 14 lies between the other low barrier (111) hollow sites and the high barrier bridge sites. There is a slight increase in the cluster distortion energies when comparing the IS and TS clusters, where the TS clusters tend to have greater distortion energies associated with them. Furthermore, the cluster distortion energies at the TS for Pt_{116} tend to be greater than those for the Pt_{38} and Pt_{79} TS clusters.

At the FS, the cluster distortion energies are all found to be greater than for the Pt slab. Furthermore, positions 8 and 9 have comparable cluster distortion energies, both $\sim$0.10 eV higher in energy than the slab model. The cluster distortion energies for positions 8 and 9 are lower than other sites as adsorption on the bridge positions typically leads to less distortion of the cluster. Positions 10 has a larger distortion energy than the other bridge positions. At position 10, O_2 dissociation occurs over the central atom of the (100) facet. This leads to similar distortions to the (111) facet, with the central atom being pulled out of the plane. However, for the (100) facet, this distortion does not lead to the very low dissociation barriers observed for the (111) facet; instead, a very large barrier of 0.69 eV is calculated. Position 14 has a higher distortion energy than the bridge sites, although this is lower than the distortion energy for the other hollow sites. As discussed previously, there is less distortion of the "short" facet edge,

leading to a reduced distortion energy compared to positions 11 and 12.

The calculated RMSD values for Pt_{116} are smaller than those for the 38- and 79-atom systems. This is because when cluster size increases, the average displacement of atoms will decrease as the interaction between the cluster and O_2 molecule is affecting a smaller proportion of the cluster's atoms. However, it is found that there are generally greater displacements associated with the TS and FS. This is expected as the oxygen binds more strongly to the Pt surface as the system progresses from the IS to the FS. There are fewer trends when comparing the various sites being studied. Generally, there is a large RMSD associated with sites 11 and 12, which have larger cluster distortion energies than other sites.

$\Delta E(Pt_{n-m}Ti_m)/RMSD$ gives the energy associated with a RMSD of 1.0 Å. It is found that at the IS, there is generally no trend between $\Delta E(Pt_{n-m}Ti_m)/RMSD$ and site, although site 8 is found to have the lowest displacement energy while site 12 has the highest. For the TS and FS there is a more general trend that there are greater displacement energies associated with the hollow sites compared to the bridge site. As the cluster size increases, $\Delta E(Pt_{n-m}Ti_m)/RMSD$ also increases. This shows that as the size increases, it is more difficult to displace the atoms to this degree. However, it is still possible to displace a small subset of atoms, interacting with O_2, in order to give the low dissociation barriers at the hollow sites, even with the larger clusters.

At the IS, the oxygen distortion energy shows that there is greater distortion of the of O_2 for the hollow sites, positions 11, 12 and 14. This shows that at the positions for which there are very low dissociation barriers, there is greater distortion, away from the gas phase structure, of O_2. Conversely, at the TS, this trend inverts, where higher O_2 distortion barriers are found for the bridge sites, 8, 9 and 10. This shows that at the TS, there is less distortion of the O_2 on the hollow sites

E_{int} gives an idea of the strength of the O_2 bond to the cluster surface. From the IS studies, it is found that there is little difference between the interaction energies for the various sites. This trend changes at the TS, where greater interaction energies are found for the bridge sites than for the hollow sites. This shows that at the bridge sites, where there is typically less distortion

of Pt_{116} and greater distortion of O_2, there is a stronger Pt–O interaction. This is the opposite trend to that of the hollow sites, where there is greater distortion of Pt_{116} and less of O_2. Similar trends to this are found for the binding energy, although in this case the trends are not as obvious because E_b includes the energetic contributions of distortions from gas phase structures.

5.3.4.3 Geometric Analysis

Analysis of the system geometries can be found in Table 5.13. At the IS, there is generally little difference in the O–O bond length for the various sites. However, at the TS, shorter O–O distances are found on the hollow sites, compared to the bridge sites. On the hollow sites, the O–O distances are on average only 0.25 Å longer at the TS compared to the IS. This compares to an 0.84 Å average increase in the O–O distances when comparing the TS to the IS on the bridge sites. This trend is in good agreement with Pt_{38} and Pt_{79} and once again shows that early transition states are located on the (111) facet where O_2 dissociation results in very small energetic barriers. As the system progresses from the IS to the TS, the Pt–O bond length are shortest at the TS. Pt–O bond lengths are increased when comparing the FS to the TS, although those at the FS are generally still shorter than at the IS. This is due to the increased binding energies observed as the system progresses from the IS to the FS, leading to the reduction in the Pt–O bond length. Longer Pt–O bond lengths are observed when O_2 is adsorbed on the hollow sites than on the bridge sites.

When comparing Pt–Pt bond lengths, several trends become apparent. On the bridge sites, the Pt–Pt TS bond length is increased when compared to the IS, whilst the FS bond length is generally shorter than the IS and TS. The TS will have the longest Pt–Pt bond lengths because of the stronger Pt–O interactions when compared to the IS. The Pt–Pt bond lengths are then generally reduced for the FS because, whilst the Pt–O binding is stronger, it is only a single O atom occupying the site. The trends are less well defined for the hollow sites, although in this case, there are a greater number of bonds that can be distorted. This can lead to less overall distortion of a certain bond type, compared to the bridge sites where ≤ 2 bonds are being distorted. Pt-X^{centre} values are calculated for all hollow sites. In all cases, there is a greater

Table 5.13: Data for oxygen - oxygen distances (O–O), average platinum - oxygen bond lengths (Pt–O), average platinum - platinum bond lengths (Pt–Pt) for specific bonds defined in Figure 5.8 and distances from the octahedral core to the central (111) atom in the y-direction (Pt-X^{centre}). Average Pt–Pt bond lengths are calculated for those atoms directly below the adsorbed O_2 molecule. The type of the bond is shown in brackets according to Figure 5.20.

	O–O			Pt–O			Pt–Pt			Pt-X^{centre}		
	IS	TS	FS	IS	TS	FS	IS	TS	FS	IS	TS	FS
Pt_{116}-8	1.40	2.00	5.58	1.97	1.82	1.94	2.78[1]	3.03[1]	2.98[2]	-	-	-
Pt_{116}-9	1.38	2.21	3.24	1.96	1.80	1.94	3.16[2]	3.22[2]	2.91[2]	-	-	-
Pt_{116}-10	1.38	2.47	3.29	1.98	1.81	1.95	3.10[3]	3.14[3]	2.93[3]	-	-	-
Pt_{116}-11	1.42	1.62	3.13	2.12	2.01	2.05	2.78[2]	2.78[2]	2.86[2]	4.03	4.65	4.48
							2.76[4]	2.31[4]	3.12[4]			
							2.87[5]	3.19[5]	2.88[5]			
									3.00[6]			
Pt_{116}-12	1.43	1.67	2.52	2.07	1.99	2.07	3.33[4]	3.35[4]	3.21[4]	3.99	4.04	4.41
							2.92[6]	2.93[6]	3.03[6]			
Pt_{116}-14	1.43	1.74	3.62	2.12	2.00	2.05	2.79[1]	2.83[1]	2.86[1]	4.03	4.12	4.11
							2.93[5]	3.06[5]	2.87[5]			
									2.96[6]			

distortion of the central (111) facet atom at the TS and FS when compared to the IS. This shows that as the Pt–O interaction energy increases, the (111) facet distorts to a greater extent.

5.3.4.4 Bader Charge Analysis

Results from the Bader charge analysis can be seen in Table 5.14. As with Pt_{38} and Pt_{79}, it is once again found that there is significant charge transfer from the Pt, which becomes positively charged, to the O, which becomes negatively charged. At the IS it is found that there is less charge transfer from Pt for site 8 compared to sites 9 and 10. Instead, it is found that site 8 is comparable to the hollow sites, which are slightly less positively charged. When studying O_2 charge, it is found that there is a greater charge to the O associated with the hollow sites. For the hollow sites, charge is transfer is investigated for the three Pt atoms directly bonded to O_2, instead of the two of the bridge sites. This means that, although there is typically less charge transfer away from the Pt, as there are more Pt atom interacting with O, the average charge on the O is greater.

The charge transfer at the TS is greater than tat at the IS. As the O_2 dissociates, the interaction energy increases, coupled with a greater transfer of charge from the Pt to the O. At the TS, there is greater charge transfer at the bridge sites which is due to the coordination number of the O, where each O atom is bonded to a single Pt atom. For the hollow sites the charge transfer is spread over three Pt atoms, which results in the smaller transfer of charge per Pt. A similar trend is found for the FS, where once again, greater charge transfer is found than at the IS or TS. Each O atom is now strongly bonded to the Pt surface and able to extract a greater charge than the molecular O_2. At the FS, there less difference in charge transfer between the bridge and hollow sites. This is because the charge transfer is spread over a greater number of atoms at each site.

5.3.4.5 Conclusions

Trends observed for the 38- and 79-atom cluster are also seen for the larger Pt_{116}. The expansion of the study to larger systems has enabled a more detailed study of size effects. It is seen that the

Table 5.14: Average charges (|e|) of the initial (IS), transition (TS) and final (FS) state structures of O_2 dissociation on Pt_{116}.

	Pt Charges[a]			O Charges		
	IS	TS	FS	IS	TS	FS
Pt_{116}-8	0.19	0.46	0.32	-0.33	-0.54	-0.75
Pt_{116}-9	0.29	0.51	0.44	-0.33	-0.58	-0.72
Pt_{116}-10	0.28		0.45	-0.31		-0.73
Pt_{116}-11	0.20	0.28	0.31	-0.36	-0.45	-0.77
Pt_{116}-12	0.24	0.31	0.39	-0.38	-0.48	-0.75
Pt_{116}-14	0.19	0.28	0.30	-0.37	-0.49	-0.76

[a]Pt atoms interacting directly with O atoms.

presence of the small O_2 dissociation barriers first observed on Pt_{38} was not because calculations were performed on a small cluster. For Pt_{116} very small dissociation barriers are observed on the (111) facet, when compared to the Pt (111) slab. A slightly larger dissociation barrier is found for site 14 (the *fcc* hollow), although this is significant lower than for the Pt slab, or other bridge sites on the 116-atom cluster.

For Pt_{116} other sites were also investigated: these included bridge sites on the (111) facet as well as the (111) facet edge bridge site. When studying the bridge sites on the (111) facet, it was found that O_2 did not dissociate on these sites, but would instead overcome small barriers to migrate to hollow sites. The edge bridge site exhibited similar characteristics to the edge bridge site of the (100) facet. An additional bridge site on the (100) facet was also investigated, this being the central bridge site. It was found that there was a larger dissociation barrier for this site, than for the edge bridge sites. This demonstrates the advantages of clusters made with greater numbers of (111) facet sites compared to (100) facet sites.

5.3.5 Nanoparticles vs Slab Models

The three-fold *fcc* site on the Pt(111) slab has similar binding energies to the central three-fold *fcc* site (position 12) on the Pt_{79} cluster, -0.86 and -0.88 eV, respectively, though, as mentioned previously, position 12 on Pt_{79} is not favourable for O_2 dissociation. It is therefore probable that the central three-fold *fcc* site on Pt_{79} is unlikely to facilitate oxygen dissociation, because

binding to edge hollow and bridge sites is much more favourable. These sites are absent on the slab Pt(111) model (as no steps or defects are included in the model) so it is more likely that dissociation will occur at these three-fold *fcc* hollow sites, however with a notable barrier of 0.45 eV. The rigidity of the bulk slab generally leads to weaker Pt–O bonding compared to the majority of sites on the Pt_{38} and Pt_{79} clusters. However, Pt–O bonding is generally found to be stronger than on the clusters where alloying leads to changes in electronic effects that results in the weaker bonding, as discussed earlier. Hence, the dissociation barrier on the slab model is found to lie between the Pt clusters, with low dissociation barriers coupled with stronger Pt–O bonding and the Ti@Pt clusters with higher dissociation barriers and weaker Pt–O bonding.

It is once again possible to study the central hollow site on Pt_{116} (position 13) to compare to the 79-atom cluster and Pt slab. On the Pt_{116} central hollow sites, weaker O_2 binding energies are observed, -0.68 eV compared to -0.86 and -0.88 eV for the slab and Pt_{79}, respectively. This means that it is more likely that the O_2 molecule will migrate to a site resulting in stronger binding prior to dissociation. As position 13 is in the centre of the (111) facet, all of the surrounding hollow sites result in stronger O_2 binding.

5.3.6 Surface Flexibility

From the discussion in subsections 5.3.2.3, 5.3.3.3 and 5.3.4.3, it is seen that the surface flexibility has a profound effect on the potential of catalysts for activation of O_2 dissociation. It is therefore of interest that the bulk Pt(111) surface lacks the ability to distort and therefore displays very different properties for oxygen dissociation when compared to pure Pt nanoparticles. It has further been shown that surface flexibility is not inherent in nanoparticles. Core-shell interactions stabilise the Pt shell of Ti@Pt clusters, thereby reducing flexibility. Calculating $\Delta E^{\neq}/RMSD$ gives an idea of the dependence of the dissociation barrier on surface flexibility. Values for this ratio are presented in Table 5.15 for the 38- and 79-atom clusters. The relationship between the RMSD at the TS and dissociation barrier $\Delta E^{\neq}$ is plotted in Figure 5.27, while $\Delta E^{\neq}/RMSD$ against E_b is presented in Figure 5.28.

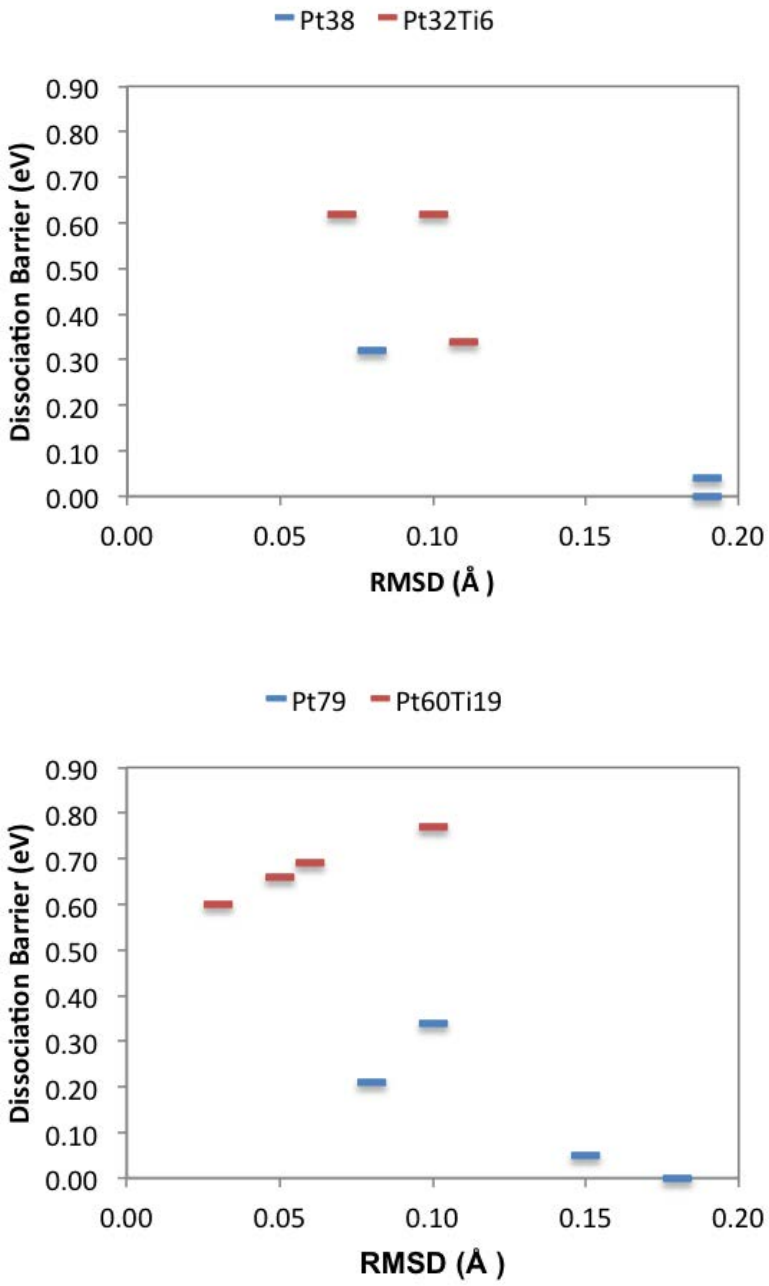

Figure 5.27: Plot of RMSD against dissociation barrier at the TS for 38 atom (top) and 79 atom (bottom) clusters.

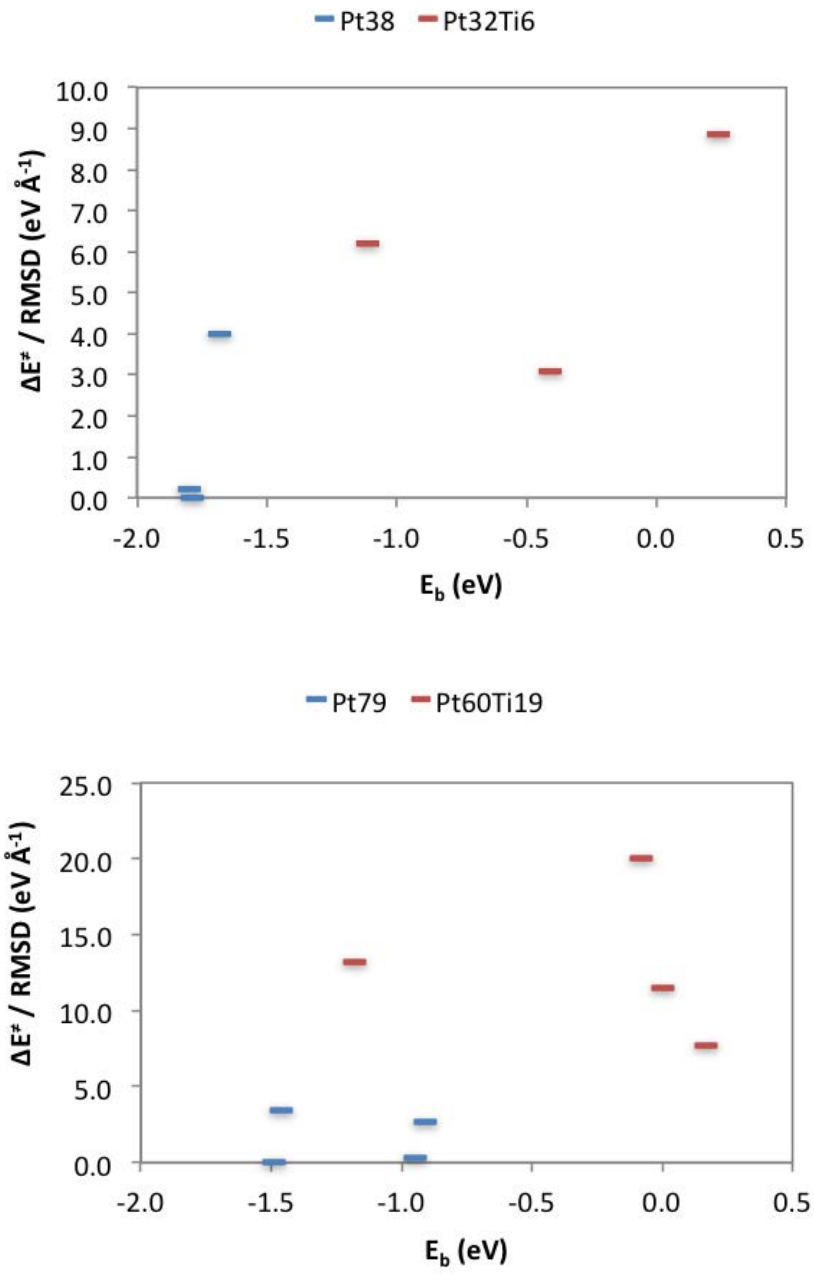

Figure 5.28: Plot of $\Delta E^{\neq}/RMSD$ against E_b at the TS for 38-atom (top) and 79-atom (bottom) clusters.

Table 5.15: Dissociation barrier $\Delta E^{\neq}$ against RMSD ($eV\mathring{A}^{-1}$) for the 38- and 79-atom clusters at theTS. The value for the Pt(111) slab has also been calculated for comparisons.*

38-Atom Cluster		79-Atom Cluster	
Site	$\Delta E^{\neq}/RMSD$	Site	$\Delta E^{\neq}/RMSD$
Pt_{38}-5	4.00	Pt_{79}-8	3.40
$Pt_{32}Ti_6$-5	6.20	$Pt_{60}Ti_{19}$-8	13.20
Pt_{38}-6	0.21	Pt_{79}-9	2.63
$Pt_{32}Ti_6$-6	3.09	$Pt_{60}Ti_{19}$-9	20.00
Pt_{38}-7	0.00	Pt_{79}-10	0.00
$Pt_{32}Ti_6$-7	8.86	$Pt_{60}Ti_{19}$-10	11.50
		Pt_{79}-11	0.33
		$Pt_{60}Ti_{19}$-11	7.70

*$\Delta E^{\neq}/RMSD$ for the Pt(111) surface is 9.00 eV Å^{-1}.

Significantly lower $\Delta E^{\neq}/RMSD$ values were obtained for the 3-fold hollow sites on the Pt_{38} (111) facet, at which barrier free dissociation occurs. Higher values are found for all positions on $Pt_{32}Ti_6$ as well as position 5 on Pt_{38}. This shows a strong relationship between the dissociation barrier and cluster distortion. For Pt_{79}, significantly lower values are obtained for the 3-fold hollow sites 10 and 11, at which barrier free dissociation occurs. $\Delta E^{\neq}/RMSD$ for positions 8 and 9 on Pt_{79} are higher than those for 10 and 11 on Pt_{79} but lower than all positions on $Pt_{60}Ti_{19}$. In general, values for Pt_{79} were comparable with those for Pt_{38}, one more indication that dissociation barrier and cluster distortion are strongly related.

The $\Delta E^{\neq}/RMSD$ for the Pt(111) surface is 9.00 eV Å^{-1}. This is greater than that for all positions on Pt_{38} or $Pt_{32}Ti_6$. The $\Delta E^{\neq}/RMSD$ for the Pt(111) slab is greater than those for Pt_{79}. This once again demonstrates the very important differences between the Pt clusters and slab. For the $Pt_{60}Ti_{19}$ cluster, the majority of the $\Delta E^{\neq}/RMSD$ values are greater than those for the slab (excluding position 11), due to the reduced oxygen adsorption energy, coupled with the lack of flexibility in the Pt shell.

5.4 Conclusions

When the adsorption strength of the O_2 molecule on the cluster surface increases, the dissociation barrier decreases. Hence, dissociation barriers on the alloyed Ti@Pt clusters are found to be greater than those for the pure Pt clusters that exhibit larger E_b values. Pure Pt clusters are easily distorted when O_2 is adsorbed on the (111) facet. Furthermore, sites which are relatively easily distorted facilitate barrier-free dissociation of O_2, a trend which is not only seen for the small 38-atom clusters but also the larger 79- and 116-atom clusters. As for the alloyed Ti@Pt clusters, in all cases significant barriers are observed for all sites, which are greater than the barriers found for the pure Pt clusters.

The presence of the O_2 dissociation barriers for the Ti@Pt clusters is attributed to rigidity enhancement of the Pt shell by the Ti core. Significant electron donation is observed from Ti to Pt, suggesting strong interactions between the two, which coincides with significantly less distortion of the Ti@Pt clusters upon binding O_2 when compared to the pure Pt clusters.

The presence of the barrierless distortion on the (111) facet of the pure Pt cluster suggests that small Pt clusters would efficiently dissociate O_2. However, the relatively strong adsorption strength of oxygen to the Pt surface, compared to the alloyed Ti@Pt cluster found in previous studies, means that it would be difficult to remove the resulting oxygen species from the pure Pt cluster surface. Therefore, whilst O_2 dissociation would require greater energetic input on the surface of the Ti@Pt clusters, the resulting species (following further transformations to e.g. H_2O or H_2O_2) would be easier to remove from the surface due to the weaker Pt–O interactions compared to the pure Pt cluster.

A very attractive development in the direction of optimum catalyst properties, resulting from findings of the present study, would be substitution of Ti in the core of Pt-based bimetallic particles by another metal (M). The ideal M core would weaken adsorption of atomic oxygen compared to pure Pt, to allow for fast ORR kinetics in the later stages of the reaction (as Ti does) but forms Pt-M bonds which are weaker than Pt-Ti bonds, thereby keeping the advantageous Pt shell flexibility for fast O_2 dissociation.

Chapter 6

Comparison of M@Pt Core-Shell Systems for 3d, 4d and 5d Transition Metals

6.1 Introduction

In this chapter, a range of possible d-block cores (groups 3–12 and 3d–5d metals of the periodic table) have been considered for the model M@Pt system discussed in Chapters 4 and 5. Initially, the focus has been on 38-atom clusters, although studies have also progressed to 79-atom systems. In Chapter 4 it has been determined that charge transfer, resulting in filling of the *d*-band, is important for reducing Pt–OH binding energies, thus improving kinetics for the latter stages of the ORR. However, strongly interacting systems have a negative impact on O_2 dissociation, where the Pt shell is no longer able to distort, as discussed in Chapter 5. In this chapter, the aim is to investigate the relationship between shifts in the *d*-band centre and core-shell interactions. The ideal electrocatalyst will have a downshift in the *d*-band centre to weaken Pt-OH interactions while having a weakly interacting core and shell to allow for shell distortions.

6.2 Computational Details

Calculations have been performed using the Vienna Ab initio Simulation Package (VASP) 5.2 [127–130]. Ionic cores were represented by the projected augmented wave (PAW) method [178, 179]. Electronic exchange and correlation was described using the generalised gradient approximation (GGA) using the Perdew Wang 91 (PW91) *xc* functional [180, 181]. The Methfessel-Paxton smearing method was used, with a width of 0.1 eV and an energy cutoff of 415.0 eV has been employed. All clusters were placed in the centre of a supercell large enough to ensure sufficient separation between periodic images, the Γ point was used to sample the Brillouin Zone. Atoms are relaxed according to the calculated atomic forces, with convergence criteria for energies and forces required to be better than 1.0×10^{-4} eV/atom and 0.02 eV/Å, respectively.

Geometry optimisations were performed using the standard VASP code. Dissociation pathways were investigated using the VTST implementation of the VASP code, by first generating an approximate pathway using the Nudged Elastic Band (NEB) method [182], with further refinements achieved using the Dimer method [183]. Bader charges [136] were calculated using the standard VASP code, with analysis performed using the Bader code [184] also from the Henkelman Group.

6.3 Results and Discussion

6.3.1 Geometric Analysis

The investigation of complete 38-atom M@Pt core-shell TO clusters is presented, with analysis of the data presented in Table 6.1. From the previous studies presented in Chapter 5, it is apparent that weak core-shell interactions give rise to the surface flexibility that is beneficial for fast O_2 dissociation. Therefore, when considering a wider range of M@Pt d-block core-shell clusters, it is likely to be beneficial for the M core to have a similar electronegativity to Pt. From Figure 6.1 it is seen that Pt has an electronegativity of 2.28 on the Pauling scale, compared with

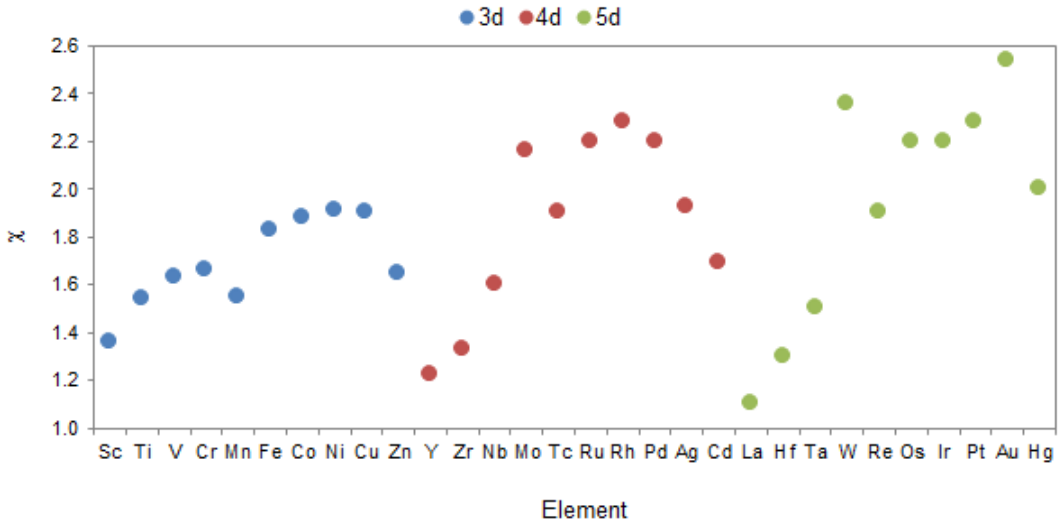

Figure 6.1: Plot of electronegativity [203, 204] across the range of d-block metals being investigated.

1.54 for Ti. With Pt and Ti having very different electronegativities, it is to be expected that there will be particularly strong core-shell interactions with large charge transfer.

Figure 6.1 shows that in general, moving from early to late d-block metals is coupled with an increase in electronegativity (except group 12 metals which all decrease relative to the previous group), while moving from 3d–5d results is less well defined trends. This suggests that late d-block metals are likely to result in the desirable weaker core-shell interactions. Studies have shown that alloys formed between platinum and early transition metals are particularly stable, a result of the strong Pt–M interactions [41]. To test this, dimer binding energies were calculated for Pt–M dimers. From Figure 6.2 it is possible to see a strong correlation between metal group and the Pt–M binding energy. It is evident that late d-block metals have significantly reduced binding energies compared to early metals. Furthermore, there appears to be little period dependence.

When performing geometry optimisations on the bare 38-atom clusters, all M@Pt compositions apart from the Co@Pt system locally minimised to the TO structure. It is possible that a number of these systems could form clusters with a TO structure [206–210]. However, in this study the TO structure is used as a model and is not suggested to be the most favourable experimentally. The RMSD for the Pt shell was calculated comparing Pt shell of the pure Pt_{38} cluster

Table 6.1: Electronegativity (χ) [203, 204] of the M@Pt core, Pt–M dimer binding energy (E_b) in eV, calculated atomic radii [205] in pm and RMSD values of the Pt shell associated with all systems investigated in Å.

	Row 1					Row 2					Row 3			
M@Pt	χ	E_b	Atomic Radii	RMSD	M@Pt	χ	E_b	Atomic Radii	RMSD	M@Pt	χ	E_b	Atomic Radii	RMSD
Sc	1.36	-4.22	184	0.09	Y	1.22	-4.28	212	0.18	La	1.10	-3.94	1.95	0.24
Ti	1.54	-4.18	176	0.15	Zr	1.33	-4.40	206	0.14	Hf	1.30	-5.61	208	0.14
V	1.63	-4.30	171	0.24	Nb	1.60	-4.34	198	0.19	Ta	1.50	-4.82	200	0.19
Cr	1.66	-4.49	166	0.13	Mo	2.16	-4.31	190	0.15	W	2.36	-4.73	193	0.21
Mn	1.55	-4.67	161	0.14	Tc	1.90	-4.18	183	0.13	Re	1.90	-4.53	188	0.12
Fe	1.83	-3.85	156	0.15	Ru	2.20	-3.45	178	0.10	Os	2.20	-3.75	185	0.11
Co	1.88	-2.98	152	-	Rh	2.28	-2.87	173	0.06	Ir	2.20	-3.00	180	0.05
Ni	1.91	-2.36	149	0.14	Pd	2.20	-2.24	169	0.06	Pt	2.28	-2.38	177	0.00
Cu	1.90	-1.77	145	0.16	Ag	1.93	-1.49	165	0.07	Au	2.54	-1.49	174	0.06
Zn	1.65	-1.13	142	0.14	Cd	1.69	-0.98	161	0.08	Hg	2.00	-1.45	171	0.09

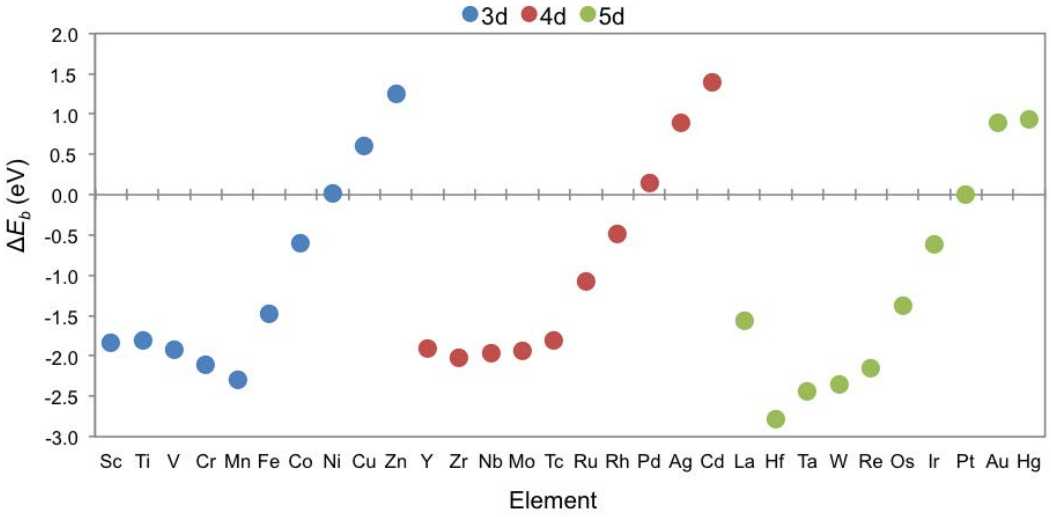

Figure 6.2: Pt–M dimer binding energies, relative to Pt_2, calculated for the range of d-block metals investigated.

with the Pt shell of the M@Pt core-shell cluster, the results of which are plotted in Figure 6.3. It is seen that there is a general reduction of the RMSD for late d-block metals. Furthermore, moving from 3d to 5d leads to a reduction in the RMSD. With the vast majority of clusters minimising to the TO structure, this gives a viable model to analyse Pt shell flexibility when related to varying core composition.

The RMSD will not only be influenced by the Pt–M binding energy, but also by the atomic radii of the alloyed element. It is likely that deviation from the approximate atomic radii of Pt (177 pm) will result in strain because of the size mismatch between the core and the shell atoms. The atomic radii of the various elements are shown in Table 6.1, where it is seen that progression from early to late transition metals leads to a general decrease in atomic radii. Furthermore, moving from 3d to 5d metals, results in a general expansion of the atomic radii. Strain also has an effect on the binding energy of adsorbates, where an increase in the Pt–Pt bond length will result in stronger binding and a decrease will lead to a weakening of adsorbate binding [211–214].

The relationship between the electronegativity and the binding energy is presented in Figure 6.4a. This shows the general trend that as the electronegativity increases, towards that of Pt, the relative binding energy decreases. However, there are a lot of outliers on this data set, so whilst

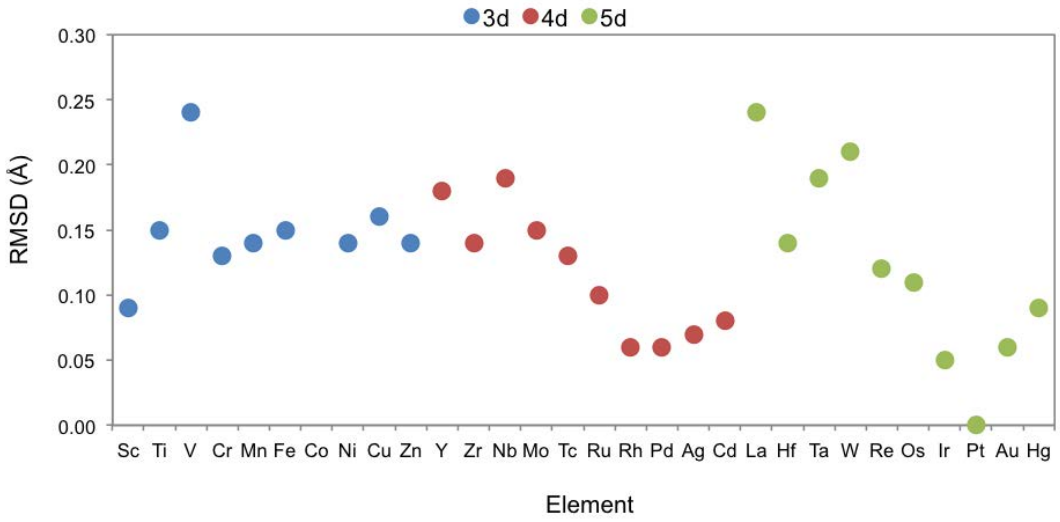

Figure 6.3: RMSD values calculated for the Pt shell of the 38-atom M@Pt clusters for the range of d-block metals investigated.

it is possible that the electronegativity has an effect on the binding energy, it is not possible to select potential metals based on this property alone because geometric effects, such as strain, also play an important role. In Figure 6.4b, the relationship between binding energy and the RMSD is plotted. It is possible to see that for stronger binding energies, RMSD is increased. This suggests that, as expected, weaker core-shell interactions result in less distortion of the outer Pt shell, when compared to the Pt_{38} cluster.

6.3.2 O_2 Chemisorption Studies

Sites 6 and 7 on the 38-atom M@Pt TO clusters were investigated. For 3d metals, it is found that there is slight distortion of the (111) facet for the Sc@Pt cluster, while there is little distortion of the (111) facet for groups 4–8. In the initial study, Co was not investigated due to the fact that during the relaxation of the bare cluster, the structure distorted from the TO. For groups 10–12, similar distortions of the (111) facet to those of the pure Pt cluster are observed. For groups 10–12, when O_2 is adsorbed on site 7, there is spontaneous dissociation of the O_2 molecule. In the studies presented in Chapter 5, O_2 dissociation barriers on the Pt_{38} cluster are $\leq$ 0.04 eV. In fact, the exact dissociation barriers are 0.04 and 0.00 eV, for sites 6 and 7, respectively. This shows that for the Pt_{38} cluster, the dissociation barrier on site 7 is slightly smaller than that

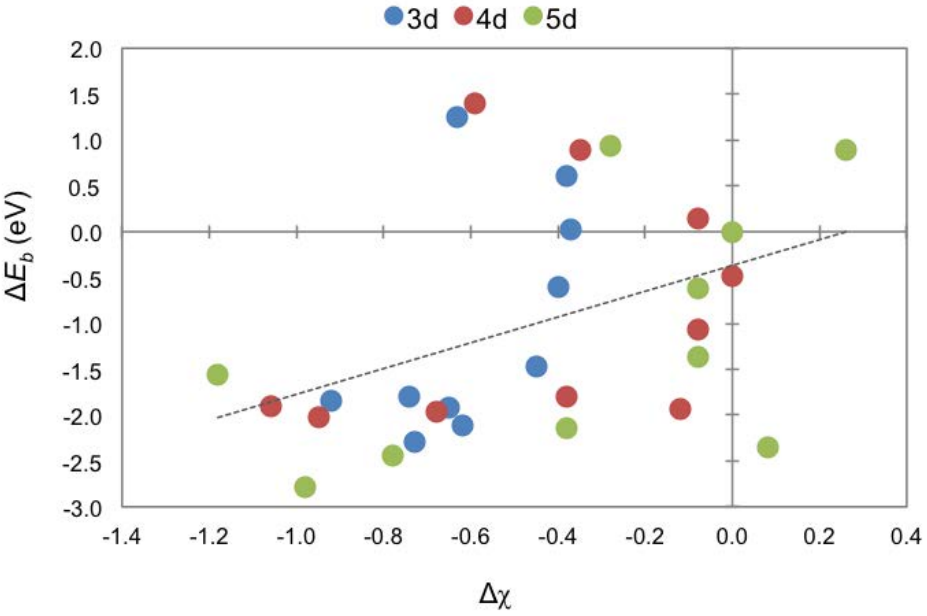

(a)

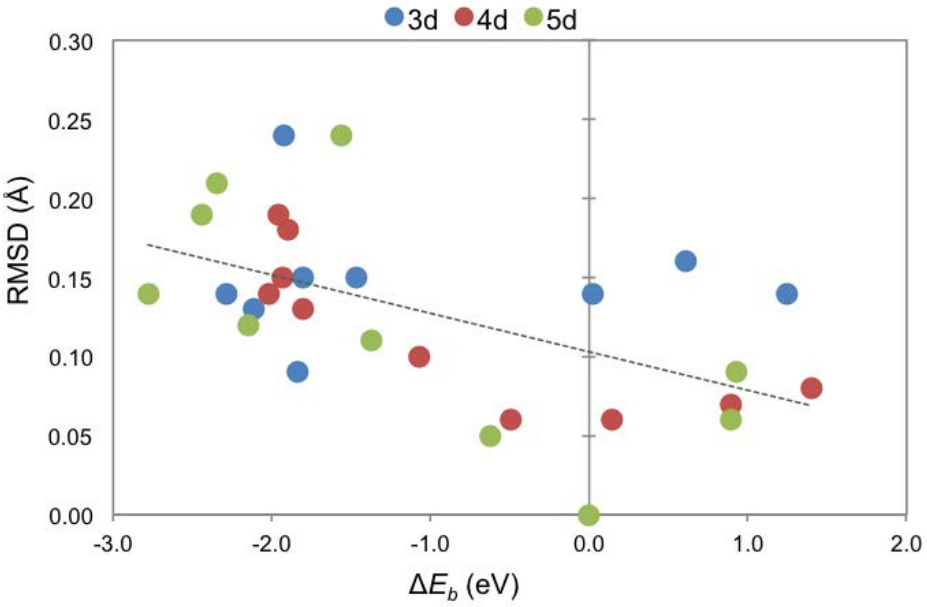

(b)

Figure 6.4: Plots of the relationship between (a) electronegativity and binding energy, with a R^2 fit of 0.16 and (b) binding energy and RMSD for the Pt shell of the 38-atom M@Pt clusters, with a R^2 fit of 0.30. In both cases the values are normalised for Pt_{38} set at zero.

for site 6. It could therefore be expected that the dissociation barriers at sites 7 on the M@Pt clusters are also lower than those for site 6. It follows that, where the Pt–M binding energies are reduced compared to those for Pt–Pt, the dissociation barrier at site 7 results in spontaneous dissociation, while heavy distortion of the (111) facet is observed at site 6.

4d M@Pt clusters exhibit similar behaviour to 3d metals, although now group 9 can be investigated, with Rh@Pt locally minimising to the TO structure. One interesting difference between 3d and 4d metals is that, whilst the Y@Pt cluster distorts from the TO structure, with the core atoms occupying surface sites to form a Y–O bond, the Zr@Pt alloy exhibits the same (111) facet distortions as the Pt_{38} cluster. The behaviour of the Zr@Pt cluster is in stark contrast to the Ti@Pt cluster. From Section 6.3.1 it is found that Zr has a strong dimer binding energy, at -4.40 eV, which is in fact stronger than that of the Pt–Ti binding energy of -4.18 eV. The other early d-block metal clusters exhibit similar properties to those in row 4, where there is little distortion of the (111) facet upon adsorption of O_2. The (111) facet of the Rh@Pt clusters are found to distort, as is the case with groups 10–12. Once again, spontaneous O_2 dissociation is observed on site 7 for group 9–12 metals, as well as Zr. Some distortions are observed for earlier metals, although these seem to be related to instabilities in the TO structures, with some tending towards e.g. Ico structures. However, these distortions do not provide the favourable (111) facet distortions that are of interest in this study.

Similar trends to those observed for 3d and 4d metals are also observed for 5d metals. Distortions to the central atom of the (111) facet are observed for the later d-block metals (groups 9–12) while little distortion is observed for earlier d-block metals. The La@Pt cluster distorted upon O_2 binding in a similar fashion to Y@Pt, where the core atoms are pulled to surface sites forming a La–O bond, although once again, it appears that adsorbing O_2 on some TO structures allows for an energetic barrier to be overcome for cluster distortions away from the TO. For 5d metals, it is also found that the Hg@Pt cluster distorts away from the TO when O_2 is adsorbed on site 6. In this case, an Hg atom is drawn to the surface which has been seen experimentally, where surface stabilised Hg atoms form on Pt nanoparticles [215]. Spontaneous O_2 dissociation occurs on site 7 for Ir@Pt, Au@Pt and Hg@Pt, although this spontaneous

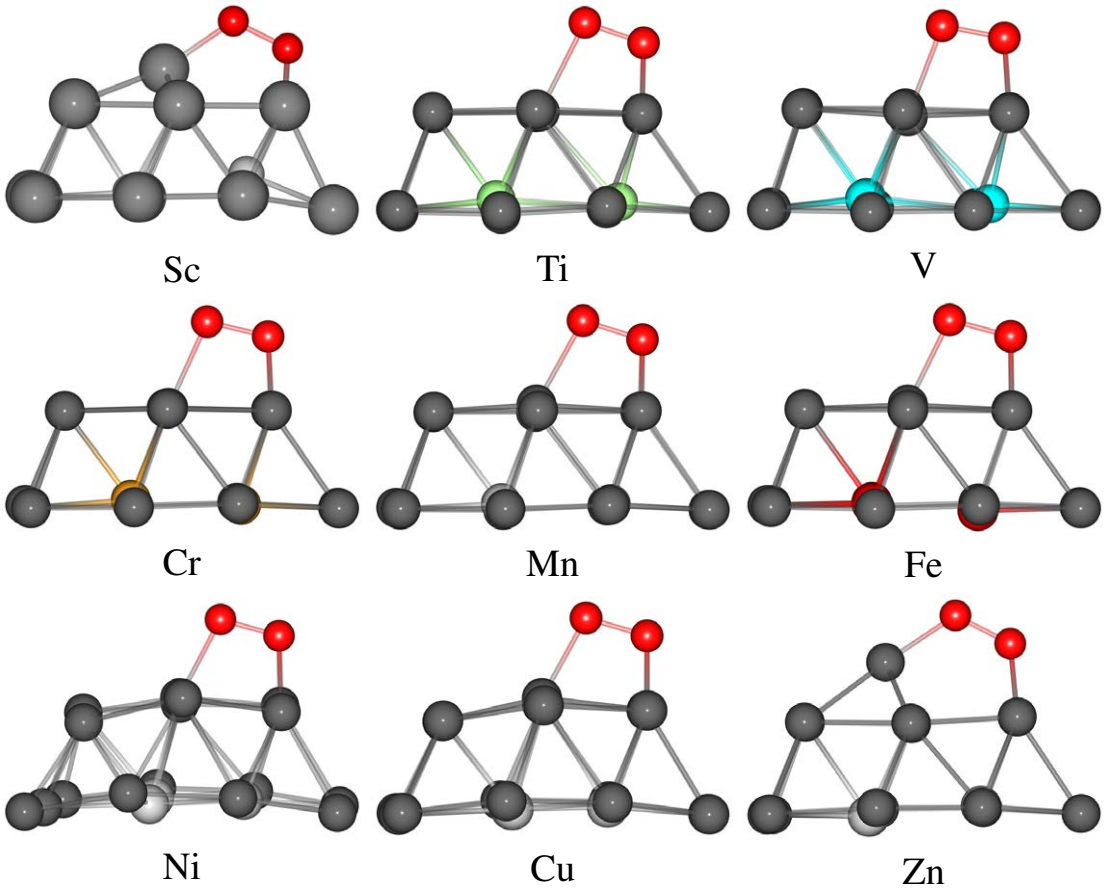

Figure 6.5: O_2 adsorption on site 6 for 3d M@Pt clusters. Co@Pt is not shown as the bare cluster distorts away from the TO structure.

dissociation was not observed for Pt_{38}.

From the study of O_2 adsorption on the 38-atom M@Pt clusters, several trends become apparent. The late d-block metals from groups 9–12 appear to be the most promising candidates for fast O_2 dissociation. It is found that where weaker Pt–M binding energies are found, compared to that of Pt–Pt, distortions of the (111) facet are observed in all cases. However, it is also found that the Rh and Ir systems, with stronger Pt-M binding energies by ≤ 0.62 eV, also exhibit surface distortion by O_2. However, clusters with Pt–M binding energies ≥ 1.07 do not exhibit this behaviour. All structures can be found in Figures 6.5 – 6.10.

The binding energies for sites 6 and 7 are presented in Table 6.2. In general, later d-block metal systems, for which Pt shell distortions are observed, have greater O_2 binding energies than for earlier d-block metal systems, where distortions to the (111) facet are not observed. This is

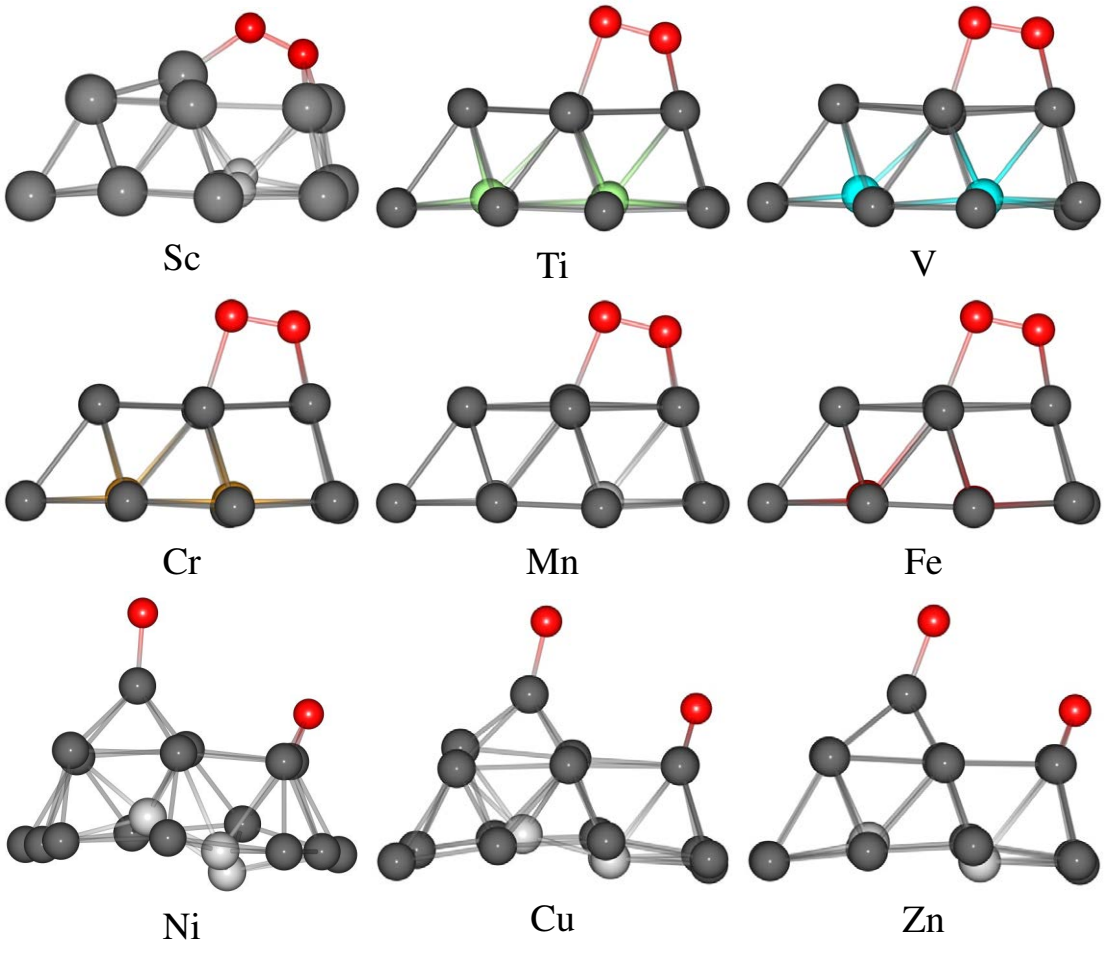

Figure 6.6: O_2 adsorption on site 7 for 3d M@Pt clusters. Co@Pt is not shown as the bare cluster distorts away from the TO structure.

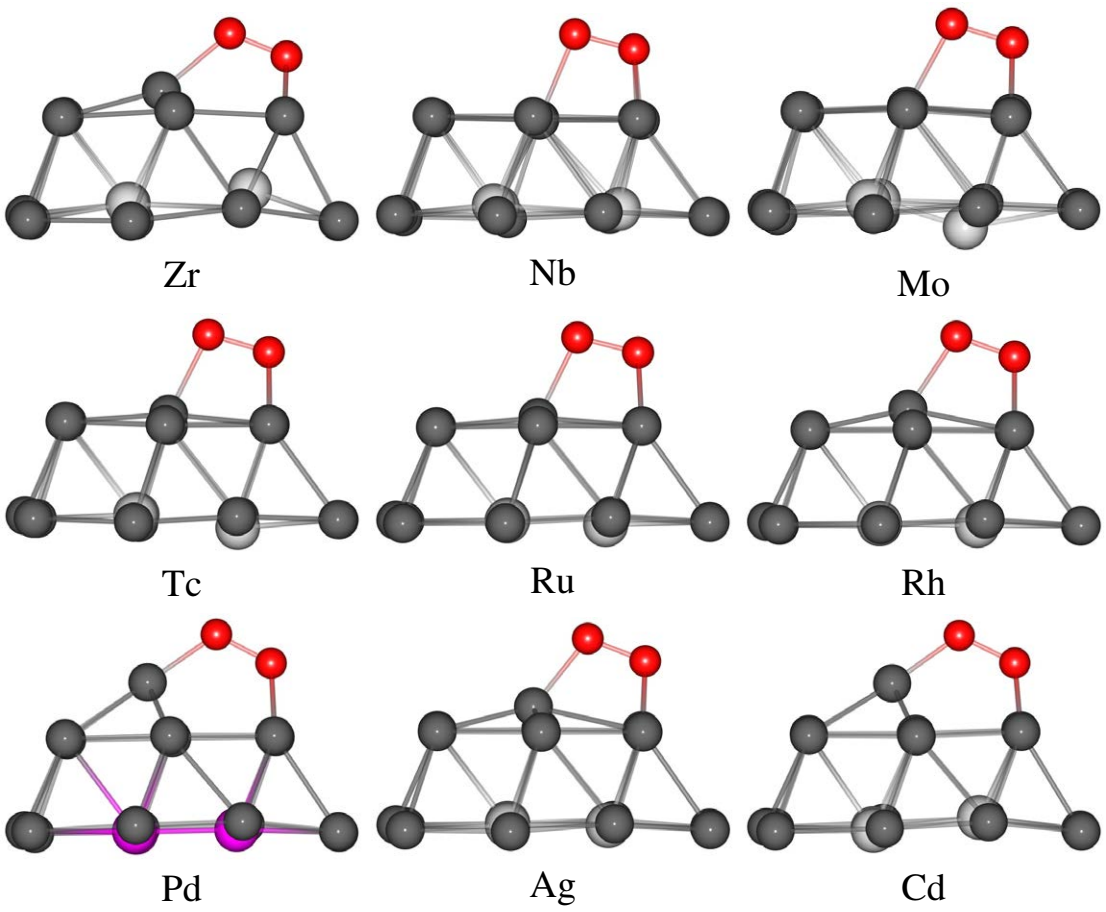

Figure 6.7: O_2 adsorption on site 6 for 4d M@Pt clusters. Y@Pt is not shown as O_2 adsorption results in large cluster distortions away from the TO structure.

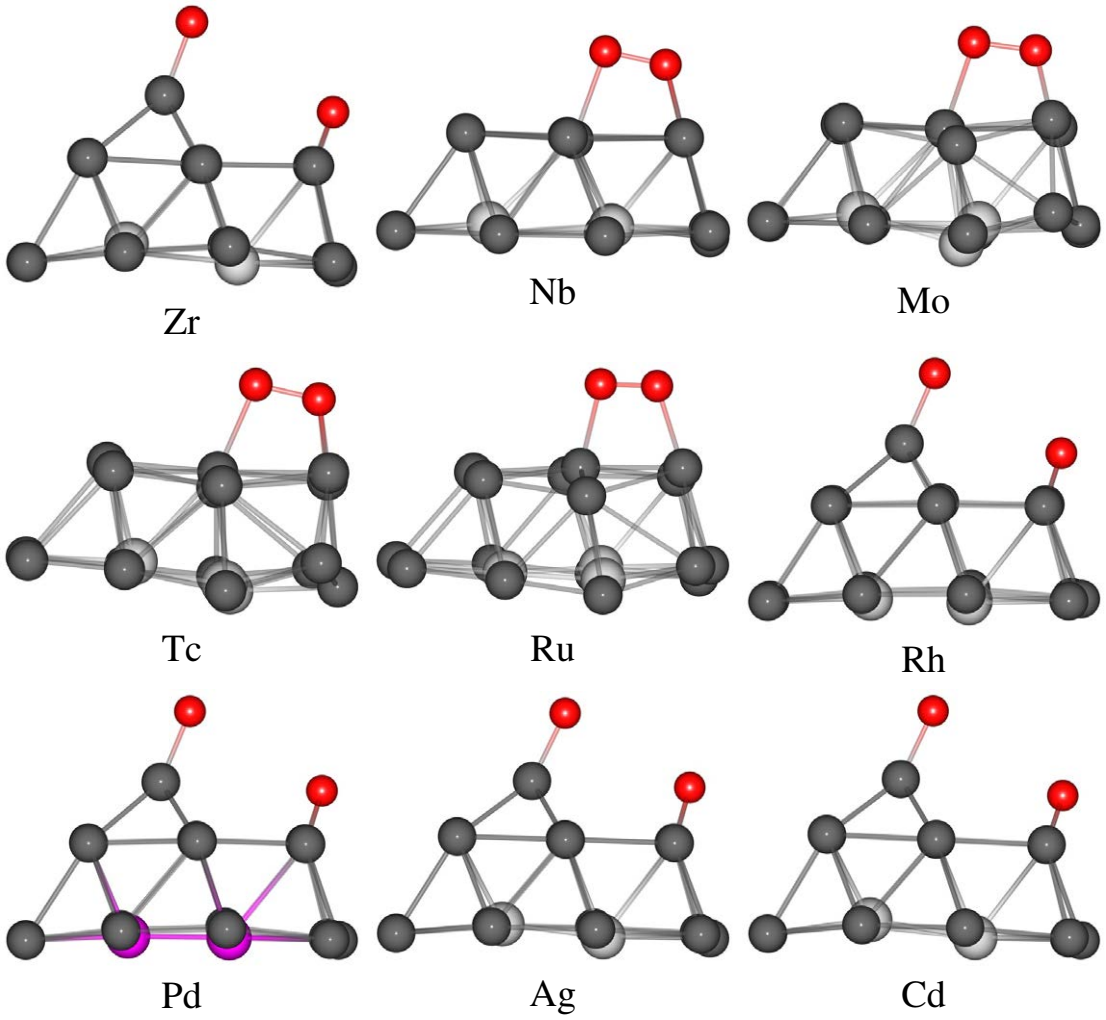

Figure 6.8: O_2 adsorption on site 7 for 4d M@Pt clusters. Y@Pt is not shown as O_2 adsorption results in large cluster distortions away from the TO structure.

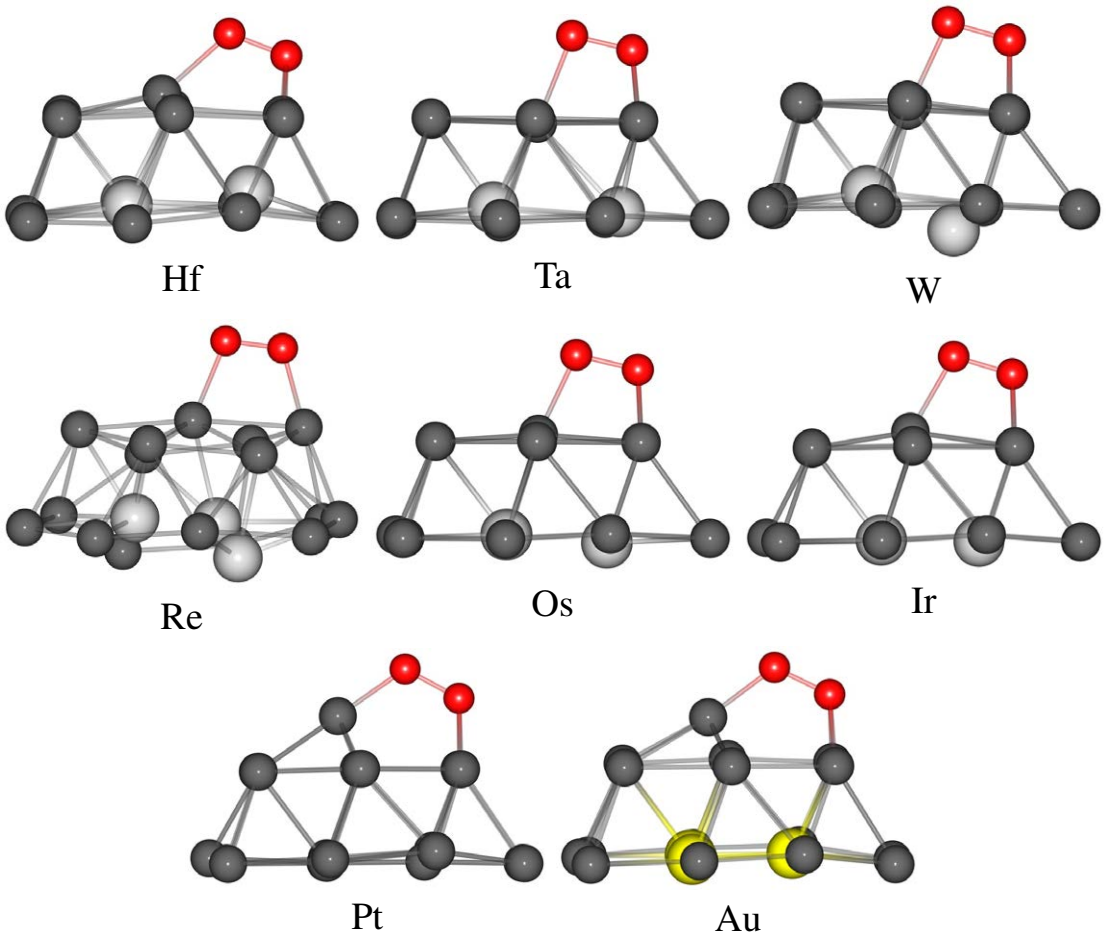

Figure 6.9: O_2 adsorption on site 6 for 5d M@Pt clusters. La@Pt and Hg@Pt are not shown as O_2 adsorption results in large cluster distortions away from the TO structure.

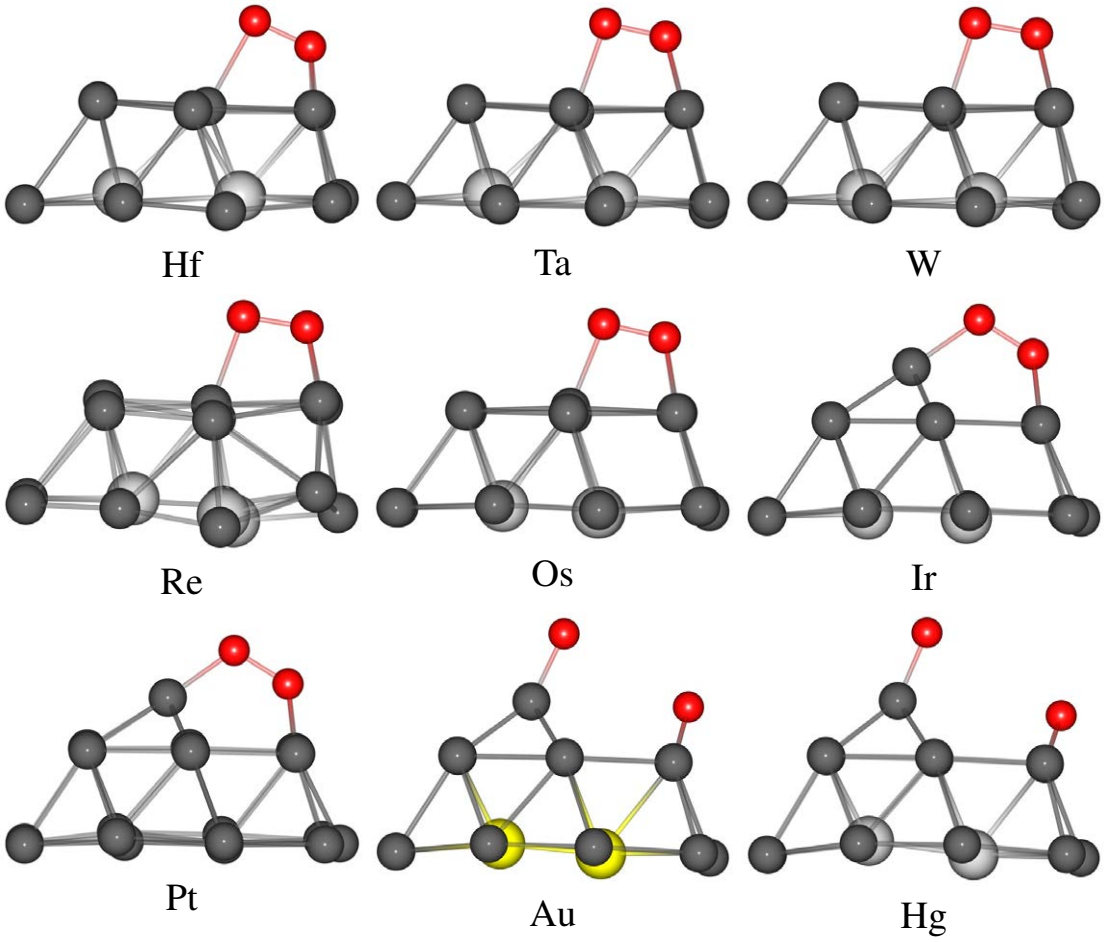

Figure 6.10: O_2 adsorption on site 7 for 5d M@Pt clusters. La@Pt is not shown as O_2 adsorption results in large cluster distortions away from the TO structure.

Table 6.2: O_2 binding energy (E_b) for sites 6 and 7 on the range of M@Pt clusters. All values are in eV.

	3d			4d			5d	
M@Pt	Site 6	Site 7	M@Pt	Site 6	Site 7	M@Pt	Site 6	Site 7
Sc	-1.22	-0.79	Y	-	-	La	-	-
Ti	-0.77	-0.40	Zr	-1.11	-2.46	Hf	-0.95	-0.43
V	-0.89	-0.77	Nb	-0.79	-0.67	Ta	-0.77	-0.66
Cr	-0.96	-0.64	Mo	-2.01	-2.14	W	-1.91	-0.91
Mn	-2.06	-1.69	Tc	-1.69	-3.03	Re	-3.75	-3.09
Fe	-0.91	-0.48	Ru	-1.34	-1.40	Os	-1.54	-1.10
Co	-	-	Rh	-1.26	-2.21	Ir	-1.24	-2.22
Ni	-1.99	-4.00	Pd	-1.26	-2.34	Pt	-1.80	-1.76
Cu	-1.18	-2.56	Ag	-1.18	-2.20	Au	-1.36	-2.34
Zn	-1.52	-2.55	Cd	-1.55	-2.26	Hg	-5.16	-2.48

likely due to two effects, firstly, the distorted (111) facet will provide a more favourable surface for O_2 to bind. Secondly, it is likely *d*-band characteristics will have an effect on O_2 binding energy. As the *d*-band is filled, the corresponding downshift in the *d*-band centre will result in weakening of the O_2 binding energy, a result commonly seen for early transition metals [216]. Pt alloyed with later d-block metals does not yield a downshift in the *d*-band centre, and will more likely result in an upshift. This upshift in the *d*-band centre will therefore likely also play a role in the increased binding energies for later M@Pt clusters.

As with the studies in Chapter 5, RMSD as well as Pt-X^{centre} of the cluster upon adsorption of O_2, have been studied. The calculated values for RMSD and Pt-X^{centre}, associated with O_2 adsorption are listed in Table 6.3. Several systems exhibit large RMSD values associated with structural rearrangements away from the TO structure upon O_2 adsorption, e.g. Y, Mo, La, Re, Hg. Particularly strong M–O binding is found for a number of these metals, which could partly responsible for the structural distortions where oxygen binding draws core atoms to the surface [163]. For those structures which do not distort away from the model TO system, the later d-block metals tend to have larger RMSD values associated with them. This is largely a result of the distortions of the (111) facet, particularly around the central atom. There also tend to be larger RMSD values associated with site 7 compared to those for site 6. This is because of the heavy distortions associated with the spontaneous O_2 dissociation found at site 7.

In Table 6.3, negative Pt-X^{centre} values show that there has been a contraction of the central

Table 6.3: RMSD of the whole cluster following O_2 adsorption and Pt-X^{centre} for the bare cluster as well as relative Pt-X^{centre} following O_2 adsorption on sites 6 and 7 for the range of M@Pt clusters. All values are in Å, a negative Pt-X^{centre} value corresponds to cluster contraction, whereas a positive value shows cluster expansion.

Row 4					
M@Pt	RMSD			Pt-X^{centre}	
	Site 6	Site 7	Bare	Site 6	Site 7
Sc	0.19	0.24	2.38	-0.62	-0.38
Ti	0.03	0.06	2.27	-0.08	-0.15
V	0.05	0.07	2.13	-0.04	-0.06
Cr	0.05	0.08	2.27	-0.10	-0.15
Mn	0.07	0.09	2.24	0.06	0.01
Fe	0.04	0.07	2.24	-0.01	-0.04
Co	-	-	-	-	-
Ni	0.34	0.70	2.27	0.10	-
Cu	0.30	0.48	2.24	1.14	1.28
Zn	0.28	0.40	2.25	1.21	1.34
Row 5					
M@Pt	RMSD			Pt-X^{centre}	
	Site 6	Site 7	Bare	Site 6	Site 7
Y	0.66	0.51	2.48	-	-
Zr	0.17	0.46	2.38	0.36	-
Nb	0.04	0.07	2.27	-0.10	-0.08
Mo	0.20	0.29	2.25	0.01	-0.10
Tc	0.08	0.53	2.27	0.07	-
Ru	0.04	0.22	2.31	-0.01	0.03
Rh	0.05	0.26	2.36	0.20	1.12
Pd	0.22	0.29	2.37	0.98	1.13
Ag	0.07	0.27	2.37	0.32	1.08
Cd	0.21	0.30	2.40	0.89	1.09
Row 6					
M@Pt	RMSD			Pt-X^{centre}	
	Site 6	Site 7	Bare	Site 6	Site 7
La	0.61	0.77	2.56	-	-
Hf	0.16	0.17	2.68	0.33	-0.18
Ta	0.04	0.07	2.25	-0.09	-0.09
W	0.35	0.07	2.19	-0.07	-0.05
Re	0.49	0.53	2.29	-	-
Os	0.05	0.06	2.30	-0.01	-0.03
Ir	0.04	0.27	2.38	0.05	1.11
Pt	0.19	0.19	2.44	0.82	0.83
Au	0.18	0.26	2.41	0.79	1.02
Hg	0.95	0.30	2.46	-	1.01

atom of the (111) facet, which has moved closer to the core. Conversely, a positive Pt-X^{centre} value shows that the central atom has moved away from the cluster core. Distortions of the (111) facet resulting in a positive Pt-X^{centre} value are of interest for fast O_2 dissociation. Generally, when O_2 is adsorbed on early M@Pt clusters, there is a contraction in Pt-X^{centre}. For the later M@Pt clusters, there is generally an expansion of Pt-X^{centre}, comparable to Pt_{38}. Clusters with strong core-shell Pt–M binding energies show a contraction of the Pt shell upon adsorption of O_2, whereas when M@Pt systems with weaker core-shell interactions are investigated there is an expansion of the Pt shell, a trend that has been observed before [217].

Figure 6.11 shows the relationship between Pt-X^{centre} and the binding energy. For site 6, there is no clear trend, suggesting that distortions of the (111) facet do not lead to significantly stronger O_2 binding. For site 7 there is a more obvious trend: in this case, the M@Pt clusters that result in spontaneous O_2 dissociation exhibit significantly stronger binding energies. However, the values of Pt-X^{centre} for those clusters where distortions of the (111) facet are observed do not vary significantly for O_2 adsorbed at site 6 or 7. Whilst there is generally little difference in binding energies between sites 6 and 7 for the early d-block metals, there are significant differences for the later d-block metals, where stronger binding energies are found at site 7.

The relationship between RMSD and the binding energies are shown in Figure 6.12. Aside from two outliers (Re and Hg, where distortions away from the TO were observed) there is no general trend for site 6. Once again, for site 7 there is a general trend that as the RMSD increases, the binding energy is stronger. When comparing sites 6 and 7, there is a greater range of RMSD values for site 7 than for site 6, if the outliers are excluded. This shows that when O_2 is adsorbed on site 7 the structure of the cluster is distorted to a greater amount than for site 6.

6.3.3 Density of States Analysis

As in Chapter 4, it is possible to calculate the *d*-band centre to give an indication of ORR kinetics. In this chapter, there is not only an interest in the initial stages of the ORR, O_2 dissociation, but also in the latter stages, where OH binding too strongly to the Pt surface will result in slow reaction kinetics. It is expected that a downshift in *d*-band centre will result in weakening of

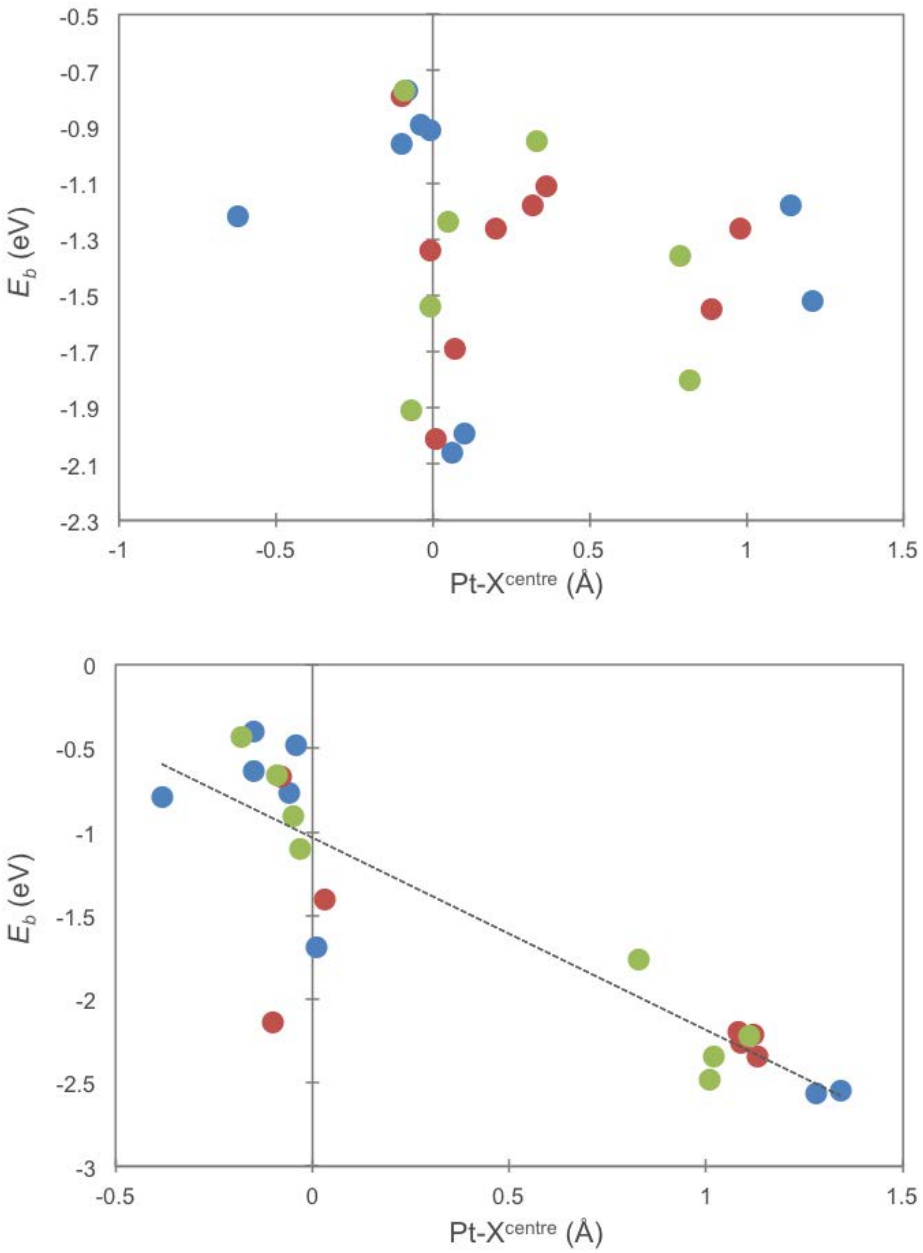

Figure 6.11: Plot of Pt-X^{centre} and O_2 binding energies for sites 6 (top) and 7 (bottom) on the range of M@Pt clusters. Data plotted for site 7 has a R^2 fit of 0.78.

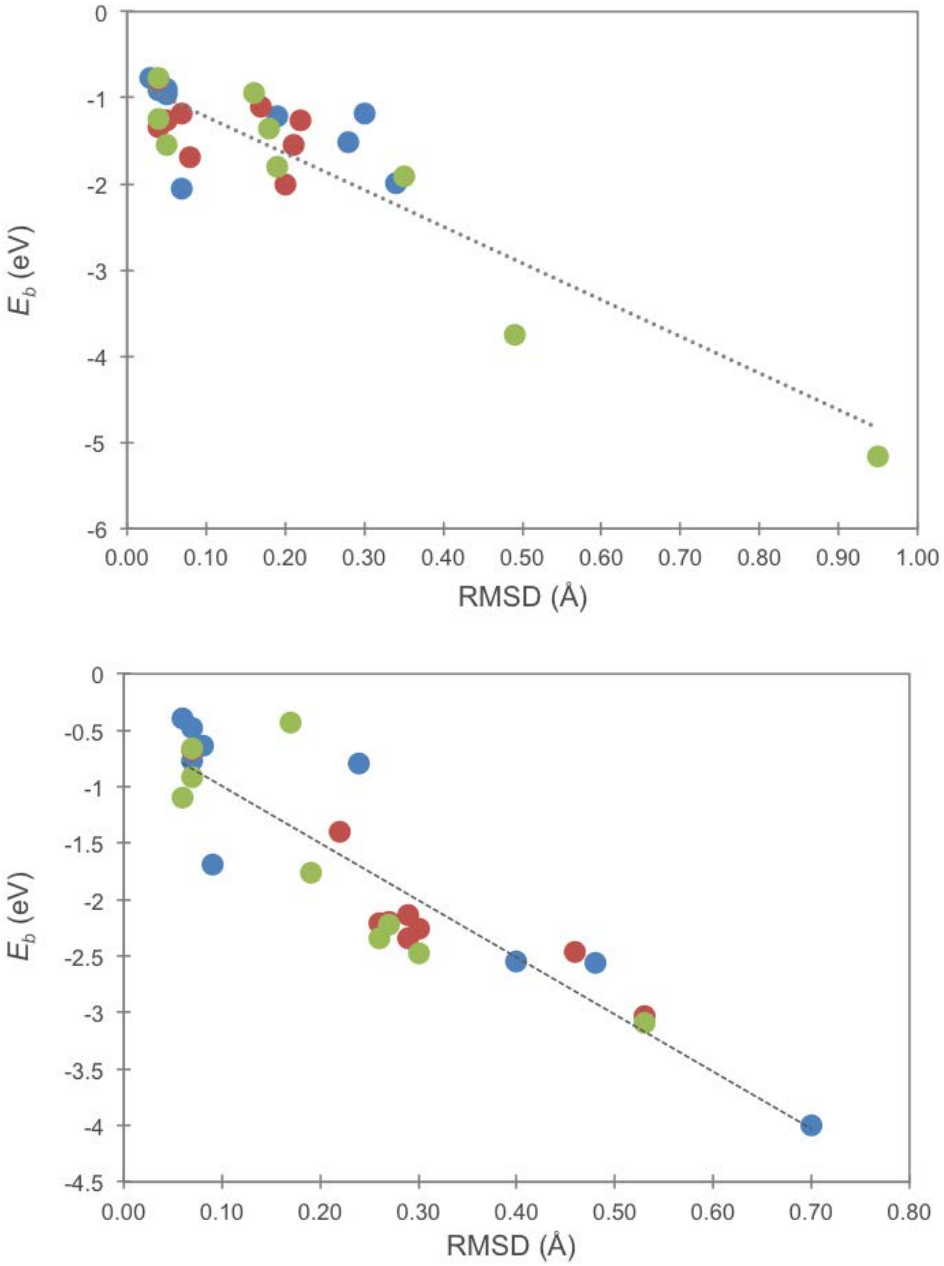

Figure 6.12: Plot of RMSD and O_2 binding energies for sites 6 (top) and 7 (bottom) on the range of M@Pt clusters. The data for sites 6 and 7 have a R^2 fit of 0.78 and 0.82, respectively.

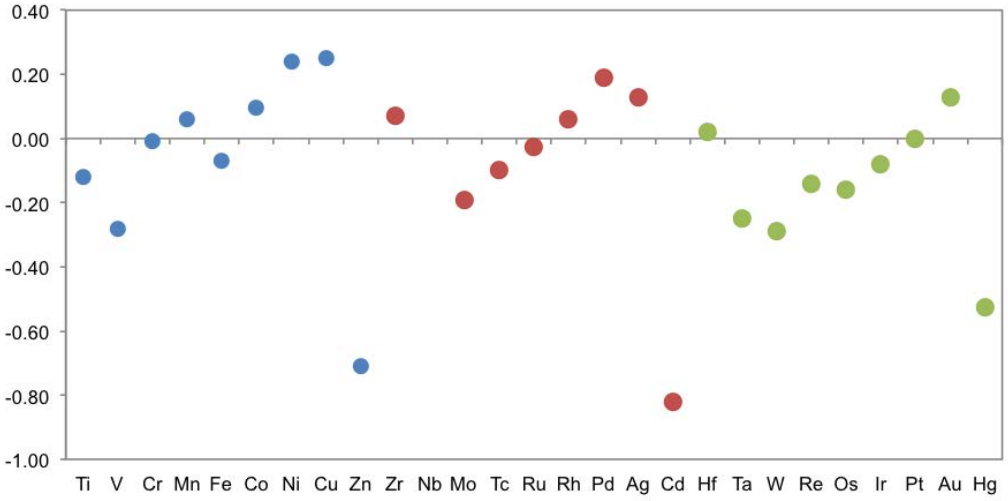

Figure 6.13: Variation of calculated *d*-band centres for the range of M@Pt clusters, relative to that of Pt.

molecular (e.g. OH, O_2) interactions to the Pt shell. Conversely, an upshift in the *d*-band centre will probably result in strengthening of these interactions. It is known that stronger Pt–O interactions lead to lower dissociation barriers [218–220], which is contrary to the need for reduced Pt–O binding to allow for desorption of oxygen containing species and formation, for example of H_2O from OH + H.

In Figure 6.13, the *d*-band centre of the Pt shell for varying compositions is plotted relative to that of the pure Pt_{38} cluster shell. It is possible to see that, in general, when Pt is alloyed with early d-block metals, such as Ti, significant downshifts in the *d*-band centre are observed. A number of Pt based alloys with early transition exhibit favourable ORR kinetics [221]. For the later d-block metals (around group 9) the shifts in the *d*-band centre become positive, showing an upshift. Shifts in the *d*-band centre arise from electronic and geometric effects. For the early d-block metals, it is likely that electronic effects dominate the changes in *d*-band characteristics, where significant charge transfer is observed between the M core and the Pt shell; charge transfer has been found to correlate with the Pt–M binding energy [222]. For the later d-block metals, where there is less charge transfer, it is likely that geometric effects dominate the changes in the *d*-band centre.

However, there are three exceptions to this general trend, where alloying Pt with group 12

elements leads to a significant downshift in the *d*-band centre. From the Bader analysis, charge transfer from the M core to the Pt shell is less than for early d-block metals. On average the core gains a charge of +0.63, +0.60 and +0.37 $|e|$ for Zn, Cd and Hg, respectively, while the Pt shell has an average charge of -0.09, -0.08 and -0.04 $|e|$. This compares to an average charge of +1.81 and -0.34 for the W@Pt core and shell, respectively (W@Pt results in the most negative *d*-band centre for group 3–11 metals). The Pt shell of W@Pt has a relative *d*-band centre of -0.29 eV, this compares to relative *d*-band centres of -0.71, -0.82 and -0.53 for Zn, Cd and Hg, respectively.

It also seems unlikely that geometric effects could account for this dramatic shift in *d*-band centre. The RMSD of the Pt shell is calculated to be 0.14, 0.08 and 0.09 Å for Zn, Cd and Hg, respectively relative to the Pt shell of the pure cluster. This suggests that there is not a significant deviation in the geometry of the Pt shell that might result in such a shift in *d*-band centre.

6.3.4 PtCo System

As mentioned in Section 6.3.1, the bare 38-atom Co@Pt TO cluster is "unstable" when optimised at the DFT level. During the geometry optimisation, the bare cluster distorts away from the TO structure towards the octahedral-icosahedral (Oh-Ih) structure as shown in Figure 6.14 [223]. As this was the only composition that resulted in significant structural rearrangement of the bare cluster, a GA search was performed on Co_6Pt_{32}, using the Gupta empirical potential with Cleri and Rosato parameters presented in Table 6.4. The GA search resulted in TO clusters being energetically favourable, suggesting they are stable when compared to other structural motifs. Furthermore, the GA search favours complete core-shell configurations, where structures with Co occupying surface positions result in higher energies. The fact that the Gupta-GA generates the Co@Pt TO cluster as the GM suggests that, in this case, perhaps the parameters are not reliable for the alloyed system.

DFT calculations reveal that Pt–Co is more weakly interacting (E_b = -2.98 eV) than the Pt–Ti dimer (E_b = -4.18 eV), but has a slightly stronger binding energy than Pt_2 (E_b = -2.38

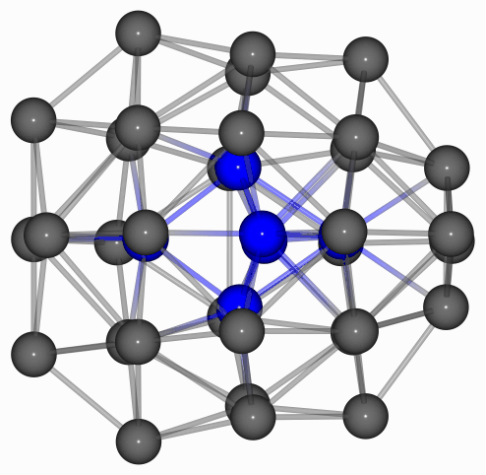

Figure 6.14: Distorted bare $Pt_{32}Co_6$ cluster with Oh-Ih structure.

Table 6.4: Cleri and Rosato potential parameters for Pt-Pt and Co-Co interactions, Pt-Co interactions are taken as the arithmetic mean. [156]

	Pt-Pt	Pt-Co	Co-Co
A (eV)	0.298	0.196	0.095
ξ (eV)	2.695	2.092	1.488
p	10.612	11.108	11.604
q	4.004	3.145	2.286
r0 (Å)	2.775	2.641	2.506

eV). However, as distortions of the (111) facet are found for Rh@Pt and Ir@Pt, which also have slightly stronger Pt–M dimer binding energies than the Pt–Co dimer, Co@Pt may be a promising candidate if a more suitable model system could be found.

6.3.5 Summary

Pt-Cu alloys have been demonstrated to give favourable ORR reaction kinetics [56, 100]. In the initial O_2 chemisorption studies, there was significant distortion of the (111) facet. The O_2 dissociation barrier on site 6 is 0.06 eV, while spontaneous O_2 dissociation was found at site 7 during geometry relaxation. This is in line with the O_2 dissociation barrier at position 6 on Pt_{38}, which is 0.04 eV. It is therefore confirmed that the Cu@Pt cluster displays favourable properties for O_2 dissociation as for the pure Pt system. However, from the investigations of *d*-band centre, an upshift of 0.25 eV is found suggesting that there will be increased Pt–O binding. It should be noted that copper is significantly cheaper than platinum, at a cost of around £0.06 g^{-1} (as of

June 2014 [224]) and £27.25 g^{-1} (as of June 2014 [224]), respectively. This means considerable cost reductions could be made through forming Cu@Pt electrocatalysts.

Pt-Rh alloys have been considered for fuel cell applications, [225], although Rh costs £21.06 g^{-1} (as of June 2014 [224]) so there would be relatively little cost reduction through alloying. As stated in Section 6.3.2, Rh_6Pt_{32} demonstrates favourable (111) facet distortions when O_2 is adsorbed. When a transition state search is performed on site 6, a dissociation barrier of 0.07 eV is found. Again, this is in line with the O_2 dissociation barrier of position 6 on the Pt_{38} cluster. When investigating site 7, as the Rh_6Pt_{32}–O_2 system is locally relaxed, the O_2 molecule dissociates. This suggests that the distortion of the (111) facets spontaneously overcomes the small O_2 dissociation barrier which has been observed previously. As with other late M@Pt systems, there is an upshift in the *d*-band centre, although in the case of Rh@Pt, the upshift is small (0.06 eV).

A similar trend is found for Pt alloyed with Pd and Cd, where the O_2 dissociation barriers at site 6 are 0.04 and 0.01 eV, respectively. At site 7 spontaneous dissociation is observed for both systems. For Pd@Pt, there is a slightly larger upshift in *d*-band centre, of 0.19 eV, compared to Rh@Pt although this is reduced slightly compared to Cu@Pt. Unlike the other late d-block metals, the Cd@Pt system results in a significant downshift in the *d*-band centre by 0.82 eV. Furthermore, whilst the cost of Pd is £15.42 g^{-1} (as of June 2014 [224]), Cd costs significantly less at £0.02 g^{-1} (as of June 2014 [226]). PtPd nanoparticles have been investigated for use in PEFCs and have been found to exhibit improved catalytic activity when compared to pure Pt electrocatalysis [227, 228].

The Pt-Ir system is slightly different from the others, with an O_2 dissociation barrier of 0.27 eV for site 6 and spontaneous dissociation observed at site 7. A barrier of 0.27 eV is still significantly below that for the bulk Pt system ($\sim$ 0.40 eV), although it is not as low as for other systems that have been investigated. However, the Ir@Pt system does have a slight downshift in the *d*-band centre, which could suggest that the alloyed system has advantages over the pure Pt system. Furthermore, the price of Ir is £11.38 g^{-1} (as of June 2014 [224]), which could still provide a reduction in the cost of the electrocatalyst. Furthermore, the formation of PtIr alloys

has previously been found to improve ORR kinetics [229].

6.4 Conclusions

It has been shown that favourable distortions of the (111) facet to facilitate O_2 dissociation are not confined to the pure Pt clusters. It has been found that late d-block metals with relatively weak Pt–M interactions also exhibit this behaviour. Furthermore, the weakened core–shell interactions facilitate O_2 dissociation to give very low dissociation barriers of < 0.10 eV. Weakening of the Pt–M core-shell interactions can have an adverse effect on cluster stability, where under-coordinated surface atoms are already less stable in clusters than the bulk [230]. This means that of the systems studied, each has distinct advantages and disadvantages associated with it, meaning the most promising system will have to be a compromise between the different characteristics being investigated.

Chapter 7

Concluding Remarks

7.1 Conclusions

The research presented in this thesis was aimed at investigating potential electrocatalysts for PEFCs. Beginning in Chapter 3, it was shown that global optimisation searches could be performed on potential sub-nanometre electrocatalysts. Utilising a combined GA-DFT approach yielded more accurate results than the traditional GA-EP method. This methodology is particularly important for systems that exhibit strong electronic effects upon alloying (charge effects), or have significantly different elemental properties (atomic sizes). This is particularly true for late transition metals alloyed with early transition metals, such as the PtTi and PtV systems. Furthermore, the importance of investigating spin effects was shown, where for small clusters spin can play an important role, changing the GM structure compared to the singlet.

In Chapter 4, chemisorption studies were performed on clusters of sizes up to 201-atoms. Alloying Pt with Ti results in significant shifts in the *d*-band properties with respect to the pure clusters. For the Ti@Pt core-shell cluster, these shifts are found to result in favourable weakening of Pt–OH and Pt–CO binding, where weakening of the Pt–Oh bond results in faster ORR kinetics and weakening of Pt–Ti binding results in reduced susceptibility to CO poisoning. However, these favourable sifts in the *d*-band are found for the monolayered Pt-shell, with bilayered shells leading to little deviation in *d*-band characteristics from the pure cluster. Fur-

thermore, it is found that the *d*-band shifts associated with the onion-like structures are also reduced with respect to the complete monolayered core-shell structure. If Ti were to occupy the surface sites, this would result in significantly stronger binding of both OH and CO and thus would not be desirable for a PEFC electrocatalyst. For the latter stages of the ORR, Ti@Pt clusters exhibit superior properties to the pure Pt clusters.

Oxygen dissociation on Ti@Pt clusters, up to the size of 116-atoms, was studied in Chapter 5 and compared with results for the Pt(111) slab. Very low dissociation barriers (typically below 0.1 eV) are found for the hollow sites on the (111) surface of the pure Pt cluster. These low dissociation barriers are attributed to the flexibility of the Pt shell, where binding of O_2 leads to distortions of the (111) facet that facilitate dissociation. These distortions of the (111) facet were not observed for the Pt(111) slab, where the surface infinite surface is constrained, thus a higher dissociation barrier was found ($\sim$0.4 eV). Significantly higher O_2 dissociation barriers were found on the (111) facet of the Ti@Pt clusters. The strong electronic effects observed in Chapters 3 and 4 resulted in a more rigid Pt-shell. This meant that favourable distortions of the (111) facet upon binding of O_2 were not possible, which resulted in higher dissociation barriers ($>$0.4 eV). Higher dissociation barriers ($>$0.3 eV) were also found on the (100) facet, for both the pure Pt and Ti@Pt clusters, where significant distortions were not observed. For the early stages of the ORR, the pure Pt cluster has significant advantages over the Ti@Pt cluster, where lower dissociation barriers will aid fast ORR kinetics.

Finally, in Chapter 6 some of the studies from Chapters 4 and 5 were expanded to the full range of *d*-block metals. Favourable distortions of the (111) facet are found for a number of M@Pt late *d*-block metals, which in turn facilitate O_2 dissociation with low barriers. However, for the majority of these M@Pt systems, where distortions of the (111) facet are observed, there are less significant shifts in the *d*-band. This means that a compromise must be found where competition between the weak M–Pt interactions to facilitate early stages of the ORR must be weighed up against the advantages of strong M–Pt interactions affecting the later stages of the ORR.

Table 7.1: CO stretching frequencies for binding sites on the Pt_5 cluster. The sites are displayed in Figure 7.1.

2S+1	Frequency (cm^{-1})								
	Site 1	Site 2	Site 3	Site 4	Site 5	Site 6	Site 7	Site 8	Site 9
Pt_5									
1	2019.41	2021.28	2020.68	1748.47	-	1832.17	-	1716.44	1732.59
3	2021.80	2018.24	2016.81	1826.17	1837.64	1823.52	-	1743.30	-
5	2024.89	2032.65	2025.09	1829.54	-	1871.65	-	1745.95	-
7	-	2029.41	2013.28	1834.80	1847.23	1804.79	1830.34	-	-
9	-	-	-	1835.80	1835.05	1827.39	-	-	-

7.2 Further Work

From the GA-DFT searches performed in Chapter 3, it is possible to extend the work in several directions. Firstly, it is possible to widen the size range being studied to include larger clusters. This will give a better idea of the size effects, which were briefly discussed within the Chapters 4 and 5. Secondly, it is possible to perform chemisorption studies on the sub-nanometre clusters in order to locate favourable binding sites as well as study the effect of chemisorption on the spin effects already investigated. An example of such a study is shown in 7.1, where CO adsorption is studied on all sites of the Pt_5 cluster at varying spin multiplicities. For CO chemisorption, it is also possible to probe CO stretching frequencies. The CO vibrational frequency has long been used as a structural probe, as it is susceptible to its local environment [231, 232]. CO stretching frequencies are influenced by coverage, particle size, charge, and structural rearrangement [233]. Results for the CO stretching frequencies for all sites at all multiplicities are shown in Figure 7.1. It would also be possible to expand the study to look at a greater array of alloys. The GA-DFT methodology has shown great promise for performing accurate searches on the PES but has only been used for a small set of alloyed systems.

The O_2 dissociation studies presented in Chapter 6 can be progressed in a number of directions. It is possible to study larger cluster sizes, in a similar fashion to the studies presented in Chapter 5. This would allow for the study of size effects, as well as the possible stabilisation of certain compositions that are not stable for the M_6Pt_{32} structure. Furthermore, for a number of that late transition metal systems, it would be possible to perform GA-EP structural

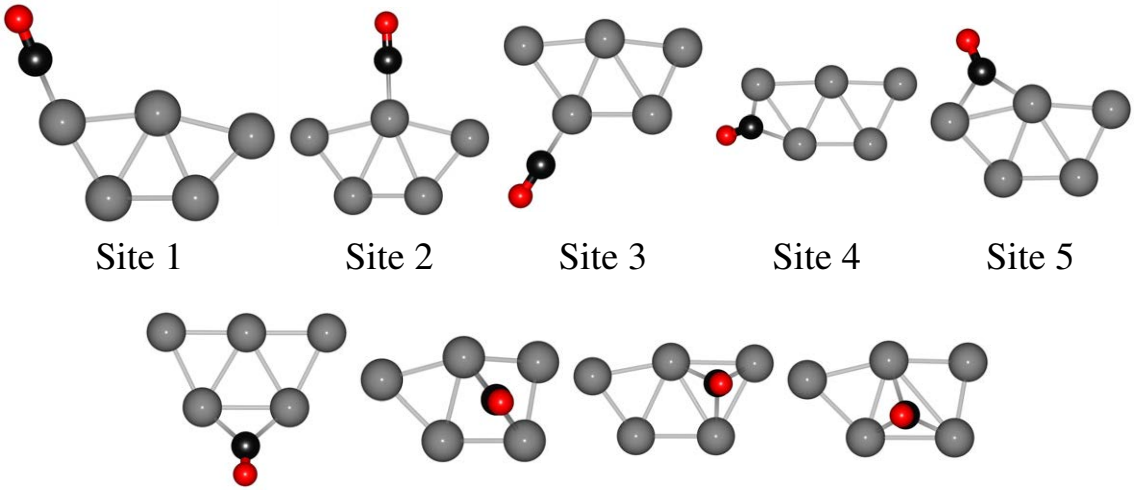

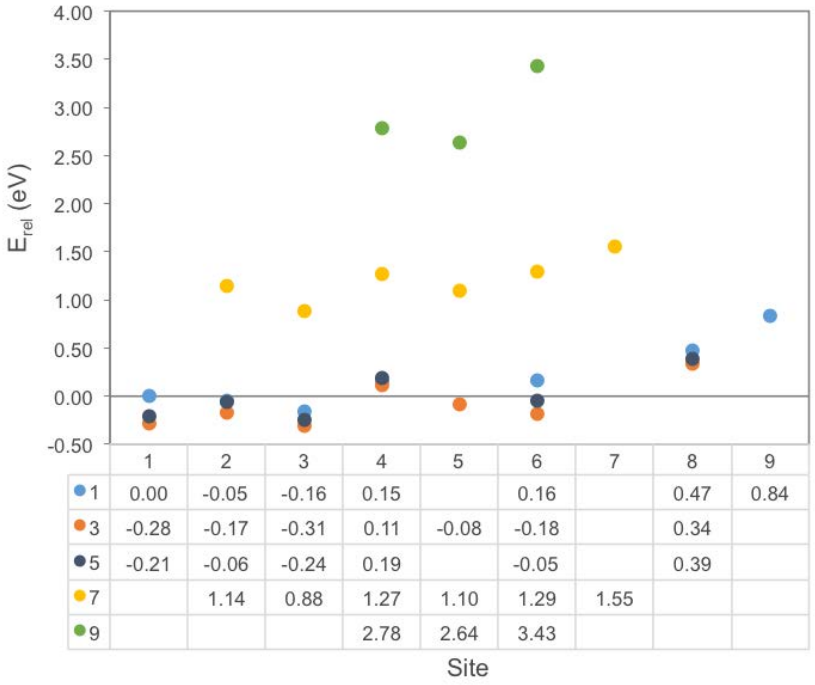

	1	2	3	4	5	6	7	8	9
1	0.00	-0.05	-0.16	0.15		0.16		0.47	0.84
3	-0.28	-0.17	-0.31	0.11	-0.08	-0.18		0.34	
5	-0.21	-0.06	-0.24	0.19		-0.05		0.39	
7		1.14	0.88	1.27	1.10	1.29	1.55		
9				2.78	2.64	3.43			

Figure 7.1: Chemisorption sites for CO on Pt_5, with their respective binding energies at varying spin multiplicities.

searchs, to allow for the study to progress on more realistic structures. Finally, a promising direction that has recently been gaining increased interest is the investigation of tri-metallic systems [234–239]. Through the inclusion of a third metal, it may be possible to produce structures with a compromise between core–shell interaction strength, whilst simultaneously shifting the *d*-band centre to slightly weaken Pt–OH binding.

Bibliography

[1] "bp.com/statisticalreview (Accessed 20/05/2014)."

[2] S. J. Davis, K. Caldeira, and H. D. Matthews, "Future CO2 emissions and climate change from existing energy infrastructure.," *Science*, vol. 329, pp. 1330–3, Sept. 2010.

[3] G. Gamboa and G. Munda, "The problem of windfarm location: A social multi-criteria evaluation framework," *Energy Policy*, vol. 35, pp. 1564–1583, Mar. 2007.

[4] N. Armaroli and V. Balzani, "The future of energy supply: Challenges and opportunities.," *Angew. Chem. Int. Ed. Engl.*, vol. 46, pp. 52–66, Jan. 2007.

[5] D. L. Gallup, "Production engineering in geothermal technology: A review," *Geothermics*, vol. 38, pp. 326–334, Sept. 2009.

[6] N. Zamel and X. Li, "Life cycle analysis of vehicles powered by a fuel cell and by internal combustion engine for Canada," *J. Power Sources*, vol. 155, pp. 297–310, Apr. 2006.

[7] A. Emadi, K. Rajashekara, S. Williamson, and S. Lukic, "Topological Overview of Hybrid Electric and Fuel Cell Vehicular Power System Architectures and Configurations," *IEEE Trans. Veh. Technol.*, vol. 54, pp. 763–770, May 2005.

[8] M. Ni, D. Y. Leung, and M. K. Leung, "A review on reforming bio-ethanol for hydrogen production," *Int. J. Hydrogen Energy*, vol. 32, pp. 3238–3247, Oct. 2007.

[9] A. Haryanto, S. Fernando, N. Murali, and S. Adhikari, "Current Status of Hydrogen Production Techniques by Steam Reforming of Ethanol: A Review," *Energy & Fuels*, vol. 19, pp. 2098–2106, Sept. 2005.

[10] M. Ni, M. K. Leung, D. Y. Leung, and K. Sumathy, "A review and recent developments in photocatalytic water-splitting using TiO2 for hydrogen production," *Renew. Sustain. Energy Rev.*, vol. 11, pp. 401–425, Apr. 2007.

[11] "http://www.dailymail.co.uk/news/article-2388417/Wind-farms-paid-30-million-year-stand-idle-grid-cope-energy-produce.html (Accessed 20/05/2014)."

[12] B. Sakintuna, F. Lamaridarkrim, and M. Hirscher, "Metal hydride materials for solid hydrogen storage: A review," *Int. J. Hydrogen Energy*, vol. 32, pp. 1121–1140, June 2007.

[13] S. Park, J. Vohs, and R. Gorte, "Direct oxidation of hydrocarbons in a solid-oxide fuel cell," *Nature*, vol. 404, pp. 265–7, Mar. 2000.

[14] N. H. Behling, *Fuel Cells: Current Technology Challenges and Future Research Needs*. Elsevier, 2012.

[15] K. Kendall, B. Pollet, A. Dhir, I. Staffell, B. Millington, and J. Jostins, "Hydrogen fuel cell hybrid vehicles (HFCHV) for Birmingham campus," *J. Power Sources*, vol. 196, pp. 325–330, Jan. 2011.

[16] A. I. Bevan, A. Züttel, D. Book, and I. R. Harris, "Performance of a metal hydride store on the Ross Barlow hydrogen powered canal boat," *Faraday Discuss.*, vol. 151, p. 353, Aug. 2011.

[17] A. Lanzini, M. Santarelli, and G. Orsello, "Residential Solid Oxide Fuel Cell Generator Fuelled by Ethanol: Cell, Stack and System Modelling with a Preliminary Experiment," *Fuel Cells*, vol. 10, pp. 654–675, June 2010.

[18] L. Shaw, J. Pratt, L. Klebanoff, T. Johnson, M. Arienti, and M. Moreno, "Analysis of H2 storage needs for early market man-portable fuel cell applications," *Int. J. Hydrogen Energy*, vol. 38, pp. 2810–2823, Feb. 2013.

[19] B. C. Steele and A. Heinzel, "Materials for fuel-cell technologies.," *Nature*, vol. 414, pp. 345–52, Nov. 2001.

[20] F. Barbir, *PEM Fuel Cells: Theory and Practice*. Academic Press, 2013.

[21] V. Mehta and J. S. Cooper, "Review and analysis of PEM fuel cell design and manufacturing," *J. Power Sources*, vol. 114, pp. 32–53, Feb. 2003.

[22] L. Carrette, K. A. Friedrich, and U. Stimming, "Fuel cells: principles, types, fuels, and applications.," *Chemphyschem*, vol. 1, pp. 162–93, Dec. 2000.

[23] M. Miller and A. Bazylak, "A review of polymer electrolyte membrane fuel cell stack testing," *J. Power Sources*, vol. 196, pp. 601–613, Jan. 2011.

[24] S. Peighambardoust, S. Rowshanzamir, and M. Amjadi, "Review of the proton exchange membranes for fuel cell applications," *Int. J. Hydrogen Energy*, vol. 35, pp. 9349–9384, Sept. 2010.

[25] Q. Li, J. O. Jensen, R. F. Savinell, and N. J. Bjerrum, "High temperature proton exchange membranes based on polybenzimidazoles for fuel cells," *Prog. Polym. Sci.*, vol. 34, pp. 449–477, May 2009.

[26] Y. Shao, G. Yin, Z. Wang, and Y. Gao, "Proton exchange membrane fuel cell from low temperature to high temperature: Material challenges," *J. Power Sources*, vol. 167, pp. 235–242, May 2007.

[27] J. Zhang, Z. Xie, J. Zhang, Y. Tang, C. Song, T. Navessin, Z. Shi, D. Song, H. Wang, D. P. Wilkinson, Z.-S. Liu, and S. Holdcroft, "High temperature PEM fuel cells," *J. Power Sources*, vol. 160, pp. 872–891, Oct. 2006.

[28] G. A. Camara, E. A. Ticianelli, S. Mukerjee, S. J. Lee, and J. McBreen, "The CO Poisoning Mechanism of the Hydrogen Oxidation Reaction in Proton Exchange Membrane Fuel Cells," *J. Electrochem. Soc.*, vol. 149, p. A748, June 2002.

[29] J. K. Nø rskov, J. Rossmeisl, A. Logadottir, L. Lindqvist, J. R. Kitchin, T. Bligaard, and H. Jónsson, "Origin of the Overpotential for Oxygen Reduction at a Fuel-Cell Cathode," *J. Phys. Chem. B*, vol. 108, pp. 17886–17892, Nov. 2004.

[30] R. Jinnouchi, "New Insight Into Microscale Transport Phenomena In PEFC By Quantum MD," *Microscale Thermophys. Eng.*, vol. 7, pp. 15–31, Jan. 2003.

[31] B. B. Xiao, Y. F. Zhu, X. Y. Lang, Z. Wen, and Q. Jiang, "Al13@Pt42 core-shell cluster for oxygen reduction reaction.," *Sci. Rep.*, vol. 4, p. 5205, Jan. 2014.

[32] J. A. Keith, G. Jerkiewicz, and T. Jacob, "Theoretical investigations of the oxygen reduction reaction on Pt(111).," *Chemphyschem*, vol. 11, pp. 2779–94, Sept. 2010.

[33] Y. Sha, T. H. Yu, B. V. Merinov, P. Shirvanian, and W. A. Goddard, "Oxygen Hydration Mechanism for the Oxygen Reduction Reaction at Pt and Pd Fuel Cell Catalysts," *J. Phys. Chem. Lett.*, vol. 2, pp. 572–576, Mar. 2011.

[34] L. Qi, J. Yu, and J. Li, "Coverage dependence and hydroperoxyl-mediated pathway of catalytic water formation on Pt (111) surface.," *J. Chem. Phys.*, vol. 125, p. 054701, Aug. 2006.

[35] A. B. Anderson and T. V. Albu, "Catalytic Effect of Platinum on Oxygen Reduction An Ab Initio Model Including Electrode Potential Dependence," *J. Electrochem. Soc.*, vol. 147, p. 4229, Nov. 2000.

[36] V. Tripković, E. Skúlason, S. Siahrostami, J. K. Nø rskov, and J. Rossmeisl, "The oxygen reduction reaction mechanism on Pt(111) from density functional theory calculations," *Electrochim. Acta*, vol. 55, pp. 7975–7981, Nov. 2010.

[37] A. Michaelides and P. Hu, "Catalytic Water Formation on Platinum: A First-Principles Study," *J. Am. Chem. Soc.*, vol. 123, pp. 4235–4242, May 2001.

[38] O. T. Holton and J. W. Stevenson, "The Role of Platinum in Proton Exchange Membrane Fuel Cells," *Platin. Met. Rev.*, vol. 57, pp. 259–271, Oct. 2013.

[39] A. Cybulski, J. A. Moulijn, and A. Stankiewicz, eds., *Novel Concepts in Catalysis and Chemical Reactors*. Weinheim, Germany: Wiley-VCH Verlag GmbH & Co. KGaA, Aug. 2010.

[40] J. M. Jaksic, N. M. Ristic, N. V. Krstajic, and M. M. Jaksic, "Electrocatalysis for hydrogen electrode reactions in the light of fermi dynamics and structural bonding FACTORSI. individual electrocatalytic properties of transition metals," *Int. J. Hydrogen Energy*, vol. 23, pp. 1121–1156, Dec. 1998.

[41] J. Greeley, I. E. L. Stephens, A. S. Bondarenko, T. P. Johansson, H. A. Hansen, T. F. Jaramillo, J. Rossmeisl, I. Chorkendorff, and J. K. Nø rskov, "Alloys of platinum and early transition metals as oxygen reduction electrocatalysts.," *Nat. Chem.*, vol. 1, pp. 552–6, Oct. 2009.

[42] C. M. Sánchez-Sánchez and A. J. Bard, "Hydrogen peroxide production in the oxygen reduction reaction at different electrocatalysts as quantified by scanning electrochemical microscopy.," *Anal. Chem.*, vol. 81, pp. 8094–100, Oct. 2009.

[43] I. E. L. Stephens, A. S. Bondarenko, U. Grø nbjerg, J. Rossmeisl, and I. Chorkendorff, "Understanding the electrocatalysis of oxygen reduction on platinum and its alloys," *Energy Environ. Sci.*, vol. 5, p. 6744, Apr. 2012.

[44] F. Xu, R. Xu, and S. Mu, "Enhanced SO2 and CO poisoning resistance of CeO2 modified Pt/C catalysts applied in PEM fuel cells," *Electrochim. Acta*, vol. 112, pp. 304–309, Dec. 2013.

[45] L. Roses, F. Gallucci, G. Manzolini, and M. van Sint Annaland, "Experimental study of steam methane reforming in a Pd-based fluidized bed membrane reactor," *Chem. Eng. J.*, vol. 222, pp. 307–320, Apr. 2013.

[46] J.-J. Hwang, "Sustainability study of hydrogen pathways for fuel cell vehicle applications," *Renew. Sustain. Energy Rev.*, vol. 19, pp. 220–229, Mar. 2013.

[47] S. M. M. Ehteshami and S. H. Chan, "A review of electrocatalysts with enhanced CO tolerance and stability for polymer electrolyte membarane fuel cells," *Electrochim. Acta*, vol. 93, pp. 334–345, Mar. 2013.

[48] Y. Wang, K. S. Chen, J. Mishler, S. C. Cho, and X. C. Adroher, "A review of polymer electrolyte membrane fuel cells: Technology, applications, and needs on fundamental research," *Appl. Energy*, vol. 88, pp. 981–1007, Apr. 2011.

[49] J. S. Spendelow and D. C. Papageorgopoulos, "Progress in PEMFC MEA Component R&Dat the DOE Fuel Cell Technologies Program," *Fuel Cells*, vol. 11, pp. 775–786, Dec. 2011.

[50] "http://www.platinum.matthey.com/prices/price-charts (Accessed 20/03/2014)."

[51] B. Millington, V. Whipple, and B. G. Pollet, "A novel method for preparing proton exchange membrane fuel cell electrodes by the ultrasonic-spray technique," *J. Power Sources*, vol. 196, pp. 8500–8508, Oct. 2011.

[52] F. Jaouen, E. Proietti, M. Lefèvre, R. Chenitz, J.-P. Dodelet, G. Wu, H. T. Chung, C. M. Johnston, and P. Zelenay, "Recent advances in non-precious metal catalysis for oxygen-reduction reaction in polymer electrolyte fuel cells," *Energy Environ. Sci.*, vol. 4, p. 114, Dec. 2011.

[53] V. Nallathambi, J.-W. Lee, S. P. Kumaraguru, G. Wu, and B. N. Popov, "Development of high performance carbon composite catalyst for oxygen reduction reaction in PEM Proton Exchange Membrane fuel cells," *J. Power Sources*, vol. 183, pp. 34–42, Aug. 2008.

[54] R. Bashyam and P. Zelenay, "A class of non-precious metal composite catalysts for fuel cells.," *Nature*, vol. 443, pp. 63–6, Sept. 2006.

[55] Z. Chen, D. Higgins, A. Yu, L. Zhang, and J. Zhang, "A review on non-precious metal electrocatalysts for PEM fuel cells," *Energy Environ. Sci.*, vol. 4, p. 3167, Aug. 2011.

[56] P. Mani, R. Srivastava, and P. Strasser, "Dealloyed Pt-Cu Core-Shell Nanoparticle Electrocatalysts for Use in PEM Fuel Cell Cathodes," *J. Phys. Chem. C*, vol. 112, pp. 2770–2778, Feb. 2008.

[57] A. Sarkar and A. Manthiram, "Synthesis of Pt@Cu CoreShell Nanoparticles by Galvanic Displacement of Cu by Pt 4+ Ions and Their Application as Electrocatalysts for Oxygen Reduction Reaction in Fuel Cells," *J. Phys. Chem. C*, vol. 114, pp. 4725–4732, Mar. 2010.

[58] T. Toda, "Enhancement of the Electroreduction of Oxygen on Pt Alloys with Fe, Ni, and Co," *J. Electrochem. Soc.*, vol. 146, p. 3750, Oct. 1999.

[59] S. Mukerjee, "Role of Structural and Electronic Properties of Pt and Pt Alloys on Electrocatalysis of Oxygen Reduction," *J. Electrochem. Soc.*, vol. 142, p. 1409, May 1995.

[60] J. Zeng, S. Liao, J. Y. Lee, and Z. Liang, "Oxygen reduction reaction operated on magnetically-modified PtFe/C electrocatalyst," *Int. J. Hydrogen Energy*, vol. 35, pp. 942–948, Feb. 2010.

[61] J. J. Baschuk and X. Li, "Carbon monoxide poisoning of proton exchange membrane fuel cells," *Int. J. Energy Res.*, vol. 25, pp. 695–713, June 2001.

[62] S. Mukerjee and S. Srinivasan, "Enhanced electrocatalysis of oxygen reduction on platinum alloys in proton exchange membrane fuel cells," *J. Electroanal. Chem.*, vol. 357, pp. 201–224, Oct. 1993.

[63] H. R. Colón-Mercado, H. Kim, and B. N. Popov, "Durability study of Pt3Ni1 catalysts as cathode in PEM fuel cells," *Electrochem. commun.*, vol. 6, pp. 795–799, Aug. 2004.

[64] P. Yu, M. Pemberton, and P. Plasse, "PtCo/C cathode catalyst for improved durability in PEMFCs," *J. Power Sources*, vol. 144, pp. 11–20, June 2005.

[65] M. Götz and H. Wendt, "Binary and ternary anode catalyst formulations including the elements W, Sn and Mo for PEMFCs operated on methanol or reformate gas," *Electrochim. Acta*, vol. 43, pp. 3637–3644, Aug. 1998.

[66] C. He, H. R. Kunz, and J. M. Fenton, "Electro-oxidation of Hydrogen with Carbon Monoxide on Pt/Ru-Based Ternary Catalysts," *J. Electrochem. Soc.*, vol. 150, p. A1017, Aug. 2003.

[67] X. Li, S. Park, and B. N. Popov, "Highly stable Pt and PtPd hybrid catalysts supported on a nitrogen-modified carbon composite for fuel cell application," *J. Power Sources*, vol. 195, pp. 445–452, Jan. 2010.

[68] A. C. Garcia, V. A. Paganin, and E. A. Ticianelli, "CO tolerance of PdPt/C and PdPtRu/C anodes for PEMFC," *Electrochim. Acta*, vol. 53, pp. 4309–4315, May 2008.

[69] D. C. Papageorgopoulos, M. Keijzer, J. B. J. Veldhuis, and F. A. de Bruijn, "CO Tolerance of Pd-Rich Platinum Palladium Carbon-Supported Electrocatalysts," *J. Electrochem. Soc.*, vol. 149, p. A1400, Nov. 2002.

[70] B. Fçclar, A. Bayrakçeken, and . Erolu, "Effect of Pd loading in Pd-Pt bimetallic catalysts doped into hollow core mesoporous shell carbon on performance of proton exchange membrane fuel cells," *J. Power Sources*, vol. 193, pp. 17–23, Aug. 2009.

[71] D. J. Ham, Y. K. Kim, S. H. Han, and J. S. Lee, "Pt/WC as an anode catalyst for PEMFC: Activity and CO tolerance," *Catal. Today*, vol. 132, pp. 117–122, Mar. 2008.

[72] D. Papageorgopoulos, M. Keijzer, and F. de Bruijn, "The inclusion of Mo, Nb and Ta in Pt and PtRu carbon supported electrocatalysts in the quest for improved CO tolerant PEMFC anodes," *Electrochim. Acta*, vol. 48, pp. 197–204, Nov. 2002.

[73] S. Mukerjee, "Investigation of Enhanced CO Tolerance in Proton Exchange Membrane Fuel Cells by Carbon Supported PtMo Alloy Catalyst," *Electrochem. Solid-State Lett.*, vol. 2, p. 12, Jan. 1999.

[74] T. Schmidt, Z. Jusys, H. Gasteiger, R. Behm, U. Endruschat, and H. Boennemann, "On the CO tolerance of novel colloidal PdAu/carbon electrocatalysts," *J. Electroanal. Chem.*, vol. 501, pp. 132–140, Mar. 2001.

[75] S.-Y. Huang, P. Ganesan, S. Park, and B. N. Popov, "Development of a titanium dioxide-supported platinum catalyst with ultrahigh stability for polymer electrolyte membrane fuel cell applications.," *J. Am. Chem. Soc.*, vol. 131, pp. 13898–9, Oct. 2009.

[76] G. Liu, H. Zhang, Y. Zhai, Y. Zhang, D. Xu, and Z.-g. Shao, "Pt4ZrO2/C cathode catalyst for improved durability in high temperature PEMFC based on H3PO4 doped PBI," *Electrochem. commun.*, vol. 9, pp. 135–141, Jan. 2007.

[77] A. Lima, C. Coutanceau, J.-M. LÉger, and C. Lamy, "Investigation of Ternary Catalysts for Methanol Electrooxidation," *J. Appl. Electrochem.*, vol. 31, pp. 379–386, Apr. 2001.

[78] C. Roth, M. Goetz, and H. Fuess, "Synthesis and characterization of carbon-supported PtRuWOx catalysts by spectroscopic and diffraction methods," *J. Appl. Electrochem.*, vol. 31, pp. 793–798, July 2001.

[79] R. Venkataraman, H. R. Kunz, and J. M. Fenton, "Development of New CO Tolerant Ternary Anode Catalysts for Proton Exchange Membrane Fuel Cells," *J. Electrochem. Soc.*, vol. 150, p. A278, Mar. 2003.

[80] Y. Liang, H. Zhang, Z. Tian, X. Zhu, X. Wang, and B. Yi, "Synthesis and structure-activity relationship exploration of carbon-supported PtRuNi nanocomposite as a CO-tolerant electrocatalyst for proton exchange membrane fuel cells.," *J. Phys. Chem. B*, vol. 110, pp. 7828–34, Apr. 2006.

[81] Y. Liang, H. Zhang, H. Zhong, X. Zhu, Z. Tian, D. Xu, and B. Yi, "Preparation and characterization of carbon-supported PtRuIr catalyst with excellent CO-tolerant performance for proton-exchange membrane fuel cells," *J. Catal.*, vol. 238, pp. 468–476, Mar. 2006.

[82] E. Antolini, "Platinum-based ternary catalysts for low temperature fuel cells," *Appl. Catal. B Environ.*, vol. 74, pp. 337–350, July 2007.

[83] A. Seo, J. Lee, K. Han, and H. Kim, "Performance and stability of Pt-based ternary alloy catalysts for PEMFC," *Electrochim. Acta*, vol. 52, pp. 1603–1611, Dec. 2006.

[84] G. Tamizhmani, "Life Tests of Carbon-Supported Pt-Cr-Cu Electrocatalysts in Solid-Polymer Fuel Cells," *J. Electrochem. Soc.*, vol. 141, p. L132, Sept. 1994.

[85] J. Shim, D.-Y. Yoo, and J.-S. Lee, "Characteristics for electrocatalytic properties and hydrogenoxygen adsorption of platinum ternary alloy catalysts in polymer electrolyte fuel cell," *Electrochim. Acta*, vol. 45, pp. 1943–1951, Feb. 2000.

[86] M. E. Geusic, R. R. Freeman, and M. A. Duncan, "Photofragmentation of antimony and bismuth cluster cations at 248 nm," *J. Chem. Phys.*, vol. 88, p. 163, Jan. 1988.

[87] A. S. K. Hashmi and G. J. Hutchings, "Gold catalysis.," *Angew. Chem. Int. Ed. Engl.*, vol. 45, pp. 7896–936, Dec. 2006.

[88] D. J. Trevor, R. L. Whetten, D. M. Cox, and A. Kaldor, "Gas phase platinum cluster reactions with benzene and several hexanes: evidence of extensive dehydrogenation and size-dependent chemisorption," *J. Am. Chem. Soc.*, vol. 107, pp. 518–519, Jan. 1985.

[89] S. E. Apsel, J. W. Emmert, J. Deng, and L. A. Bloomfield, "Surface-Enhanced Magnetism in Nickel Clusters," *Phys. Rev. Lett.*, vol. 76, pp. 1441–1444, Feb. 1996.

[90] P. H. Acioli and J. Jellinek, "Electron Binding Energies of Anionic Magnesium Clusters and the Nonmetal-to-Metal Transition," *Phys. Rev. Lett.*, vol. 89, p. 213402, Nov. 2002.

[91] O. C. Thomas, W. Zheng, S. Xu, and K. H. Bowen, "Onset of Metallic Behavior in Magnesium Clusters," *Phys. Rev. Lett.*, vol. 89, p. 213403, Nov. 2002.

[92] M. Schmidt, R. Kusche, W. Kronmüller, B. von Issendorff, and H. Haberland, "Experimental Determination of the Melting Point and Heat Capacity for a Free Cluster of 139 Sodium Atoms," *Phys. Rev. Lett.*, vol. 79, pp. 99–102, July 1997.

[93] P. Dugourd, D. Rayane, P. Labastie, B. Vezin, J. Chevaleyre, and M. Broyer, "Measurements of lithium cluster ionization potentials," *Chem. Phys. Lett.*, vol. 197, no. 45, pp. 433–437, 1992.

[94] G. von Helden, M.-T. Hsu, P. R. Kemper, and M. T. Bowers, "Structures of carbon cluster ions from 3 to 60 atoms: Linears to rings to fullerenes," *J. Chem. Phys.*, vol. 95, p. 3835, Sept. 1991.

[95] M. F. Jarrold and V. A. Constant, "Silicon cluster ions: Evidence for a structural transition," *Phys. Rev. Lett.*, vol. 67, pp. 2994–2997, Nov. 1991.

[96] A. Ding and J. Hesslich, "The abundance of Ar and Kr microclusters generated by supersonic expansion," *Chem. Phys. Lett.*, vol. 94, pp. 54–57, Jan. 1983.

[97] P. W. Stephens and J. G. King, "Experimental Investigation of Small Helium Clusters: Magic Numbers and the Onset of Condensation," *Phys. Rev. Lett.*, vol. 51, pp. 1538–1541, Oct. 1983.

[98] O. Echt, K. Sattler, and E. Recknagel, "Magic Numbers for Sphere Packings: Experimental Verification in Free Xenon Clusters," *Phys. Rev. Lett.*, vol. 47, pp. 1121–1124, Oct. 1981.

[99] A. Chandan, M. Hattenberger, A. El-kharouf, S. Du, A. Dhir, V. Self, B. G. Pollet, A. Ingram, and W. Bujalski, "High temperature (HT) polymer electrolyte membrane fuel cells (PEMFC) A review," *J. Power Sources*, vol. 231, pp. 264–278, June 2013.

[100] P. Mani, R. Srivastava, and P. Strasser, "Dealloyed binary PtM3 (M=Cu, Co, Ni) and ternary PtNi3M (M=Cu, Co, Fe, Cr) electrocatalysts for the oxygen reduction reaction: Performance in polymer electrolyte membrane fuel cells," *J. Power Sources*, vol. 196, pp. 666–673, Jan. 2011.

[101] R. L. Johnston, *Atomic & Molecular Clusters*. London: Taylor & Francis, 2002.

[102] S. Vajda, M. J. Pellin, J. P. Greeley, C. L. Marshall, L. A. Curtiss, G. A. Ballentine, J. W. Elam, S. Catillon-Mucherie, P. C. Redfern, F. Mehmood, and P. Zapol, "Subnanometre platinum clusters as highly active and selective catalysts for the oxidative dehydrogenation of propane.," *Nat. Mater.*, vol. 8, pp. 213–6, Mar. 2009.

[103] R. Ferrando, J. Jellinek, and R. L. Johnston, "Nanoalloys: from theory to applications of alloy clusters and nanoparticles.," *Chem. Rev.*, vol. 108, pp. 845–910, Mar. 2008.

[104] "Nanoalloys: From Theory to Application," *Faraday Discuss.*, vol. 138, p. 440, Feb. 2008.

[105] W. Miehle, O. Kandler, T. Leisner, and O. Echt, "Mass spectrometric evidence for icosahedral structure in large rare gas clusters: Ar, Kr, Xe," *J. Chem. Phys.*, vol. 91, p. 5940, Nov. 1989.

[106] J. A. Zimmerman, J. R. Eyler, S. B. H. Bach, and S. W. McElvany, "Magic number carbon clusters: Ionization potentials and selective reactivity," *J. Chem. Phys.*, vol. 94, p. 3556, Mar. 1991.

[107] H. Tsunoyama and T. Tsukuda, "Magic numbers of gold clusters stabilized by PVP.," *J. Am. Chem. Soc.*, vol. 131, pp. 18216–7, Dec. 2009.

[108] K. M. Bratlie, H. Lee, K. Komvopoulos, P. Yang, and G. A. Somorjai, "Platinum nanoparticle shape effects on benzene hydrogenation selectivity.," *Nano Lett.*, vol. 7, pp. 3097–101, Oct. 2007.

[109] F. Baletto, R. Ferrando, A. Fortunelli, F. Montalenti, and C. Mottet, "Crossover among structural motifs in transition and noble-metal clusters," *J. Chem. Phys.*, vol. 116, p. 3856, Mar. 2002.

[110] J. Jellinek, ed., *Theory of Atomic and Molecular Clusters*. Springer Series in Cluster Physics, Berlin, Heidelberg: Springer Berlin Heidelberg, 1999.

[111] N. Marković, R. Adžić, B. Cahan, and E. Yeager, "Structural effects in electrocatalysis: oxygen reduction on platinum low index single-crystal surfaces in perchloric acid solutions," *J. Electroanal. Chem.*, vol. 377, pp. 249–259, Oct. 1994.

[112] F. El Kadiri, R. Faure, and R. Durand, "Electrochemical reduction of molecular oxygen on platinum single crystals," *J. Electroanal. Chem. Interfacial Electrochem.*, vol. 301, pp. 177–188, Feb. 1991.

[113] H. A. Gasteiger and P. N. Ross, "Oxygen Reduction on Platinum Low-Index Single-Crystal Surfaces in Alkaline Solution: Rotating Ring Disk Pt(hkl) Studies," *J. Phys. Chem.*, vol. 100, pp. 6715–6721, Jan. 1996.

[114] N. M. Marković, T. J. Schmidt, V. Stamenković, and P. N. Ross, "Oxygen Reduction Reaction on Pt and Pt Bimetallic Surfaces: A Selective Review," *Fuel Cells*, vol. 1, pp. 105–116, July 2001.

[115] J. Greeley, J. Rossmeisl, A. Hellmann, and J. K. Norskov, "Theoretical Trends in Particle Size Effects for the Oxygen Reduction Reaction," *Zeitschrift für Phys. Chemie*, vol. 221, pp. 1209–1220, Oct. 2007.

[116] D. Wales, *Energy Landscapes: Applications to Clusters, Biomolecules and Glasses*. Cambridge University Press, 2003.

[117] R. Gupta, "Lattice relaxation at a metal surface," *Phys. Rev. B*, vol. 23, pp. 6265–6270, June 1981.

[118] A. P. Sutton and J. Chen, "Long-range FinnisSinclair potentials," *Philos. Mag. Lett.*, vol. 61, pp. 139–146, Mar. 1990.

[119] J. N. Murrell and R. E. Mottram, "Potential energy functions for atomic solids," *Mol. Phys.*, vol. 69, pp. 571–585, Feb. 1990.

[120] R. L. Johnston, "Evolving better nanoparticles: Genetic algorithms for optimising cluster geometries," *Dalt. Trans.*, no. 22, p. 4193, 2003.

[121] S. Heiles, A. J. Logsdail, R. Schäfer, and R. L. Johnston, "Dopant-induced 2D-3D transition in small Au-containing clusters: DFT-global optimisation of 8-atom Au-Ag nanoalloys.," *Nanoscale*, vol. 4, pp. 1109–15, Feb. 2012.

[122] P. A. Derosa, J. M. Seminario, and P. B. Balbuena, "Properties of Small Bimetallic NiCu Clusters," *J. Phys. Chem. A*, vol. 105, pp. 7917–7925, Aug. 2001.

[123] P. Hohenberg and W. Kohn, "Inhomogeneous Electron Gas," *Phys. Rev.*, vol. 136, pp. B864–B871, Nov. 1964.

[124] W. Kohn and L. J. Sham, "Self-Consistent Equations Including Exchange and Correlation Effects," *Phys. Rev.*, vol. 140, pp. A1133–A1138, Nov. 1965.

[125] M. Valiev, E. Bylaska, N. Govind, K. Kowalski, T. Straatsma, H. Van Dam, D. Wang, J. Nieplocha, E. Apra, T. Windus, and W. de Jong, "NWChem: A comprehensive and scalable open-source solution for large scale molecular simulations," *Comput. Phys. Commun.*, vol. 181, pp. 1477–1489, Sept. 2010.

[126] P. Giannozzi, S. Baroni, N. Bonini, M. Calandra, R. Car, C. Cavazzoni, D. Ceresoli, G. L. Chiarotti, M. Cococcioni, I. Dabo, A. Dal Corso, S. de Gironcoli, S. Fabris, G. Fratesi, R. Gebauer, U. Gerstmann, C. Gougoussis, A. Kokalj, M. Lazzeri, L. Martin-Samos, N. Marzari, F. Mauri, R. Mazzarello, S. Paolini, A. Pasquarello, L. Paulatto, C. Sbraccia, S. Scandolo, G. Sclauzero, A. P. Seitsonen, A. Smogunov, P. Umari, and R. M. Wentzcovitch, "QUANTUM ESPRESSO: a modular and open-source software project for quantum simulations of materials.," *J. Phys. Condens. Matter*, vol. 21, p. 395502, Sept. 2009.

[127] G. Kresse and J. Hafner, "Ab initio molecular dynamics for liquid metals," *Phys. Rev. B*, vol. 47, pp. 558–561, Jan. 1993.

[128] G. Kresse, "Efficient iterative schemes for ab initio total-energy calculations using a plane-wave basis set," *Phys. Rev. B*, vol. 54, pp. 11169–11186, Oct. 1996.

[129] G. Kresse and J. Furthmüller, "Efficiency of ab-initio total energy calculations for metals and semiconductors using a plane-wave basis set," *Comput. Mater. Sci.*, vol. 6, pp. 15–50, July 1996.

[130] G. Kresse and J. Hafner, "Ab initio molecular-dynamics simulation of the liquid-metalamorphous-semiconductor transition in germanium," *Phys. Rev. B*, vol. 49, pp. 14251–14269, May 1994.

[131] R. S. Mulliken, "Electronic Population Analysis on LCAO[Single Bond]MO Molecular Wave Functions. I," *J. Chem. Phys.*, vol. 23, p. 1833, Dec. 1955.

[132] R. S. Mulliken, "Criteria for the Construction of Good Self-Consistent-Field Molecular Orbital Wave Functions, and the Significance of LCAO-MO Population Analysis," *J. Chem. Phys.*, vol. 36, p. 3428, July 1962.

[133] P.-O. Löwdin, "The historical development of the electron correlation problem," *Int. J. Quantum Chem.*, vol. 55, pp. 77–102, July 1995.

[134] L. Cusachs and P. Politzer, "On the problem of defining the charge on an atom in a molecule," *Chem. Phys. Lett.*, vol. 1, pp. 529–531, Jan. 1968.

[135] P.-O. Löwdin, "Quantum Theory of Many-Particle Systems. I. Physical Interpretations by Means of Density Matrices, Natural Spin-Orbitals, and Convergence Problems in the Method of Configurational Interaction," *Phys. Rev.*, vol. 97, pp. 1474–1489, Mar. 1955.

[136] R. F. W. Bader, *Atoms in Molecules: a Quantum Theory*. New York: Oxford University Press, 1994.

[137] W. Tang, E. Sanville, and G. Henkelman, "A grid-based Bader analysis algorithm without lattice bias.," *J. Phys. Condens. Matter*, vol. 21, p. 084204, Feb. 2009.

[138] G. Henkelman, A. Arnaldsson, and H. Jónsson, "A fast and robust algorithm for Bader decomposition of charge density," *Comput. Mater. Sci.*, vol. 36, pp. 354–360, June 2006.

[139] E. Sanville, S. D. Kenny, R. Smith, and G. Henkelman, "Improved grid-based algorithm for Bader charge allocation.," *J. Comput. Chem.*, vol. 28, pp. 899–908, May 2007.

[140] C. Xiao and F. Hagelberg, "Charge transfer mechanism in Cu-doped silicon clusters: a density functional study," *J. Mol. Struct. THEOCHEM*, vol. 529, pp. 241–257, Sept. 2000.

[141] P. Boski, S. Dennler, and J. Hafner, "Strong spin-orbit effects in small Pt clusters: geometric structure, magnetic isomers and anisotropy.," *J. Chem. Phys.*, vol. 134, p. 034107, Jan. 2011.

[142] V. Kumar and Y. Kawazoe, "Evolution of atomic and electronic structure of Pt clusters: Planar, layered, pyramidal, cage, cubic, and octahedral growth," *Phys. Rev. B*, vol. 77, p. 205418, May 2008.

[143] H. Yuan, H. Chen, A. Kuang, and B. Wu, "Spinorbit effect and magnetic anisotropy in Pt clusters," *J. Magn. Magn. Mater.*, vol. 331, pp. 7–16, Apr. 2013.

[144] C. Heredia, V. Ferraresi-Curotto, and M. López, "Characterization of Ptn (n=212) clusters through global reactivity descriptors and vibrational spectroscopy, a theoretical study," *Comput. Mater. Sci.*, vol. 53, pp. 18–24, Feb. 2012.

[145] A. Sebetci, "Does spin-orbit coupling effect favor planar structures for small platinum clusters?," *Phys. Chem. Chem. Phys.*, vol. 11, pp. 921–5, Feb. 2009.

[146] K. Bhattacharyya and C. Majumder, "Growth pattern and bonding trends in Ptn (n=213) clusters: Theoretical investigation based on first principle calculations," *Chem. Phys. Lett.*, vol. 446, pp. 374–379, Oct. 2007.

[147] L.-S. Wang, H. Wu, and H. Cheng, "Photoelectron spectroscopy of small chromium clusters: Observation of even-odd alternations and theoretical interpretation," *Phys. Rev. B*, vol. 55, pp. 12884–12887, May 1997.

[148] J. Zhao, Q. Qiu, B. Wang, J. Wang, and G. Wang, "Geometric and electronic properties of titanium clusters studied by ultrasoft pseudopotential," *Solid State Commun.*, vol. 118, pp. 157–161, Apr. 2001.

[149] E. Antolini, R. R. Passos, and E. A. Ticianelli, "Electrocatalysis of oxygen reduction on a carbon supported platinumvanadium alloy in polymer electrolyte fuel cells," *Electrochim. Acta*, vol. 48, pp. 263–270, Dec. 2002.

[150] B. Wang, "Recent development of non-platinum catalysts for oxygen reduction reaction," *J. Power Sources*, vol. 152, pp. 1–15, Dec. 2005.

[151] R. Koffi, C. Coutanceau, E. Garnier, J.-M. Léger, and C. Lamy, "Synthesis, characterization and electrocatalytic behaviour of non-alloyed PtCr methanol tolerant nanoelectrocatalysts for the oxygen reduction reaction (ORR)," *Electrochim. Acta*, vol. 50, pp. 4117–4127, July 2005.

[152] C. W. Bezerra, L. Zhang, H. Liu, K. Lee, A. L. Marques, E. P. Marques, H. Wang, and J. Zhang, "A review of heat-treatment effects on activity and stability of PEM fuel cell catalysts for oxygen reduction reaction," *J. Power Sources*, vol. 173, pp. 891–908, Nov. 2007.

[153] C. J. Heard and R. L. Johnston, "A density functional global optimisation study of neutral 8-atom Cu-Ag and Cu-Au clusters," *Eur. Phys. J. D*, vol. 67, p. 34, Mar. 2013.

[154] S. Heiles and R. L. Johnston, "Global Optimization of Clusters using Electronic Structure Methods," *Int. J. Quantum Chem.*, pp. n/a–n/a, May 2013.

[155] A. J. Logsdail, Z. Y. Li, and R. L. Johnston, "Development and optimization of a novel genetic algorithm for identifying nanoclusters from scanning transmission electron microscopy images.," *J. Comput. Chem.*, vol. 33, pp. 391–400, Feb. 2012.

[156] F. Cleri and V. Rosato, "Tight-binding potentials for transition metals and alloys," *Phys. Rev. B*, vol. 48, pp. 22–33, July 1993.

[157] M. B. Airola and M. D. Morse, "Rotationally resolved spectroscopy of Pt[sub 2]," *J. Chem. Phys.*, vol. 116, p. 1313, Jan. 2002.

[158] H. Grönbeck and W. Andreoni, "Gold and platinum microclusters and their anions: comparison of structural and electronic properties," *Chem. Phys.*, vol. 262, pp. 1–14, Dec. 2000.

[159] S. Yanagisawa, T. Tsuneda, and K. Hirao, "An investigation of density functionals: The first-row transition metal dimer calculations," *J. Chem. Phys.*, vol. 112, p. 545, Jan. 2000.

[160] M. DoverstaŁl, B. Lindgren, U. Sassenberg, C. A. Arrington, and M. D. Morse, "The 3Π0u X3Δ1g band system of jet-cooled Ti2," *J. Chem. Phys.*, vol. 97, p. 7087, Nov. 1992.

[161] E. M. Spain and M. D. Morse, "Bond strengths of transition-metal dimers: titanium-vanadium(TiV), vanadium dimer, titanium-cobalt (TiCo), and vanadium-nickel (VNi)," *J. Phys. Chem.*, vol. 96, pp. 2479–2486, Mar. 1992.

[162] H. Xin, A. Vojvodic, J. Voss, J. K. Nø rskov, and F. Abild-Pedersen, "Effects of ¡span class="aps-inline-formula"¿¡math¿¡mi¿d¡/mi¿¡/math¿¡/span¿-band shape on the surface reactivity of transition-metal alloys," *Phys. Rev. B*, vol. 89, p. 115114, Mar. 2014.

[163] A. Vojvodic, J. K. Nø rskov, and F. Abild-Pedersen, "Electronic Structure Effects in Transition Metal Surface Chemistry," *Top. Catal.*, vol. 57, pp. 25–32, Nov. 2013.

[164] X. Shao, X. Wu, and W. Cai, "Growth Pattern of Truncated Octahedra in Al N (Nâ 310) Clusters," *J. Phys. Chem. A*, vol. 114, pp. 29–36, Jan. 2009.

[165] P. S. West, R. L. Johnston, G. Barcaro, and A. Fortunelli, "The Effect of CO and H Chemisorption on the Chemical Ordering of Bimetallic Clusters," *J. Phys. Chem. C*, vol. 114, pp. 19678–19686, Nov. 2010.

[166] V. Tripković, F. Abild-Pedersen, F. Studt, I. Cerri, T. Nagami, T. Bligaard, and J. Rossmeisl, "Metal Oxide-Supported Platinum Overlayers as Proton-Exchange Membrane Fuel Cell Cathodes," *ChemCatChem*, vol. 4, pp. 228–235, Feb. 2012.

[167] R. R. Adzic, J. Zhang, K. Sasaki, M. B. Vukmirovic, M. Shao, J. X. Wang, A. U. Nilekar, M. Mavrikakis, J. A. Valerio, and F. Uribe, "Platinum Monolayer Fuel Cell Electrocatalysts," *Top. Catal.*, vol. 46, pp. 249–262, Nov. 2007.

[168] J. Zhang, Y. Mo, M. B. Vukmirovic, R. Klie, K. Sasaki, and R. R. Adzic, "Platinum Monolayer Electrocatalysts for O 2 Reduction: Pt Monolayer on Pd(111) and on Carbon-Supported Pd Nanoparticles," *J. Phys. Chem. B*, vol. 108, pp. 10955–10964, July 2004.

[169] J. Zhang, M. B. Vukmirovic, Y. Xu, M. Mavrikakis, and R. R. Adzic, "Controlling the catalytic activity of platinum-monolayer electrocatalysts for oxygen reduction with different substrates.," *Angew. Chem. Int. Ed. Engl.*, vol. 44, pp. 2132–5, Mar. 2005.

[170] Y. Chen, Z. Liang, F. Yang, Y. Liu, and S. Chen, "NiPt CoreShell Nanoparticles as Oxygen Reduction Electrocatalysts: Effect of Pt Shell Coverage," *J. Phys. Chem. C*, vol. 115, no. 49, pp. 24073–24079, 2011.

[171] J. R. Kitchin, J. K. Nø rskov, M. A. Barteau, and J. G. Chen, "Modification of the surface electronic and chemical properties of Pt(111) by subsurface 3d transition metals.," *J. Chem. Phys.*, vol. 120, pp. 10240–6, June 2004.

[172] B. Hammer and J. Nø rskov, "Electronic factors determining the reactivity of metal surfaces," *Surf. Sci.*, vol. 343, pp. 211–220, Dec. 1995.

[173] V. Stamenkovic, B. S. Mun, K. J. Mayrhofer, P. N. Ross, N. M. Markovic, J. Rossmeisl, J. Greeley, and J. K. Nø rskov, "Changing the Activity of Electrocatalysts for Oxygen Reduction by Tuning the Surface Electronic Structure," *Angew. Chemie*, vol. 118, pp. 2963–2967, Apr. 2006.

[174] L. G. S. Pereira, V. A. Paganin, and E. A. Ticianelli, "Investigation of the CO tolerance mechanism at several Pt-based bimetallic anode electrocatalysts in a PEM fuel cell," *Electrochim. Acta*, vol. 54, pp. 1992–1998, Feb. 2009.

[175] G. Blyholder, "Molecular Orbital View of Chemisorbed Carbon Monoxide," *J. Phys. Chem.*, vol. 68, pp. 2772–2777, Oct. 1964.

[176] B. Hammer, Y. Morikawa, and J. Nø rskov, "CO Chemisorption at Metal Surfaces and Overlayers," *Phys. Rev. Lett.*, vol. 76, pp. 2141–2144, Mar. 1996.

[177] I. Chorkendorff and J. W. Niemantsverdriet, *Concepts of Modern Catalysis and Kinetics*. Wiley-VCH Verlag GmbH & Co. KGaA, 2nd ed., 2006.

[178] G. Kresse, "From ultrasoft pseudopotentials to the projector augmented-wave method," *Phys. Rev. B*, vol. 59, pp. 1758–1775, Jan. 1999.

[179] P. E. Blöchl, "Projector augmented-wave method," *Phys. Rev. B*, vol. 50, pp. 17953–17979, Dec. 1994.

[180] J. Perdew, J. Chevary, S. Vosko, K. Jackson, M. Pederson, D. Singh, and C. Fiolhais, "Erratum: Atoms, molecules, solids, and surfaces: Applications of the generalized gradient approximation for exchange and correlation," *Phys. Rev. B*, vol. 48, pp. 4978–4978, Aug. 1993.

[181] J. P. Perdew, K. A. Jackson, M. R. Pederson, D. J. Singh, C. Fiolhais, J. Chevary, and S. Vosko, "Erratum: Atoms, molecules, solids, and surfaces: Applications of the generalized gradient approximation for exchange and correlation," *Phys. Rev. B*, vol. 46, pp. 6671–6687, Aug. 1992.

[182] D. Sheppard, P. Xiao, W. Chemelewski, D. D. Johnson, and G. Henkelman, "A generalized solid-state nudged elastic band method.," *J. Chem. Phys.*, vol. 136, p. 074103, Feb. 2012.

[183] J. Kästner and P. Sherwood, "Superlinearly converging dimer method for transition state search.," *J. Chem. Phys.*, vol. 128, p. 014106, Jan. 2008.

[184] W. Tang, E. Sanville, and G. Henkelman, "A grid-based Bader analysis algorithm without lattice bias.," *J. Phys. Condens. Matter*, vol. 21, p. 084204, Mar. 2009.

[185] S. M. Kozlov and K. M. Neyman, "Catalysis from First Principles: Towards Accounting for the Effects of Nanostructuring," *Top. Catal.*, vol. 56, pp. 867–873, May 2013.

[186] H. Steininger, S. Lehwald, and H. Ibach, "Adsorption of oxygen on Pt(111)," *Surf. Sci.*, vol. 123, pp. 1–17, Dec. 1982.

[187] C. Puglia, A. Nilsson, B. Hernnäs, O. Karis, P. Bennich, and N. Må rtensson, "Physisorbed, chemisorbed and dissociated O2 on Pt(111) studied by different core level spectroscopy methods," *Surf. Sci.*, vol. 342, pp. 119–133, Nov. 1995.

[188] A. Eichler and J. Hafner, "Molecular Precursors in the Dissociative Adsorption of O2 on Pt(111)," *Phys. Rev. Lett.*, vol. 79, pp. 4481–4484, Dec. 1997.

[189] K. Gustafsson and S. Andersson, "Infrared spectroscopy of physisorbed and chemisorbed O2 on Pt(111).," *J. Chem. Phys.*, vol. 120, pp. 7750–4, Apr. 2004.

[190] Z. Duan and G. Wang, "A first principles study of oxygen reduction reaction on a Pt(111) surface modified by a subsurface transition metal M (M = Ni, Co, or Fe)," *Phys. Chem. Chem. Phys.*, vol. 13, p. 20178, Nov. 2011.

[191] Q. Fu, J. Yang, and Y. Luo, "A First Principles Study on the Dissociation and Rotation Processes of a Single O 2 Molecule on the Pt(111) Surface," *J. Phys. Chem. C*, vol. 115, pp. 6864–6869, Apr. 2011.

[192] A. Smeltz, R. Getman, W. Schneider, and F. Ribeiro, "Coupled theoretical and experimental analysis of surface coverage effects in Pt-catalyzed NO and O2 reaction to NO2 on Pt(111)," *Catal. Today*, vol. 136, pp. 84–92, July 2008.

[193] D. J. Miller, H. Öberg, L.-A. Näslund, T. Anniyev, H. Ogasawara, L. G. M. Pettersson, and A. Nilsson, "Low O2 dissociation barrier on Pt(111) due to adsorbate-adsorbate interactions.," *J. Chem. Phys.*, vol. 133, p. 224701, Dec. 2010.

[194] L. Qi, J. Yu, and J. Li, "Coverage dependence and hydroperoxyl-mediated pathway of catalytic water formation on Pt (111) surface.," *J. Chem. Phys.*, vol. 125, p. 054701, Aug. 2006.

[195] v. Šljivančanin and B. Hammer, "Oxygen dissociation at close-packed Pt terraces, Pt steps, and Ag-covered Pt steps studied with density functional theory," *Surf. Sci.*, vol. 515, pp. 235–244, Aug. 2002.

[196] B. Stipe, M. Rezaei, W. Ho, S. Gao, M. Persson, and B. Lundqvist, "Single-Molecule Dissociation by Tunneling Electrons," *Phys. Rev. Lett.*, vol. 78, pp. 4410–4413, June 1997.

[197] P. Gambardella, v. Šljivančanin, B. Hammer, M. Blanc, K. Kuhnke, and K. Kern, "Oxygen Dissociation at Pt Steps," *Phys. Rev. Lett.*, vol. 87, p. 056103, July 2001.

[198] P. Feibelman, S. Esch, and T. Michely, "O Binding Sites on Stepped Pt(111) Surfaces," *Phys. Rev. Lett.*, vol. 77, pp. 2257–2260, Sept. 1996.

[199] M. Shao, A. Peles, and K. Shoemaker, "Electrocatalysis on Platinum Nanoparticles: Particle Size Effect on Oxygen Reduction Reaction Activity," *Nano Lett.*, vol. 11, no. 9, pp. 3714–3719, 2011.

[200] Z. Duan and G. Wang, "Comparison of Reaction Energetics for Oxygen Reduction Reactions on Pt(100), Pt(111), Pt/Ni(100), and Pt/Ni(111) Surfaces: A First-Principles Study," *J. Phys. Chem. C*, vol. 117, no. 12, pp. 6284–6292, 2013.

[201] P. C. Jennings, B. G. Pollet, and R. L. Johnston, "Theoretical studies of Pt-Ti nanoparticles for potential use as PEMFC electrocatalysts.," *Phys. Chem. Chem. Phys.*, vol. 14, pp. 3134–9, Mar. 2012.

[202] P. C. Jennings, B. G. Pollet, and R. L. Johnston, "Electronic Properties of PtTi Nanoalloys and the Effect on Reactivity for Use in PEMFCs," *J. Phys. Chem. C*, vol. 116, pp. 15241–15250, July 2012.

[203] L. Pauling, *The Nature of the Chemical Bond and the Structure of Molecules and Crystals: An Introduction to Modern Structural Chemistry*. Cornell University Press, 1960.

[204] A. Allred, "Electronegativity values from thermochemical data," *J. Inorg. Nucl. Chem.*, vol. 17, pp. 215–221, June 1961.

[205] E. Clementi and D. L. Raimondi, "Atomic Screening Constants from SCF Functions," *J. Chem. Phys.*, vol. 38, p. 2686, July 1963.

[206] J. Wu and H. Yang, "Synthesis and electrocatalytic oxygen reduction properties of truncated octahedral Pt3Ni nanoparticles," *Nano Res.*, vol. 4, pp. 72–82, Oct. 2010.

[207] J. Wu, J. Zhang, Z. Peng, S. Yang, F. T. Wagner, and H. Yang, "Truncated octahedral Pt(3)Ni oxygen reduction reaction electrocatalysts.," *J. Am. Chem. Soc.*, vol. 132, pp. 4984–5, Apr. 2010.

[208] R. Narayanan and M. A. El-Sayed, "Shape-Dependent Catalytic Activity of Platinum Nanoparticles in Colloidal Solution," *Nano Lett.*, vol. 4, pp. 1343–1348, July 2004.

[209] C. Massen, T. V. Mortimer-Jones, and R. L. Johnston, "Geometries and segregation properties of platinumpalladium nanoalloy clusters," *J. Chem. Soc. Dalt. Trans.*, p. 4375, Nov. 2002.

[210] Y.-Y. Chu, Z.-B. Wang, Z. Dai, D.-M. Gu, and G.-P. Yin, "Synthesis of Truncated-Octahedral Pt-Pd Nanocrystals Supported on Carbon Black as a Highly Efficient Catalyst for Methanol Oxidation," *Fuel Cells*, vol. 14, pp. 49–55, Feb. 2014.

[211] J. Greeley and J. K. Nø rskov, "A general scheme for the estimation of oxygen binding energies on binary transition metal surface alloys," *Surf. Sci.*, vol. 592, pp. 104–111, Nov. 2005.

[212] P. Strasser, S. Koh, T. Anniyev, J. Greeley, K. More, C. Yu, Z. Liu, S. Kaya, D. Nordlund, H. Ogasawara, M. F. Toney, and A. Nilsson, "Lattice-strain control of the activity in dealloyed core-shell fuel cell catalysts.," *Nat. Chem.*, vol. 2, pp. 454–60, June 2010.

[213] M. Mavrikakis, B. Hammer, and J. Nø rskov, "Effect of Strain on the Reactivity of Metal Surfaces," *Phys. Rev. Lett.*, vol. 81, pp. 2819–2822, Sept. 1998.

[214] J. Kitchin, J. Nø rskov, M. Barteau, and J. Chen, "Role of Strain and Ligand Effects in the Modification of the Electronic and Chemical Properties of Bimetallic Surfaces," *Phys. Rev. Lett.*, vol. 93, p. 156801, Oct. 2004.

[215] S. Siahrostami, A. Verdaguer-Casadevall, M. Karamad, D. Deiana, P. Malacrida, B. Wickman, M. Escudero-Escribano, E. A. Paoli, R. Frydendal, T. W. Hansen, I. Chorkendorff, I. E. L. S. Stephens, I. E. Stephens, and J. Rossmeisl, "Enabling direct H2O2 production through rational electrocatalyst design.," *Nat. Mater.*, vol. 12, pp. 1137–43, Dec. 2013.

[216] S. Mukerjee, "Role of Structural and Electronic Properties of Pt and Pt Alloys on Electrocatalysis of Oxygen Reduction," *J. Electrochem. Soc.*, vol. 142, p. 1409, May 1995.

[217] Z. Gu and P. Balbuena, "Absorption of Atomic Oxygen into Subsurfaces of Pt(100) and Pt(111): Density Functional Theory Study," *J. Phys. Chem. C*, vol. 111, pp. 9877–9883, July 2007.

[218] A. Michaelides, Z.-P. Liu, C. J. Zhang, A. Alavi, D. A. King, and P. Hu, "Identification of general linear relationships between activation energies and enthalpy changes for dissociation reactions at surfaces.," *J. Am. Chem. Soc.*, vol. 125, pp. 3704–5, Apr. 2003.

[219] Y. Xu, A. V. Ruban, and M. Mavrikakis, "Adsorption and dissociation of O2 on Pt-Co and Pt-Fe alloys.," *J. Am. Chem. Soc.*, vol. 126, pp. 4717–25, Apr. 2004.

[220] J. Nø rskov, "Universality in Heterogeneous Catalysis," *J. Catal.*, vol. 209, pp. 275–278, July 2002.

[221] I. E. L. Stephens, A. S. Bondarenko, L. Bech, and I. Chorkendorff, "Oxygen Electroreduction Activity and X-Ray Photoelectron Spectroscopy of Platinum and Early Transition Metal Alloys," *ChemCatChem*, vol. 4, pp. 341–349, Mar. 2012.

[222] J. A. Rodriguez and D. W. Goodman, "The nature of the metal-metal bond in bimetallic surfaces.," *Science*, vol. 257, pp. 897–903, Aug. 1992.

[223] L. O. Paz-Borbón, R. L. Johnston, G. Barcaro, and A. Fortunelli, "Structural motifs, mixing, and segregation effects in 38-atom binary clusters.," *J. Chem. Phys.*, vol. 128, p. 134517, Apr. 2008.

[224] "http://www.infomine.com/investment/metal-prices/ (Accessed June 2014)."

[225] J.-H. Choi, K.-W. Park, I.-S. Park, W.-H. Nam, and Y.-E. Sung, "Methanol electrooxidation and direct methanol fuel cell using Pt/Rh and Pt/Ru/Rh alloy catalysts," *Electrochim. Acta*, vol. 50, pp. 787–790, Nov. 2004.

[226] "http://www.metalprices.com/p/CadmiumFreeChart (Accessed June 2014)."

[227] K. Sasaki, H. Naohara, Y. Cai, Y. M. Choi, P. Liu, M. B. Vukmirovic, J. X. Wang, and R. R. Adzic, "Core-protected platinum monolayer shell high-stability electrocatalysts for fuel-cell cathodes.," *Angew. Chem. Int. Ed. Engl.*, vol. 49, pp. 8602–7, Nov. 2010.

[228] S.-Y. Huang, P. Ganesan, and B. N. Popov, "Electrocatalytic Activity and Stability of Titania-Supported PlatinumPalladium Electrocatalysts for Polymer Electrolyte Membrane Fuel Cell," *ACS Catal.*, vol. 2, pp. 825–831, May 2012.

[229] T. Ioroi and K. Yasuda, "Platinum-Iridium Alloys as Oxygen Reduction Electrocatalysts for Polymer Electrolyte Fuel Cells," *J. Electrochem. Soc.*, vol. 152, p. A1917, Oct. 2005.

[230] E. Roduner, "Size matters: why nanomaterials are different.," *Chem. Soc. Rev.*, vol. 35, pp. 583–92, July 2006.

[231] S. Park, S. A. Wasileski, and M. J. Weaver, "Electrochemical Infrared Characterization of Carbon-Supported Platinum Nanoparticles: A Benchmark Structural Comparison with

Single-Crystal Electrodes and High-Nuclearity Carbonyl Clusters," *J. Phys. Chem. B*, vol. 105, pp. 9719–9725, Oct. 2001.

[232] U. Heiz, A. Sanchez, S. Abbet, and W.-D. Schneider, "Catalytic Oxidation of Carbon Monoxide on Monodispersed Platinum Clusters: Each Atom Counts," *J. Am. Chem. Soc.*, vol. 121, pp. 3214–3217, Apr. 1999.

[233] R. M. Watwe, B. E. Spiewak, R. D. Cortright, and J. A. Dumesic, "Density functional theory (DFT) and microcalorimetric investigations of CO adsorption on Pt clusters," *Catal. Letters*, vol. 51, pp. 139–147, May 1998.

[234] K. Mohanraju and L. Cindrella, "Impact of alloying and lattice strain on ORR activity of Pt and Pd based ternary alloys with Fe and Co for proton exchange membrane fuel cell applications," *RSC Adv.*, vol. 4, p. 11939, Feb. 2014.

[235] S. Zhang, S. Guo, H. Zhu, D. Su, and S. Sun, "Structure-induced enhancement in electrooxidation of trimetallic FePtAu nanoparticles.," *J. Am. Chem. Soc.*, vol. 134, pp. 5060–3, Mar. 2012.

[236] B. Fang, J. Luo, P. N. Njoki, R. Loukrakpam, B. Wanjala, J. Hong, J. Yin, X. Hu, J. Last, and C.-J. Zhong, "Nano-engineered PtVFe catalysts in proton exchange membrane fuel cells: Electrocatalytic performance," *Electrochim. Acta*, vol. 55, pp. 8230–8236, Nov. 2010.

[237] C. Lamy, S. Baranton, and C. Coutanceau, "The Electrocatalytic Oxidation of Ethanol in a Proton Exchange Membrane Electrolysis Cell (PEMEC): A Way to Produce Clean Hydrogen for PEFC," *ECS Trans.*, vol. 58, pp. 1907–1921, Oct. 2013.

[238] B. Li and S. H. Chan, "PtFeNi tri-metallic alloy nanoparticles as electrocatalyst for oxygen reduction reaction in proton exchange membrane fuel cells with ultra-low Pt loading," *Int. J. Hydrogen Energy*, vol. 38, pp. 3338–3345, Mar. 2013.

[239] B. Fang, B. N. Wanjala, J. Yin, R. Loukrakpam, J. Luo, X. Hu, J. Last, and C.-J. Zhong, "Electrocatalytic performance of Pt-based trimetallic alloy nanoparticle catalysts in proton exchange membrane fuel cells," *Int. J. Hydrogen Energy*, vol. 37, pp. 4627–4632, Mar. 2012.

Appendix A

Papers Published

PCCP

/ Journal Homepage / Table of Contents for this issue
Dynamic Article Links

Cite this: *Phys. Chem. Chem. Phys.*, 2012, **14**, 3134–3139

www.rsc.org/pccp

PAPER

Theoretical studies of Pt–Ti nanoparticles for potential use as PEMFC electrocatalysts

Paul C. Jennings,[a] Bruno G. Pollet[a] and Roy L. Johnston*[b]

Received 31st October 2011, Accepted 5th January 2012
DOI: 10.1039/c2cp23430k

A theoretical investigation is presented of alloying platinum with titanium to form binary Pt–Ti nanoalloys as an alternative to the expensive pure platinum catalysts commonly used for Proton Exchange Membrane Fuel Cell cathode electrocatalysts. Density Functional Theory calculations are performed to investigate compositional effects on structural properties as well as Oxygen Reduction Reaction kinetics and poisoning effects. High symmetry A_{32}–B_6 clusters are studied to investigate structural properties. From these structures binding energies of hydroxyl and carbon monoxide are studied on a range of sites on the surface of the clusters. Promising results are obtained suggesting that the bimetallic Pt–Ti nanoalloys may exhibit enhanced properties compared to pure platinum catalysts.

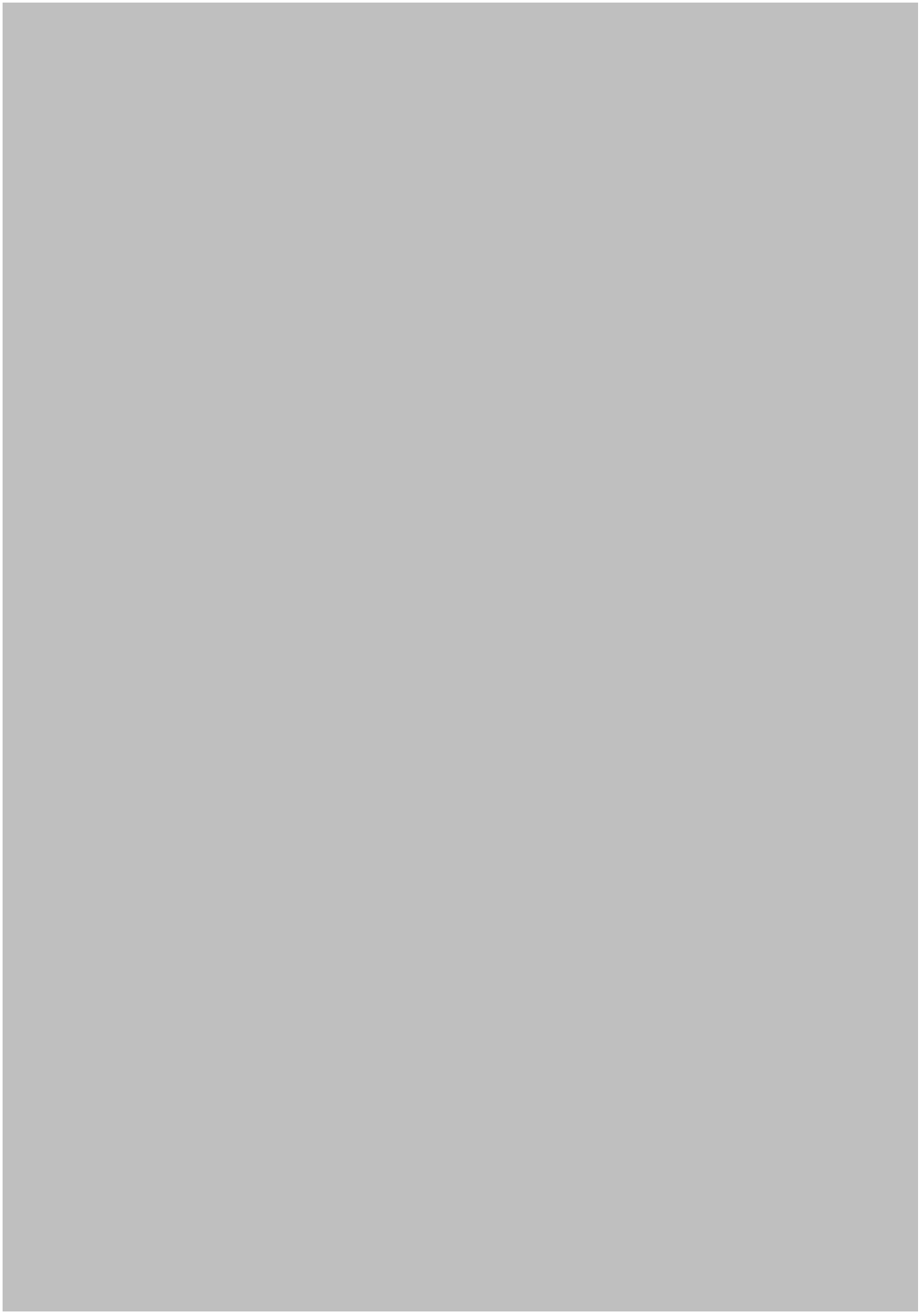

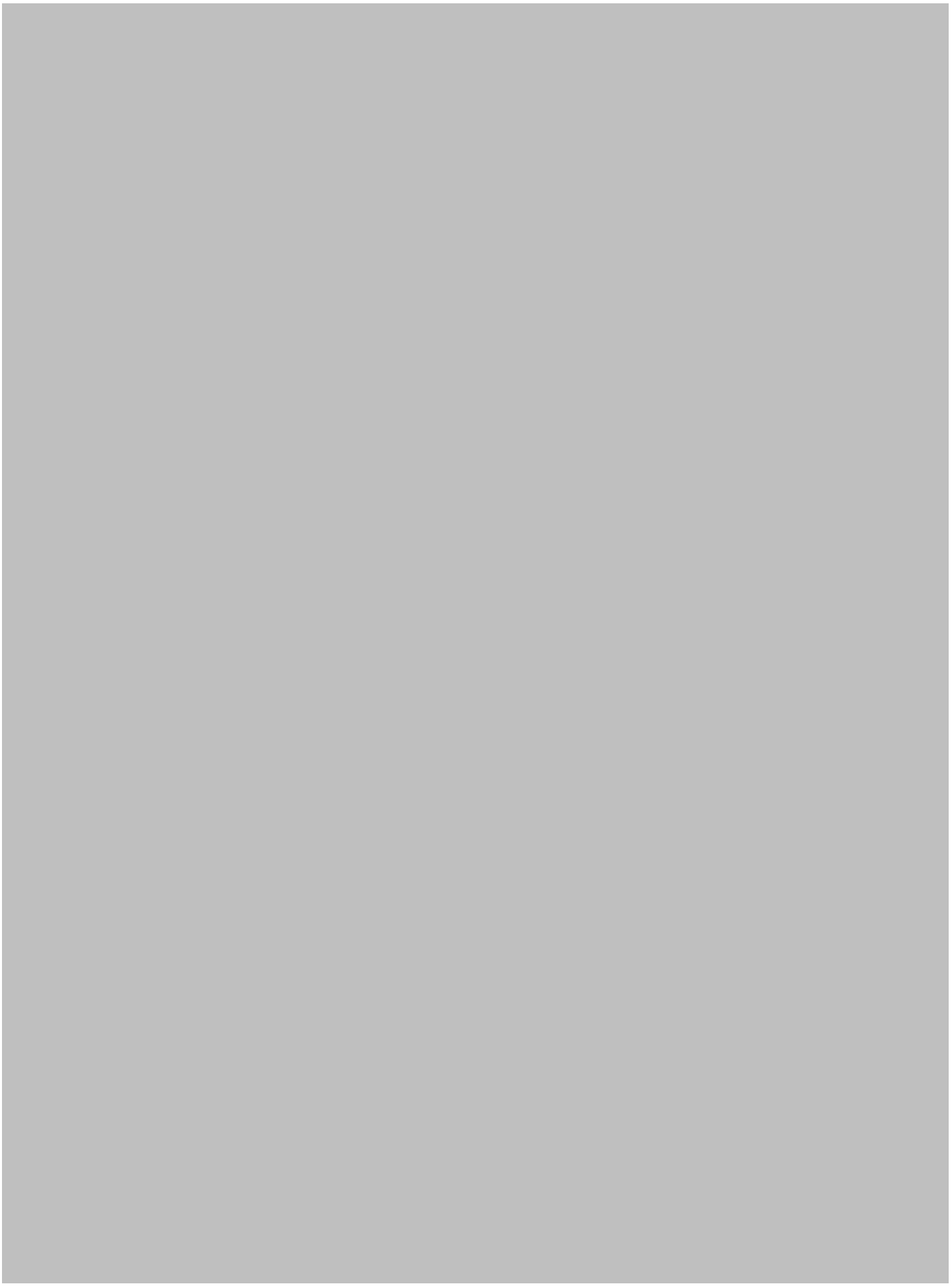

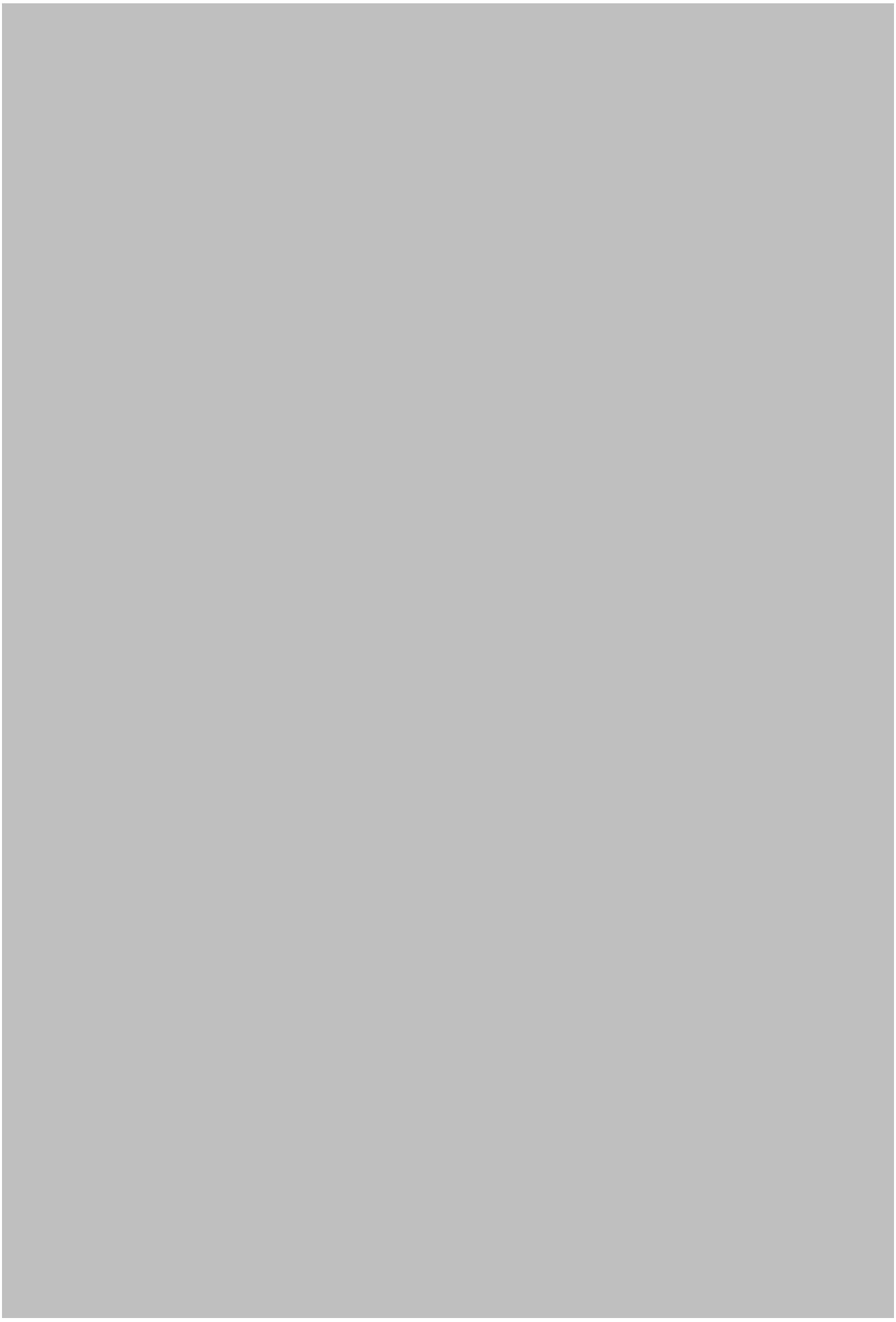

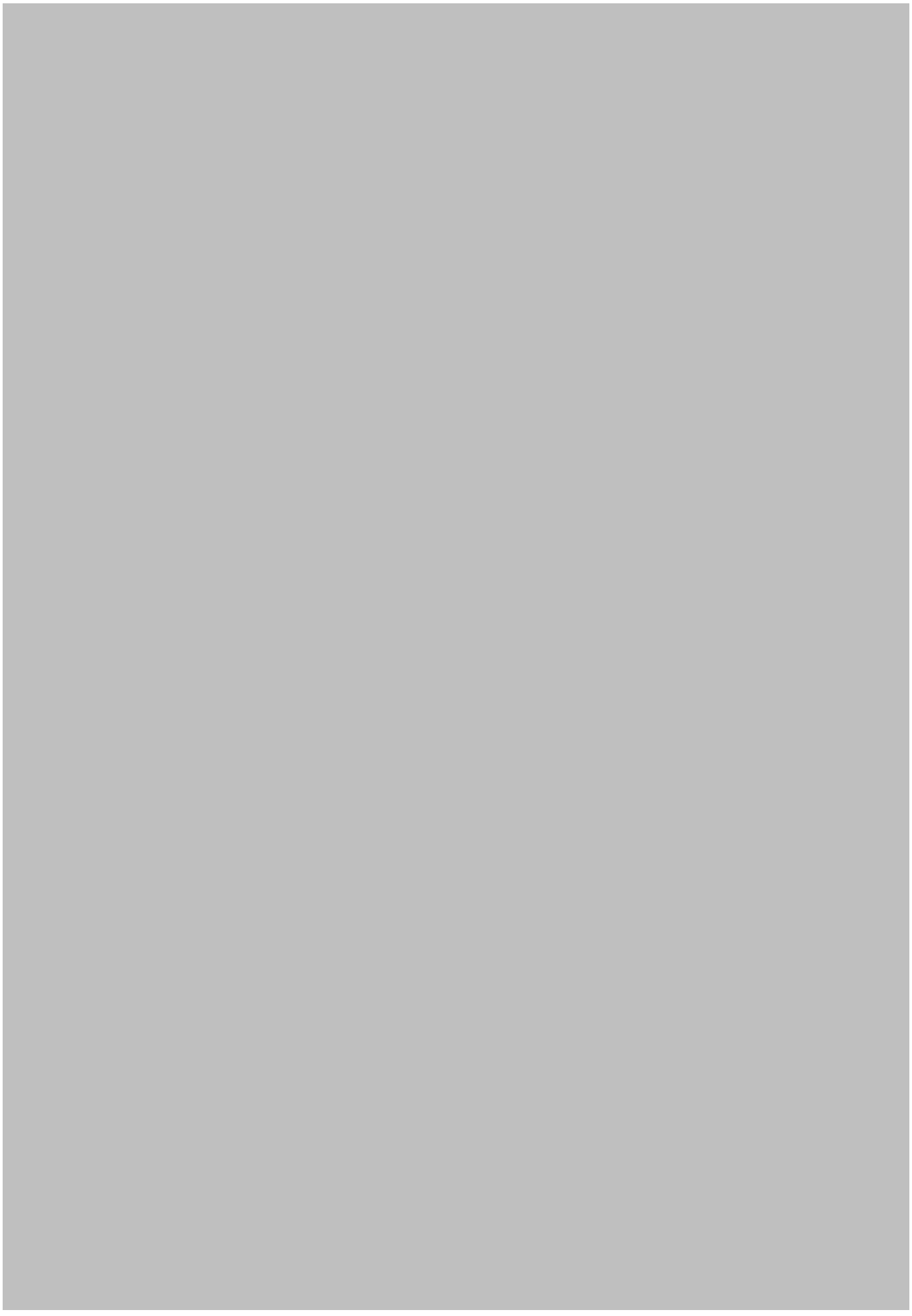

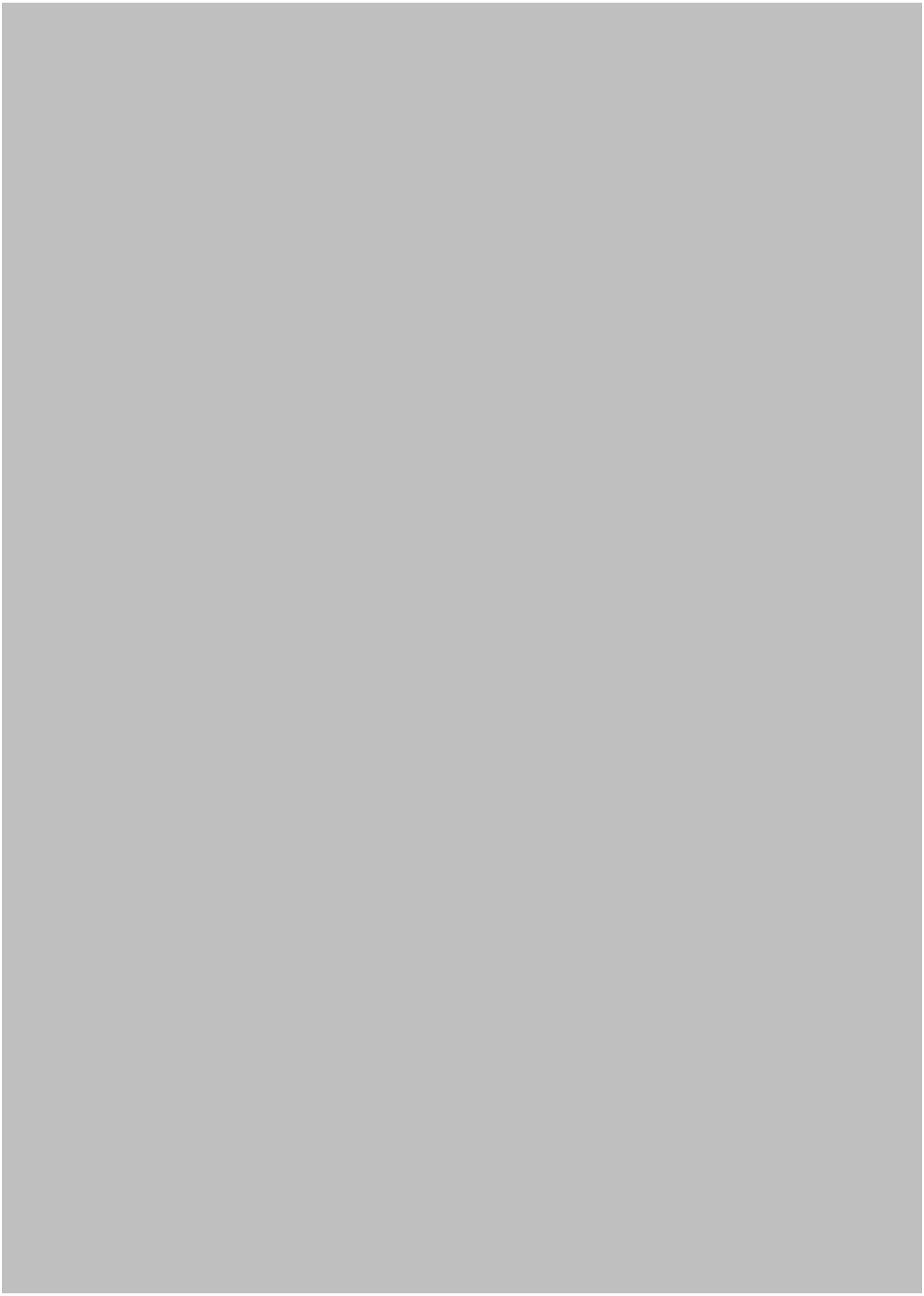

THE JOURNAL OF PHYSICAL CHEMISTRY C

Article

pubs.acs.org/JPCC

Electronic Properties of Pt−Ti Nanoalloys and the Effect on Reactivity for Use in PEMFCs

Paul C. Jennings,[†] Bruno G. Pollet,[‡] and Roy L. Johnston*[,§]

[†]PEM Fuel Cell Research group, School of Chemical Engineering, Centre for Hydrogen and Fuel Cell Research, The University of Birmingham, Edgbaston, Birmingham B15 2TT, U.K.

[‡]HySA Systems, SAIAMC, University of the Western Cape, Private Bag X17, Modderdam Road, Bellville 7535, Cape Town, South Africa

[§]School of Chemistry, The University of Birmingham, Edgbaston, Birmingham B15 2TT, U.K.

ABSTRACT: Theoretical investigations of Pt−Ti nanoparticles are presented using density functional theory (DFT) to study clusters up to sizes of 1.7 nm (201 atoms). Several compositions have been studied for varying sizes, and a projected density of states analysis has been performed. Changes in *d*-band properties have been correlated with differences in OH and CO binding energies with relation to changes in composition. It was found that a Pt-rich Pt−Ti alloy shows promise for potential use in a PEMFC with the alloy resulting in a downshift in *d*-center, compared to pure Pt clusters, which correlates with a weakening of the OH and CO adsorption energies. Furthermore, it was observed that varying the size of the cluster gives rise to changes in the *d*-band center with larger clusters typically having a more negative *d*-band center, although values obtained are not as negative as the *d*-band center for bulk Pt_3Ti reported in the literature.

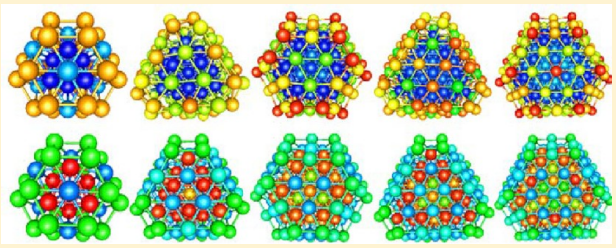

Computational and Theoretical Chemistry 1021 (2013) 91–100

Contents lists available at SciVerse ScienceDirect

Computational and Theoretical Chemistry

journal homepage: www.elsevier.com/locate/comptc

Structures of small Ti- and V-doped Pt clusters: A GA-DFT study ☆

P.C. Jennings [a], R.L. Johnston [b,*]

[a] School of Chemical Engineering, University of Birmingham, Edgbaston, Birmingham B15 2TT, UK
[b] School of Chemistry, University of Birmingham, Edgbaston, Birmingham B15 2TT, UK

ARTICLE INFO

Article history:
Received 17 May 2013
Received in revised form 25 June 2013
Accepted 25 June 2013
Available online 5 July 2013

Keywords:
Clusters
Platinum
Titanium
Vanadium
GA-DFT

ABSTRACT

High level GA-DFT searches are performed on small platinum clusters doped with early transition metal atoms, $Pt_{x-y}M_y$ (M = Ti, V), where $x = 2–6$, $y = 1, 2$. Spin effects are studied and the global minimum structures are presented for the various spin multiplicities. It is found that varying spin can have significant effects on the pure Pt clusters, while spin has less effect for the doped clusters.

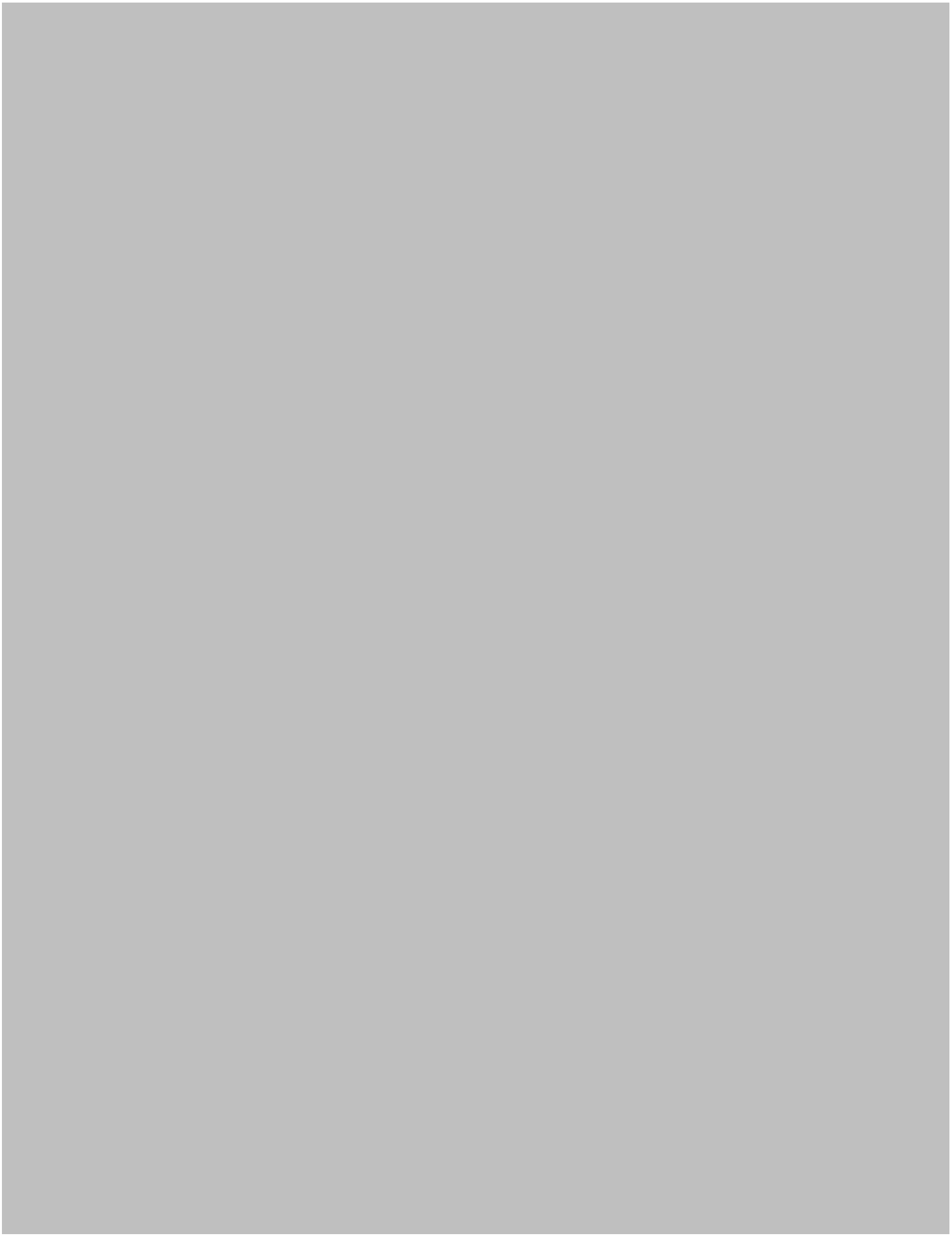

Nanoscale

PAPER

Cite this: *Nanoscale*, 2014, **6**, 1153

A DFT study of oxygen dissociation on platinum based nanoparticles†

Paul C. Jennings,[a] Hristiyan A. Aleksandrov,[bc] Konstantin M. Neyman[bd] and Roy L. Johnston*[e]

Received 5th September 2013
Accepted 13th November 2013

DOI: 10.1039/c3nr04750d

www.rsc.org/nanoscale

Density functional theory calculations are performed on 38 and 79 metal atom truncated octahedron clusters to study oxygen dissociation as a model for the initial stage of the oxygen reduction reaction. Pure platinum and alloyed platinum–titanium core–shell systems are investigated. It is found that barrierless oxygen dissociation occurs on the (111) facet of the pure platinum clusters. A barrier of ~0.3 eV is observed on the (100) facet. For the alloyed cluster, dissociation barriers are found on both facets, typically ~0.6 eV. The differences between the two systems are attributed to the ability of oxygen to distort the (111) surface of the pure platinum clusters. We show that flexibility of the platinum shell is crucial in promotion of fast oxygen dissociation. However, the titanium core stabilises the platinum shell upon alloying, resulting in a less easily distortable surface. Therefore, whilst an alloyed platinum-titanium electrocatalyst has certain advantages over the pure platinum electrocatalyst, we suggest alloying with a more weakly interacting metal will be beneficial for facilitating oxygen dissociation.